

# Mechanistic investigations of dynamics in supramolecular polymer networks

Dissertation

zur Erlangung des Doktorgrades der Naturwissenschaften  
(Dr. rer. nat.)

der  
Naturwissenschaftlichen Fakultät II  
Chemie, Physik und Mathematik

der Martin-Luther-Universität  
Halle-Wittenberg

vorgelegt von

**Anton Mordvinkin**

geboren am 13. Juli 1989 in Volzhsky

Gutachter:

1. Prof. Dr. Kay Saalwächter (Martin-Luther-Universität Halle-Wittenberg)
2. Prof. Dr. Mario Beiner (Martin-Luther-Universität Halle-Wittenberg)
3. Prof. Dr. Michael Vogel (Technische Universität Darmstadt)

Öffentliche Verteidigung: 04.12.2019

”All models are wrong, but some are useful.”

George E. P. Box (1919-2013)



# Contents

<b>1</b>	<b>Introduction: supramolecular polymer networks</b>	<b>1</b>
<b>2</b>	<b>Static and dynamic properties of polymer chains</b>	<b>5</b>
2.1	Polymer chain conformation . . . . .	5
2.2	Rubber elasticity . . . . .	7
2.3	Polymer dynamics . . . . .	8
2.3.1	(Sticky) Rouse model . . . . .	8
2.3.2	(Sticky) reptation model . . . . .	12
<b>3</b>	<b>NMR fundamentals</b>	<b>17</b>
<b>4</b>	<b>Used NMR methods</b>	<b>19</b>
4.1	The Free Induction Decay and Magic-Sandwich Echo . . . . .	19
4.2	Proton MQ NMR . . . . .	21
<b>5</b>	<b>Power-law segmental orientation autocorrelation function</b>	<b>29</b>
<b>6</b>	<b>The OACF master curve construction: Model cases</b>	<b>37</b>
6.1	Reptating polymer melts . . . . .	37
6.2	Unentangled telechelic polymer networks . . . . .	40
6.3	Highly inhomogeneous polymer networks . . . . .	43
6.4	Systematic errors due to a too large temperature increment . . . . .	46
<b>7</b>	<b>Objects of investigation</b>	<b>49</b>
7.1	Bromobutyl rubber samples . . . . .	49
7.2	Telechelic poly(isobutylene) samples . . . . .	50
<b>8</b>	<b>Sticky chain and sticker dynamics in entangled butyl rubber ionomers</b>	<b>53</b>
8.1	Structural analysis by SAXS . . . . .	53
8.2	Dynamic and structural studies by $^1\text{H}$ MQ NMR . . . . .	57
8.2.1	Quasi-static analysis of $^1\text{H}$ MQ NMR data . . . . .	57
8.2.2	Assessment of the OACF shape . . . . .	62
8.3	Structural and dynamic studies by DMA. Correlation with the $^1\text{H}$ MQ NMR . . . . .	68
8.4	Sticker dynamics by broadband dielectric spectroscopy . . . . .	72
8.5	Influence of internal stresses on the effective bond lifetime . . . . .	76
8.6	Summary . . . . .	78
<b>9</b>	<b>Dynamics in micellar networks of telechelic PIBs</b>	<b>81</b>
9.1	Identification of the micellar network structure by SAXS . . . . .	81
9.2	Phase composition analysis by NMR relaxometry . . . . .	85
9.3	Sticky dynamics of telechelic chains by MQ NMR and rheology . . . . .	85
9.4	Intra-aggregate dynamics by dielectric spectroscopy . . . . .	95

9.5 Summary . . . . .	99
<b>10 Summary</b>	<b>101</b>
<b>A Experimental Details</b>	<b>105</b>
A.1 SAXS measurements . . . . .	105
A.2 Solid-state NMR experiments . . . . .	105
A.3 Mechanical experiments . . . . .	108
A.4 Broadband dielectric spectroscopy (DS) . . . . .	109
A.4.1 Analysis of dielectric spectra . . . . .	109
<b>B Supplementary results</b>	<b>111</b>
B.1 Supplementary SAXS results . . . . .	111
B.2 Supplementary NMR results . . . . .	112
B.3 Supplementary mechanical results (DMA, rheology) . . . . .	116
B.3.1 Influence of the used frequency window on the bond lifetime extracted from a master curve. . . . .	116
B.4 Supplementary dielectric spectroscopy results . . . . .	121
B.5 Influence of free, unbound alkylimidazoles on dynamic properties. Data reproducibility . . . . .	123
<b>References</b>	<b>125</b>

# 1 Introduction: supramolecular polymer networks

Synthetic polymers have become ubiquitous and nowadays it is hard to imagine our life without them. They enjoy diverse applications in nearly all areas of human life ranging from household everyday products, such as packaging materials (bottles, films), clothing, and disposable tableware, up to automotive, aircraft, and aerospace industries requiring high-performance materials [1, 2].

However, technological progress pushes the limits of polymer science further by a constant demand for new innovative solutions to various challenges around us. The central challenges faced by polymer science are material improvements endowing polymers with new functional properties which would render them more durable, versatile, and sustainable. The significance of durability enhancement of polymer materials can be exemplified by the following statistics: at the moment of writing of this thesis, one serious commercial aircraft accident (in 2001) and seven further incidents involving exclusively the failure of polymer composite materials have been reported in total [3, 4]. Thus, one can see that the durability of currently used polymer materials can be further improved. The durability of polymer materials in the aircraft industry is becoming even more relevant with time, as the weight fraction of polymer composite materials used for aircraft construction increases, e.g. the Boeing 777 comprises around 10% of polymer composites by weight [5], whereas in the currently newest Boeing 787 the fraction of polymer composites amounts already to 50% [6]. The challenge of sustainability has been gaining in importance over the years in the light of oil depletion and enormous amounts of plastic wastes polluting our environment. To be more exact, currently the total oil consumption for the production of polymer materials constitutes around 8% of the extracted oil, and rubber waste in the form of used tires alone amounts to 17 million tons annually, which can be nowadays re-used or recycled only up to 60% (at least in Europe, in other countries the statistics can be worse) with the rest 5% and 35% to be landfilled or burnt for energy recovery, respectively, with the latter bringing back only around 30% of the invested oil energy [7, 8]. The prolongation of the lifetime of used materials, related to the mentioned material durability, can thus also help reduce the amounts of consumed oil, plastic wastes, and energy losses. To address the mentioned challenges at once, one can resort to modification of conventional polymer materials by means of attachment of supramolecular moieties (stickers) to polymer chains.

Supramolecular moieties enable polymer chains to establish reversible bonds between each other, which are stable at operating temperatures and become labile as the temperature increases [9], leading to formation of dynamic networks. The reversibility imparts a number of valuable properties to polymers encompassing stimuli response [10], including shape memory [10–13], self-healing [14–17], and, importantly for thermosets, recyclability [18, 19] and melt processability [20], which paves the way for new potential applications in various fields such as (but not restricted to) biomedicine (artificial muscles, drug-delivery systems [21–23]), robotics (actuators [22–24]), electronics (sensors [24]), automotive and aerospace industries (self-healing structural and coating materials [25–27]).

In this work, we studied two sets of samples consisting of (i) relatively simple model systems of unentangled poly(isobutylene) (PIB) chains of a well-defined size, end-functionalized with hydrogen-bonding species, differing in molecular architecture and sticker strength as well as (ii) more complex entangled PIB systems (bromobutyl rubbers, BIIR) featuring a wide distribution of chain sizes with laterally introduced ionic moieties of a variable attraction strength. Previously, the systems were established as dynamic networks possessing intrinsic "self-healing"<sup>1</sup> properties [16, 17, 28–30]. The main objective of the given work was an investigation of effects of molecular details on the microscale dynamics, which is a central aspect in understanding of macroscopic properties.

Clearly, to purposefully tune properties of dynamic networks, one needs to establish the relationship between microscale dynamics of reversible bonds and macroscopic responses such as shear modulus, conductivity, or self-healing efficiency. The characterization of supramolecular polymer networks providing insights into a dynamic mechanism on different time scales is a complex task requiring employment of several methods within one study. A combination of small angle scattering techniques, dynamic mechanical analysis (DMA) or rheology, infrared spectroscopy (IR), and broad-band dielectric spectroscopy (BDS) proved to be insightful to deliver a detailed elucidation of a structural picture and dynamic mechanisms of systems with reversible bonding [31–36]. Also, transmission electron microscopy (TEM) was used to visualize supramolecular aggregates [37, 38]. Notably, the correlation of DMA/rheology and BDS data showed that the bond lifetimes of the interacting supramolecular groups found by the two methods can be either similar [32, 39] or differ by a factor of 100 [33, 36, 39], depending on whether the density of stickers is large or not, respectively. In the case of sparsely arranged stickers, the large difference in the observed time scales was explained by the assumption that BDS detects a single bond opening event (bare bond lifetime  $\tau_{\text{st}}$ ), whereas DMA/rheology is more sensitive to large-scale relaxations such as aggregate exchange, which occurs only after numerous dissociation/association processes (renormalized, effective bond lifetime  $\tau_{\text{st}}^*$ ) [36, 40]. In contrast, in this work it will be shown that BDS does not necessarily always deliver the bare bond lifetime and the theory on the molecular picture with numerous returns to the initial partner should be revisited for the case of aggregates. Specifically, it will be shown that rheology is sensitive to sticky dynamics of a single chain, as opposed to a model of macroscopic micellar rearrangement driving the stress relaxation, proposed by Semenov and Rubinstein [41].

To unambiguously study sticky dynamics on a microscale, solid-state Nuclear Magnetic Resonance (NMR) can be readily utilized. In numerous previous works the molecular dynamics of supramolecular polymers was studied only qualitatively by the analysis of the spectral width [42], transverse relaxation times [43], chemical shift [44], dipolar couplings [45–47], or shapes of <sup>2</sup>H NMR spectra [48]. Further, in a number of NMR studies a quantification of segmental dynamics of supramolecular polymer systems was performed via  $T_1$  measurements [49, 50], which are, however, sensitive to fast nanosecond motions,

---

<sup>1</sup>strictly speaking, the materials cannot be called self-healing due to the lack of permanent junctions imparting the solid properties

---

so that merely the effects of the supramolecular groups on the chain's flexibility could be estimated. Recently, utilizing neutron scattering, Monkenbusch et al. [51] managed to pinpoint the supramolecular bond lifetime of hydrogen-bonded assembly of short end-modified poly(ethylene oxide) chains. To this end, they fitted neutron spin echo decays with the Rouse-model-based theoretical prediction accounting for the reduction of chain modes as a result of scissions of supramolecular chains, where the translational diffusion coefficients predetermined by pulsed field gradient NMR were plugged in. Although the theoretical predictions were in good agreement with the experimental data, the analytical model holds true only for the specific case of unentangled linear associates. Therefore, various deviations such as a different polarity of a polymer backbone, a network formation, or a presence of entanglements would change the dynamic mechanism and necessitate the use of a more refined model.

In the given thesis, it will be shown how to extract an effective bond lifetime in a model-free way relying on multiple-quantum (MQ) NMR, which can be used for dynamic studies of any system in question [52]. Brown et al. [53] have shown first how  $^1\text{H}$  MQ NMR can be employed to determine supramolecular bond lifetimes of small molecules. Here, in turn, we will show for the first time the extraction of supramolecular bond lifetimes of associating macromolecules.

The thesis is structured as follows. In Chapter 2, we firstly present static and dynamic properties of polymer chains without and with attached stickers, respectively, and introduce therein relevant aspects of rubber elasticity, Doi-Edwards' tube model as well as sticky Rouse and sticky reptation models. Then, an essential NMR theory and all used NMR experiments are detailed in Chapters 3 and 4, respectively. Subsequently, we introduce a power-law model of the segmental autocorrelation function in Chapter 5 which enables us to study segmental dynamics of polymeric systems using MQ NMR data. The power-law model is firstly tested on reference samples such as polymer melts of various molecular weights and permanent networks with different structural homogeneity, followed by discussion of its systematic errors in Chapter 6. Finally, experimental results of a multitechnique study of ionic BIIR and telechelic PIB samples are presented in Chapters 8 and 9, respectively, which are then summarized in Chapter 10.



## 2 Static and dynamic properties of polymer chains

### 2.1 Polymer chain conformation

A polymer chain manifests itself as a long macromolecule consisting of numerous connected repetitive monomeric units. Owing to the entropic reasons, suggesting a larger variety of different coiled conformations as compared to extended conformations, in equilibrium, in the amorphous state, a polymer chain takes on a conformation of a so-called random coil. A random coil is not related to some fixed conformation common for the whole ensemble of polymer chains and not frozen in time, but rather represents a family of all possible coiled conformations experiencing constant temporal changes of state following the Boltzmann statistics. The size of such a polymer random coil can be described by its end-to-end distance  $\vec{R} \equiv R$ , being a vector quantity comprising the sum of all bond vectors of the macromolecule. Since there is no preferred orientation of a polymer chain, the magnitude of the end-to-end distance averaged over all bond orientations is zero, i.e.  $\langle R \rangle = 0$ . Therefore, instead we use the mean-square average  $\langle R^2 \rangle$  (to be more exact, the square root of this average  $\sqrt{\langle R^2 \rangle}$ , called the root-mean-square average) to characterize the size of a random coil, which is the simplest non-zero average.  $\langle R^2 \rangle$  for the polymer chain with  $n$  bonds of length  $l$  (for simplicity a root-mean-square average of all bonds is taken) can be found as follows [54]:

$$\langle R^2 \rangle = \left\langle \sum_{i=1}^n \sum_{j=1}^n \vec{l}_i \vec{l}_j \right\rangle = \sum_{i=1}^n \langle (\vec{l}_i)^2 \rangle + 2 \sum_{i=1}^n \sum_{j>i}^n \langle \vec{l}_i \vec{l}_j \rangle = nl^2 + 2 \sum_{i=1}^n \sum_{j>i}^n \langle \vec{l}_i \vec{l}_j \rangle \quad (2.1)$$

The relation 2.1 depicts the size of a real chain with consideration of orientational restrictions imposed by the microstructure: bond and torsional angles ( $\theta$  and  $\phi$ , respectively) that render different bonds orientationally correlated ( $\langle \vec{l}_i \vec{l}_j \rangle \neq 0$ ). In particular, torsional angles can take on three most energetically stable states, called trans ( $t, \phi = 0^\circ$ ) and (+/-)-gauche ( $g_{+/-}, \phi = \pm 120^\circ$ ). Trans conformations lead to extended parts of the chain, whereas gauche conformations are responsible for chain turns.

The total influence of the microstructure on  $\langle R^2 \rangle$  can be regarded by a quantity called the characteristic ratio  $C_\infty$ . Eq. 2.1 takes then the form:

$$\langle R^2 \rangle = C_\infty nl^2 \quad (2.2)$$

$C_\infty$  is a measure of stiffness of a polymer chain and ranges from 4 to 12 for different polymers [54]. In the special case of  $C_\infty = 1$ , the backbone bonds are completely orientationally uncorrelated with respect to each other. Such hypothetical chains are called freely jointed chains. In practice, it is possible to substitute real chains with equivalent freely-jointed chains (Kuhn chains) by combining several monomeric units in larger seg-

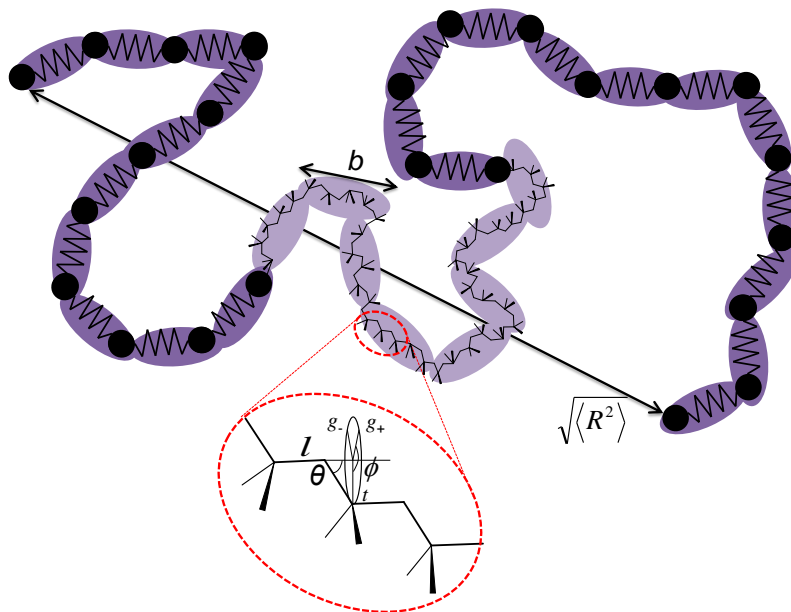


**Figure 2.1:** Random coil of size  $\sqrt{\langle R^2 \rangle}$  on the example of poly(isobutylene). The purple ovals denote Kuhn segments with the length of  $b$ , containing about 5 monomeric units each. A combination of beads and springs is an alternative representation of a Gaussian chain. The ovals in the middle and the enlargement show microstructure details.

ments that become orientationally uncorrelated, see Fig. 2.1 for details. The mean-square end-to-end distance of a Kuhn chain reads [54–56]:

$$\langle R^2 \rangle = Nb^2, \quad (2.3)$$

where  $b$  is the length of a Kuhn segment,  $N$  is the number of Kuhn segments in the chain. To define a unique value for  $b$ , one needs to additionally express the length of a fully extended chain, the contour length  $L$ :

$$L = Nb \quad (2.4)$$

Thus, knowing  $\langle R^2 \rangle$  and  $L$ , equal to the corresponding quantities of a real chain, the Kuhn segment length can be defined as:

$$b = \frac{\langle R^2 \rangle}{L}. \quad (2.5)$$

As was mentioned above, the Kuhn model assumes that Kuhn segments can take on any orientation, meaning that remote parts of the chain are allowed to cross (ideal chains), which is in reality certainly not the case. The inability of real chain segments to cross is driven by excluded volume interactions. The excluded volume interactions lead to an increase of the chain's size in dilute polymer solutions, but are screened in melts, which

implies that Eq. 2.3 remains valid.

Since Kuhn segments possess random orientations and are statistically uncorrelated, the end-to-end distance  $R$ , being the sum of all Kuhn segments, follows the normal distribution according to the central limit theorem [57]:

$$P(R) = \left( \frac{3}{2\pi Nb^2} \right)^{3/2} \exp\left( -\frac{3R^2}{2Nb^2} \right) \quad (2.6)$$

The chains that manifest the normal distribution of  $R$  on all length scales, i.e. for every subchain chosen within the given chain, resulting in  $L \rightarrow \infty$ , are called Gaussian (or Brownian) chains. This property of chains is of fractal nature and called self-similarity. Strictly speaking, the equality 2.6 is valid for  $b \ll R \ll L$ , and, therefore, can be used for description of chain conformation of long chains in the unperturbed state or at small deformations [55, 56]. Gaussian chains can also be represented as a combination of beads connected by springs with a harmonic potential, since such a representation provides the same set of available conformations in equilibrium. The bead-spring representation will be seen to be convenient for description of polymer dynamics [58], see Section 2.3.

## 2.2 Rubber elasticity

If to connect flexible polymer chains in a common network by chemical bonds, one obtains a rubber material featuring a unique reversible extensibility up to hundreds percents of the original length. This phenomenon is called rubber elasticity. Rubber elasticity is, as a rule, of entropic origin, meaning that the force needed to stretch a rubber sample is directed exclusively to reduction of the (conformational) entropy, which takes place as a result of increase of the end-to-end distance upon stretching [55, 59]. The stress exerted on the rubber material upon uniaxial stretching, assuming affine deformation, Gaussian network chains, and incompressibility (constant volume), can be found as:

$$\sigma_{\text{eng}} = n_c k_B T \left( \lambda - \frac{1}{\lambda^2} \right), \quad (2.7)$$

where  $\sigma_{\text{eng}}$  is the engineering stress, equal to the force divided by the original cross-section,  $n_c$  is the number density of network chains ( $= \rho N_A / M_x$ ,  $\rho$ : the mass density,  $N_A$ : the Avogadro constant,  $M_x$ : the molecular weight of network chains),  $k_B$  is the Boltzmann constant,  $T$  is the absolute temperature,  $\lambda$  is the extension ratio, equal to  $\epsilon + 1$ , with  $\epsilon$  being the strain.

The proportionality to  $T$  in Eq. 2.7 indicates the entropic origin, mentioned above. The elastic modulus  $E$  for the affine model, found in the linear regime at  $\lambda = 1$ , is then:

$$E = 3G = \frac{3\rho RT}{M_x}, \quad (2.8)$$

where  $G$  is the shear modulus,  $R$  is the gas constant.

The assumptions made for derivation of  $\sigma_{\text{eng}}$  and  $E$ , although enabling correct qualitative predictions, do not take into account several aspects: (i) cross-links can fluctuate; (ii) a network contains inelastic defects (loops, dangling chains); (iii) network chains can cross leading to entanglements; (iv) polymer chains have a finite length. The aspects (i) and (ii) lead to lower real  $\sigma_{\text{eng}}$  and  $E$ , as compared to their predictions from Eqs. 2.7 and 2.8, respectively. In turn, the aspect (iii) leads to a larger effective  $E$ , as entanglements can carry stress too, and a lower real  $\sigma_{\text{eng}}$  at intermediate strains, as compared to predictions from Eq. 2.7, owing to disentanglements of polymer chains under deformation (strain softening). In the linear regime, entanglements can be accounted by a simple addition of the entanglement plateau modulus  $E_e = 3\rho RT/M_e$  of an equivalent uncrosslinked melt, where  $M_e$  is the molecular weight of the entangled strand. Finally, the aspect (iv) causes a real  $\sigma_{\text{eng}}$  at large strains to exceed its theoretical prediction (strain hardening) and ultimately diverge upon  $R \rightarrow L$  because of the resistance of chemical bonds (finite extensibility), which is a result of violation of Eq. 2.6 for subchains approaching the size of a Kuhn segment [55, 59]. To account for the aforementioned deviations, more sophisticated models must be employed such as phantom network (for (i)), Edwards-Vilgis, or Davidson-Goulbourne models (for (iii) and (iv)) [60–63].

## 2.3 Polymer dynamics

In the following section, details on dynamics of unentangled and entangled polymers will be given. Additionally, the effects of stickers on polymer dynamics will be covered for both cases. The microscopic dynamics will be studied in the form of the segmental orientational autocorrelation function (OACF,  $C(t)$ ), readily accessed by MQ NMR.  $C(t)$  can be found according to the following relation:

$$C(t) = 5 \langle P_2(\cos \theta(t)) P_2(\cos \theta(0)) \rangle, \quad (2.9)$$

where  $\theta$  is the segmental orientation with respect to a reference direction (external magnetic field), the brackets  $\langle \dots \rangle$  represent the ensemble and time average.  $C(t)$  gives the probability to find the polymer segment in the same orientation after some time  $t$ . Subsequently, since  $C(t)$  is proportional to the tube survival probability in the Doi/Edwards/de Gennes model, and is thus proportional to the shear relaxation modulus,  $C(t)$  will be compared with the macroscopic dynamic storage modulus based on the microscopic picture.

### 2.3.1 (Sticky) Rouse model

Dynamics of melts of unentangled polymer chains can be successfully described by the Rouse model [64]. The Rouse model employs the aforementioned bead-spring representation of a Gaussian chain, wherein beads experience friction upon coordinated thermal motion and can interact only through harmonic springs of root-mean-square size  $b$ , close to the Kuhn length. Originally, the Rouse model was devised for the case of dilute so-

lutions, with the friction being the result of interactions of beads with solvent molecules causing the viscous drag. However, since hydrodynamic interactions are excluded in the Rouse model, it turned out to be only valid for concentrated polymer solutions or polymer melts, where the hydrodynamic interactions are screened. In this limit, the beads' friction is defined by the effective melt viscosity of surrounding polymer molecules. The thermal motion of connected beads can be described by the force balance of the Langevin equation:

$$\underbrace{\xi \frac{d\vec{r}_i}{dt}}_{F_{\text{vis},i}} = \underbrace{\frac{k_B T}{b^2} (r_{i+1} + r_{i-1} - 2r_i)}_{F_{\text{el},i}} + F_{\text{v},i}, \quad (2.10)$$

where  $F_{\text{vis},i}$  denotes the viscous force, with  $\xi$  being the friction coefficient of an individual bead and  $d\vec{r}_i/dt$  the velocity of the  $i$ -th bead;  $F_{\text{el},i}$  is the elastic force, including the spring constant  $k_B T/b^2$  and the radius-vectors  $\vec{r}_i$ ,  $\vec{r}_{i+1}$ ,  $\vec{r}_{i-1}$  of the  $i$ -th,  $(i+1)$ -th, and  $(i-1)$ -th beads, respectively;  $F_{\text{v},i}$  is the random thermal force involving all the forces arising due to collisions between the molecules,  $F_{\text{v},i}$  pertains to the friction coefficient via the fluctuation-dissipation theorem [55, 56, 58, 64].

One can solve the system of equations 2.10 by introduction of normal modes (cosine transformations of beads' positions), which are independent from each other. The solution reads:

$$\tau_p(T) = \frac{\xi(T)b^2}{3\pi^2 k_B T} \left( \frac{N}{p} \right)^2, \quad (2.11)$$

where  $N$  is the number of springs in a polymer chain,  $p$  is the mode index.

As can be seen, all subchains with  $N/p$  segments within the actual chain relax in the same way as their whole-chain counterparts would do. Also, larger  $p$  corresponds to shorter subchains. In particular,  $p = 1$  is related to relaxation of the whole chain ( $\tau_R$ , the Rouse time),  $p = N/N_e$  corresponds to motions of the part of the chain between two entanglements that are not considered in the Rouse model, but will become important in the reptation model below, and, finally,  $p = N$  refers to the relaxation time of one segment ( $\tau_s$ ), being the shortest possible relaxation time in the Rouse model. The numerical prefactor in the denominator depends on the derived time-dependent quantity. In Eq. 2.11, relaxation times with a prefactor  $3\pi^2$  are specified for the end-to-end vector correlation function. In turn, relaxation times of the stress relaxation are two times shorter with a prefactor  $6\pi^2$ . Also, a prefactor of 1 can be found in literature [56, 58]. We will, therefore, use a prefactor somewhere in between of the mentioned values, following ref 65, namely, a value of  $\pi$ , which turned out to represent experimentally studied dynamics of real systems better, at least for the case of poly(butadiene)s [66] and poly(isobutylene)s (see Chapter 8).

Further, it can be seen from Eq. 2.11 that the temperature dependence of relaxation times of all modes is alike and proportional to  $\xi(T)/T$ , which is normally the case for polymer melts at temperatures exceeding the glass transition temperature [67]. This circumstance implies that any time-dependent observable, such as the OACF or the dynamic modulus, measured at different temperatures can be superimposed. This is called the time-temperature superposition principle (TTS). Often, the TTS is applied to extend experimental time (or frequency) windows of measuring devices. The shift factors  $a_T$ , required to superimpose data at different temperatures on data at a reference temperature  $T_{\text{ref}}$ , are simply the ratios  $(\xi(T)/T) / (\xi(T_{\text{ref}})/T_{\text{ref}})$ . The ratio of temperatures  $T_{\text{ref}}/T$  can be neglected as compared to much stronger temperature dependence of the monomeric friction coefficient, which reads:

$$\xi(T) = \xi_0 \exp \{ [\alpha(T - T_V)]^{-1} \}, \quad (2.12)$$

where  $\xi_0$  is the monomeric friction coefficient at infinitely large temperature,  $\alpha$  is the thermal expansion coefficient of the free volume,  $T_V$  is the Vogel temperature.

The empirical temperature dependence in Eq. 2.12 is called the Vogel-Fulcher-Tamann (VFT) equation. The decimal logarithm of the shift factor can be shown to be equal to the relation called Williams-Landel-Ferry (WLF) equation:

$$\log a_T = -C_1 \frac{T - T_{\text{ref}}}{T - T_{\text{ref}} + C_2}, \quad (2.13)$$

where  $C_1$  and  $C_2$  are empirical constants, depending on the choice of  $T_{\text{ref}}$  and equal to a combination of the VFT parameters.

It should be stressed that the TTS holds true only if all relaxation times are governed by the same activation process. If, however, another activation process additionally contributes to the overall dynamics (see Eq. 2.16 below), the TTS is violated, and such polymer systems are called thermorheologically complex [68]. One can then either choose between shifting to one of the two dynamic processes, as is the case in rheology, or an uncontrolled switching occurs when the characteristic relaxation time of the second process at the studied temperature lies within the analyzed time interval (the NMR case). All supramolecular polymer systems serve as a good example of thermorheological complexity.

The time and frequency dependencies of  $C(t)$  and the storage modulus (elastic  $E'(\omega)$  or shear  $G'(\omega)$ ), respectively, in the framework of the Rouse model can be seen in Fig. 2.2 (black curves). It can be seen that the curves of both quantities resemble each other in shape, which is not surprising in the light of identical microscopic backgrounds. As was mentioned, the shortest relaxation time considered by the Rouse model is the segmental relaxation time  $\tau_s$ , before which the system is in a glassy state not experiencing loss of orientational correlations or stress relaxation. At longer times up to  $\tau_R$ , subdiffusive free segmental motions take place (Rouse regime, or regime I, according to the Doi/Edwards

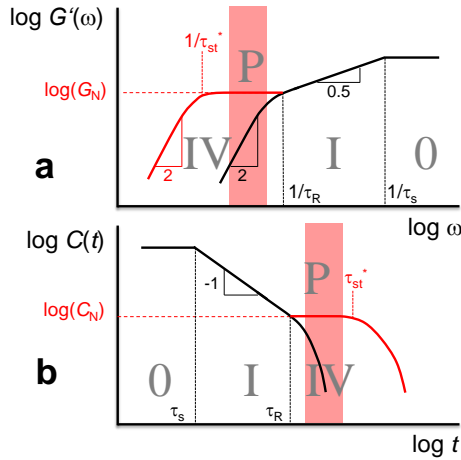


**Figure 2.2:** The storage modulus  $G'$  (a) and the orientation autocorrelation function  $C(t)$  (b) following the predictions of the Rouse and sticky Rouse models. The dynamic regimes are specified, see text for details. The black curves correspond to chains without stickers, whereas the red curves represent end-functionalized associating polymers. The red shaded boxes indicate time/frequency windows where the temperature dependence switches from being driven by segmental to sticky dynamics.

denotation in their tube model [58]), after which a polymer chain moves diffusively as a whole object (regime IV). In regime I,  $C(t)$  and  $E'(\omega)$  (or  $G'(\omega)$ ) decay with power laws of -1 and -0.5, respectively, followed in regime IV by either an exponential decay in the case of  $C(t)$  or by a steeper power law of -2 in the case of  $E'(\omega)$  (or  $G'(\omega)$ ). The power-law predictions in regime I are not, however, found in real systems due to too few<sup>2</sup> Rouse modes available in polymer chains. Typically, the power laws in regime I were reported to be 0.7-0.9 for  $C(t)$  [66, 69] and 0.6-0.8 for  $E'(\omega)$  (or  $G'(\omega)$ ) [70].

Dynamics in associating unentangled polymer networks, formed by reversible bonding such as hydrogen bonding (4-120 kJ/mol), pi-pi stacking (0-50 kJ/mol), metal-ligand bonding (20-300 kJ/mol), or electrostatic interactions (5-300 kJ/mol) [71], can be described by the sticky Rouse model, expanding the conventional Rouse model by adding the effect of stickers [32, 64]. According to this model, polymer chains undergo segmental dynamics characteristic to regime I until they feel the constraints imposed by stickers that act as permanent cross-links on the time scales shorter than the sticker's bond lifetime  $\tau_{st}^*$ , leading to the formation of the plateau (P) in the stress relaxation and the OACF. In the case of telechelic associating polymers the plateau begins at the Rouse time of the whole molecule. Beyond  $\tau_{st}^*$ , stickers open and exchange their aggregation sites causing further stress relaxation or reduction of the orientational memory via the free diffusion of chains as a whole (regime IV). Notably, the return of an open sticker to the same aggregation site does not lead to a reduction in  $C(t)$  or  $E'(\omega)$  (or  $G'(\omega)$ ). The described molecular picture can be likewise seen in Fig. 2.2 (red curves). It should be stressed that

<sup>2</sup>entanglements become important before a sufficient number of modes can accumulate

the appearance of the storage modulus presupposes stress relaxation through relaxation of chains. Thus, it is assumed that the terminal relaxation time is equal to the relaxation time of a single chain. This stands in contrast to the predictions in refs 72 and 41 relevant for cluster-forming stickers, according to which stress relaxation occurs via macroscopic rearrangements of micelles involving breaking of all bridges with old neighbors and their reestablishment with new neighbors after diffusion of the micellar core to the new micellar site. This notion results in the stress relaxation time  $\tau_{\text{stress}}$  being exponentially larger than the relaxation time of a single chain  $\tau_{\text{chain}}$ :  $\tau_{\text{stress}} \propto \tau_{\text{chain}} \exp\left(\frac{E}{k_{\text{B}}T}\right)$ , where  $E$  includes contributions of the deformation energy of a micelle and its neighborhood, energy required for debridging, chain relaxation, and micellar diffusion. In the present work, however, it will be shown that stress relaxation is a single-chain event in the studied systems.

### 2.3.2 (Sticky) reptation model

When polymer chains become longer than some critical value, defined by the critical molecular weight  $M_c = 2 - 3M_e$ , they start to interpenetrate, thus imposing constraints on their segmental motions. These topological constraints are called entanglements. Entanglements do not change an ideal chain conformation, but lead to a modulation of Rouse dynamics, assuming that polymer chains do not hinder each other in their motion. Thus, additional dynamic regimes are expected. The collective restriction of segmental motions of a considered polymer chain by surrounding chains can be approximated by a quadratic potential, confining segmental fluctuations in an imaginary tube [58, 73]. When segmental motions are local, they do not feel the tube constraints and resemble free segmental motions of the Rouse model (regime I). Such dynamics persists until lateral fluctuations of polymer segments become comparable to the tube's diameter  $a = bN_e^{1/2}$ . This happens on the time scale of the entanglement relaxation time  $\tau_e$ . Beyond  $\tau_e$ , segments are restricted in their lateral motions and only free to move along the contour of the tube, the primitive path (constrained Rouse, or local reptation, or regime II). As a result, such lateral wriggling of polymer chains become unimportant and can be neglected, and thus the time-averaged chain conformation coincides with the primitive path (primitive chain). Starting from  $\tau_R$ , the primitive chain performs 1D-diffusion along the tube, during which the center of mass of the chain is displaced. This kind of motion is called reptation (regime III). Eventually, the chain leaves its original tube at the disengagement time  $\tau_d$  and participates in free diffusion (regime IV).  $\tau_d$  can be found as  $3Z\tau_R$ , where  $Z = N/N_e$ .

In regime II,  $C(t)$  is proportional to the return-to-origin probability and obeys the scaling law of  $t^{-1/4}$ , whereas in regimes III-IV  $C(t)$  is proportional to the product of the return-to-origin and the tube survival probabilities [74], i.e.  $\propto t^{-1/2} \sum_{p \text{ odd}} (8/\pi^2) \exp(-p^2 t/\tau_d)$ . The relaxation modulus is in turn not sensitive to segmental motions in regime II, but also proportional to the tube survival probability in regimes III-IV.

The manifestation of entanglements can be observed in the change of scaling laws of

molecular weight dependencies of chain relaxation time ( $\tau_{\text{chain}}$ ), viscosity ( $\eta$ ), self-diffusion coefficient ( $D_{\text{cm}}$ ) at  $M_c$ , predicted by the Rouse and reptation models:

$$M < M_c : \tau_{\text{chain}} \propto M^2, \eta \propto M, D_{\text{cm}} \propto M^{-1} \quad (2.14)$$

$$M > M_c : \tau_{\text{chain}} \propto M^{3(3.4)}, \eta \propto M^{3(3.4)}, D_{\text{cm}} \propto M^{-2(-2.4)} \quad (2.15)$$

The exponents in Eq. 2.15 shown in brackets correspond to empirical values found in real systems and are seen to deviate from the model predictions. The deviations come about due to violation of the reptation model's assumption that the tube stays unchanged with time. Only very high molecular weight polymers ( $Z > 200$ ) do possess stable tubes, thus fulfilling the model predictions. For lower molecular weights, however, additional tube relaxation mechanisms occur boosting the entangled chain dynamics. Among the most prominent tube relaxation processes constraint release (CR) and contour length fluctuations (CLF) can be distinguished. In particular, CLF were verified to be responsible for the larger power laws for  $\tau_{\text{chain}}$  and  $\eta$  [66, 75], whereas CR leads to the lower power law of  $D_{\text{cm}}$  and also causes the molecular weight dependence of the  $C(t)$ 's power law in regime II, being lower than the predicted value of  $-1/4$  [58, 66].

Fig. 2.3 summarizes the aforementioned dynamic regimes along with characteristic crossover times and scaling laws found in entangled polymer chains for the case of  $C(t)$  and  $E'(\omega)$  (or  $G'(\omega)$ ).

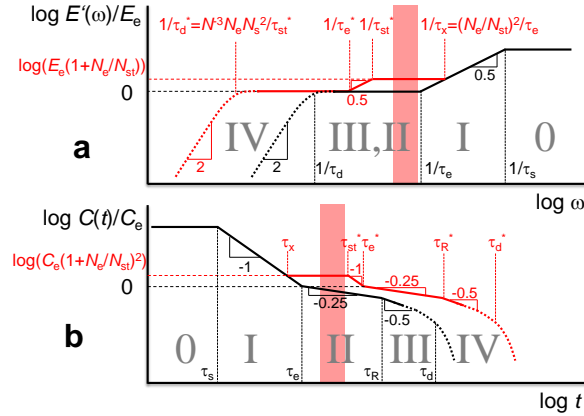


**Figure 2.3:** Dynamic regimes and characteristic crossover times of an entangled polymer melt and a dynamic network ( $N_e \geq N_{st}$ ) observed for the storage modulus  $E'$  (a) and orientation autocorrelation function  $C(t)$  (b) normalized by the corresponding quantity at the level of entanglements. The dotted lines correspond to the parts that could not be accessed in our experiments. The red shaded boxes show the region of transition from the segmental to the sticky temperature dependence. The times governed by the sticker activation are marked with asterisks. See text for details. Reprinted with permission from [76]. Copyright 2019 American Chemical Society.

For permanent networks, starting from the Rouse time of the part of the chain between two cross-links ( $\tau_x$ ) one expects a well-defined plateau with a slope approaching zero, as no long-range dynamics occurs. In the case of dynamic networks, the long-range dynamics becomes feasible via stickers hopping from one aggregate to another, but is much more delayed than in the case of polymer melts [77–79]. Various theoretical models have been developed to treat the effect of stickers on segmental dynamics of entangled networks. Some models, such as the slip-link and time-marching algorithm models, consider stickers as additional sources of molecular friction [78, 79]. While the models correctly predict such qualitative features as the observed double plateau and the delayed terminal flow, they are not yet refined enough to fully capture the experimental data. The most established model is nowadays the sticky reptation model firstly formulated by Leibler, Rubinstein, and Colby in 1991 [77] and then further improved by Chen, Zhang, and Colby in 2016 [80] by accounting for the inter-chain relaxations (double reptation), molecular weight polydispersity, and stickers distributions to improve reproduction of experimental results. According to the sticky reptation model, stickers freeze the center of mass transport, which carries on once  $\tau_{st}^*$  is reached. In other words,  $\tau_{st}^*$  is much longer than any other polymeric relaxation time and therefore governs all the relevant dynamic time scales. If stickers are arranged more densely than entanglements,  $N_e > N_{st}$  ( $N_e$  and  $N_{st}$  are the numbers of Kuhn segments per entanglement or sticker, respectively),  $E'(\omega)$  (or  $G'(\omega)$ ) and  $C(t)$  within the time interval  $\tau_x < t < \tau_{st}^*$  exhibit a plateau defined by both entanglements and stickers.  $E'(\omega)$  (or  $G'(\omega)$ ) and  $C(t)$  stay at this level until the stickers start to open at  $\tau_{st}^*$  enabling an entangled strand with stickers to equilibrate via the sticky Rouse mechanism [32]. Once all the entangled strands relaxed,  $E'(\omega)$  (or  $G'(\omega)$ ) and  $C(t)$  reach the level of entanglements ( $E_e$  (or  $G_e$ ) and  $C_e$ ) at  $\tau_e^*$ , after which the chain continues to disentangle until  $\tau_d^*$ , at which it leaves the original tube.

Clearly, the key quantity of the sticky Rouse and (double) sticky reptation models, governing long-range time scales and macroscopic properties, is  $\tau_{st}^*$ . Its temperature dependence is assumed to follow the relation [40, 41, 80, 81]:

$$\tau_{st}^*(T) = \tau_0(T) e^{E_a^{st}/RT}, \quad (2.16)$$

where  $\tau_0(T)$  is the attempt time associated with the segmental relaxation time following the VFT temperature dependence,  $E_a^{st}$  is the activation energy of the sticker dissociation including a binding energy ( $E_{bind}$ ) and an activation barrier ( $\Delta E$ ) (see the illustrating energy diagram in Fig. 2.4),  $R$  is the gas constant.

Since the temperature dependence of  $\tau_0(T)$  can approximately follow an Arrhenius-like behavior within a suitably narrow temperature interval, i.e.  $\propto \exp(E_{a,segm}/RT)$ , with  $E_{a,segm}$  being the activation energy of segmental motion, Eq. 2.16 predicts an observation of the apparent activation energy  $E_{a,app} = E_{a,segm} + E_a^{st}$  from the analysis of the temperature dependence of the sticky bond lifetimes or horizontal shift factors  $\log a_T$ . For the case of the electric conductivity in a system with ionic stickers, detected by BDS, which can be realized via transport of two counterions bound to one carrying group through the

polymer matrix, one needs to additionally include a Pauli repulsion and Coulomb attraction potentials into the energy term in Eq. 2.16, which effectively leads to an addition of the dissociation energy of a contact ion pair  $E_{\text{diss}}$  and an inverse distance dependence of the overall potential energy at distances larger than the internuclear distance  $r_m$  between the interacting ions.

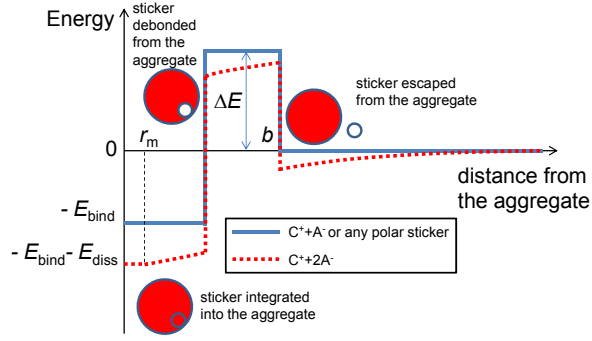


**Figure 2.4:** Energy diagram of sticky dynamics. The blue line indicates the dissociation of one contact ion pair ( $C^+ + A^-$ ,  $C^+$  - cation,  $A^-$  - anion) or any polar sticker from the supramolecular aggregate, detected by rheology/DMA and NMR, whereas the red dotted line corresponds to the dissociation of a sticker with two counterions ( $C^+ + 2A^-$ ) associated with the conductivity mechanism seen by BDS. The Pauli repulsion contribution at distances shorter than the internuclear distance  $r_m$  between the interacting ions is not shown. A sticker integrated into an aggregate possesses a binding energy of  $-E_{\text{bind}}$  or  $-E_{\text{bind}} - E_{\text{diss}}$  for rheology/DMA/NMR and BDS cases, respectively. For the successful dissociation of one sticker, i.e. debonding from the aggregate and escaping from it by a distance of one Kuhn segment  $b$ , the aggregate must receive a total energy of the sum of a binding energy and an activation barrier  $\Delta E$ .

A similar notion for the temperature dependence of the bond lifetime of one contact ion pair was presented in ref 82, where by means of hybrid molecular dynamics/monte-carlo (MD/MC) simulations effects of thermodynamics ( $\exp(E_{\text{bind}}/RT)$ ) and kinetics (a prefactor in Eq. 2.16) on dynamic and mechanical properties were studied independently. In particular, it was shown that kinetics has a similar impact on the properties as thermodynamics: a slowdown of breaking and reformation of sticky bonds at a fixed bond strength renders ultimate relaxation behavior more arrested. The kinetics can be influenced by rate of segmental motions, as is assumed by the above theories.

At present, however, it is not possible to fully exclude experimentally that the prefactor in Eq. 2.16 is, apart from the segmental dynamics, additionally dependent on e.g. stickers' chemical details or size and shape of aggregates. Nevertheless, in the following for a more consistent comparison between the samples we assume that the prefactor is solely contributed by the segmental dynamics and, hence, the only way of influence of the sticker's chemistry on the bond lifetime is through  $E_a^{\text{st}}$ .



### 3 NMR fundamentals

Since its first practical application by the research groups of Bloch and Purcell as early as 1946, resulting in the Nobel Prize, NMR spectroscopy has revolutionized material science allowing one to conduct a thorough analysis of various material properties. Polymer science benefited tremendously as well. For instance, NMR has become already an indispensable standard technique in polymer chemistry for elucidation of chemical details (molecular structure, tacticity). Also, NMR has paved its way in the field of polymer physics where structure, phase composition, and dynamics of solid materials are a matter of interest.

The NMR phenomenon relies on the intrinsic nuclear property called spin angular momentum  $\hat{I}$  (or just spin), characterized by a spin quantum number  $I$ . Notably, only nuclei with odd atomic numbers possess a non-zero spin and are NMR active.  $I$  can take on either half-integer or integer values, depending on the number of protons and neutrons [83]. The most utilized NMR-active nucleus is proton ( $^1\text{H}$ ) with a spin of  $1/2$ . When placed in the external magnetic field with strength  $B_0 \equiv |\vec{B}_0|$ , conventionally chosen to be oriented along the z-axis, spins may precess around it under action of torque imposed by the field trying to align the spins along its direction (unless they are in an Eigenstate of spin-up or spin-down). The precession occurs with a characteristic frequency  $\omega_0 = \gamma B_0$  ( $\gamma$  is the gyromagnetic ratio), called Larmor frequency. The total angular momentum  $\hat{J}$  of individual spins and its projection on the z-axis  $J_z$  read [84]

$$|\hat{J}| = \hbar\sqrt{I(I+1)} \quad (3.1)$$

$$J_z = \hbar m, \quad (3.2)$$

where  $m$  is the magnetic quantum number covering the interval from  $-I, -I+1, \dots, I$ .  $\hat{J}$  and  $J_z$  are related to the corresponding magnetic moment  $\hat{\mu}$  and its projection on the z-axis  $\mu_z$  by the equations:

$$\hat{\mu} = \gamma\hat{J} \quad (3.3)$$

$$\mu_z = \gamma J_z \quad (3.4)$$

From Eqs. 3.2 and 3.4 it follows that we have Eigenstates where the spin orientations with respect to  $\vec{B}_0$  are strictly defined, they are said to be quantized. Protons can take two orientations (parallel or antiparallel) with respect to  $\vec{B}_0$ , with  $m = \mp 1/2$ , corresponding to  $\alpha$  and  $\beta$  states, respectively. The interaction with the field  $B_0$  leads to splitting of energy levels (Zeeman splitting), with the  $\alpha$  state having a lower energy than the  $\beta$  state. According to Boltzmann statistics, the  $\alpha$  state is more populated than the  $\beta$  state. The difference in the populations causes the net magnetic moment (macroscopic longitudinal magnetization) to be directed along  $\vec{B}_0$ . The macroscopic magnetization (or spin states) in equilibrium can be manipulated by radio-frequency (rf) pulses, associated with the magnetic field  $\vec{B}_1$ , applied to the sample in the coil

orthogonally to  $\vec{B}_0$ . When an rf pulse with a carrier frequency of  $\omega_0$  (resonance condition) is applied for a time  $t$ , usually being several microseconds, the magnetization tilts away from  $\vec{B}_0$  by a flip angle of  $\omega_1 t$ , wherein  $\omega_1 = \gamma B_1$  is the nutation frequency. Quantum-mechanically, an rf pulse creates a coherence. When the rf pulse is switched off, the tilted magnetization starts to precess around the field  $\vec{B}_0$ , which induces a measurable signal in the coil, known as free induction decay (FID). The system then tends to come back to the equilibrium state by two relaxation mechanisms causing the obtained signal to decay and the longitudinal magnetization to restore. The former relaxation mechanism is called spin-spin (or transverse) relaxation, characterized by the decay constant  $T_2$ , whereas the latter mechanism is known as spin-lattice (or longitudinal) relaxation with the time constant  $T_1$ . The spin-spin relaxation is driven by spin interactions and their thermal fluctuations that modulate the Larmor frequency causing faster dephasing and, hence, a signal decay. In order to excite all the spins with different Larmor frequencies in the first place, one can use so-called hard rf pulses with large  $B_1$ . The spin-lattice relaxation, in turn, is sensitive to fast molecular motions with a rate close to the Larmor frequency [84–86].

The most important spin-1/2 interactions in solids are the chemical shift (CS) and the dipole-dipole coupling (DDC). The CS, often shown with a symbol  $\delta$ , is the result of interaction of electronic environment surrounding the observed nucleus with the field  $\vec{B}_0$ .  $\vec{B}_0$  induces the local magnetic field  $B_{\text{loc}}$  in the electron cloud which adds up with  $\vec{B}_0$  on the nuclear site thus altering the Larmor frequency of the nucleus. The CS is dependent on the strength of  $\vec{B}_0$  and the orientation of the molecule with respect to  $\vec{B}_0$ . The latter dependence is called the chemical shift anisotropy (CSA) represented by a  $3 \times 3$ -tensor. In dilute solutions, the orientational dependence is abolished owing to fast isotropic thermal motion leading to a single value of the CS (isotropic CS). In the proton spectrum, the resonances caused by different isotropic CSs can spread over 20 ppm (parts per million). The DDC is a direct through-space interaction of two spins via local magnetic fields generated by them. DDCs in the system of isolated spin pairs result in splitting of spectral lines depending on the angle  $\theta$  between the internuclear vector  $\vec{r}$  and  $\vec{B}_0$  in accordance with the second Legendre polynomial  $P_2(\cos \theta) = (3 \cos^2 \theta - 1)/2$  leading to a Pake spectrum. In real systems, however, spin pairs are normally not isolated (especially abundant protons), despite a strong distance dependence of DDCs  $|\vec{r}|^{-3}$ , which results in multiple couplings leading to numerous splittings of a spectral line approaching a Gaussian shape. The measurement of DDCs provides an access to estimation of structural and dynamics properties, which will be more closely elucidated in the next section [84–86].

## 4 Used NMR methods

In the given project, two types of NMR experiments were employed. The first type relies on the analysis of FID signals generated either after a single  $90^\circ$  pulse or after refocusing of DDCs by creation of a magic-sandwich echo (MSE). The second type encompasses a family of different pulse sequences united by the name multiple-quantum (MQ) NMR.

### 4.1 The Free Induction Decay and Magic-Sandwich Echo

FID and MSE-refocused FID experiments [87–89] yield signal curves with characteristic decays, which are predominantly governed by DDCs that exhibit strong distance and orientation dependencies. The latter dependence causes averaging of DDCs due to thermal motion to a certain value, defined by the anisotropy in the system, called residual DDCs (RDDCs). Both dependencies lead to different RDDCs in the phase regions with different structure and mobility. Thus, the analysis of signal decays can provide information about the phase composition in a considered system.

As was alluded to, a simple FID signal is obtained after a single  $90^\circ$  pulse and therefore suffers from the dead time problem. The dead time is the period of time when the reliable signal acquisition is not possible due to the residual pulse energy left in the coil. Thus, an initial part of the signal within some microseconds gets lost complicating the analysis. This problem can be circumvented by application of MSE-refocusing, which creates an echo with the maximum set at zero of the acquisition time (see Fig. 4.1). The used mixed MSE pulse sequence is capable of time reversal of multi-spin DDCs, resonance offsets, and magnetic field inhomogeneities. The action of homonuclear DDCs between spins  $\hat{I}_1$  and  $\hat{I}_2$  can be described by the dipolar Hamiltonian  $\hat{H}_D$  using the secular approximation [84]:

$$H_D = -\omega_D(3\hat{I}_{1z}\hat{I}_{2z} - \hat{I}_1\hat{I}_2), \quad (4.1)$$

where  $\omega_D$  is the dipolar frequency,  $\hat{I}_{1z}$  and  $\hat{I}_{2z}$  are projections of spin angular momenta on the z-axis.

The MSE experiment, as any echo experiment, exhibits some signal attenuation as compared to a simple FID-signal. At low temperatures (rigid limit), the signal loss amounts to around 10-20% and is due to the pulse sequence's efficiency problems to refocus strong dipolar interactions which are larger compared to the inverse length of the pulse sequence. At high temperatures (fast limit), the loss is minimal and is due to the experimental imperfections in pulse lengths and their phases. Importantly, the maximal loss (about 40%) occurs at temperatures higher than the calorimetric glass transition temperature by about  $40^\circ\text{C}$ . At such temperatures segmental motions are "intermediate", i.e. on a microsecond range, which changes the strength of dipolar interactions during the pulse sequence and thus impede the signal's refocusing [90–94].

The phase composition can be empirically quantified by fitting the data with a sum

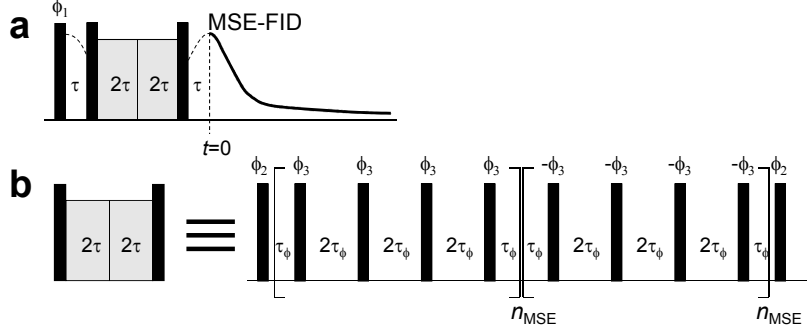


**Figure 4.1:** Mixed MSE pulse sequence. The maximum of the echo shows up after  $6\tau$ , where  $\tau$  is defined by the pulse length  $\tau_{p90}$ , the phase switching time  $\tau_\phi$ , and the number of MSE cycles  $n_{MSE}$  via the relation:  $\tau = (2\tau_{p90} + 4\tau_\phi)n_{MSE}$ .  $n_{MSE}$  was set to 1 and  $\tau_\phi$  was set to a value sufficient to overcome the spectrometer dead time. The MSE phase cycle is  $\Phi_1 = x\bar{x}\bar{x}\bar{x}\bar{x}\bar{x}$ ,  $\Phi_2 = \bar{y}\bar{y}\bar{y}\bar{y}\bar{x}\bar{x}\bar{x}$ ,  $\Phi_3 = x\bar{x}\bar{x}\bar{y}\bar{y}\bar{y}\bar{y}$ . Adapted from ref 89.

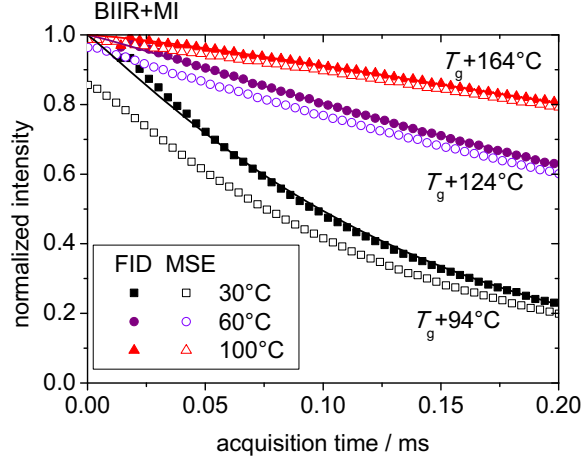


**Figure 4.2:** Phase composition analysis done on the basis of FID and MSE results of BIIR+MI at indicated temperatures. The solid lines correspond to the single stretched exponential fits.

of stretched exponential functions  $\sum_{i=1}^n f_i \exp(-(t/T_{2,i*})^{\beta_i})$ , where  $f_i$  is the phase fraction,  $T_{2,i*}$  and  $\beta_i$  are the apparent relaxation time and the shape exponent [88, 89, 94] of the phase  $i$ , respectively. One can see an example of FID and MSE-refocused FID signals for the case of ionic network studied in this work (BIIR+MI) in Fig. 4.2. For more reliable fitting of FID signals suffering from the dead-time problem, the total signal intensity was firstly determined at the highest temperature by extrapolation to zero acquisition time. Subsequently, the total signal intensities at lower temperatures were determined using the Curie law according to which the total signal intensity is proportional to  $1/T$  in the high-temperature approximation as a result of the decrease of the spin population difference [95]. For the data in Fig. 4.2, the fits with just one component ( $f_{i=1}=1$ ) were found to describe the data rather well suggesting the absence of the phase separation of

polymer chains and presence of just one phase of mobile network chains. This contrasts with observations in other ionomeric systems [47] and allows us to conclude that a too sparse arrangement of ionic groups does not lead to formation of large ionic clusters with a nano-sized continuous region of restricted mobility inside of them [96], but rather to scattered multiplets causing the immobilization on the scale of the persistence length [97] which could not be detected by NMR. Moreover, as it will be seen in Chapter 8, a high internal mobility in the ionic aggregates can also contribute to the one-phase picture.

## 4.2 Proton MQ NMR

$^1\text{H}$  MQ NMR is sensitive to the RDDCs left in the system due to anisotropic segmental motion set by topological constraints such as entanglements or cross-links of covalent or supramolecular nature (see Fig. 4.3). Therefore,  $^1\text{H}$  MQ NMR can access structural and dynamic information using RDDCs. Provided that the chain motion between topological constraints is fast enough, so that all the possible conformations can be realized on the ms time scale (inverse of the RDDC), the local dynamic order parameter  $S_b$ , which is proportional to the observable RDDCs and equal to the time average of the dipolar coupling orientation, is related to the entanglement or cross-link density ( $1/N$ , where  $N$ : the number of Kuhn segments between topological constraints), or to the sum of both, via the formula [98, 99]:

$$S_b = \langle P_2(\cos \theta) \rangle_{t,ens} = \frac{D_{res}}{D_{eff}} = \frac{3 r^2}{5 N}, \quad (4.2)$$

where  $D_{eff}$  is the average static-limit DDCs constant (rad/s), describing a rigid system without large-scale thermal motion, corrected for very fast motions inside Kuhn segments (on a ps time scale),  $r$  is the ratio of the end-to-end distance of the polymer chain to its value in the unperturbed state,  $D_{res}$  is the average strength of RDDCs.  $D_{eff}$  and  $D_{res}$  are second-moment quantities in a multispin system, characteristic for all protons in a monomer unit as a result of the dipolar truncation effect ( $D_{res} = \sqrt{\sum_{i<j} (D_{res}^{ij})^2}$ , rad/s) [100]. The square of  $S_b$  corresponds to the kink of the OACF's plot (Fig. 2.2 and 2.3) where it transits from Rouse regime to a plateau or constrained Rouse regime.

Thus, we can already see the connection between RDDCs and dynamics of polymeric systems: namely, relying on the orientational dependence of DDCs, we can probe dynamics through the OACF (Eq. 2.9). More details on dynamic studies will be given below. As a next step, we will introduce the MQ-NMR experiment.

$^1\text{H}$  MQ NMR represents a broad class of pulse sequences with a general form given in Fig. 4.4 [98, 101]. The given pulse sequence is complemented with spin-temperature-inversion (STI) pulses that remove the effects of  $T_1$  relaxation occurring in the course of the pulse sequence. The STI pulses are especially important if  $T_1$  is short. The STI pulses are followed by the excitation block of variable duration  $\tau_{DQ}$ , containing a group of pulses and evolution delays, wherein predominantly coherences of second order ( $p = \pm 2$ ), so-

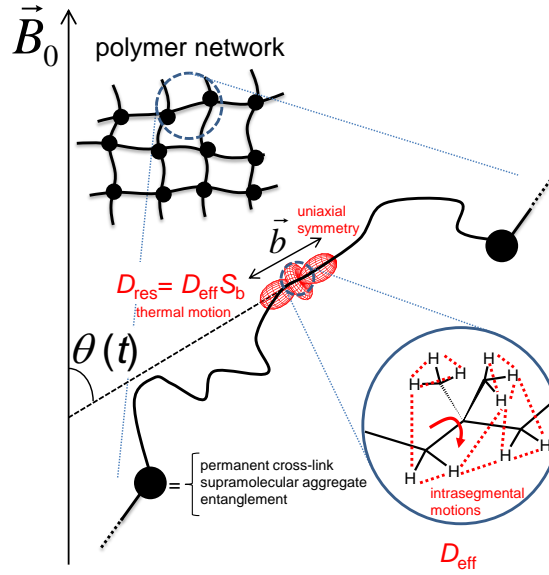


**Figure 4.3:** PIB network chains in the external magnetic field  $\vec{B}_0$ .

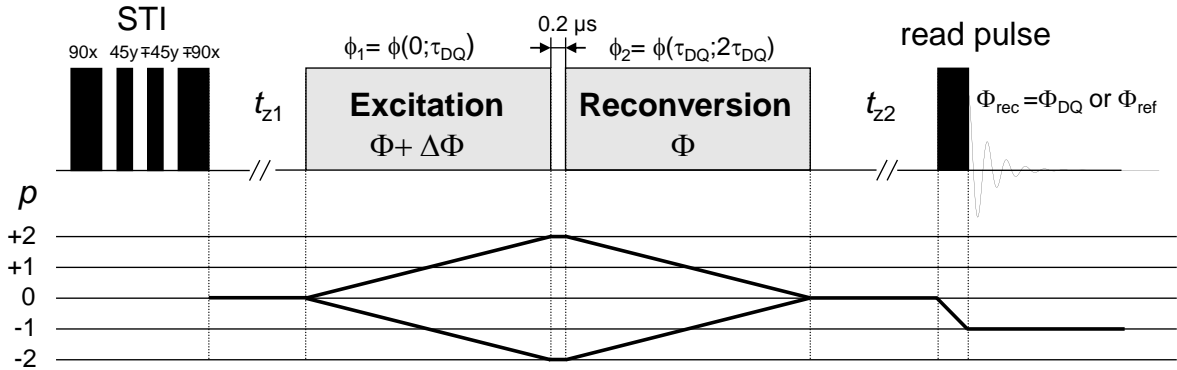


**Figure 4.4:** MQ-NMR pulse sequence. The lower part demonstrates an evolution of a coherence order  $p$  in the course of the pulse sequence. See text for details.

called Double-Quantum (DQ) coherences, are generated by means of DDCs established within the spin pairs. At the same time, a longitudinal magnetization dephases. Thus, DQ coherences are related to DDCs and can be used to determine them. However, DQ coherences do not yield a measurable magnetization and, hence, cannot be detected. Therefore, they need to be firstly reconverted back to the longitudinal magnetization ( $p = 0$ ) in the reconversion block of the same duration  $\tau_{DQ}$ , which is subsequently read off by a  $90^\circ$ -pulse tilting it to the transverse plane ( $p = -1$ ). The obtained dipolar refocused signal ( $I_{\Sigma MQ}$ ) contains contributions of both the DQ coherences ( $I_{DQ}$ ) and dephased longitudinal magnetization (so-called reference term  $I_{ref}$ ). After the STI pulses and before the last read pulse, additional delays  $t_{z1}$  and  $t_{z2}$  of 1 ms are introduced to let

the unwanted coherences, generated by the STI pulses, relax away. To select the depicted coherence transfer pathway (CTP) (see also the lower part of Fig. 4.4), we resort to phase cycling. The coherence selection is based on a change of pulse and receiver phases in a predefined way and repetition of the pulse sequence after each phase change. As a result, desired coherences accumulate and unwanted coherences disappear. According to the coherence selection rules, a shift of the phase of a pulse (or group of pulses) by  $\Phi$ , causing the change in coherence order by  $\Delta p$ , endows the generated coherence with the phase  $-\Delta p \times \Phi$ , which persists until the end of the pulse sequence [102, 103]. The receiver phase  $\Phi_{\text{rec}}$  must then be set equal to the phase acquired by the coherence to select it. Here, we combine three phase cycles. Firstly, DQ or zero-order coherences are selected by cycling the carrier phase difference  $\Delta\Phi$  of the excitation block as  $[0^\circ, 90^\circ, 180^\circ, 270^\circ]$  with  $\Phi_{\text{rec}}$  set to  $[0^\circ, 180^\circ, 0^\circ, 180^\circ]$  and  $[0^\circ, 90^\circ, 180^\circ, 270^\circ]$ , respectively. In fact, the four-step phase cycles lead to selection of all  $(4n+2)$ - and  $(4n)$ -order coherences ( $n$  is a positive integer), thus justifying the name MQ NMR, that, however, become observable only at longer  $\tau_{\text{DQ}}$  [98]. Secondly, for the read pulse, the CYCLOPS phase cycle was applied to suppress artifacts related to imperfections in detectors, including quadrature images and a DC spike. The phase of the read pulse  $\Phi_{\text{r}}$  is cycled as  $[0^\circ, 90^\circ, 180^\circ, 270^\circ]$ , with  $\Phi_{\text{rec}} = [0^\circ, 90^\circ, 180^\circ, 270^\circ]$ . Thus, one can see that the CTP of CYCLOPS corresponds to  $\Delta p = -1$ , which means that the measured signal is exclusively contributed by the zero-order coherences present before the read pulse, and hence, the reconversion block does not require its own phase cycle to deliberately select  $p = 0$ . Thirdly, the two last STI pulses are phase-cycled in such a way that the magnetization before the excitation block is firstly directed along the z-axis and then inverted to the  $-z$ -direction [98]. In other words, the whole group of the STI pulses represents a composite pulse [104].  $\Phi_{\text{rec}}$  should be inverted along with the phases of the STI pulses. As a result, the relaxed  $T_1$  signal contribution, which is always directed along z-axis, eliminates, and all other coherences add up. The total 32-step phase cycle can be seen in Table A1.

Notably, in the given representation of the phase cycle, one firstly needs to go through all 32 steps of this pseudo-2D experiment acquiring the signal with  $\Phi_{\text{rec}}(\text{DQ})$  and then to repeat the whole procedure again, but this time with  $\Phi_{\text{rec}}(\text{ref})$ . When  $\Phi_{\text{rec}}(\text{DQ})$  is chosen, all reference terms are eliminated by summation and DQ terms are left, and, in turn, acquisition with  $\Phi_{\text{rec}}(\text{ref})$  results in addition of reference terms and cancellation of DQ terms. Thus, one ends up with 64 repetitions per  $\tau_{\text{DQ}}$ . This procedure does not seem to be the most efficient since at each set  $\Phi_{\text{rec}}$  we lose part of the signal (DQ or reference) due to its subtraction. Instead, it is possible to organize data acquisition and data collection differently so that we obtain both DQ and reference terms at the same time, which can be subsequently used to compute pure DQ and reference signals. This procedure implies a reduction of the experimental time by a factor of two. To this end, as was suggested and implemented by my colleague Frank Lange we need to keep the phase shift of the excitation block constant while cycling through the phases of the read pulse and STI pulses and using  $\Phi_{\text{rec}} = \Phi_{\text{ref}}$  upon acquisition. The described procedure of data acquisition and data collection can be seen in Table A2. In such a way, we become a data

set consisting of four columns, corresponding to four phase shifts of the excitation block, each of which comprises a combination of DQ and reference terms. As can be seen in Table A2, owing to  $\Phi_{\text{rec}} = \Phi_{\text{ref}}$ , reference terms have a positive sign in all cases, whereas DQ terms are positive for  $\Phi = 0^\circ$  and  $180^\circ$  and negative for  $\Phi = 90^\circ$  and  $270^\circ$ . Hence, summation of the four columns yields the reference signal, whereas alternate summation and subtraction done every  $90^\circ$  results in the DQ signal.

MQ NMR can be performed either under static conditions, when the focus is laid on network chains prevailing the signal, and the spectral resolution is not important, or employing additional sample spinning at magic angle to resolve and study separate resonances. In the static case, a pulse sequence based on the one developed by Baum and Pines was utilized [98, 105], while, in the case of the high resolution measurements under MAS, a DQ recoupling pulse sequence, denoted as BaBa-xy16 and introduced in ref 101, was employed. Both pulse sequences feature a phase evolution under a pure DQ Hamiltonian  $H_{\text{DQ}}$  which enables a reconversion of multispin dipolar couplings (Eq. 4.3).

$$H_{\text{DQ}} = \sum_{i < j} b(t)^{ij} (\hat{I}_+^i \hat{I}_+^j + \hat{I}_-^i \hat{I}_-^j), \quad (4.3)$$

where  $b(t)$  is a prefactor equal to  $D_{\text{res}} P_2(\cos \theta)$  and  $\left(\frac{3}{\pi\sqrt{2}}\right) D_{\text{res}} \sin 2\beta \sin \gamma$  ( $\beta$  and  $\gamma$ : the Euler angles connecting the principal and rotor frames) for Baum/Pines and BaBa-xy16 pulse sequences, respectively;  $\hat{I}_+^{i,j}, \hat{I}_-^{i,j}$  are the raising and lowering operators of spins  $i$  and  $j$ , respectively.

It can be shown by means of the product operator formalism that DQ, reference, and total dipolar refocused signals correspond to the relations [98–100]:

$$I_{\text{DQ}} = \langle \sin \phi_1 \sin \phi_2 \rangle \quad (4.4)$$

$$I_{\text{ref}} = \langle \cos \phi_1 \cos \phi_2 \rangle \quad (4.5)$$

$$I_{\Sigma\text{MQ}} = \langle \sin \phi_1 \sin \phi_2 \rangle + \langle \cos \phi_1 \cos \phi_2 \rangle, \quad (4.6)$$

where  $\phi_1 = \phi(0, \tau_{\text{DQ}})$  and  $\phi_2 = \phi(\tau_{\text{DQ}}, 2\tau_{\text{DQ}})$  are the evolution phases in the excitation and reconversion blocks, respectively. The evolution phases can be found as

$$\phi(t_a, t_b) = \int_{t_a}^{t_b} b(t) dt,$$

It should be stressed that a DQ signal can originate only from the coupled protons which correspond to elastically active chains, whereas a reference signal combines all the magnetization which did not evolve into the DQ signal, which also includes a non-coupled component from the isotropically moving chain parts such as dangling chains, loops, etc. (so-called defects).

Further, it is possible to remove the relaxation effects of fast motions from regimes 0 and I causing the decay in the DQ signal. To this end, the normalization of the DQ signal is done via the point-by-point division through  $I_{\Sigma\text{MQ}}$  corrected for the defects fraction originating from the reference signal. The resulting relaxation-free quantity is called a normalized DQ intensity ( $I_{\text{nDQ}}$ ) and can be unambiguously analyzed to extract the value of  $D_{\text{res}}$  and also its predefined distribution. According to the second-moment approximation [98, 106], which assumes the distribution of frequencies to be normal,  $I_{\text{nDQ}}$  reads

$$I_{\text{nDQ}} = \frac{1}{2} \left( 1 - e^{-2\langle\phi^2\rangle} \right). \quad (4.7)$$

Eq. 4.7 can be applied for polymer networks and highly entangled polymer melts after all the conformations between topological constraints can be realized on the NMR time scale (at  $T \gg T_g$ ) [98, 107–110]. Note that the aforementioned differences in the DQ Hamiltonians of the Baum/Pines-based and BaBa-xy16 pulse sequences in the form of the prefactor  $b(t)$  lead to the differences in prefactors of the square phase factors  $\langle\phi^2\rangle$  becoming  $\frac{1}{5}D_{\text{res}}^2\tau_{\text{DQ}}^2$  for the static case and  $\frac{6}{5\pi^2}D_{\text{res}}^2\tau_{\text{DQ}}^2$  for BaBa-xy16. Thus, the normalized DQ build-up curves of the BaBa-xy16 pulse sequence is by a factor of  $\sqrt{6/\pi^2} = 0.78$  slower on the  $\tau_{\text{DQ}}$  axis than in the static case, which must be accounted for upon direct comparison of the build-up curves from the two pulse sequences.

As cross-link densities usually manifest distributions,  $D_{\text{res}}$  are also distributed. To address this, we resort to a numerical integration over a predefined distribution:

$$I_{\text{nDQ}}(\tau_{\text{DQ}}) = \int P(D_{\text{res}}) I_{\text{nDQ}}(D_{\text{res}}, \tau_{\text{DQ}}) d(D_{\text{res}}), \quad (4.8)$$

where  $P(D_{\text{res}})$  is the predefined distribution function,  $I_{\text{nDQ}}(D_{\text{res}}, \tau_{\text{DQ}})$  is the kernel function.

The function in Eq. 4.7 can be used as a kernel function, but with caution. Previously, it was found that in the case of very homogenous networks the given equation cannot approximate the full range of  $I_{\text{nDQ}}$  data. Specifically, Eq. 4.7 is not able to capture the maximum appearing in the  $I_{\text{nDQ}}$  build-up as a result of an additional contribution of four-quantum coherences. Thus, the use of Eq. 4.7 as a kernel function can lead to potential errors in the extracted distribution of  $D_{\text{res}}$ . Instead, it is better to use an empirical, Abragam-like function of the form [111]:

$$I_{\text{nDQ}} = 0.5 \left( 1 - \exp \left[ -(0.378D_{\text{res}}\tau_{\text{DQ}})^{1.5} \right] \cos[0.583D_{\text{res}}\tau_{\text{DQ}}] \right), \quad (4.9)$$

which was previously shown to capture the maximum in the  $I_{\text{nDQ}}$  build-up.

For a distribution function in Eq. 4.8, various probability density functions can be employed. Normally, we apply a Gaussian function for homogeneous networks featuring the arithmetic average of  $D_{\text{res}}$  ( $\langle D_{\text{res}} \rangle$ ) being larger than the distribution width ( $\sigma$ ) [98]. For highly heterogeneous networks, in turn, one can use a Gamma or log-normal distribution

[17, 112].

The Gaussian, Gamma, and log-normal distributions read as follows:

$$P_{\text{Gauss}}(D_{\text{res}}) = \frac{1}{\sigma\sqrt{2\pi}} \exp\left[-\frac{(D_{\text{res}} - \langle D_{\text{res}} \rangle)^2}{2\sigma^2}\right] \quad (4.10)$$

$$P_{\text{Gamma}}(D_{\text{res}}) = \sqrt{\frac{27D_{\text{res}}}{2\pi D_{\text{av}}^3}} \exp\left[-\frac{3D_{\text{res}}}{2\langle D_{\text{res}} \rangle}\right] \quad (4.11)$$

$$P_{\text{log}}(\ln(D_{\text{res}})) = \frac{1}{\sigma_{\ln}\sqrt{2\pi}} \exp\left[-\frac{(\ln(D_{\text{res}}) - \ln(D_{\text{med}}))^2}{2\sigma_{\ln}^2}\right]. \quad (4.12)$$

In Eq. 4.12,  $D_{\text{med}}$  is the median and  $\sigma_{\ln}$  is the standard deviation on the  $\ln(D_{\text{res}})$  scale. The most elegant way to perform the numerical integration for the log-normal distribution is on the  $\ln(D_{\text{res}})$  scale. The analytical form of the resulting fitting function for the case of the log-normal distribution reads

$$I_{\text{nDQ}}(\tau_{\text{DQ}}) = \int P(\ln(D_{\text{res}})) I_{\text{nDQ}}(D_{\text{res}}, \tau_{\text{DQ}}) d \ln(D_{\text{res}}). \quad (4.13)$$

In Figure 4.5(a), the log-normal distribution is compared with the normal and gamma distributions on the example of the  $I_{\text{nDQ}}$  curve of BIIR+MI exhibiting a broad distribution of  $D_{\text{res}}$ . It can be seen that the log-normal distribution provides the best fit. The resulting  $D_{\text{res}}$  distributions are shown in Fig. 4.5(b).

One can see that the normal distribution cannot be used for wide distributions, because its width can become larger than the mean value of  $D_{\text{res}}$  and a significant part of the distribution curve ends up in the negative quadrant, rendering a trustworthy fit impossible. The gamma distribution [112], on the other hand, is bound to zero and, hence, does not have this problem. However, the lack of the variable distribution width parameter, which always has a fixed ratio with the mean value of  $\sqrt{2/3}$  ( $\approx 0.82$ ), worsens the fit quality and also deprives the analysis from such an important piece of information as the network heterogeneity, related to the width parameter. The log-normal distribution allows us to alleviate both problems and will be our choice throughout the whole work [17, 112]. Since the mean value of the log-normal distribution is dependent on  $\sigma_{\ln}$  and, namely, biased towards larger  $D_{\text{res}}$  values for larger  $\sigma_{\ln}$ , we stick to the distribution-width-independent  $D_{\text{med}}$  reflecting the middle of the distribution.

In order carry out measurements in regimes 0 and I, featuring strong DDCs on the order of several kHz, one needs to access short  $\tau_{\text{DQ}}$ . To this end, in the static case, shorter excitation and reconversion blocks must be utilized, as compared to the Baum/Pines pulse sequence containing twelve pulses in one block. For example, one can resort to two- or three-pulse-segment pulse sequences. The two-pulse sequence includes two  $90^\circ$  pulses per block, whereas the three-pulse sequence has an additional  $180^\circ$  pulse in between.

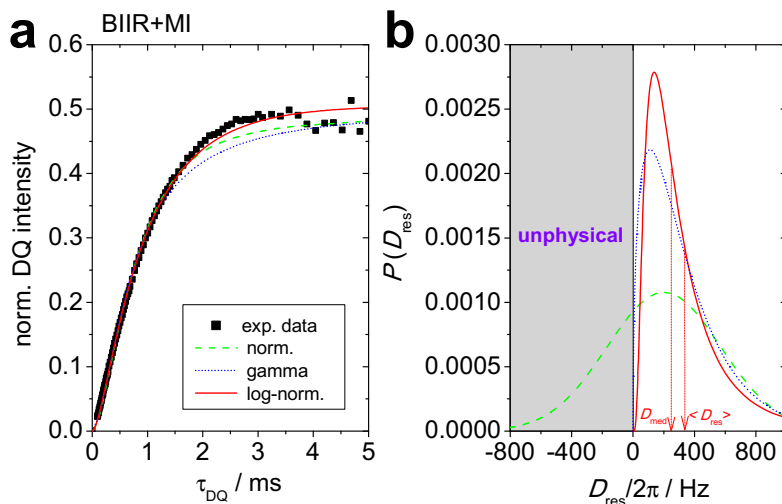


**Figure 4.5:** (a)  $I_{nDQ}$  build-up curve on the example of BIIR+MI at 100°C. The lines represent fits assuming different  $D_{res}$  distributions, as indicated. (b) Comparison of the extracted log-normal, normal, and gamma distributions of  $D_{res}$  for BIIR+MI at 100°C. The median  $D_{med}$  and the arithmetic average  $\langle D_{res} \rangle$  of the log-normal distribution are specified. Reprinted with permission from [76]. Copyright 2019 American Chemical Society.

Note that the time scale of the Baum/Pines pulse sequence should be corrected for the dipolar evolution within pulses with a duty-cycle dependent factor, found using the Average Hamiltonian Theory (AHT), whereas the time scales of the non-cyclic 2-pulse- and 3-pulse-segment pulse sequences had to be defined via spin dynamics simulations in the SIMPSON software [66] and correspond to the distance between the centers of the 90° pulses. For the three-pulse-segment pulse sequence, an additional subtraction of half of the 180° pulse had to be done as no dipolar evolution takes place within this time period. To enable a direct comparison of performances of the three pulse sequences on the common time scale, the time scales of the two-pulse- and three-pulse-segment pulse sequences must be additionally scaled with a factor of 3/2 to account for a faster dipolar evolution as compared to the Baum-Pines pulse sequence. One can see the MQ data of the three pulse sequences on the example of telechelic PIB network 6kBA3 studied in this work in Fig. 4.6.

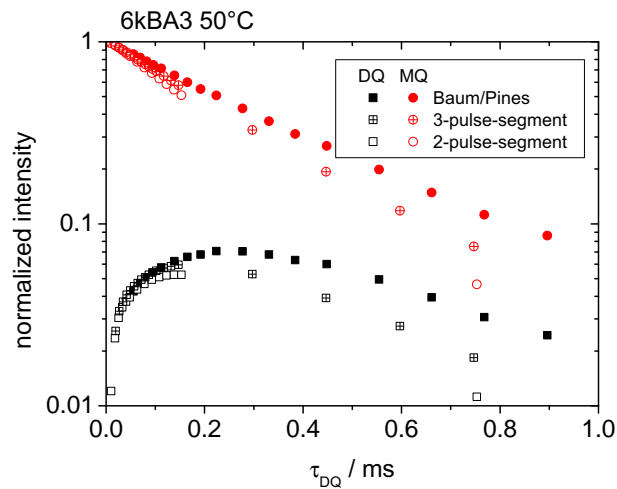


**Figure 4.6:** MQ data of 6kBA3 at 50°C acquired with Baum/Pines-based, three-pulse, and two-pulse-segment pulse sequences. The time scales for the latter two are scaled to account for different phase evolution.

It can be seen that all the data coincide at short times ( $< 100 \mu\text{s}$ ), where DQ coherences are dominant, and deviate at longer times. The deviation is caused by inability of shorter pulse sequences to refocus higher orders coherences of multispin couplings, which leads to faster intensity decays. On top of that, the 2-pulse-segment pulse sequence, lacking a  $180^\circ$  pulse, is not able to refocus chemical shift and off-resonance effects which explains its worst performance at longer times.

## 5 Power-law segmental orientation autocorrelation function

In the given chapter, a new analytical approach developed to estimate the slope and amplitude of the OACF at any given temperature is presented and discussed. The new approach is demonstrated on simulated and also experimental MQ NMR data of polymer melts of various molecular weights as well as networks with different structural inhomogeneity. The advantages of the new analysis as compared to older analytical strategies, and potential systematic errors are likewise discussed. The obtained results led to a scientific publication [52].

As was alluded to in Section 2.3, polymers, due to their chain structure, exhibit their dynamics on various time scales covering more than ten orders of magnitude, which can be broken down into several dynamic regimes (0-IV). We probe the polymer dynamics in the form of the OACF of the second Legendre polynomial  $C(t) = 5 \langle P_2(\cos \theta(t)) P_2(\cos \theta(0)) \rangle$ . Each of the dynamic regimes features a characteristic scaling exponent in  $C(t)$  [74, 107, 108, 113].

In refs 108 and 114, it was shown how to obtain the slopes of the OACF by means of the derivative analysis of the constructed master curve or the isothermal analysis of the initial rise of the  $I_{\text{nDQ}}$  curve relying on the short-time approximation  $I_{\text{nDQ}} \propto C(t) \times \tau_{\text{DQ}}^2 \propto \tau_{\text{DQ}}^{2-\kappa}$ , where  $\kappa$  is the slope of  $C(t)$  in the double logarithmic coordinates [115]. However, as will be seen below, the two previous approaches can suffer from significant uncertainties stemming from either the used shift factor or parasitic signals, experimental noise, and structural inhomogeneities. Therefore, a more robust approach to extract characteristic slopes and amplitudes of the OACF is required. To this end, the modeling strategy from ref 116 was employed. The modeling strategy starts with the simplification of equations 4.4 and 4.6 via the second-moment approximation [106]. As a result, the signal functions become

$$I_{\text{DQ}} = \sinh(\langle \phi_1 \phi_2 \rangle \exp(-\langle \phi_1^2 \rangle)) \quad (5.1)$$

$$I_{\Sigma\text{MQ}} = \exp(\langle \phi_1 \phi_2 \rangle) \exp(-\langle \phi_1^2 \rangle) \quad (5.2)$$

with

$$\langle \phi_1^2 \rangle = \frac{4}{9} M_{2\text{eff}} \times 2 \int_0^{\tau_{\text{DQ}}} (\tau_{\text{DQ}} - t') C(t') dt' \quad (5.3)$$

and

$$\langle \phi_1 \phi_2 \rangle = \frac{4}{9} M_{2\text{eff}} \left[ \int_0^{\tau_{\text{DQ}}} t' C(t') dt' + \int_{\tau_{\text{DQ}}}^{2\tau_{\text{DQ}}} (2\tau_{\text{DQ}} - t') C(t') dt' \right], \quad (5.4)$$

where  $M_{2\text{eff}} = \frac{9}{20} D_{\text{eff}}^2$ .

Different analytical representations of  $C(t)$  can now be nested into Eqs. 5.3 and 5.4 to obtain resulting signal functions. Neglecting motions faster than the minimal  $\tau_{\text{DQ}}$ , the OACF was assumed to decay according to a power law ( $\kappa$ ) starting from a certain residual anisotropy level at  $t_0$ . Such an OACF is given as

$$C(t) = \begin{cases} S_b^2 & \text{for } |t| < t_0 \\ S_b^2(t_0/t)^\kappa & \text{for } |t| > t_0 \end{cases} \quad (5.5)$$

Introduction of Eq. 5.5 into Eqs. 5.3 and 5.4 and their subsequent inclusion into the Anderson-Weiss-modified signal functions 5.1 and 5.2 results in [116]

$$I_{\text{DQ}} = e^{-\frac{2\tau_{\text{DQ}}}{T_2}} \exp \left\{ -\frac{\frac{1}{5}D_{\text{res}}^2}{(\kappa-2)(\kappa-1)} \left( (\kappa-\kappa^2)t_0^2 + (2\kappa^2-4\kappa)\tau_{\text{DQ}}t_0 + 2\tau_{\text{DQ}}^{2-\kappa}t_0^\kappa \right) \right\} \\ \times \sinh \left\{ \frac{\frac{1}{5}D_{\text{res}}^2}{2(\kappa-2)(\kappa-1)} \left( (\kappa^2-\kappa)t_0^2 + (2^{3-\kappa}-4)\tau_{\text{DQ}}^{2-\kappa}t_0^\kappa \right) \right\}, \quad (5.6)$$

$$I_{\Sigma\text{MQ}} = e^{-\frac{2\tau_{\text{DQ}}}{T_2}} \exp \left\{ -\frac{\frac{1}{5}D_{\text{res}}^2}{(\kappa-2)(\kappa-1)} \times \left( \frac{3}{2}(\kappa-\kappa^2)t_0^2 + (2\kappa^2+4\kappa)\tau_{\text{DQ}}t_0 \right. \right. \\ \left. \left. + (4-2^{2-\kappa})\tau_{\text{DQ}}^{2-\kappa}t_0^\kappa \right) \right\}, \quad (5.7)$$

where  $D_{\text{res}}$  is the residual dipolar coupling strength at  $t_0$  ( $= D_{\text{eff}}S_b$ ),  $\kappa > 0$ ,  $\kappa \neq 1, 2$ . The value of  $t_0$  is to be fixed just below the first experimental data point  $\tau_{\text{DQ}_{\text{min}}}$ . The term  $e^{-2\tau_{\text{DQ}}/T_2}$  was additionally introduced into the relations 5.6 and 5.7 to account for  $T_2$  relaxation due to fast molecular motions taking place on a time scale shorter than  $t_0$ , where  $T_2$  is the transverse relaxation time associated with these fast molecular motions. Also, it should be mentioned here that a chosen fitting interval between  $\tau_{\text{DQ}_{\text{min}}}$  and  $\tau_{\text{DQ}_{\text{max}}}$  is related to the same real-time dynamic interval of correlation loss.

Essentially, the above developed power-law-model-based signal functions represent a modified version of the functions based on the model from ref 116 used for networks which assumes that after some time  $\tau_0$ , before which  $C(t < \tau_0) = 1$  (corresponding to regime 0), the OACF loses its orientation memory according to a power law  $\kappa'$  up to the non-decaying plateau with a defined order parameter  $S_b$ .

This model with its predefined slopes of the OACF ranging between  $\kappa'$  and zero, will serve us a suitable reference to simulate the MQ NMR signal functions for the first test fits with the new relations 5.6 and 5.7. In Fig. 5.1a five non-normalized correlation function ( $C(t) \times (D_{\text{eff}}/2\pi)^2$ ) curves were constructed with varying  $\tau_0$ ,  $\kappa' = 0.9$  (regime I), and the plateau value set by  $D_{\text{res}}/2\pi = 0.2$  kHz. The corresponding DQ and  $\Sigma$ MQ signals were then generated (Fig. 5.1c) within the usual time window for the Baum/Pines pulse sequence between 0.1 and 10 ms and simultaneously fitted with the relations 5.6

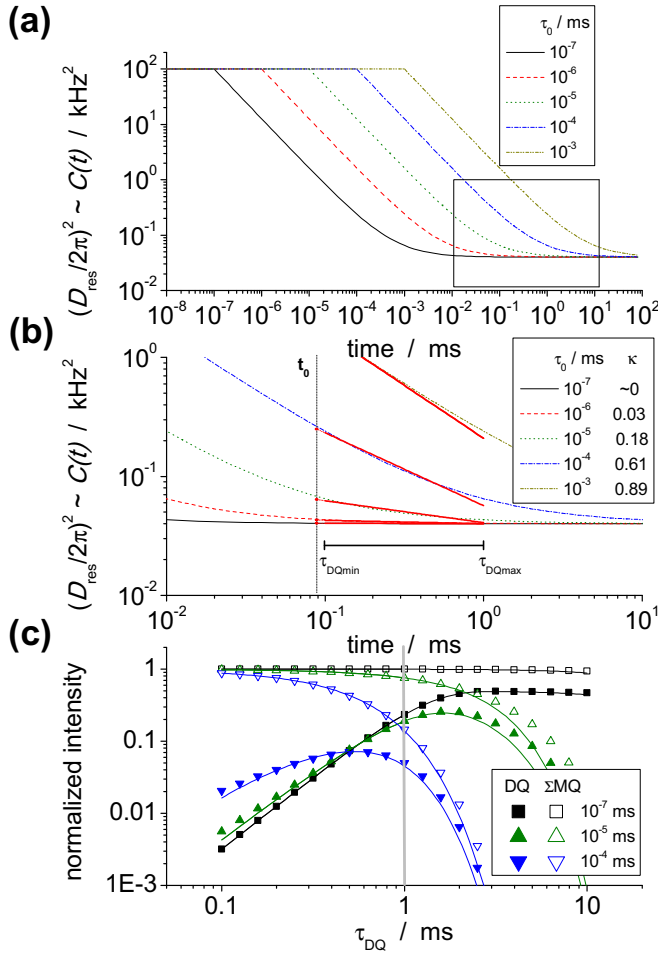


**Figure 5.1:** Test of the new power-law model on the simulated data based on the power-law model from ref 116: (a) non-normalized  $C(t) \times (D_{\text{eff}}/2\pi)^2$  curves exhibiting a correlation loss starting at different times  $\tau_0$  until the plateau level  $(D_{\text{res}}/2\pi)^2 = 0.2^2 \text{ kHz}^2$ ; (b) enlargement of the region highlighted in (a) by the box, the solid lines indicate average slopes between  $\tau_{\text{DQmin}}$  and  $\tau_{\text{DQmax}}$ ; (c) the DQ and  $\Sigma$ MQ signal functions corresponding to  $C(t)$  in (a) and generated according to Eqs. 33 and 34 from ref [116]. The solid lines represent the new power-law fits (Eqs. 5.6 and 5.7) done until 1 ms; the DQ/ $\Sigma$ MQ curves with  $\tau_0 = 10^{-5}$  ms were additionally fitted within the whole time range. Reproduced from [52], with the permission of AIP Publishing.

and 5.7. The extracted  $D_{\text{res}}(t_0)$  and  $\kappa$  values were then compared with the corresponding values obtained by power-law fits applied directly to the correlation function model curves within the same time intervals, shown in Fig. 5.1(b) (Table 5.1).

In Fig. 5.1a, it can be seen that with increase of  $\tau_0$  the accessed time window (0.1...10 ms) covers different parts of the  $C(t)$  curves. At  $\tau_0 = 10^{-7}$  and  $10^{-6}$  ms the  $C(t)$  curves are virtually completely in the plateau range, at  $\tau_0 = 10^{-5}$  ms the  $C(t)$  curve transitions from regime I to the plateau, and, finally, at  $\tau_0 = 10^{-4}$  and  $10^{-3}$  ms almost the whole studied region of  $C(t)$  is in regime I. In all the simultaneous DQ/ $\Sigma$ MQ fits, except in the case of  $\tau_0 = 10^{-3}$  ms,  $t_0$  was fixed to be 0.09 ms. The simulated MQ data with  $\tau_0 = 10^{-3}$  ms, corresponding to  $C(t)$  being virtually completely in regime I, exhibit a fast DQ build-up governed by strong dipolar couplings, which necessitates data points at shorter times. Therefore, in this case the DQ/ $\Sigma$ MQ data were generated starting from 0.01 ms and, therefore,  $t_0$  was chosen to be 0.005 ms.

Let us now take a closer look at the extracted fit values in Table 5.1. It can be seen that the  $D_{\text{res}}(t_0)$  values increase with  $\tau_0$  upon approaching regime I because the motional averaging is getting increasingly incomplete. Due to the same reason the  $T_2$  values decrease with  $\tau_0$ . The  $\kappa$  values increase with  $\tau_0$ , as expected. Both  $D_{\text{res}}(t_0)$  and  $\kappa$  values approximated

## 5 POWER-LAW SEGMENTAL ORIENTATION AUTOCORRELATION FUNCTION

---

**Table 5.1:** The power-law model fitting results obtained from the generated DQ/ $\Sigma$ MQ data in Fig. 5.1.

$\tau_0$ / ms	$10^{-7}$	$10^{-6}$	$10^{-5}$	$10^{-4}$	$10^{-3}$	
$\tau_{\text{DQmax}}$ / ms	1	1	1	10	1	1
From power-law fits to $C(t)$ curves (Fig. 5.1b):						
$D_{\text{res}}(t_0)/2\pi$ / kHz	0.200	0.207	0.253	0.242	0.502	4.84
$\kappa$	0.00	0.03	0.18	0.1	0.61	0.89
From fits to DQ/ $\Sigma$ MQ data (Eqs. 5.6 and 5.7):						
$t_0^{\text{a}}$ / ms	0.09	0.09	0.09	0.09	0.09	0.005
$D_{\text{res}}(t_0)/2\pi$ / kHz	0.200	0.205	0.237	0.212	0.519	5.00
$\kappa$	0.00	0.01	0.11	0.00	0.64	0.92
$T_2$ / ms	170.5	25.3	4.0	3.05	0.8	0.46
$b$	1.05	1.05	1.05	1.14	1.00	1.00

<sup>a</sup> fixed parameter.

by the simultaneous DQ/ $\Sigma$ MQ fits are found to be in good agreement with the average slopes obtained by the direct power-law fits to the  $C(t)$  curves.

For the DQ/ $\Sigma$ MQ data set with  $\tau_0 = 10^{-5}$  ms the impact of the used fit interval on the fit results was additionally studied. In this case the correlation function exhibits a transition from regime I to a plateau without a constant power-law value. Therefore, the obtained result for  $\kappa$  is a forced average value completely defined by the choice of the time interval. The more data points closer to the plateau region are chosen for the fit, the lower  $\kappa$  becomes.

In such a way one can even predict what kind of transition takes place. If the increase of the fitting interval causes reduction of  $\kappa$ , it corresponds to the transition from a dynamic regime with a larger exponent to a regime with a lower exponent, e.g. the current case, transition from regime I to a plateau. If the increase of the fitting interval leads to elevation of  $\kappa$ , it would point to an opposite situation, e.g. the transition from regime II to regime III of a polymer melt.

It is expected that fast molecular motions on the time scale before  $t_0$  lead to an exponential relaxation term. To check this, a stretched exponential term with an exponent  $b$  was utilized for the fits. It can be seen in Table 5.1 that  $b$  takes on values close to unity which proves the aforementioned statement.

Further, the new approach was tested on reference samples with well-defined power laws obtained from the corresponding OACF master curves. These are poly(butadiene) (PB)

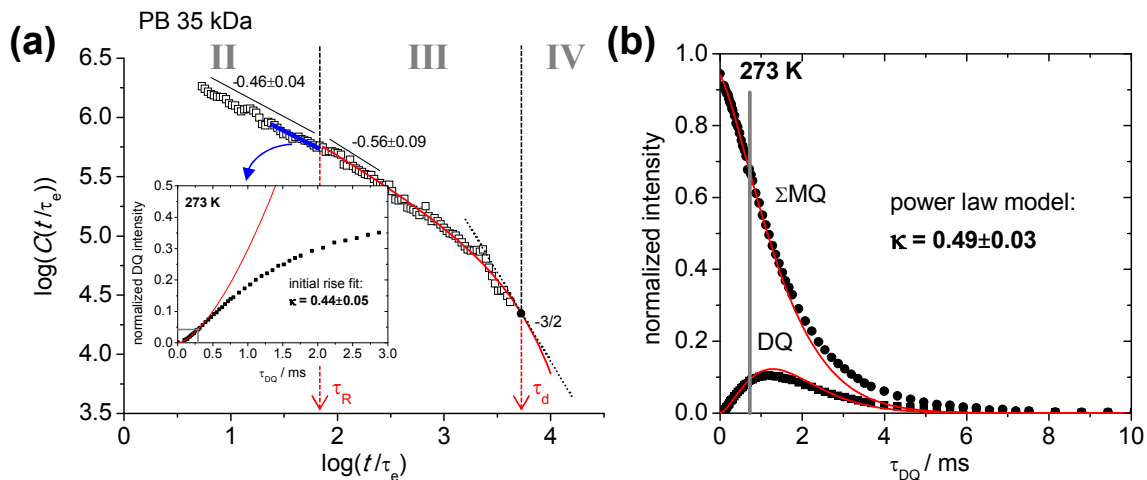


**Figure 5.2:** Demonstration of the different fitting approaches in action on the example of PB 35 kDa: (a) the derivative analysis of the OACF master curve; the inset shows the  $I_{nDQ}$  initial rise analysis at 273 K, and the corresponding part of the OACF is marked with a blue line. The dotted line indicates the tangential value of the effective power-law exponent of  $3/2$  at which the transition time  $\tau_s$  is reached. (b) The new power-law-model-based fitting approach. In the inset of (a) and in (b), the thick grey lines indicate fitting limits. Reproduced from [52], with the permission of AIP Publishing.

polymer melt samples of different molar masses with low polydispersity which were studied in ref [108]. In Fig. 5.2, the new fitting approach can be seen in action, and the power laws obtained from the OACF master curve construction, initial rise analysis of  $I_{nDQ}$ , and the power-law model are compared on the example of PB 35 kDa in the constrained Rouse regime of the tube model. The details of the OACF master curve construction can be found in ref [108]. The indicated slopes were obtained by means of the derivative analysis of the master curve. The initial rise analysis of  $I_{nDQ}$  was performed within approximately 10% of signal intensities, whereas the power-law-model fit was restricted to the time interval until  $\tau_{DQ}$  before the  $I_{DQ}$  maximum to avoid an overestimation of the power-law, as the  $C(t)$  approaches the transition to reptation at the given temperature. It can be seen that in the case of a polymer melt all approaches give similar results within the indicated errors.

For completeness, the three approaches were compared within a wider temperature range for PB samples of different molecular weights (see Fig. 5.3). It should be stressed here that the  $I_{nDQ}$  initial rise analysis yields the largest errors since it relies on the data points of low intensity. The derivative analysis of the OACF master curve overcomes this problem by using several data sets upon the master curve construction. However, the derivative analysis of master curves is subject to uncertainties of the chosen shift factor, which was  $\tau_e(T)$  in this case. Fig. 5.3 demonstrates that all three used strategies give consistent results within the whole temperature range and hence within all dynamic regimes. The best agreement is expectedly achieved in regime II with its constant scaling

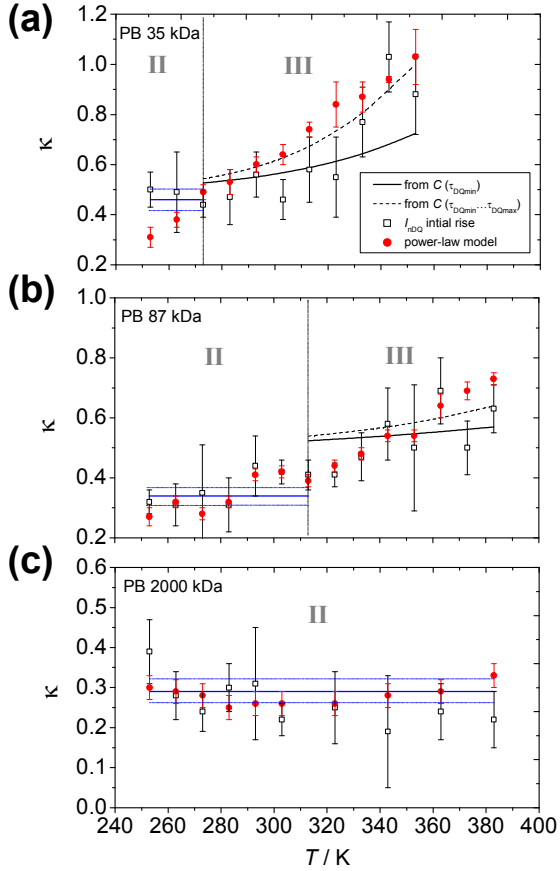


**Figure 5.3:** Comparison of the extracted power laws obtained by the derivative analysis of the OACF master curve (solid and dashed lines), the initial rise analysis of  $I_{nDQ}$ , and the power-law model within the wide temperature range on the example of PB samples of different molecular weights: (a) PB 35 kDa, (b) PB 87 kDa, (c) PB 2000 kDa. The dotted vertical lines indicate the borders between regimes II and III. Reproduced from [52], with the permission of AIP Publishing.

law. Some discrepancies between the analytical approaches appear in regime III, which can be described by a smooth transition from the power law of  $-0.5$  to a multiexponential decay [74, 108]. The abrupt change of the exponent upon transition between regimes II and III, seen in the slope analysis of the master curves of PB 35 and 87 kDa, is therefore caused merely by the tube model assumptions. Moreover, since the power-law model approximates  $\kappa$  in the larger time interval as compared to the initial rise analysis, the values of the former are expected to be a priori larger. To illustrate this point, the  $C(t)$  master curves were fitted with the analytical formula covering regimes III and IV [74, 108] and then the  $C(t)$  slopes were evaluated from either the derivative analysis at  $\tau_{DQmin}/\tau_e(T)$  or from the power-law fit over the whole interval  $\tau_{DQmin} \cdots \tau_{DQmax}$ . As expected, the former estimation resembles the initial rise approximation, whereas the latter depicts the DQ/ $\Sigma$ MQ-fitting results better.

The next test was done on rubber samples, the  $C(t)$  of which exhibit a plateau once chains between cross-links sweep all possible conformations. Clearly, a plateau implies a power law of the OACF equal to zero, which makes rubbers perfect reference samples. In (a) and (b) of Fig. 5.4, the results from the  $I_{nDQ}$  initial rise analysis and the power-law model are compared for the cases of homogeneous and inhomogeneous rubber samples. Natural rubber (NR) cross-linked with 0.5 phr dicumyl peroxide (DCP) served

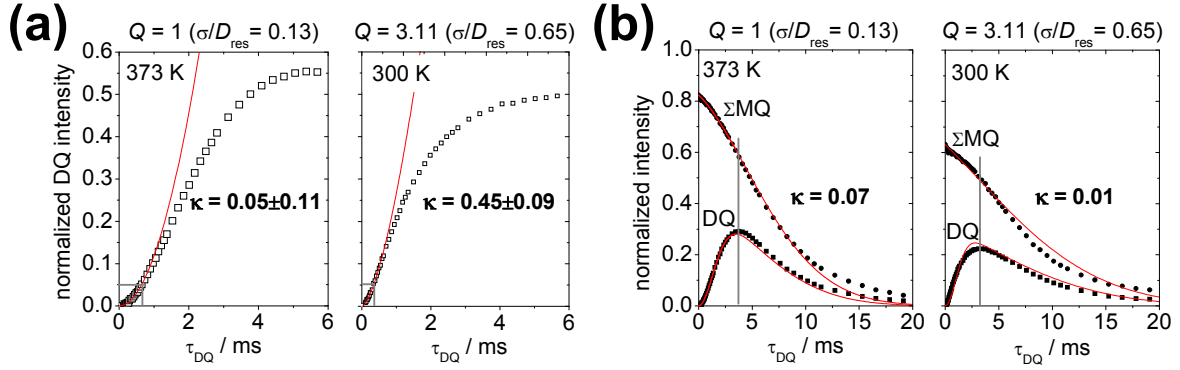


**Figure 5.4:** Comparison of the fitting results from the  $I_{\text{nDQ}}$  initial rise analysis (a) and the power-law model (b) tested on homogeneous (natural rubber cross-linked with 0.5 phr DCP, unswollen ( $Q=1$ )) and inhomogeneous (natural rubber cross-linked with 3.1 phr sulfur swollen up to  $Q=3.11$ ) rubber samples. Reproduced from [52], with the permission of AIP Publishing.

as a homogeneous sample. The cross-link density distribution, a measure of structural inhomogeneity, defined by the ratio of the standard deviation of the assumed Gaussian distribution ( $\sigma$ ) of  $D_{\text{res}}$  to the mean value of  $D_{\text{res}}$  was found to be around 0.13, which corresponds to a very homogeneous sample. Both fitting approaches gave in this case power law values very close to zero. Then, the same comparison was done on an inhomogeneous sample, namely NR cross-linked with 3.1 phr sulfur swollen to a swelling degree  $Q=3.11$ . Details on the sample preparations and NMR experiments with swollen elastomers can be found elsewhere [117]. The swollen sample showed  $\sigma/D_{\text{res}}=0.65$ , which is attributed to non-uniform stretching deformations of network chains upon swelling. As can be seen in Fig. 5.4, the  $I_{\text{nDQ}}$  initial rise analysis exhibits an apparent power law of 0.45, whereas the power-law model still gives a value close to zero. Thus, the power-law model is less sensitive to structural inhomogeneities and gives true dynamic information. Additionally, the power-law model is much more robust in terms of the effect of the fitting interval on the obtained result. The error for power-law exponent, depending on the end of the chosen fitting interval varied from somewhere before the  $I_{\text{DQ}}$  maximum and beyond it, was not larger than 0.05. In the case of the  $I_{\text{nDQ}}$  initial rise analysis, the error could reach as high values as 0.2 depending on the chosen fitting interval.

The above tests were performed exclusively on  $^1\text{H}$  MQ NMR data, where the Anderson-Weiss approximation is justified due to multi-spin coupling rendering an interaction frequency to be normally distributed. The same theory should be valid for  $^2\text{H}$  MQ NMR data too, yet with some restriction to shorter times as a Gaussian distribution can approximate only the initial part of the quadrupolar frequency distribution with a well-defined Pake shape as seen in the time domain. Thus, additional tests were done on  $^2\text{H}$  MQ NMR data of a fully deuterated entangled PB sample. The power laws extracted by the described approaches were also found to be in good agreement with each other. However, in this case, as expected and mentioned above, the power-law-model fits had to be restricted to shorter times to obtain consistent results and, hence, one cannot probe the

shape of the OACF by prolongation of the fitting interval in this case.

To recapitulate, a new power-law-model approach was presented and implemented for fitting of various  $^1\text{H}$  and  $^2\text{H}$  MQ NMR data sets of polymer melts and elastomers to extract the OACF slopes and amplitudes thus accessing the shape of the OACF and dynamic information on the microscopic level. The new approach was found to be applicable for structurally homogeneous systems (narrow  $D_{\text{res}}$  distribution) equally well as the smoothed derivative analysis of constructed OACF master curves and the  $I_{\text{NDQ}}$  initial rise analysis. In this case, apparent advantages of the new approach are the lack of necessity to use the TTS principle with its inherent uncertainties related to the used shift factors and the robustness of the fitting results associated with the use of higher intensity data as compared to the initial rise analysis plagued by experimental noise. Moreover, it was shown that the power-law model analysis delivers consistent and true dynamic results for structurally heterogeneous systems with a large distribution of dipolar couplings, whereas the other approaches clearly fail. Also, in transition zones between neighboring dynamic regimes the presented power-law model enables a prediction of the transition nature by variation of the evaluated time interval.

In the next chapter, it will be shown how  $C(t)$  master curves can be constructed using the results obtained from the power-law modeling, which can be done independently without rheologically determined shift factors. The  $C(t)$  master curve construction is especially important when the activation energy of the supramolecular bonding is a matter of interest. However, using the procedure to obtain activation energies is expected to be subject to potentially large systematic errors, which will be discussed in detail for the model cases.

## 6 The OACF master curve construction: Model cases

The presented power-law model can be utilized for the construction of  $C(t)$  master curves independently from the rheological shift factor. Given a rather crude approximation of real shapes of the OACF one can expect certain systematic errors in the determined values of characteristic relaxation times and, in particular, activation energies of molecular dynamics, especially for smooth transitions between the dynamic regimes and for (multi)exponential decays. How robust and trustworthy this mastering procedure is, should depend on the real shape of the OACF. Different model cases will be discussed in the following.

### 6.1 Reptating polymer melts

The entangled PB 87 kDa sample, shown in the previous chapter, will serve us as a good example for the demonstration of the master curve construction in the case of a  $C(t)$  curve exhibiting either a power law or multiexponential decay because it covers two cases at once: the well-defined power-law decay in regime II transitioning then to terminal flow.

The master curve construction of the OACF is very similar to the procedure employed in rheology [56]. One firstly needs to build isothermal  $C(t)$  parts approximated from DQ/ $\Sigma$ MQ data over studied time intervals ( $\tau_{\text{DQmin}} \cdots \tau_{\text{DQmax}}$ ) at all experimental temperatures.  $\tau_{\text{DQmax}}$  was set to the point corresponding to the 80% of the DQ maximum before the maximum. Such choice of  $\tau_{\text{DQmax}}$  ensures stable fits and minimizes overestimation of  $C(t)$  slopes. Note that in double logarithmic coordinates the  $C(t)$  parts appear to decay linearly. After that, a reference temperature is selected, and the  $C(t)$  parts at all other temperatures are shifted along the time axis with respect to the reference  $C(t)$ . Since the full overlap of the  $C(t)$  parts at neighboring temperatures is not possible, as is usually done in rheology, the shifting can be done either until the first point or the middle point or the last point of each  $C(t)$  part at a higher temperature, corresponding to  $C(\tau_{\text{DQmin}})$ ,  $C(\tau_{\text{DQmid}})$ , and  $C(\tau_{\text{DQmax}})$ , respectively, matches with the  $C(t)$  part at a lower temperature. We firstly proceed with shifting using matching of the  $C(\tau_{\text{DQmin}})$  points. The whole procedure is illustrated in Fig.6.1a.

It can be seen that the power-law exponent  $\kappa$  firstly fluctuates around its average value of 0.34 in regime II, and beyond around 313 K, upon the transition to regime III, constantly increases. One could hypothesize that the master curve construction based on the power-law-model approximation works best for the region of  $C(t)$  with a constant power law and exhibits some deviations once  $\kappa$  becomes variable. To check this hypothesis, one can simply compare the  $C(t)$  master curve constructed using the power-law-model results with the construction employing the previous strategy of the short-time approximation, well established for polymer melts [66, 107, 108]. In short, according to the short-time-approximation strategy  $C(t) \propto I_{\text{nDQ}}/\tau_{\text{DQ}}^2$  at short times corresponding to around 10% of normalized DQ signal intensities, and the shifting of isothermal  $C(t)$  parts relies on the rheological shift factor.

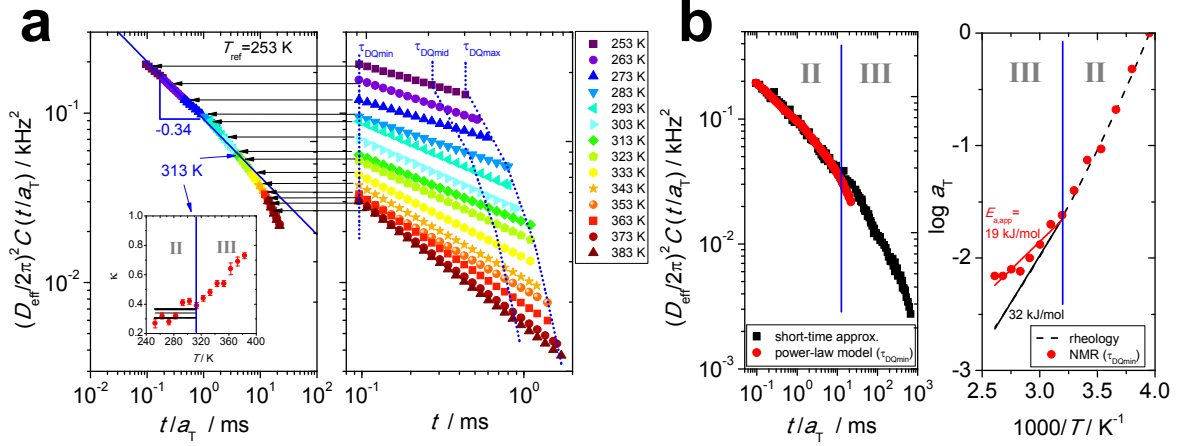


**Figure 6.1:** (a) Demonstration of a  $C(t)$  master curve construction using the power-law-model-fit results on the example of PB 87 kDa at  $T_{\text{ref}} = 253$  K. The shifting is done such that the first point  $C(\tau_{\text{DQmin}})$  of each  $C(t)$  part at a higher temperature matches with the lower temperature  $C(t)$  part. The inset shows the power-law exponents  $\kappa$  at the studied experimental temperatures within regimes II and III. The regime-II/III transition featuring the deviation from the average power law of 0.34 at around 313 K is marked with blue arrows. In the right panel, the first  $\tau_{\text{DQmin}}$ , middle  $\tau_{\text{DQmid}}$ , and last  $\tau_{\text{DQmax}}$  points of the fit intervals are shown. (b) Comparison of  $C(t)$  master curves obtained with two different analytical approaches: the power-law model and the short-time approximation. Left panel: the resulting  $C(t)$  master curves; right panel: the corresponding used shift factors. The deviation between the two approaches is seen to occur at the regime-II/III transition. The apparent activation energies  $E_{a,\text{app}}$  determined after the regime-II/III transition assuming the Arrhenius temperature dependence of  $\log a_T$  are indicated.

For a better comparison, the  $C(t)$  master curves constructed with the two strategies were matched at  $T_{\text{ref}}$ . As can be seen in Fig. 6.1b, the two  $C(t)$  master curves as well as their shift factors lie on top of each other in regime II, and after the transition to regime III they deviate increasingly. The deviation can be caused by the chosen shifting strategy. Thus, the matching of  $C(\tau_{\text{DQmin}})$  points seems to be not sufficient, which leads to the lower effective shift factor, as is validated in the right panel of Fig. 6.1b, and, consequently, to a shorter, apparent master curve. This in turn leads to a lower apparent characteristic transition time and activation energy. To quantify the systematic error in the activation energy,  $\log a_T$  were fitted assuming the Arrhenius temperature dependence in the deviation region. It can be seen that the apparent activation energy  $E_{a,\text{app}}$  obtained from the power-law-model-based shift factor is around 40% lower than its rheological counterpart.

It seems reasonable at this stage to test the shifting procedure involving matching the middle points of the fit intervals  $C(\tau_{\text{DQmid}})$  starting from 313 K, i.e. during the multiexponential decay. The resulting master curve and shift factor are presented in Fig. 6.2. For comparison, the shift factor resulting from the master curve construction conducted

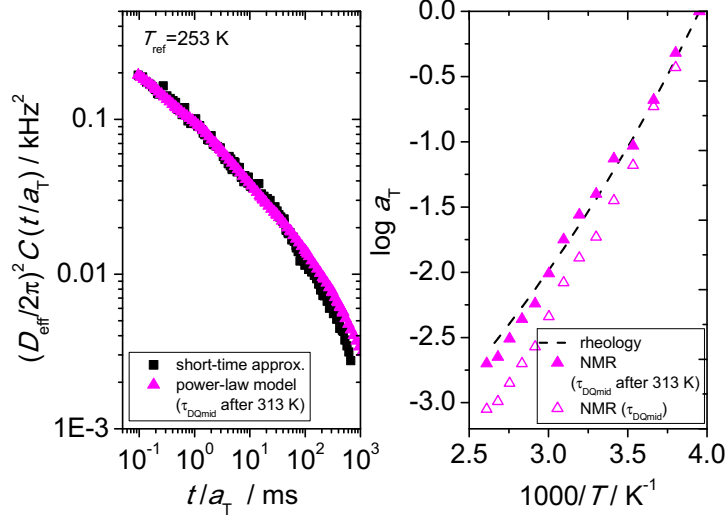


**Figure 6.2:** Left panel: the master curve constructed by matching the middle points of the fit intervals  $C(\tau_{\text{DQmin}})$  starting from 313 K (multiexponential decay). For comparison, a master curve built according to the short-time approximation is also shown. Right panel: the corresponding shift factors.

by matching  $C(\tau_{\text{DQmid}})$  within the whole temperature range is also plotted. It can be seen that the matching of  $C(\tau_{\text{DQmid}})$  points almost completely removes the deviations of the master curve and shift factor in the multiexponential decay region. However, the matching of  $C(\tau_{\text{DQmid}})$  points worsens the mastering within the power law region. Therefore, one can use a combination of the two shifting procedures for the most robust mastering. As the shifting procedure via the matching of  $C(\tau_{\text{DQmid}})$  points shows a minor overestimation of the shift factor, it is obvious that the matching of  $C(\tau_{\text{DQmax}})$  points would only lead to even larger errors.

A more thorough analysis of the shifting procedure conducted by matching of  $C(\tau_{\text{DQmid}})$  points for the case of exponential decays can be seen in the next section.

To extract a terminal relaxation time, one can either extract it from a constructed master curve, prone to systematic errors related to the shifting procedure, or, alternatively, determine it isothermally simply as a time average over the analyzed fitting interval of DQ/ $\Sigma$ MQ data at the temperature at which  $\kappa$  takes on some certain value. This  $\kappa$  value is equal to 3/2 for entangled polymer melts and 1 for the case of a monoexponential terminal flow starting from a non-decaying rubbery plateau, which can model unentangled telechelic polymer networks with no distribution of bond lifetimes. However, at temperatures corresponding to these  $\kappa$  values the dipolar couplings (and hence a DQ signal) become too low to ensure a reliable fit. To alleviate this problem, one can estimate the transition time at a lower value of  $\kappa$  instead and then correct it with an already known calibration factor (divide by  $\tau(\kappa)/\tau(\kappa = 3/2 \text{ or } 1)$ ).

In this work, we will need a calibration factor for the case of unentangled telechelic

networks. For this case, we decided to use  $\kappa = 0.5$  as a value at which the terminal flow becomes well developed. Additionally, it should be mentioned that real supramolecular systems always exhibit a distribution of bond lifetimes making it impossible to define a single value of  $\kappa$  at the average transition time, which depends on the distribution width. Instead, it is better to use a predefined average value of the transition time distribution as a reference value. Also, it is important to define the type of the transition time average. The most unbiased quantity reflecting the average of symmetric as well as asymmetric distributions is the median ( $\tau_{\text{med}}$ ) locating right in the middle of any given distribution interval. Therefore, to construct the calibration curve containing all the correction factors, one needs simply to find  $\tau(\kappa = 0.5)/\tau_{\text{med}}$  ratios at different distribution widths. The most general type of distribution to characterize a variety of transition times (and dipolar couplings too), when a real distribution is not known, is the log-normal distribution, because it is bound to zero, in contrast to the Gaussian distribution which can cover unphysical negative values if the distribution becomes too broad, and possesses a distribution width parameter  $\sigma_{\ln}$ , as opposed to the Gamma distribution [112] (see Section 4.2).

The calibration of the correction factors for the case of the correlation function decaying exponentially from the flat plateau with a log-normal distribution of terminal relaxation times will be conducted in the next section. Once the calibration factor is known, it will be discussed what time average of the analyzed fitting interval describes a real transition time in the most consistent way. Furthermore, an estimate of systematic errors in the activation energy will be considered for the aforementioned shifting procedures.

## 6.2 Unentangled telechelic polymer networks

For the calibration of the correction factors for transition times determined at  $\kappa = 0.5$ , two sets of exponential decays  $C_{\text{exp}}$  with a log-normal distribution of terminal relaxation times featuring two different median values and variable distribution widths  $\sigma_{\ln}$  were firstly generated. The analytical form of the built correlation functions reads as follows:

$$C(t) = \int P(\ln(\tau))C_{\text{model}}d \ln(\tau) \quad (6.1)$$

with

$$C_{\text{model}} = C_{\text{exp}} = S_{\text{b,pl}}^2 \exp(-t/\tau) \quad (6.2)$$

and

$$P(\ln(\tau)) = \frac{1}{\sigma_{\ln}\sqrt{2\pi}} \exp\left[-\frac{(\ln(\tau) - \ln(\tau_{\text{med}}))^2}{2\sigma_{\ln}^2}\right], \quad (6.3)$$

where  $S_{\text{b,pl}}$  is the order parameter in the plateau region.

A few selected examples of the generated  $C(t)$  curves are given in Fig.6.3. It can be seen that the decays become more protracted with  $\sigma_{\ln}$  which results in the increase of  $\tau(\kappa = 0.5)/\tau_{\text{med}}$ . Further, it can be seen that a larger  $\tau_{\text{med}}$  value leads merely to

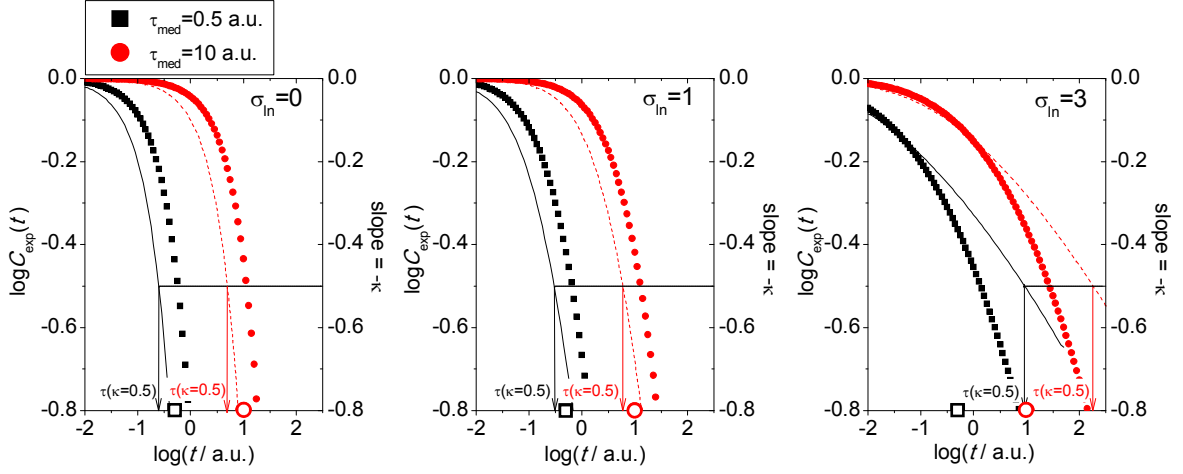


**Figure 6.3:** Extraction of transition times  $\tau(\kappa = 0.5)$  from the  $C(t)$  exponential decays with a log-normal distribution of terminal relaxation times (points). The slopes of  $\log C(t) = f(\log t)$  are presented as lines. The used median values  $\tau_{\text{med}}$  and distribution widths  $\sigma_{\text{ln}}$  are indicated. The  $\tau_{\text{med}}$  values are also marked on the  $\log(t)$  axis with large open symbols for comparison with  $\tau(\kappa = 0.5)$ .

the horizontal shift of the decays towards longer times and, therefore, the values of  $\tau(\kappa = 0.5)/\tau_{\text{med}}$  do not depend on  $\tau_{\text{med}}$ . All the drawn conclusions can be seen in Fig.6.4, showing the resulting calibration curve.

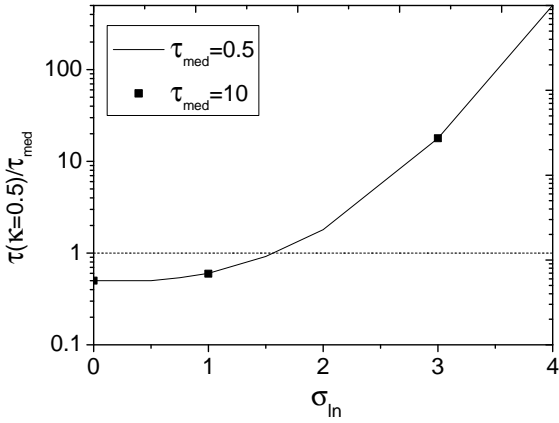


**Figure 6.4:** The calibration curve of the correction factors for  $\tau(\kappa = 0.5)$  at different  $\sigma_{\text{ln}}$ .

Let us now study the systematic errors in the activation energy and terminal relaxation times determined from DQ/ $\Sigma$ MQ metadata, simulated for the considered case, using the power-law-model fits. To simulate the DQ/ $\Sigma$ MQ metadata for the exponentially decaying  $C(t)$ , Eq. 6.2 should be plugged into Anderson-Weiss-approximated DQ/ $\Sigma$ MQ signal functions in the similar manner as was done to obtain the power-law-model fits (Eqs. 5.6 and 5.7) in Chapter 5.  $S_{\text{b,pl}}$  was set to be 0.02 and  $D_{\text{eff}}/2\pi$  to 10 kHz. For simplicity, it was assumed that the terminal relaxation time follows the Arrhenius temperature dependence  $A \exp(E_a/(RT))$ , where  $A$  is the preexponential factor,  $E_a$  is the activation energy,  $R$  is the gas constant. The sets of DQ/ $\Sigma$ MQ metadata were then generated within suitable temperature intervals for different values of  $A$  and  $E_a$  as well as  $\sigma_{\text{ln}}$  to take a thorough look at the resulting systematic errors. The power-law-model fits were

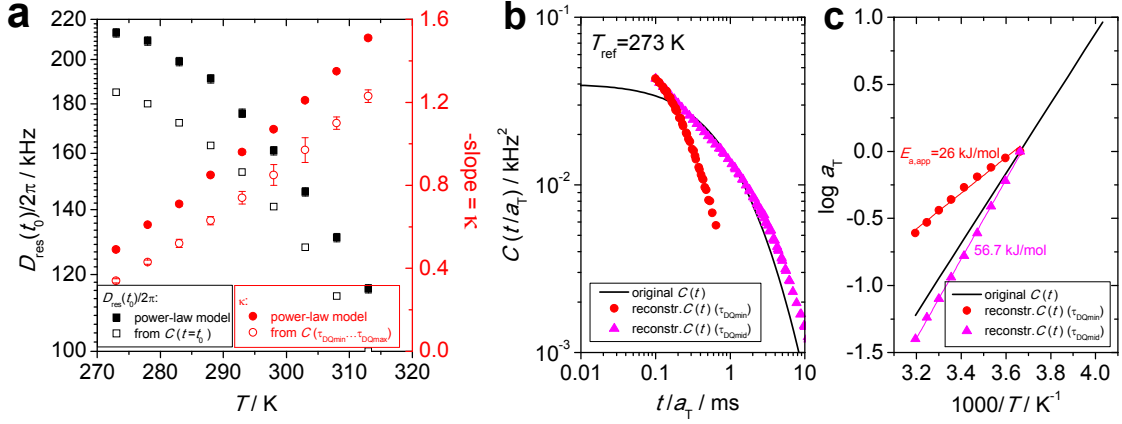


**Figure 6.5:** (a) Comparison of  $D_{\text{res}}(t_0)$  and  $\kappa$  values obtained by the power-law-model fits with the corresponding values from the direct analysis of the  $C(t)$  curves exhibiting an exponential decay with a log-normal distribution of terminal relaxation times ( $\sigma_{\text{ln}} = 1$ ). (b) Comparison of the reconstructed non-normalized  $C(t)$  master curves, using different shifting strategies, with the original  $C(t)$  curve at  $T_{\text{ref}} = 273$  K. (c) Comparison of the corresponding shift factors.  $E_{a,\text{app}}$  values in the deviation region are given as indicated.

conducted always until 80% of the maximum of DQ signals before the maximum. As was alluded to, this gives a sufficient number of data points for stable fits and improves the approximation of the real  $C(t)$ .

In Fig. 6.5(a), the extracted  $D_{\text{res}}(t_0)$  and  $\kappa$  values obtained by the power-law model fits to the DQ/ $\Sigma$ MQ metadata are compared with the corresponding values determined by direct power law fits to the exponential decays with log-normally distributed terminal times having the distribution width  $\sigma_{\text{ln}} = 1$ , changing with temperature according to the Arrhenius-equation parameters  $A = 2.4 \cdot 10^{-10}$  ms and  $E_a = 50$  kJ/mol. As can be seen, the power-law model fits to the DQ/ $\Sigma$ MQ metadata provide consistent results. Then, the  $C(t)$  master curves were constructed as explained above, giving the temperature-dependent shift factors. Fig. 6.5(b) and (c) illustrate the result of such master curve construction. It can be seen that the shifting procedure via matching of the  $C(\tau_{\text{DQmin}})$  points leads to the reconstructed master curve decaying significantly faster than the original  $C(t)$  curve at the same temperature, and the apparent activation energy estimated from the slope of the shift factor in the Arrhenius plot is approximately by a factor of two lower than the preset value. On the other hand, the shifting based on matching the  $C(\tau_{\text{DQmid}})$  points results in a substantially better reconstruction of the  $C(t)$  curve, with only 13% overestimation of the activation energy.

Then, terminal relaxation times were calculated for comparison as arithmetic ( $\langle \tau_{\text{ar}} \rangle = (\tau_{\text{DQmin}} + \tau_{\text{DQmax}})/2$ ), logarithmic ( $\langle \tau_{\text{log}} \rangle = (\tau_{\text{DQmax}} - \tau_{\text{DQmin}})/(\ln \tau_{\text{DQmax}} - \ln \tau_{\text{DQmin}})$ ), and geometric averages ( $\langle \tau_{\text{geom}} \rangle = \sqrt{\tau_{\text{DQmin}} \tau_{\text{DQmax}}}$ ) over the fitting time intervals at the temperature at which  $\kappa = 0.5$  and corrected with the calibration factors from Fig.6.4.

### 6.3 Highly inhomogeneous polymer networks

**Table 6.1:** Average characteristic times (ms) and apparent activation energies (kJ/mol) determined using the power-law-model fit results for various predefined Arrhenius-type temperature dependences ( $E_a^{\text{real}}$  in kJ/mol and  $A$  in ms) of median transition times ( $\tau_{\text{med}}^{\text{real}}$  in ms) of the log-normally distributed  $C(t)$  exponential decays.

Extracted parameter	$E_a^{\text{real}} = 50$		$E_a^{\text{real}} = 50$	$E_a^{\text{real}} = 100$	$E_a^{\text{real}} = 150$	
	$A = 2.4 \cdot 10^{-10}$		$A = 2.4 \cdot 10^{-9}$	$A = 5.8 \cdot 10^{-19}$	$A = 1.4 \cdot 10^{-26}$	
	$\sigma_{\text{ln}} = 0$	$\sigma_{\text{ln}} = 1$	$\sigma_{\text{ln}} = 2$	$\sigma_{\text{ln}} = 1$	$\sigma_{\text{ln}} = 1$	$\sigma_{\text{ln}} = 1$
$\langle \tau_{\text{ar}} \rangle$ ( $\tau_{\text{med}}^{\text{real}}$ )	1 (1)	0.92 (0.86)	0.34 (0.38)	1.02 (0.95)	0.92 (0.90)	1.02 (0.96)
$\langle \tau_{\text{log}} \rangle$	0.72	0.65	0.23	0.70	0.65	0.70
$\langle \tau_{\text{geom}} \rangle$	0.6	0.52	0.18	0.55	0.52	0.55
$E_{\text{a,app}}(\tau_{\text{DQmin}})$	23	26	27	22	51	89
$E_{\text{a,app}}(\tau_{\text{DQmid}})$	53	57	53	56	117	178

All the determined characteristic time averages and apparent activation energies  $E_{\text{a,app}}$  are presented in Table 6.1. The  $E_{\text{a,app}}$  values are shown for both shifting strategies.

It can be seen that the arithmetic average over the fitting time interval represents the real median time in the most consistent way. Also, in line with the above results, it was confirmed that the systematic error in the extracted activation energy (causing its underestimation) for mastering by matching  $C(\tau_{\text{DQmin}})$  points amounts to 40-60%. In contrast, the shifting conducted by matching  $\tau_{\text{DQmid}}$  points leads to significantly lower errors, namely, to an overestimation by around 15%, and, therefore, this procedure must be chosen when one deals with (multi)exponential decays.

### 6.3 Highly inhomogeneous polymer networks

Let us now consider another difficult case of  $C(t)$  to be estimated by the power-law model fits, namely, a power-law decay followed by a non-decaying plateau. The analytical form of such a correlation function reads:

$$C(t) = (1 - S_{\text{b,pl}}^2)(\tau_0/t)^{0.9} + S_{\text{b,pl}}^2, \quad (6.4)$$

where  $S_{\text{b,pl}}$  is the order parameter in the plateau region and  $\tau_0$  is the power-law-decay onset time.

This case can be observed in permanent networks and was already briefly addressed in Chapter 5. Note that, to consider the case of a highly inhomogeneous permanent network with a log-normal distribution of plateau order parameters, one should insert Eq. 6.4 into Eq. 6.1 on the place of  $C_{\text{model}}$  and exchange the time variable  $\tau$  with the order parameter  $S_{\text{b,pl}}$ . The examples of  $C(t)$  for both cases, with and without application of a log-normal distribution of order parameters, as well as their counterparts reconstructed with the power-law model by matching  $C(\tau_{\text{DQmin}})$  points are presented in Fig. 6.6 (a and b).

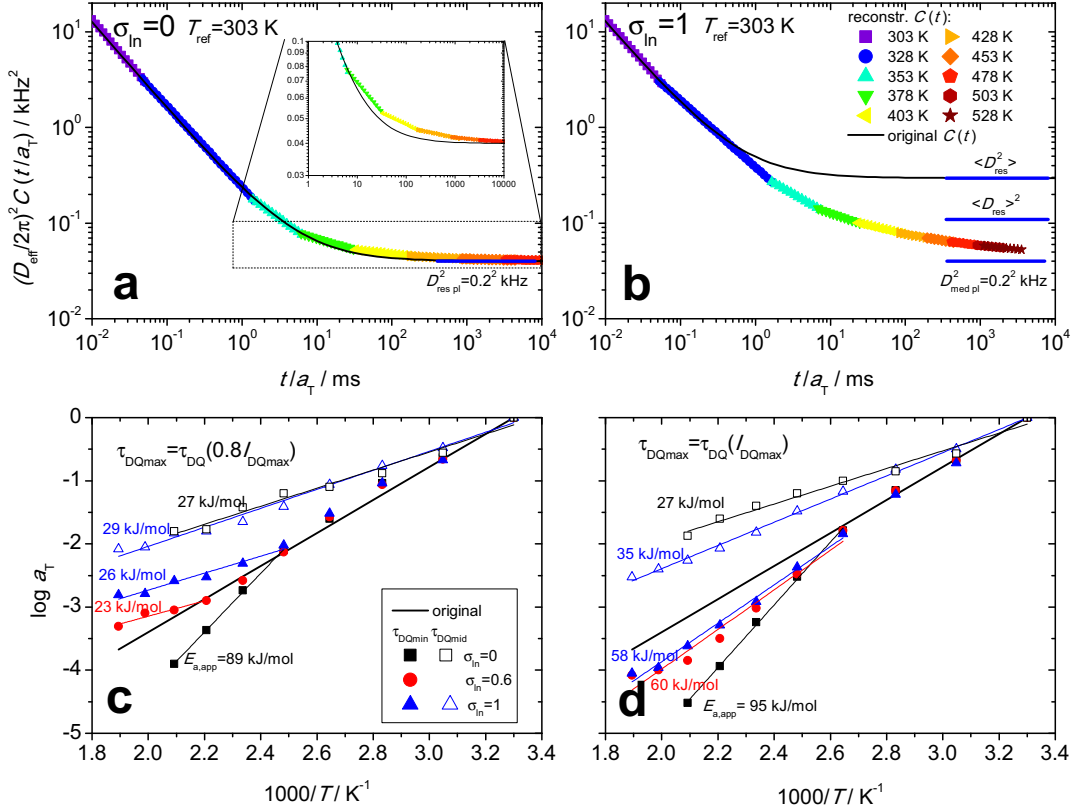


**Figure 6.6:** (a) and (b) Comparison of the reconstructed non-normalized  $C(t/a_T)$  master curves, built by matching  $C(\tau_{DQmin})$  points, with original  $C(t)$  curves for the cases without and with a log-normal distribution of order parameters at  $T_{ref} = 303$  K, respectively. For the latter case,  $\sigma_{ln} = 1$  was used. The power-law fits for extraction of  $C(t)$  parts were conducted until the maximum of the DQ signal in both cases. The thick blue horizontal lines indicate the plateau level of the residual dipolar couplings ( $D_{res pl}^2 = D_{eff}^2 S_{b,pl}^2$ ) in the case of a single order parameter, whereas, in the case with a log-normal distribution, they mark a median and two averages (mean-square  $\langle D_{res pl}^2 \rangle$  and squared mean values  $\langle D_{res pl} \rangle^2$ ) of the plateau dipolar couplings. (c) and (d) Shift factors used for the master curves construction in the cases when MQ NMR data were fitted until 80% of the maximum of the DQ signal before the maximum and until the maximum of the DQ signal, respectively. The shift factors, used for the mastering by matching  $C(\tau_{DQmid})$  points, are likewise shown for comparison.  $E_{a,app}$  values approximated by Arrhenius fits (thin solid lines) in the region of deviation of the shift factors from the predefined values are given.

It can be seen that in both cases the reconstructed  $C(t)$  master curves describe the original ones best in the power-law and worse in the plateau regions. The plateau region appears to be better represented in the case of a single order parameter than in the case of log-normally distributed order parameters, but a more careful consideration suggests that in the latter case the differences in the plateau levels in the original and reconstructed  $C(t)$  stem from different averaging of log-normally distributed order parameters. While the plateau of the original  $C(t)$  is defined as  $C_{pl} = \int D_{res pl}^2 P(\ln D_{res pl}) d \ln D_{res pl}$ , which is

identical to the mean-square value  $\langle D_{\text{res pl}}^2 \rangle$ , where  $D_{\text{res pl}}$  is the residual dipolar coupling in the plateau region directly related to the order parameter as  $D_{\text{res pl}} = S_{\text{b,pl}} D_{\text{eff}}$ , the plateau of the reconstructed  $C(t)$  appears in between of the squared average  $\langle D_{\text{res pl}} \rangle^2$  and the median value  $D_{\text{med,pl}}$  of the applied log-normal distribution of order parameters, approaching the latter with time.

For the single-order-parameter case, it can be seen that the transition to the plateau occurs more slowly for the reconstructed  $C(t)$  than for the original one. This can be explained by somewhat too low values of the extracted  $D_{\text{res}}(t_0)$  and  $\kappa$  (see Fig.5.1b). For a  $C(t)$  master curve construction by overlapping individual  $C(t)$  parts at the edges of the fitting intervals, the underestimation in  $D_{\text{res}}(t_0)$  and  $\kappa$  should lead to larger shifting factors as compared with predefined ones, and, hence, also to an overestimated activation energy. Fig.6.6 (c and d) validates this hypothesis for the case with no distribution of the order parameter. It can be seen that the shift factor deviates from the preset values upon approaching the plateau;  $E_{\text{a,app}}$  in the deviation region exceeds the predefined value by 78%. It can also be seen that the error expectedly (but not significantly) increases up to 90% if to consider larger time intervals (until the maximum of the DQ signal,  $\tau_{\text{DQmax}} = \tau_{\text{DQ}}(I_{\text{DQmax}})$ ) for the DQ/ $\Sigma$ MQ fits at each temperature.

In contrast to the single order-parameter case, the reconstructed  $C(t)$  master curves with a log-normal distribution of order parameters exhibit lower shift factors. The decrease of the shift factor becomes more pronounced with the distribution width and can be explained by the related increase of approximated  $\kappa$  values (see the plateau slopes in (a) and (b)). It is important to stress that in the plateau region with  $\kappa = 0$  the DQ/ $\Sigma$ MQ fits yield small, but non-zero  $\kappa$  values that increase with  $\sigma_{\text{ln}}$  as a result of a non-linear averaging in the presence of the order-parameter distribution and decrease if to increase the fit interval. For the fits until 80% of the maximum of the DQ signal before the maximum (i.e. until  $\tau_{\text{DQmax}} = \tau_{\text{DQ}}(0.8I_{\text{DQmax}})$ ), the resulting shift factors are seen to be even lower than the preset one upon approaching the plateau. To be more exact, the extracted  $E_{\text{a,app}}$  values for  $\sigma_{\text{ln}} = 0.6$  and 1 were estimated to be 23 and 26 kJ/mol, respectively, in the deviation region which is around 50% lower than the predefined activation energy. On the other hand, when the fits were done until the maximum of the DQ signal, the shift factors exceeded the preset one, and the errors in the activation energy for the cases with log-normally distributed order parameters reduced down to 20%.

In contrast, the mastering for both cases with single and log-normally distributed plateau order parameters done by matching  $C(\tau_{\text{DQmid}})$  points delivered substantially underestimated shift factors, observed within the entire studied temperature range, with  $E_{\text{a,app}}$  values estimated to be by 30-50% lower as compared to the predefined values.

These observations suggest that, to minimize the errors, one should resort to the shifting by matching  $C(\tau_{\text{DQmin}})$  points and use a fit interval until the maximum of the DQ signal in the case of  $C(t)$  having stable non-decaying long-time plateaus with a distribution of order parameters.

## 6.4 Systematic errors due to a too large temperature increment

An obvious source of systematic errors in the case of approximation of a smooth genuine shape of  $C(t)$  by a power law is the use of a too large temperature increment for the  $C(t)$  master curve construction. This would not only cause the shape of the reconstructed  $C(t)$  curve to appear coarse and angular, but also alter the  $C(t)$  decay time and, also, the extracted activation energy of the dynamic process. As the focus of the work is laid on determination of supramolecular bond lifetimes and activation energies associated with the supramolecular dynamics, it is especially important to access the systematic errors upon the  $C(t)$  decay featuring a constant augmentation in its slope as is the case for a (multi)exponential terminal flow or a transition from a plateau defined by entanglements and stickers (Leibler plateau) to an entanglement plateau with a distribution of bond lifetimes.

To this end, let us consider a  $C(t)$  master curve that was constructed with predefined known shift factors  $a_T$  obeying an Arrhenius temperature dependence. For simplicity, let us assume that the slope increment at each temperature is constant and equal to some number  $n$ . The initial values for  $D_{\text{res},1} = D_{\text{res}}(\tau_{\text{DQmin},1})$  and  $\kappa_1$ , corresponding to the reference temperature  $T_{\text{ref}} = T_1$ , are also known and equal to 0.2 kHz and 0.1, respectively. The task here will be to obtain  $C_i(t)$  parts at each temperature  $T_i$  to determine the additional shifts that are necessary if a larger temperature increment is chosen. Since we know  $\kappa_1$  and  $n$ , we can get  $\kappa_i$  at any temperature. Thus, the only quantity left to be defined is the amplitude of a  $C_i(t)$  part at  $T_i$ , i.e.  $D_{\text{res},i}^2$ . In principle, this task is the inverse of what is done upon a  $C(t)$  master curve construction, where one has all the information about the  $C(t)$  parts at hand and wants then to learn the shift factor.

$C_i(t)$  amplitudes at each  $T_i$  temperature can be easily accessed using the information from a  $C_{i-1}(t)$  part at the previous temperature  $T_{i-1}$ . For clarity, let us start from

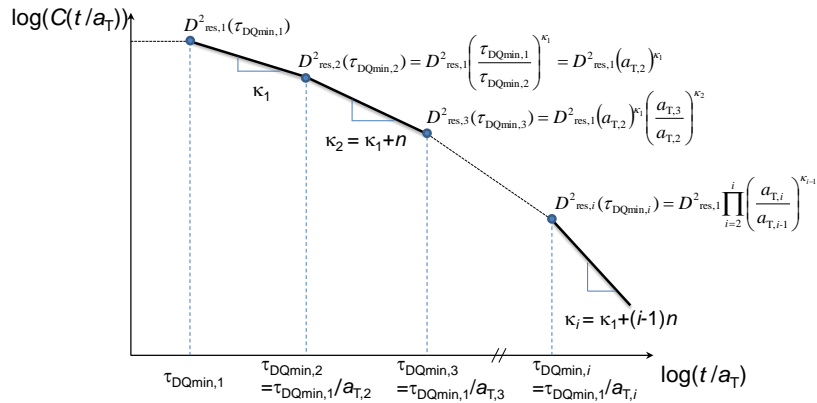


**Figure 6.7:** Modeled  $C(t)$  master curve construction with predefined shift factors and slope increment.

the known  $C_1(t)$  part at  $T_1$ , which can be found as  $D_{\text{res},i}^2(\tau_{\text{DQmin},1}/t)^{\kappa_1}$ . The  $C_2(t)$  part at the next temperature  $T_2$  matches with the  $C_1(t)$  part at  $\tau_{\text{DQmin},2}$  such that  $C_2(\tau_{\text{DQmin},2}) = D_{\text{res},2}^2 = D_{\text{res},1}^2(\tau_{\text{DQmin},1}/\tau_{\text{DQmin},2})^{\kappa_1}$ , since the shifting procedure is assumed here to be the same as used before, by matching the edges of the fit intervals at  $\tau_{\text{DQmin}}$ . Therefore, we get  $\tau_{\text{DQmin},2} = \tau_{\text{DQmin},1}/a_{T,2}$  and  $C_2(\tau_{\text{DQmin},2}) = D_{\text{res},1}^2(a_{T,2})^{\kappa_1}$ . Using the same tricks, the amplitude of  $C_3(\tau_{\text{DQmin},3})$  at  $T_3$  is equal to  $D_{\text{res},2}^2(\tau_{\text{DQmin},2}/\tau_{\text{DQmin},3})^{\kappa_2} = D_{\text{res},1}^2(a_{T,2})^{\kappa_1}(a_{T,3}/a_{T,2})^{\kappa_2}$ . One can already notice the pattern that  $D_{\text{res},i}^2$  accumulates the products of shift factors' ratios at the neighboring temperatures each of which is raised to the power of  $\kappa_1 \cdots \kappa_i$ . In other words, one gets the following:

$$D_{\text{res},i}^2 = D_{\text{res},1}^2(a_{T,2})^{\kappa_1} \left(\frac{a_{T,3}}{a_{T,2}}\right)^{\kappa_2} \cdots \left(\frac{a_{T,i}}{a_{T,i-1}}\right)^{\kappa_{i-1}} = D_{\text{res},1}^2 \prod_{i=2}^i \left(\frac{a_{T,i}}{a_{T,i-1}}\right)^{\kappa_{i-1}} \quad (6.5)$$

Eq. 6.5 gives a general description for a  $C(t)$  amplitude at any given temperature. To obtain now a time-dependent  $C(t)$  part at any given temperature, it remains to multiply the result of Eq. 6.5 with the corresponding power-law decay  $(\tau_{\text{DQmin},i}/(t/a_{T,i}))^{\kappa_i} = (\tau_{\text{DQmin},1}/t)^{\kappa_i}$  as follows:

$$C_i(t) = D_{\text{res},1}^2 \prod_{i=2}^i \left(\frac{a_{T,i}}{a_{T,i-1}}\right)^{\kappa_{i-1}} \left(\frac{\tau_{\text{DQmin},1}}{t}\right)^{\kappa_i} \quad (6.6)$$

Having a general analytical form for a  $C(t)$  master curve, we can now construct master curves with predefined slopes increments and shift factors assuming different activation energies. A small temperature interval of 1 K will be firstly chosen for the construction and then will be increased to 10 K by elimination of the  $C(t)$  parts at intermediate temperatures. The remaining  $C(t)$  parts will necessitate additional horizontal shifts for regaining an overlap which leads to elevation of the newly extracted activation energy. This procedure will be conducted for two activation energies of 50 and 250 kJ/mol with a fixed slopes increment of  $0.01 \text{ K}^{-1}$ , after which the slopes increment will be reduced to  $0.005 \text{ K}^{-1}$  keeping the activation energy to be 250 kJ/mol. The resulting original and reconstructed master curves as well as the corresponding shift factors are presented in Fig.6.8.

It can be seen that in the case of the slopes increment of  $0.01 \text{ K}^{-1}$  the apparent activation energy  $E_{\text{a,app}}$  extracted from the Arrhenius fits to the readjusted shift factors becomes around 30% larger than the predefined one upon the increase of the temperature interval from 1 to 10 K regardless of the used original activation energy. Further, when the slopes increment was reduced by half down to  $0.005 \text{ K}^{-1}$ , the overestimation of  $E_{\text{a,app}}$  decreased, too, by half down to around 15%. This means that the overestimation of the activation energy is proportional to the slopes increment.

Applying this knowledge to the experimental results of the studied samples presented below, one can conclude that for ionic BIIR and telechelic PIB samples, exhibiting average

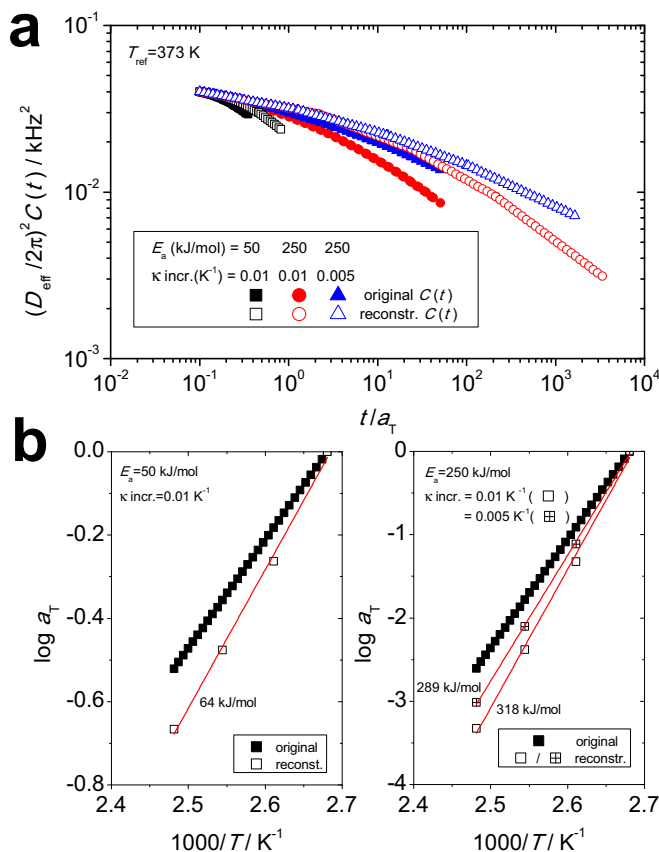


**Figure 6.8:** (a) Modeled  $C(t)$  master curves with predefined shift factors and slopes increments and their counterparts reconstructed with a larger temperature interval. An initial temperature interval is 1 K, a temperature interval for the reconstruction is 10 K. The activation energies  $E_a$  of the shift factors were taken as 50 and 250 kJ/mol with a slopes increment of 0.01  $\text{K}^{-1}$  and 250 kJ/mol with a slopes increment of 0.005  $\text{K}^{-1}$ . (b) The shift factors used for the construction of the original  $C(t)$  master curves and for the reconstruction with a larger temperature interval. Left panel:  $E_a = 50$  kJ/mol, right panel:  $E_a = 250$  kJ/mol. The red lines represent Arrhenius fits extracting apparent activation energies  $E_{a,\text{app}}$  that are given next to the fit lines.

slopes increments of around 0.001 and 0.01  $\text{K}^{-1}$ , respectively, in the supramolecular transition region and being measured every 10 K, the overestimation of the determined activation energy due to a too large temperature interval can be estimated to be around 3 and 30%, respectively. Note that the same procedure upon shifting by matching the middle points of the fit intervals  $C(\tau_{\text{DQmin}})$  resulted in similar systematic errors.

This systematic error in the activation energy adds up with the aforementioned systematic errors originating from the crude approximation of the smooth shape of the real correlation functions.

## 7 Objects of investigation

### 7.1 Bromobutyl rubber samples

The set of bromobutyl rubber (BIIR) samples is based on commercial BIIR acquired from Lanxess<sup>®</sup>. The BIIR polymer chains possess a weight-averaged molecular weight ( $M_w$ ) of 590 kg/mol with a large polydispersity index (PDI) of about 4.7. The specified  $M_w$  corresponds to highly entangled polymer chains with around  $M_w/M_e = 85$  entanglements per chain, where  $M_e (=6700 \text{ g/mol})$  is the molecular weight of the entangled strand [118].

The BIIR was studied in the as-received, uncross-linked state as well as after its vulcanization. The vulcanization was carried out either with conventional sulfur to obtain permanent networks or by introduction of ionic alkyimidazolium (alkyl: methyl-, butyl-, hexyl, or nonylimidazolium, denoted as MI, BI, HI, and NI, respectively, see Fig.7.1) moieties on bromine sites to obtain supramolecular ionic networks. The alkyl group can screen electrostatic interactions, and the effect of its length on dynamic properties of the ionic networks will be scrutinized in Chapter 8.

For preparation of the ionic networks, alkyimidazoles were added in an excess of 1.5:1 with respect to the content of brominated isoprene units  $x_c$ , constituting 0.8 mol% of the material [17]. The full conversion, confirmed by <sup>1</sup>H solution-state NMR, gives transient networks with  $N_x = 1/x_c = 125$  monomeric units between two stickers, corresponding to the molecular weight between stickers  $M_{st} = 125 \cdot 56 = 7000 \text{ g/mol}$ . Knowing the molecular weight of one Kuhn segment  $M_0 = 274 \text{ g/mol}$  at room temperature [118], we obtain the numbers of Kuhn segments between two entanglements and stickers to be  $N_e \approx 25$  and  $N_{st} = 26$ , respectively, which corresponds to the case of sparsely arranged stickers  $N_e/N_{st} \approx 1$ . Further, it was verified that structures of all the ionic networks were in equilibrium.

For high-resolution solid-state NMR measurements, the unreacted alkyimidazole species were removed by reprecipitation to exclude overlapping of their signals with the signals of the alkyimidazoliums. For low-resolution solid-state NMR and mechanical experiments, the samples were studied with unreacted alkyimidazole inside. Note that no effect of free, unreacted alkyimidazoles on the network structure and its thermal evolution was observed by the NMR and rheological analyses (see Section B.5 for more details). To pre-

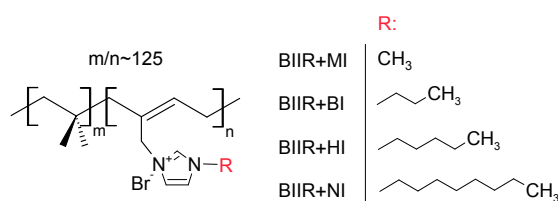


**Figure 7.1:** Chemical structure of ionic BIIR samples.

pare covalent networks with different cross-link densities sulfur was added in the amount of 0.5 and 1 parts per hundred rubber (phr) (henceforth denoted as BIIR-S X phr, where X is the amount of added sulfur in phr). More detailed information on materials and conditions of the samples' preparation can be found elsewhere [16, 17].

Importantly, the ionic modification did not increase  $T_g$  ( $= -64^\circ\text{C}$ ) of the polymer matrix, as is the case in other ionomeric systems with larger ionic content [47, 119]. Further, note that BIIR-S 1 phr had to be additionally thermally treated at  $140^\circ\text{C}$  for two hours in a protective argon atmosphere to guarantee the reaction of all the added sulfur. The chain scission processes occurred at temperatures beyond  $140^\circ\text{C}$ , and, thus, it was the highest limiting temperature used for all the experiments.

## 7.2 Telechelic poly(isobutylene) samples

The telechelic poly(isobutylene) (PIB) samples were prepared by cationic polymerization to obtain polymer chains with well-defined molecular weights ( $\text{PDI}=1.3\text{-}1.5$ ) and molecular architectures, which were subsequently end-functionalized with hydrogen-bonding moieties (barbituric acid (BA) or thymine (Th)), see Fig. 7.2 for details.

The BA-based end-group is able to establish more hydrogen bonds than the Th-group, and, therefore, is expected to exhibit a higher dissociation energy. Synthesis details can be found elsewhere [28–30]. The molecular architectures comprised linear as well as

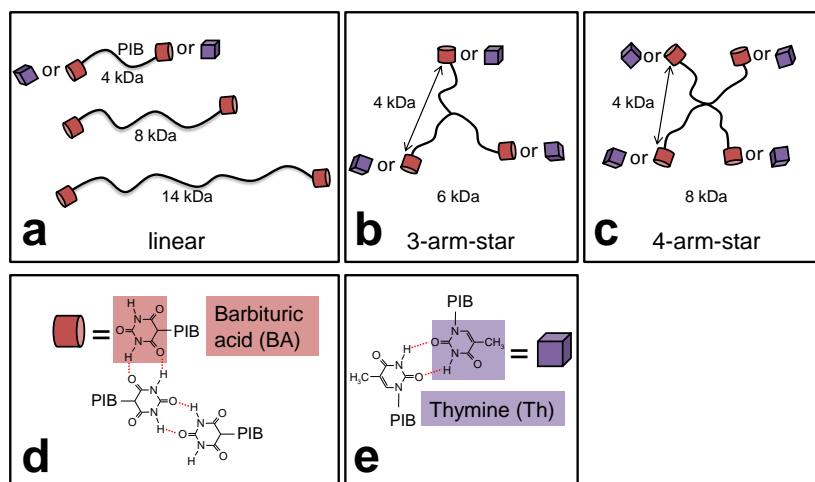


**Figure 7.2:** Telechelic PIB samples with different molecular architectures, molecular weights, and end-groups. (a), (b), and (c) show linear, 3-arm-star, and 4-arm-star structures, respectively; (d) and (e) present chemical formulas of end-groups (barbituric acid (BA) and thymine (Th), respectively) with tentative representation of established hydrogen bonding as indicated by red dotted lines. Note that the presented bonding patterns are simplified and only serve showing the difference in the number of provided hydrogen bonds per sticker for BA and Th. Total and end-to-end molecular weights are likewise specified next to the given structures.

3- and 4-arm star-shaped molecules, all featuring a constant molecular weight between the chain ends of around 4 kDa, thus yielding a total molecular weight of 4, 6, and 8 kDa, respectively. Linear BA-functionalized samples were additionally prepared in 8 and 14 kDa molecular weight versions. Henceforth, the samples will be designated specifying in the name the total number-averaged molecular weight of the polymer, the end-group (BA or Th) and the number of end-groups, e.g. 6kBA3 corresponds to the 3-arm-star end-functionalized with BA. In all cases, the used molecular weights were lower or comparable to the critical molecular weight ( $\approx 2M_e = 13.1$  kDa [118]), such that the effects of entanglements from individual molecules can be excluded. However, trapped entanglements formed upon network formation can still be present (Fig. 9.2(a)) [120]. The introduction of functional end-groups caused a slight elevation of  $T_g$  by around  $5^\circ\text{C}$  ( $= -60 \pm 2^\circ\text{C}$ ) for the samples with the molecular weight of 4 kDa between the end-groups and almost no change for the larger-molecular-weight samples. To equilibrate network structures of the telechelic samples and remove solvent residues, all the samples were thermally treated in the vacuum oven under vacuum of 40 mbar at  $100^\circ\text{C}$  for 24 hours.



## 8 Sticky chain and sticker dynamics in entangled butyl rubber ionomers

In this chapter, a thorough, multi-technique characterization of structure and dynamics of sparsely cross-linked entangled ionic networks prepared by modification of commercial bromobutyl rubber (BIIR) with alkylimidazoles is presented. The structural and dynamic properties of the ionomers can be tuned by varying the length of the alkyl group, laying a foundation for imparting a self-healing ability to this class of materials.

Structural and morphological analyses, conducted by small-angle X-ray scattering (SAXS) and NMR relaxometry, show that ionic groups are mostly in the closed state and form ionic aggregates with aggregation numbers of around 20 ionic groups, which does not lead to an appreciable number of immobilized segments and phase separation (see Fig. 4.2). The molecular dynamics of network chains and ionic cross-links, as measured by  $^1\text{H}$  multiple-quantum (MQ) NMR at low and high resolution, respectively, accelerates with the length of the alkyl group. Using an analytical approach based on the power-law model of the OACF, the bond lifetimes and corresponding activation energies can now be quantified by  $^1\text{H}$  MQ NMR.

The correlation of the results of MQ NMR and dynamic mechanical analysis (DMA) showed a quantitative agreement in the extracted activation energies and bond lifetimes, thereby validating relevant aspects of the sticky reptation theory on the microscopic level for the first time. In particular, the transition from the plateau contributed by stickers and entanglements to the entanglement plateau is shown to be the result of an aggregate exchange. Limitations of the use of master curves for a direct comparison of results from the two methods are discussed.

Broadband dielectric spectroscopy results, on the one hand, corroborate the NMR and DMA findings showing similar trends in activation energies for the ionic transport process and amplitudes of the intra-aggregate motions, but, on the other hand, exhibit a counterintuitive trend in intra-aggregate relaxation times across the samples series opposite to the trend found by NMR and DMA. The latter observation suggests that the intra-aggregate relaxation is not related to the bare bond lifetime.

Non-linear stress-strain experiments reveal a dynamic character of the studied ionic networks, defined by the relationship between the initial deformation rate and the bond lifetime, and show a decrease in the bond lifetimes upon stretching owing to the accumulation of internal stresses. The discussed results were published in two papers [17, 76].

### 8.1 Structural analysis by SAXS

To investigate structures of the ionic networks, SAXS measurements were carried out. The experiments and fitting of the scattering data were done by Prof. Dr. Kay Saalwächter, whereas I interpreted the obtained results. Firstly, it was important to find out whether

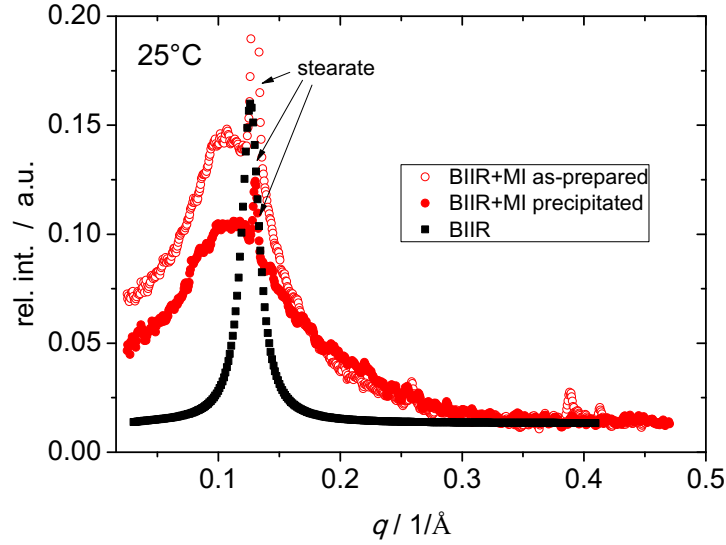


**Figure 8.1:** Comparison of SAXS data for ionic BIIR+MI network (as-prepared and reprecipitated) and non-ionic BIIR at 25°C. Reprinted with permission from [76]. Copyright 2019 American Chemical Society.

ionic aggregates are present in the ionic networks and whether structural changes occur after the reprecipitation procedure. Fig. 8.1 shows the comparison of unmodified, reprecipitated BIIR with as-prepared and reprecipitated BIIR+MI. It can be seen that the unmodified sample exhibits one narrow peak at  $q=0.13$   $1/\text{\AA}$ , whereas the modified samples show one broad peak at around  $q=0.1$   $1/\text{\AA}$  and also one narrow peak at  $q=0.13$   $1/\text{\AA}$ . The narrow peaks correspond to the stearic acid present in the formulation of the commercial BIIR [121] and, therefore, observed in all samples. The broad peak in turn is related to the electron density contrast caused by ionic aggregates. The lower intensities of the narrow and broad peaks of BIIR+MI after reprecipitation as compared to the as-prepared sample suggests that stearic acid is removed from the sample upon the reprecipitation, and the ionic aggregates become smaller as a result of the removal of the polar stearic acid and free, unbound methylimidazole molecules from them.

In Fig. 8.2a, the SAXS data of all the ionic networks obtained at 25°C are compared. The maxima of the ionic peaks are observed at  $q_{\max} \approx 0.1$   $1/\text{\AA}$  and found to be nearly invariant to the alkyl group length in the alkyylimidazolium moieties. The observed  $q_{\max}$  value corresponds to the average distance between the ionic aggregates  $r_{i-i}$  of 62.8 Å. Remarkably, the root-mean-square end-to-end distance corresponding to the part of the chain between two ionic cross-links  $\sqrt{R^2} = \sqrt{c_{\infty} n_x a_b^2} \approx 62$  Å, where  $c_{\infty}$  is the characteristic ratio of PIB (= 6.6 [118]),  $n_x = 2N_x - 1 \approx 2N_x$  is the number of bonds between two ionic cross-links,  $a_b$  is the carbon-carbon bond length [125]. Similar values of  $r_{i-i}$  and  $\sqrt{R^2}$  suggest that the ionic groups are mostly in the bound state and that the network chains are mostly in the form of relaxed Gaussian conformation. Further, it can be seen that the peaks' intensity decreases with the length of the alkyl group. This result can be

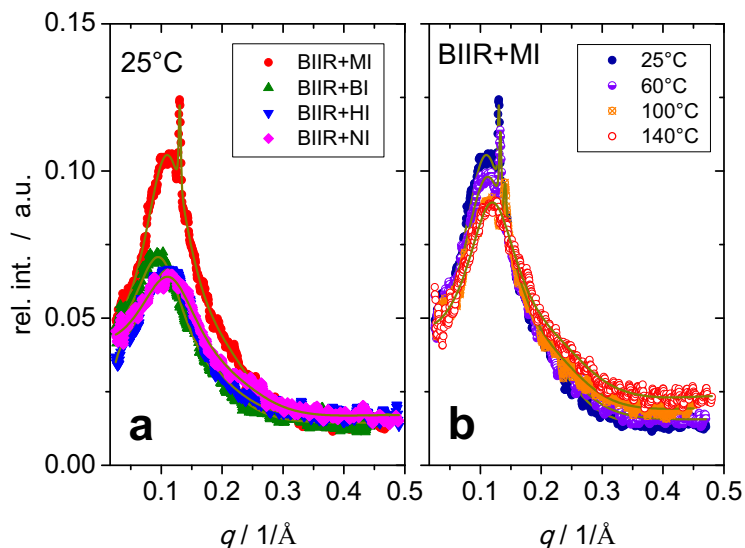


**Figure 8.2:** (a) Comparison of SAXS data of all the studied ionic networks at 25°C. (b) SAXS data of BIIR+MI at indicated temperatures. The solid lines are the fits according to a model based on a Percus-Yevick structure factor [122–124]. Reprinted with permission from [76]. Copyright 2019 American Chemical Society.

explained by decreasing electron density contrast between the ionic aggregates and the polymer matrix as the alkyl group diluting ionic multiplets becomes longer.

The temperature elevation of the ionic networks BIIR+MI and BIIR+BI (Fig. 8.2b and B1) up to 140°C showed almost no change of the peaks' positions and only around 20% intensity loss, which suggests that the average distance between the ionic aggregates does not change and the aggregates themselves stay largely intact. The decrease of the peaks' intensity can be caused by reduction of positional correlations, which can occur as a result of the acceleration of sticky dynamics of single ionic groups in the proximity of ionic aggregates and the shift of the dynamic equilibrium of open/closed stickers towards larger number of open stickers.

Because such broad, featureless peaks can result from various disordered structures of different geometry [37, 126, 127], we estimate aggregation numbers ( $AN$ ), that is a number of ionic groups per ionic aggregate, using two approaches. The estimation can be done either following space filling arguments [96, 124] with the assumption that all the ionic aggregates are arranged in a cubic crystal lattice with the size of the unit cell equal to  $r_{i-i}$  or employing a model to fit the SAXS data. In the former case, the aggregation number can be found as follows:

$$AN = \frac{r_{i-i}^3}{M_{st}/(\rho(\text{PIB})N_A)} \approx 20 \pm 6, \quad (8.1)$$

where  $\rho$  is the density of PIB ( $\approx 0.9$  g/cm<sup>3</sup>) [118],  $M_{\text{st}}$  is the molecular weight of the part of the chain between two stickers,  $N_{\text{A}}$  is the Avogadro's number.

Using the second approach for the  $AN$  estimation, for simplicity, it was assumed that the formed ionic aggregates are spherical and arranged according to a Perkus-Yevick-based structure factor [122–124], describing repulsive interactions of hard spheres of radius  $R_2$  with a volume fraction  $f$ . The  $R_2$  is an effective quantity since there is no scattering contrast on the edges of the micellar corona. The scattering contrast in turn occurs on the ionic groups constituting the cores of the assumed spheres. The sizes of the cores are described with radius  $R_1$  which is additionally assumed to be lognormally distributed ( $\sigma$  is the width of this distribution on the log scale). Knowing  $R_1$ , one can estimate  $AN$  using the following equation [124]:

$$AN = \frac{\frac{4}{3}\pi R_1^3}{M_{\text{AI}}/(\rho(\text{AI})N_{\text{A}})} \approx 22 \pm 9, \quad (8.2)$$

where  $M_{\text{AI}}$  is the molecular weight of an alkylimidazolium sticker,  $\rho(\text{AI})$  is its density. Note that the used  $\rho(\text{AI})$  values, taken from ref 128 and interpolated to the indicated temperatures, correspond to non-ionic alkylimidazoles; the magnitudes can be up to 50% lower as compared to their ionic counterparts [129], but, nevertheless, reflect the trend of the density reduction with the length of the alkyl group. For the discussion of ionic association,  $AN$  is a better parameter than  $R_1$  and  $R_2$  because it accounts for the differences in densities and sizes of individual ionic groups.

As can be seen, both estimation approaches of  $AN$  give similar values of around 20, which can, however, be underestimated because of the assumed cubic lattice with the lowest resulting size of the unit cell (e.g. the body-centered cubic cell would yield a  $\sqrt{2}$  times larger unit cell) and the somewhat too low values for  $\rho(\text{AI})$ , respectively. The observed sample-independent  $AN$  values can be explained by similar predefined spacing between the aggregates and strong associating strength in all cases. The discussion of the extracted Perkus-Yevick model parameters as well as the peaks' positions ( $q_{\text{max}}$ ) and maximal intensities ( $I(q_{\text{max}})$ ) of precipitated samples is deferred to the appendix (see Table B1).

Using scaling arguments from ref 41, we can estimate the number of bridges  $N_{\text{br}}$  connecting flower-like micelles and therefore the fraction of bridges with respect to the sum of bridges and loops:

$$N_{\text{br}}/AN = (N_{\text{st}}^{0.5}/AN)^{0.22} \approx 0.74. \quad (8.3)$$

Thus, the majority of stickers form bridging chains with a close to ideal geometry. The fraction  $N_{\text{br}}/AN$  corresponds to elastically active chains, which will be important for the calculation of the plateau modulus (see below).

## 8.2 Dynamic and structural studies by $^1\text{H}$ MQ NMR

### 8.2.1 Quasi-static analysis of $^1\text{H}$ MQ NMR data

For the BIIR samples, the  $D_{\text{res}}$  distribution was found to be rather broad. Given that the phase composition analysis showed no phase separation of network chains, we decided to use a single log-normal distribution of  $D_{\text{res}}$  for the analysis of the  $I_{\text{nDQ}}$  curves, accounting for the pronounced structural and dynamic heterogeneity [17, 112] (see Eqs. 4.12 and 4.13).

In Fig. 8.3, the results of the  $I_{\text{nDQ}}$  analysis of the  $^1\text{H}$  MQ NMR measurements, carried out under static conditions, estimating an apparent cross-link density of the studied networks in the form of  $D_{\text{med}}/2\pi$  are given as a function of temperature. The  $I_{\text{nDQ}}$  curves were found to reach the plateau of 0.5 only starting from  $70^\circ\text{C}$ , meaning that from this temperature on the conformational dynamics of the network chains was fast on a ms time scale. Fig. 8.3 compares the thermal evolution of  $D_{\text{med}}/2\pi$  of the non-ionic samples (left panel) and ionic networks (right panel).

As can be seen,  $D_{\text{med}}/2\pi$  values of the permanent networks nearly do not change with temperature due to the covalent nature of the cross-links. A larger amount of the added sulfur expectedly leads to a larger cross-link density and larger  $D_{\text{med}}/2\pi$ . The BIIR sample in turn showed a reduction of  $D_{\text{med}}/2\pi$  with temperature as a result of constrained

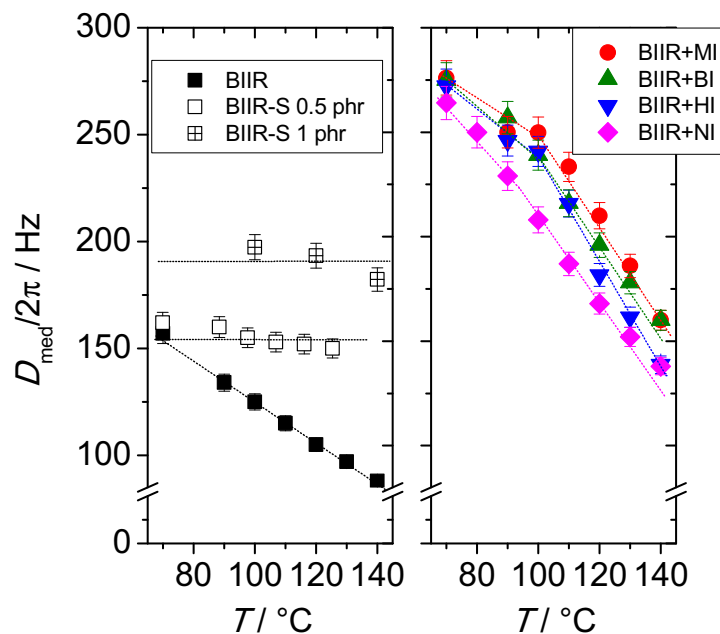


**Figure 8.3:** Results of  $I_{\text{nDQ}}$  build-up analysis under static conditions estimating the cross-link density of the studied networks in the form of  $D_{\text{med}}/2\pi$ . The left panel summarizes the non-ionic samples and the right panel ionic BIIR networks. Reprinted with permission from [76]. Copyright 2019 American Chemical Society.

Rouse dynamics. Notably, at 70°C BIIR exhibits nearly the same level of  $D_{\text{med}}/2\pi$  as BIIR-S 0.5 phr which means that the cross-link spacings of the latter are larger than the distance between two entanglements. A much smaller reduction of  $D_{\text{med}}/2\pi$  for BIIR-S 0.5 phr can be explained by transitional effects from constrained Rouse regime to a plateau.

The ionic networks show even stronger thermal evolution than BIIR, which implies that apart from the segmental motion there is an additional mechanism averaging  $D_{\text{med}}/2\pi$ . This additional mechanism can only be associated with the sticky dynamics of ionic links [77, 81]. Also, one can immediately see that the ionic networks have the same initial apparent cross-link density at 70°C, which is around two times larger than cross-link densities of the non-ionic samples, as expected in accordance with the additivity of the order parameter  $S_b \propto 1/N_e + 1/N_{\text{st}} \stackrel{N_e \approx N_{\text{st}}}{=} 2/N_{e/\text{st}}$ . This suggests that at 70°C the dynamics of ionic links is too slow and does not lead to an appreciable chain relaxation. However, beyond this temperature some of the ionic links become activated, and  $D_{\text{med}}/2\pi$  decreases. The reduction of  $D_{\text{med}}/2\pi$  speeds up with the length of the alkyl group in alkyimidazoliums as a result of steric hindrances on the molecular level leading to looser packing of ionic aggregates, weakening of ionic interactions inside them [17].

The temperature dependence of the distribution width parameter  $\sigma_{\text{ln}}$  is mostly hidden by the dynamic effects modulating the  $I_{\text{nDQ}}$  build-up and deferred to the appendix (Fig. B2).

In order to study structural and dynamic properties of alkyimidazolium groups serving as anchors binding polymer chains in a common ionic network, high resolution BaBa-xy16 measurements under MAS conditions were carried out. Since the largest differences in the apparent cross-link densities, defined by the differences in the bond lifetimes, were observed beyond 120°C (see Fig. 8.3), it was decided to perform the measurements at 120 and 140°C.

Fig. 8.4 illustrates 1D MAS spectra of the imidazolium signals ( $H_1$  and  $H_2/H_3$  at 10 and 7-8 ppm, respectively) acquired under MAS conditions. It can be seen that the signals are well resolved and, thus, could be separated from the much larger butyl signals by treating the latter as a baseline and subsequently subtracting it. After the subtraction, the integrals were determined with respect to the  $H_1$  signal. The integral ratio of the imidazolium signals close to the one defined by the molecular structure (1:2) was found. Some overestimation can be attributed to the incomplete removal of the dominant butyl signals contribution. The found butyl signals integral, reconverted to the number of monomeric units between the ionic links  $N_x$  by division by the number of protons per monomeric units  $950/8 \approx 120$ , is also in agreement with the value  $N_x = 125$  found by solution-state NMR. On the example of BIIR+MI and BIIR+HI, one can see that the spectral lines become more narrow with temperature indicating acceleration of molecular dynamics in ionic multiplets.

For the BaBa-based MQ-NMR analysis, the spectrometer frequency was set close to the

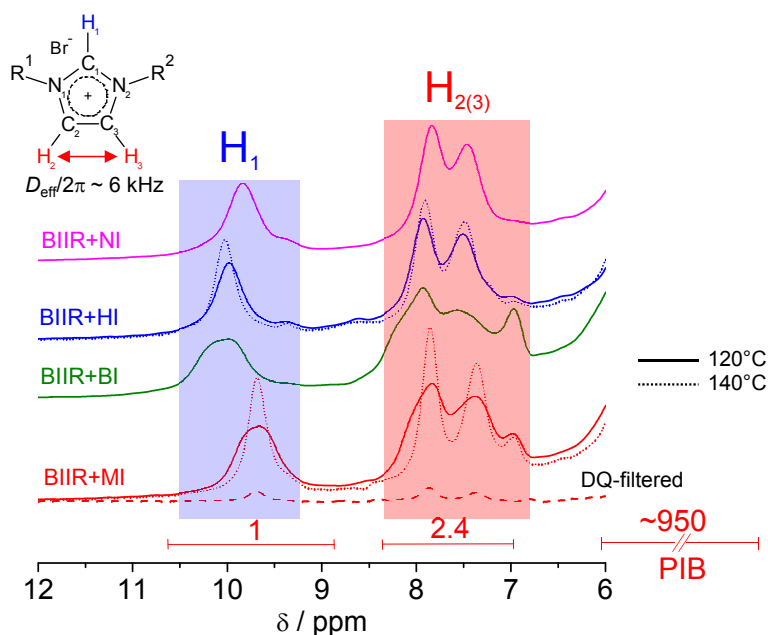


**Figure 8.4:** 1D MAS spectra of the imidazolium signals in the ionic networks (vertically shifted for clarity). The solid lines correspond to the measurements at  $120^\circ\text{C}$ , the dotted lines to the measurements at  $140^\circ\text{C}$ . The dashed line corresponds to the DQ-filtered spectrum at  $\tau_{\text{DQ}} = 2\tau_{\text{R}}$  at  $140^\circ\text{C}$ ,  $\tau_{\text{R}}$  is the rotor period, with the integrals indicated. The integral ratios of the DQ-filtered signals are equal to the integral ratios of the unfiltered signals (1:2.0), suggesting the DQ evolution under the same effective RDCC caused by establishment of the network of multispin RDCCs. At the top: a chemical structure of an alkyimidazolium moiety is given.  $\text{R}^1$  and  $\text{R}^2$  are a BIIR chain and an alkyl group, respectively. The indicated dipolar coupling is based on approximate bond lengths and angles from the literature [125, 130, 131]. Reprinted with permission from [76]. Copyright 2019 American Chemical Society.

imidazolium signals in the spectral range of around 7-8 ppm. This was necessary to avoid signal losses due to resonance offsets, which is significant at the given, comparably low MAS frequency. The effect of the resonance offset was determined on the example of butyl signals of BIIR+MI: an offset of  $\sim 3$  kHz led to  $\sim 35\%$  decrease in  $D_{\text{med}}$ . When  $D_{\text{med}}$  of butyl signals was compared on-resonance with the Baum-Pines results under static conditions, BaBa gave a comparable value with a minor decrease in intensity of 7% for the PIB main chains. A smaller resonance offset of the imidazolium signal at  $\sim 10$  ppm ( $\sim 1.5$  kHz) did not cause appreciable signal losses.

In Fig. B3, the  $I_{\text{ndQ}}$  build-ups of  $\text{H}_1$  and  $\text{H}_2/\text{H}_3$  on the example of BIIR+MI at  $120^\circ\text{C}$  are compared. One can see that the data points lie nearly on top of each other, indicating that the off-resonance effects are negligible. On the other hand, one would expect the build-up of  $\text{H}_1$  corresponding to the isolated proton (see Fig. B3a) to be lower than the build-up of more closely positioned  $\text{H}_2$  and  $\text{H}_3$ . An estimation of the distances between  $\text{H}_2$  and  $\text{H}_3$  as well as between  $\text{H}_2$  (or  $\text{H}_3$ ) and  $\text{H}_1$ , based on the values of chemical bond

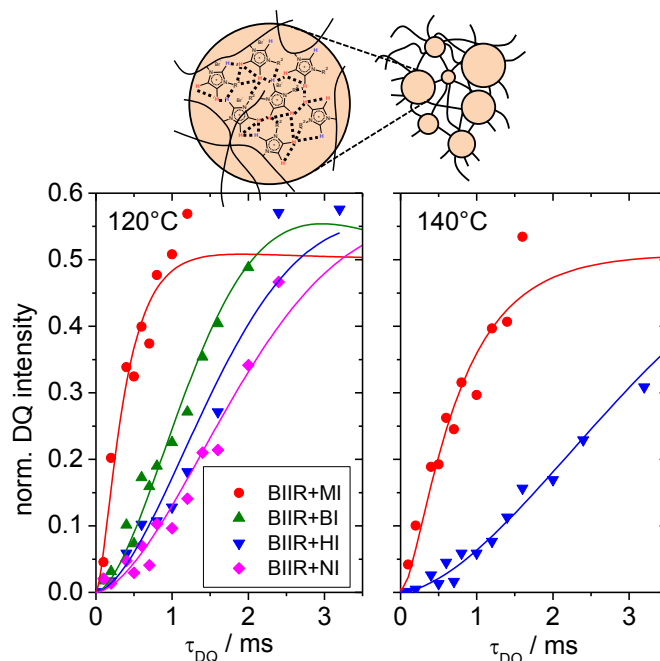


**Figure 8.5:** The  $I_{\text{nDQ}}$  data of the alkyimidazolium signals of all the ionic samples at 120 and 140°C. The solid lines correspond to the fits according to a build-up functions assuming log-normal distributed  $D_{\text{res}}$ . At the top, a tentative picture of the ionic network with distribution of sizes of ionic aggregates is given. The enlargement of an ionic aggregate shows a network of the intermolecular multispin RDDCs established inside. Reprinted with permission from [76]. Copyright 2019 American Chemical Society.

lengths and angles, taken from the literature [125, 130, 131], suggests that the protons  $H_2$  and  $H_3$  are situated 1.62 times closer to each other than the protons  $H_2$  and  $H_1$ , which translates to the ratio of the corresponding DDCs of around 4.2. Thus, the  $I_{\text{nDQ}}$  build-up ( $\propto D_{\text{res}}^2$ ) of  $H_1$  is expected to be 17.6 times slower than the build-up of the  $H_2$  and  $H_3$  protons. The overlap of the  $I_{\text{nDQ}}$  data means, therefore, that all imidazolium protons possess similar averaged RDDCs. This result can be explained by either the dipolar truncation [100] or by establishing a network of the multispin RDDCs. Both effects render effective RDDCs seen by any of the imidazolium protons identical. However, a DQ-filtered MAS spectrum again exhibits the same integral ratio between the  $H_1$  and  $H_2/H_3$  signals as in the non-filtered spectrum, which validates the presence of the coupled network of multispin RDDCs in ionic aggregates [100] (see the top of Fig. 8.5).

The  $I_{\text{nDQ}}$  data of the  $H_2/H_3$  signals of all the ionic samples are compared in Fig. 8.5. In the left panel, the comparison was done at 120°C. It can be seen that with an increase of the length of the alkyl group in the alkyimidazolium moiety the build-up becomes slower indicating the decrease in  $D_{\text{med}}$ . The trend supports the finding shown in Fig. 8.3, where the drop of  $D_{\text{med}}$  of the backbone occurring upon temperature elevation was getting more pronounced with the length of the alkyl group. Thus, Fig. 8.5 serves as an important,

**Table 8.1:** Results of the structural  $^1\text{H}$  MQ NMR analysis of the ionic links and network chains

Sample	ionic links (alkylimidazoliums)			network chains		
	$D_{\text{med}}/2\pi (\sigma_{\text{ln}}) / \text{Hz}$		$\frac{D_{\text{med}120^\circ\text{C}}}{D_{\text{med}140^\circ\text{C}}}$	$D_{\text{med}}/2\pi (\sigma_{\text{ln}}) / \text{Hz}$		$\frac{D_{\text{med}120^\circ\text{C}}}{D_{\text{med}140^\circ\text{C}}}$
	120°C	140°C		120° C	140°C	
BIIR+MI	802 (0.63)	395 (0.69)	2.04	210 (0.80)	160 (0.76)	1.32
BIIR+BI	268 (0)			196 (0.49)	160 (0.43)	1.22
BIIR+HI	206 (0)	106 (0)	1.96	182 (0.47)	139 (0.50)	1.32
BIIR+NI	170 (0)			168 (0.44)	138 (0.40)	1.22
BIIR				105 (0.43)	88 (0.42)	1.19

direct validation of the role of the alkyl group in reducing strength of the ionic links. In the right panel of Fig. 8.5, the  $I_{\text{nDQ}}$  data of BIIR+MI and BIIR+HI obtained at 140°C are presented. The shown data as compared to the ones at 120°C exhibit slower build-ups which implies that the dynamics in the ionic multiplets becomes more accelerated. The  $I_{\text{nDQ}}$  data were again fitted with Eq. 4.13 to quantify the RDDCs. The extracted MQ NMR results of the ionic links (alkylimidazoliums) and network chains can be found in Table 8.1.

The larger  $D_{\text{med}}$  values of the alkyimidazoliums as compared to the ones of the polymer backbone (note that methylene protons feature a 3.2 times larger  $D_{\text{eff}}$  than imidazolium protons due to the aforementioned strong distance dependence of the DDC) evidence again that alkyimidazoliums are less mobile due to their function as ionic cross-links in the formed dynamic networks. On the other hand, the  $D_{\text{med}}$  values are much lower than the static limit values ( $\sim 6$  kHz), corresponding to order parameters  $S_b$  in the range between 2 and 13% , which points at rather large-amplitude orientational mobility within the ionic aggregates on the time scale much faster than the inverse coupling  $(2\pi \times 6 \text{ kHz})^{-1} \approx 25 \mu\text{s}$ , as also confirmed by our BDS results and seen in other polymeric ionic liquids [38]. Additionally, the averaging of the dipolar couplings can be caused by fast exchange of stickers between open and closed state on a sub-ms time scale. At the moment, it is not possible to find out what mechanism contributes to the averaging the most.

Importantly, no slowly decaying component was found in the time decays of the MQ signals of the studied samples indicating that free unbound ionic groups can comprise only a few percent of the signal at maximum. Also, it was found that methylimidazolium exhibits large values of  $\sigma_{\text{ln}}$ , while the other alkyimidazoliums show a much narrower distribution of  $D_{\text{res}}$  not captured by the log-normal distribution. This supports the picture of a broad distribution of bond lifetimes in BIIR+MI shown in Fig. B2.

An interesting finding pertains to the ratios of the  $D_{\text{med}}$  values at 120 and 140°C. One can notice that the  $D_{\text{med}}$  ratios of the ionic links are larger than the ones of the polymer backbones. This can be explained by more prominent acceleration and isotropization of

intra-aggregate dynamics as compared to the segmental dynamics. Further, there is no effect of the length of the alkyl group on the  $D_{\text{med}}$  ratios for both ionic links and backbone at the studied elevated temperatures. The effect is possibly hidden by the errors in the determined  $D_{\text{med}}$  values and also by the distribution of the ionic groups' bond lifetimes.

### 8.2.2 Assessment of the OACF shape

MQ NMR data can deliver even more quantitative information on the molecular dynamics than probed so far only qualitatively via the temperature dependence of  $D_{\text{med}}$ . With MQ NMR one can assess the OACF, whose shape is presumed in advance. Here, it was assumed that starting from a certain anisotropy level  $D_{\text{res}}(t_0 \sim \tau_{\text{DQmin}})$  the OACF decays in accordance with the power law  $\kappa$  as follows:

$$C(t) = \begin{cases} D_{\text{res}}^2(t_0) & \text{for } |t| < t_0 \\ D_{\text{res}}^2(t_0)(t/t_0)^{-\kappa} & \text{for } |t| > t_0, \end{cases} \quad (8.4)$$

where  $t_0$  is set fixed to the time just below the first experimental point ( $\tau_{\text{DQmin}}$ ).

To perform the analysis, the DQ and MQ signals are to be fitted simultaneously with Eqs. 5.6 and 5.7 from Chapter 5 [52]. The fitting functions 5.6 and 5.7 can be used to analyze MQ data obtained from both the BaBa-xy16 and Baum/Pines-based pulse sequences, using the aforementioned rescaling factor of  $D_{\text{res}}$  for BaBa (see Section 4.2). We will start the discussion with the Baum/Pines data first.

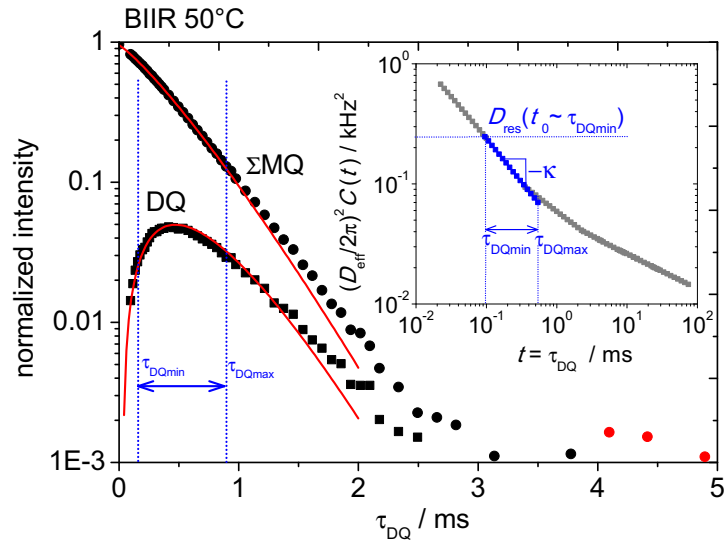


**Figure 8.6:** The power-law-model-based fits (Eqs. 5.6,5.7) (red solid lines) in action on the example of BIIR at 50°C. The inset shows a part of a piecewise-constructed  $C(t)$  master curve approximated within the fitting interval between  $\tau_{\text{DQmin}}$  and  $\tau_{\text{DQmax}}$ . Reprinted with permission from [76]. Copyright 2019 American Chemical Society.

The simultaneous fits approximate a part of  $C(t)$  within the time interval between  $\tau_{\text{DQmin}}$  and  $\tau_{\text{DQmax}}$ , where  $\tau_{\text{DQmax}}$  being the end of the fitting interval. Clearly, the choice of  $\tau_{\text{DQmax}}$  affects the extracted parameters  $D_{\text{res}}(t_0)$  and  $\kappa$  due to the according variation of the real shape of the part of  $C(t)$  taken into consideration for the forced power-law fit within the predefined fitting interval. Moreover, it was found important to bind  $\tau_{\text{DQmax}}$  in relation to  $\tau_{\text{DQ}}$  at the maximum of the DQ signal or to some certain level before or after the maximum of  $I_{\text{DQ}}$ . Apparently, this can be explained by the nature of the approximation with a validity range depending on the product of time and the RDDCs and the distribution of the RDDCs. When it was always fit until the same absolute time, no consistent results could be obtained for the master curve construction.

According to the modeling alluded in Chapter 6, to reduce the error in the shape approximation, it was decided to perform the fits until the maximum of DQ signals and then to shift the obtained  $C(t)$  parts by matching  $C(\tau_{\text{DQmin}})$  points. It should be noted that BIIR+MI, displaying the largest RDDCs distribution, expectedly required an adjustment of the fitting interval, and, namely, it was fitted until 60% of the maximum of its DQ signal after the maximum. The adjustment was done empirically so that at  $140^\circ\text{C}$   $\kappa(\text{BIIR+MI}) < \kappa(\text{BIIR+BI})$  and  $D_{\text{res}}(t_0)(\text{BIIR+MI}) \approx D_{\text{res}}(t_0)(\text{BIIR+BI})$ , as was already seen from the structural analysis (see Fig. 8.3). Without the adjustment,  $\kappa$  values of BIIR+MI appeared larger than the ones of BIIR+BI, which was, in fact, already shown to possess weaker ionic links and more mobile network chains (see Fig. 8.3) and, therefore, expected to exhibit larger  $\kappa$ . Furthermore, the necessity of the fitting interval elevation for BIIR+MI can be possibly caused by the delayed sticky dynamics for this sample. In Fig. 8.6, the simultaneous fits are shown in action for the case of BIIR.

In Fig. 8.7, the  $D_{\text{res}}(t_0)$  and  $\kappa$  values obtained with the simultaneous fits are presented as a function of temperature. It can be seen that the  $\kappa$  values of all the samples start with 0.6-0.7 at  $30^\circ\text{C}$  and firstly quickly decrease with temperature, whereas all the  $D_{\text{res}}(t_0)$  values, also strongly decreasing with temperature, are very similar across the samples series until around  $70^\circ\text{C}$ . From this we conclude that this temperature range corresponds to the transition from the Rouse regime to the dynamic regime, where chains feel topological constrains (entanglements, permanent and ionic cross-links) [66]. As the cross-link density increases in the order BIIR, BIIR-S, BIIR+alkylimidazoliums, the transition shifts to lower temperatures, as expected, since the network chains start feeling the constraints earlier. One can also see that the error bars are the largest in this regime, which is a consequence of large RDDCs leading to the lack of data points in the initial rise of the DQ signals.

Beyond  $100^\circ\text{C}$ ,  $D_{\text{res}}(t_0)$  deliver similar trends already shown by the temperature dependence of  $D_{\text{med}}$  and, therefore, it is not further discussed here. More interesting trends are provided by the analysis of  $\kappa$  values. In BIIR,  $\kappa$  reaches 0.29, which is related to regime II of a highly entangled polymer melt [108], which does not even start to reptate before the degradation temperature ( $140^\circ\text{C}$ ). Note the deviation of  $\kappa$  from the tube model prediction of 0.25 due to constraint release effects. Even lower  $\kappa$  in the permanent and

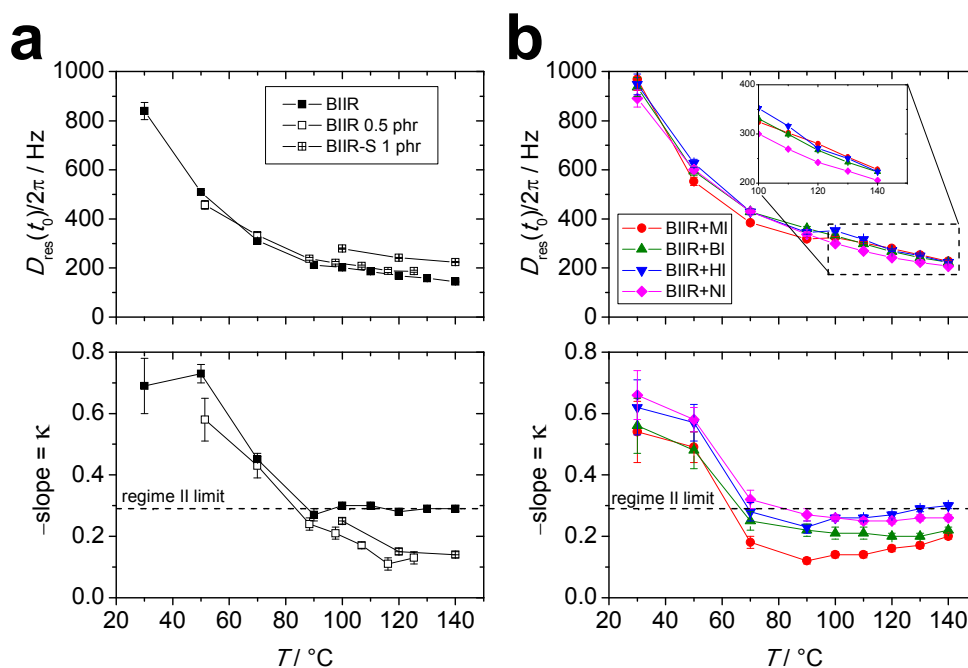


**Figure 8.7:** The temperature dependence of the extracted  $D_{\text{res}}(t_0)$  and  $\kappa$  values of non-ionic (a) and ionic (b) samples. Reprinted with permission from [76]. Copyright 2019 American Chemical Society.

ionic networks implies more constraints and corresponds to a transition to a permanent or Leibler<sup>3</sup> plateau, respectively. The non-zero  $\kappa$  values for BIIR-S can be the result of relaxation of defects or chain motions within the tube [132].

In contrast to the non-ionic samples, the ionic networks exhibit an increase of  $\kappa$  values beyond 100°C, approaching the exponent of the regime II of 0.29 at the highest studied temperatures (the entanglements plateau). The short part of the sticky Rouse transition with  $\kappa = 1$  between the plateaus, predicted by the sticky reptation model, is not observed as a result of broad distribution of bond lifetimes and crossover effects. If to compare  $\kappa$  values of the ionic samples, it can be seen that  $\kappa$  increases with the length of the alkyl group in the alkyimidazolium moieties, which means that network chains become more mobile as a result of the decrease of the bond lifetime.

To switch from the temperature to time dependence and quantify dynamic time scales, the obtained  $D_{\text{res}}(t_0)$  and  $\kappa$  values can be then used to form  $C(t)$  parts evaluated in the corresponding time intervals at different temperatures. The  $C(t)$  parts can be shifted according to the time-temperature superposition (TTS) principle [56, 133] to obtain a master curve. The shifts were always performed such that each  $C(t)$  part matched at its first experimental point with the  $C(t)$  part obtained one temperature step before. Fig.

<sup>3</sup>a double plateau with a larger-amplitude part comprising contributions from entanglements and supramolecular junctions transitioning at  $\tau_{\text{st}}^*$  to a plateau level defined by entanglements only

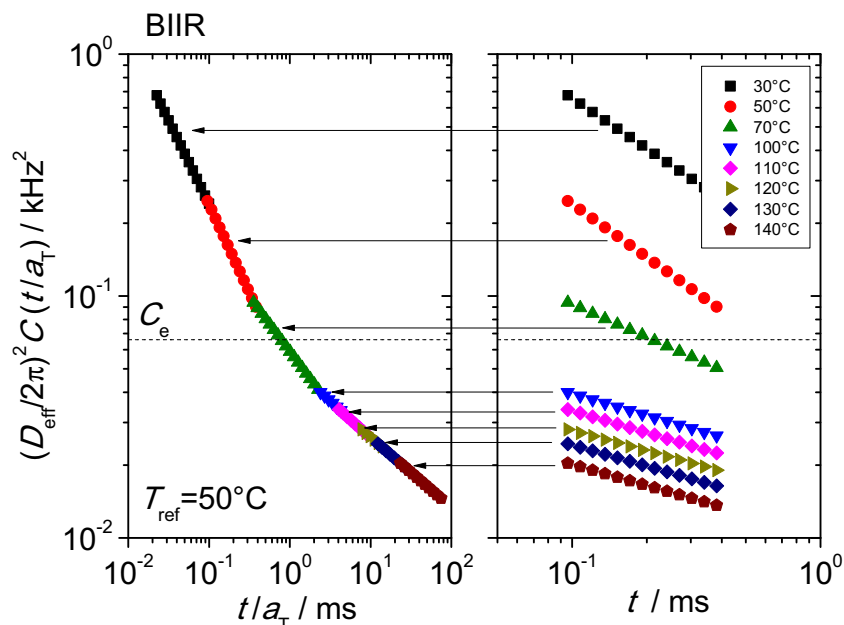


**Figure 8.8:** Demonstration of a  $C(t)$  master curve construction from the MQ NMR data on the example of BIIR.  $T_{\text{ref}} = 50^\circ\text{C}$ . The anisotropy level due to entanglements  $C_e$  is indicated. Reprinted with permission from [76]. Copyright 2019 American Chemical Society.

8.8 demonstrates how the  $C(t)$  master curve construction works on the example of BIIR (also see Chapter 6).

Using  $C(t)$  master curves one can determine characteristic transition times. For example, in Fig. 8.9, the determination of the BIIR's entanglement relaxation time ( $\tau_{e,\text{exp}}$ ) at  $T_{\text{ref}} = 50^\circ\text{C}$  is shown. Firstly, the logarithmic  $C(t)$  slopes in the regimes I and II ( $-\alpha$  and  $-\epsilon$ , respectively) averaged over approximately one decade in time were estimated by the derivative analysis involving smoothing over 20 adjacent points and taking the average slope in the middle of the analyzed interval. Even though individual slopes  $\kappa$  are piecewise known, the smoothed derivative analysis provides a more reliable analysis of the whole  $C(t)$  master curve. With the slopes set fixed, a piecewise linear fit in log-log coordinates was performed to extract  $\tau_{e,\text{exp}}$  as an intercept found to be 0.77 ms. A theoretical prediction of  $\tau_e$  according to the tube model was then calculated using the formula:

$$\tau_e = \frac{\xi_0 \exp \{ [\alpha(T - T_V)^{-1}] \} b^2 N_e^2}{\pi k_B T} = 0.46 \text{ ms}, \quad (8.5)$$

where  $\xi_0$  is the monomeric friction coefficient at infinitely large temperature ( $= 6.17 \times 10^{-17}$  Ns/m),  $\alpha$  is the thermal expansion coefficient of the free volume ( $= 2.4 \times 10^{-4} \text{ K}^{-1}$ ),  $T_V$  is the Vogel temperature ( $= 96 \text{ K}$ ),  $b$  is the Kuhn segment length ( $= 12.4 \text{ \AA}$ ),  $N_e \approx 27$  [118, 133].

The found values of the theoretical and experimentally found  $\tau_e$  are in a rather good agree-

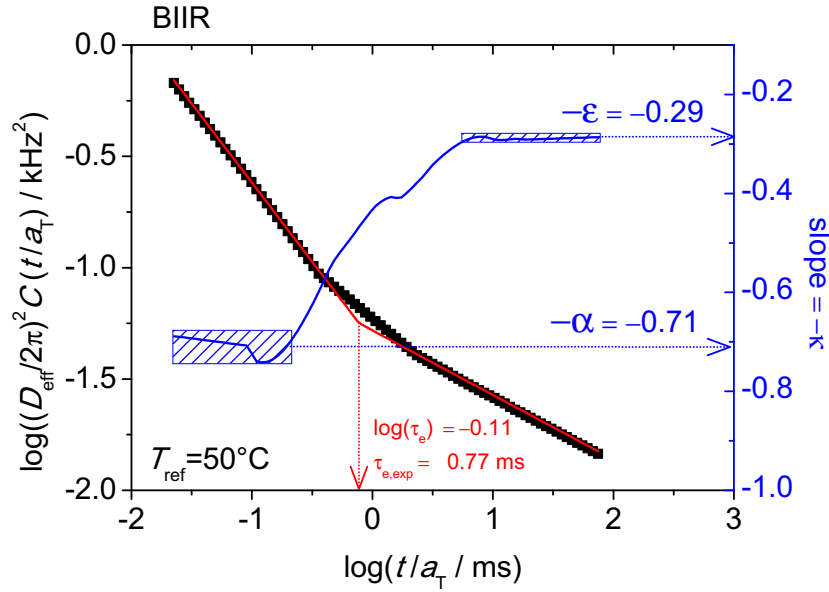


**Figure 8.9:** Determination of the entanglement relaxation time of BIIR from its  $C(t)$  master curve reduced to  $T_{\text{ref}} = 50^\circ\text{C}$  with the derivative analysis. Reprinted with permission from [76]. Copyright 2019 American Chemical Society.

ment, which is striking considering that only few temperatures were taken for the master curve construction in the transition region, yet it is reassuring that the whole master curve construction procedure performed using the  $^1\text{H}$  MQ NMR data is trustworthy.

As it was found that below  $100^\circ\text{C}$  the chain relaxation is predominantly governed by segmental motions, it was decided to reduce the  $C(t)$  data of all samples to  $50^\circ\text{C}$ . All the constructed master curves are shown in Fig. 8.10a.

At short times ( $\leq 0.3$  ms), all the master curves coincide as the samples are still in the Rouse regime (some deviations between the samples can be attributed to the aforementioned uncertainties in  $D_{\text{res}}(t_0)$  and  $\kappa$  at low temperatures), as was already discussed for Fig. 8.7. Beyond these times, the samples transit to the more restricted dynamic regimes, alluded above. As it can be seen, the decays of the master curves reach the anisotropy level defined only by entanglements  $C_e$  at lower sticky Rouse relaxation times of entangled strands ( $\tau_e^*$ ) with an increase of the length of the alkyl group in the alkyimidazole. Since  $\tau_e^* = \tau_{\text{st}}^*(N_e/N_s)^2$  [80] and the ratio  $N_e/N_s$  is close to unity in our case,  $\tau_e^* \approx \tau_{\text{st}}^*$ .  $\tau_e^*$  from MQ NMR of all the samples are listed together with the corresponding times determined by DMA in Table 8.2 below.

Another (and the most important) piece of information which can be obtained from the master curves construction is the temperature dependence of the horizontal shift factors ( $\log a_T$ ), which are plotted in Fig. 8.10b. There one can see that the shift factors of the non-ionic samples agree with the literature data rather well [133]. Further, the shift factors of the ionic networks were found to follow the BIIR's literature shift factor due to

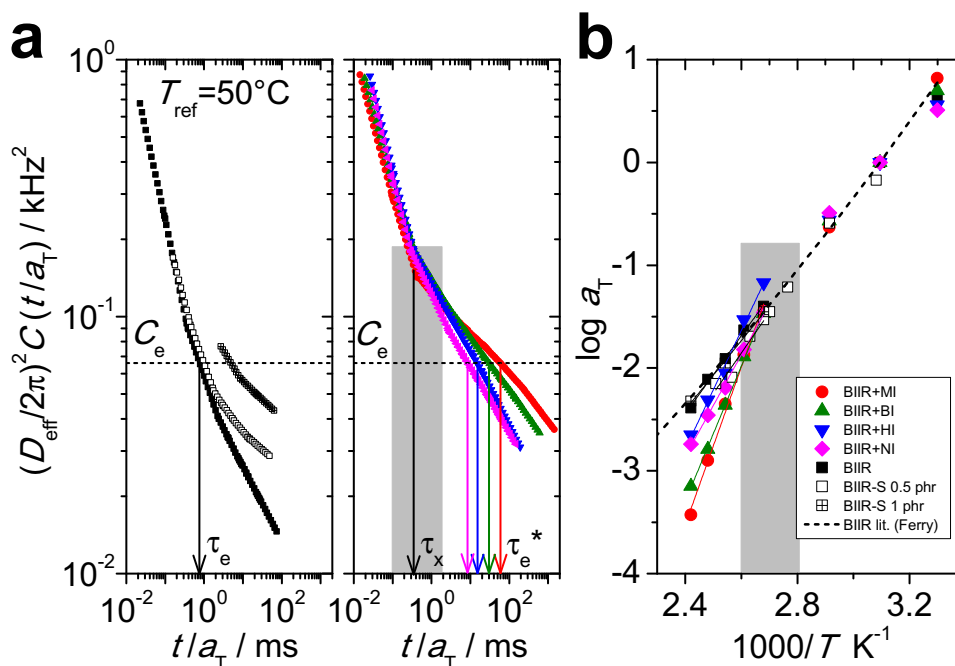


**Figure 8.10:** (a) Apparent  $C(t)$  master curves of the non-ionic (left) and ionic (right) BIIR samples reduced to  $T_{\text{ref}}=50^\circ\text{C}$ . The characteristic relaxation times are marked with the arrows. The dashed line indicates the anisotropy level defined only by entanglements ( $C_e = C(\tau_e) = C(\tau_e^{\text{st}})$ ). (b) The horizontal shift factors obtained from the master curves construction. The solid lines correspond to the Arrhenius fits. The grey shaded box in (a) highlights the experimental time window where the shifting procedure transitions from being controlled by the segmental to the sticky dynamics once the average of this time window becomes equal to the sticky bond lifetime at the studied temperature. This intrinsic to MQ NMR shifting selection defines the temperature range at which the sticky process becomes observable in the shift factor, also marked with a grey shaded box in (b). Reprinted with permission from [76]. Copyright 2019 American Chemical Society.

the segmental relaxation until around  $100^\circ\text{C}$ , beyond which the deviations caused by the ionic dissociation occurred. The temperature dependencies of the shift factors beyond  $100^\circ\text{C}$  were analyzed with the Arrhenius approximation extracting  $E_{\text{a,app}}$  (Table 8.2). As it can be seen,  $E_{\text{a,app}}$  decreases with the length of the alkyl group in the alkyimidazolium moieties, thus fortifying the above results. A comparison of the activation energies with the ones determined by DMA and with literature data reveals that the NMR analysis is prone to an average overestimation of the activation energy of around 15%. This is related to the crude approximation of the real  $C(t)$  shape (see Chapter 6).

### 8.3 Structural and dynamic studies by DMA. Correlation with the $^1\text{H}$ MQ NMR

As it was shown above, the ionic samples violate the TTS principle due to the additional activation process associated with opening of ionic groups. In contrast to MQ NMR, which delivers an approximated average dependence on time, DMA probes a true shape of the observed quantities ( $E'$  and  $E''$ ). Therefore, in the case of the DMA analysis one can expect that at larger frequencies the stress relaxation is driven mostly by the segmental motions, whereas at low frequencies by the sticky dynamics. To obtain information on the sticky dynamics, the master curves are to be constructed in such a way that the parts of the data sets superimpose at lower frequencies. The data were reduced to  $T_{\text{ref}} = 20^\circ\text{C}$ . At this temperature, the sticky dynamics was observed for three of the four samples within the studied frequency range. For BIIR+MI, possessing the largest bond lifetime, however, the sticky process could be detected only at a larger temperature. Thus, it becomes apparent that the resulting form of the mechanical master curves depends on the used experimental frequency window and on the absolute temperature, at which one chooses to switch the shifting procedure from matching higher-frequency regions governed by segmental motions to lower-frequency regions dominated by the sticky dynamics. Note that this switching temperature can differ from  $T_{\text{ref}}$ .

DMA master curves can be seen in Fig. 8.11. To locate the position of the  $E''$  maxima, the  $E''$  data were fitted around the maximum using the sum of a power law and a Havriliak-Negami function on a log-weighted  $E''$ -axis:

$$\log E'' = \log \left\{ A\omega^x + \frac{\Delta E''}{(1 + (\omega\tau)^\beta \cos(\pi\beta/2) + (\omega\tau)^{2\beta})^{\gamma/2}} \times \right. \quad (8.6)$$

$$\left. \times \sin \left( \gamma \arctan \left[ \frac{(\omega\tau)^\beta \sin(\pi\beta/2)}{1 + (\omega\tau)^\beta \cos(\pi\beta/2)} \right] \right) \right\},$$

where  $A$  is the numeric prefactor,  $\omega$  is the angular frequency,  $x$  is the exponent in the Rouse regime,  $\Delta E''$  is the amplitude of the  $E''$  maximum,  $\tau$  is the Havriliak-Negami relaxation time,  $\beta$  and  $\gamma$  are the exponents reflecting symmetric and asymmetric broadening, respectively [134].

The average bond lifetime ( $\tau_{\text{st}}^*$ ) inversely related to the position of the  $E''$  maximum ( $\omega_{\text{max}}$ ) is given as follows:

$$\tau_{\text{st}}^* = \frac{1}{\omega_{\text{max}}} = \tau \left( \frac{\sin \left( \frac{\pi\beta}{2(\gamma+1)} \right)}{\sin \left( \frac{\pi\beta\gamma}{2(\gamma+1)} \right)} \right)^{-1/\beta} \quad (8.7)$$

Here it should be noted that in general a position of a symmetric  $E''$  maximum should

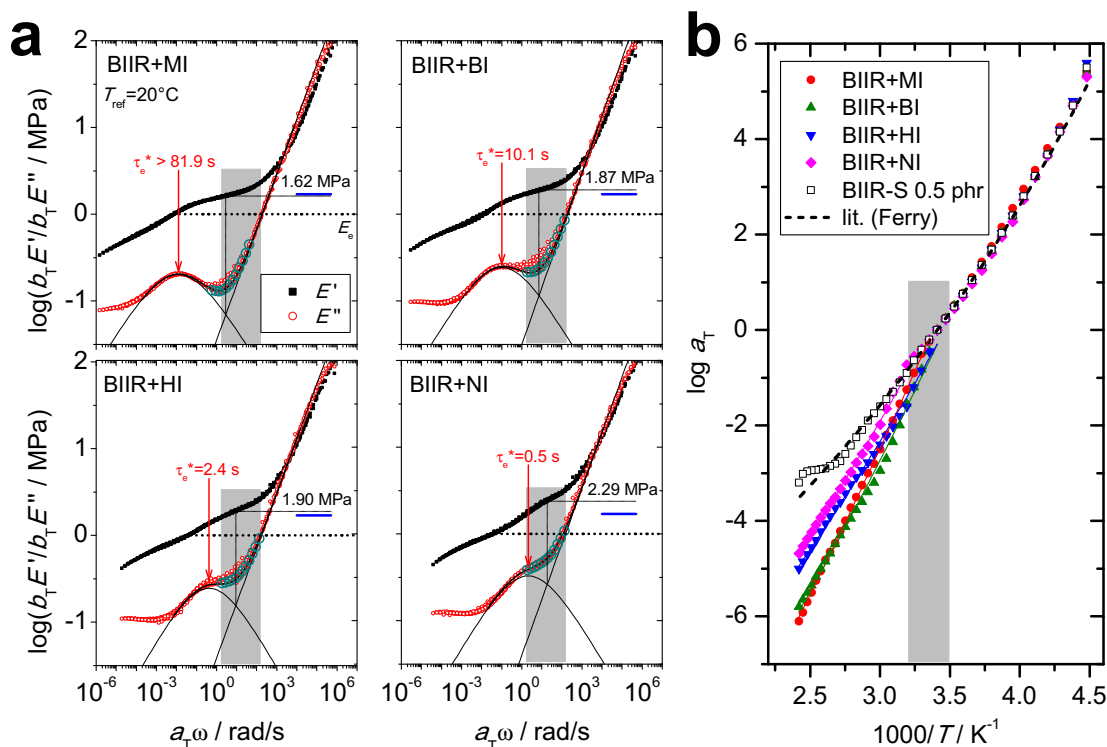


**Figure 8.11:** (a) Apparent master curves for  $E'$  and  $E''$  for all the ionic samples reduced to  $T_{\text{ref}} = 20^\circ\text{C}$ . The black thin lines represent the fits using the sum of a power law and a Havriliak-Negami function (Eq. 8.6). The blue thick horizontal lines indicate the theoretically expected level of the high frequency plateau modulus ( $E_N$ ) including contributions of both stickers and entanglements, whereas the thin dotted lines show the actual values of  $E_N$  as indicated. The thick dotted lines mark the modulus level defined by entanglements alone ( $E_e$ ). The arrows mark the positions of the  $E''$  maxima inversely related to  $\tau_e^*$ , the values of  $\beta$  and  $\gamma$  are around 0.4 and 1, respectively, in all cases. The large open circles in  $E''$  correspond to isothermal frequency sweeps at the temperature beyond which the data are shifted with respect to the lower-frequency sticky process. (b) The horizontal shift factors resulting from the master curves construction of the DMA data as well as taken from literature [133]. The solid lines represent fits according to Eq. 2.16. The grey shaded boxes indicate the experimental time window in (a) where the shifting procedure switches from being controlled by the segmental to the sticky dynamics, which converts to an uncertainty in (b) as to at which temperature to enable this switch. Reprinted with permission from [76]. Copyright 2019 American Chemical Society.

be related to the geometric average of  $\tau_{\text{st}}^*$  and  $\tau_e^*$ , but in the special case of  $N_{\text{st}} \approx N_e$  the maximum's position can be associated with both  $\tau_{\text{st}}^*$  and  $\tau_e^*$ . For consistency with MQ NMR analysis, we assign the maxima of  $E''$  to  $\tau_e^*$ . It can be seen that the maximum of  $E''$  shifts towards higher frequencies (lower times) with the length of the alkyl group of alkyimidazolium indicating the decrease of the bond lifetime, thus supporting the MQ NMR findings (for further comparison of time scales see below).  $\gamma$  was found to be always

equal to unity, whereas  $\beta$  was 0.4 in all cases suggesting a broad distribution of bond lifetimes.

The level of the high frequency plateau of  $E'$  ( $E_N$ ), defined by both stickers and entanglements, can be calculated assuming the validity of the phantom model and taking into account the fraction of elastically active chains  $N_{br}/AN$  estimated above as follows [56]:

$$E_N = 3\rho RT \left( \frac{1}{M_e} + \frac{1}{M_{st}} \frac{f - 2 N_{br}}{f AN} \right) \approx 1.70 \text{ MPa}, \quad (8.8)$$

where  $\rho$  is the density of BIIR,  $f$  is the functionality of a junction equal to  $2AN \times N_{br}/AN = 2N_{br}$ , since two chains emanate from each sticker and only bridging chains reduce fluctuation of cross-links.

As it can be seen from Fig. 8.11(a), the theoretical prediction of Eq. 8.8 agrees with the experimental data of BIIR+MI rather well verifying that all the stickers are in the closed state. The experimental plateau values for the rest of the samples appear to increase with the length of the alkyl group, which is in fact only the result of the increasing role of the Rouse contribution to  $E''$  largely overlapping with the sticky process. The same explanation is valid for the apparent delay in the frequency at which  $E' = E_e$  ( $E_e$  being the modulus level contributed only by entanglements) with respect to the peak maximum increasing with the length of the alkyl group.

The horizontal shift factors applied for the master curves construction are presented in the form of the Arrhenius plot in Fig. 8.11(b). It can be seen that the ionic samples obey the TTS principle and agree with the literature data until around 20°C, whereas BIIR-S 0.5 phr follows the literature data within the whole studied temperature range [133]. Beyond 20°C, the ionic dissociation initiates in the ionic networks as observed in the studied frequency window. These parts of  $\log a_T$  related to the ionic dissociation, now available within a larger temperature interval, can be analyzed using Eq. 2.16 with segmental Vogel-Fulcher parameters, taken from literature [133], set fixed. The performed fits delivered  $E_{a,st}$  which were then summed up with  $E_{a,segm}$  at 120°C to obtain  $E_{a,app}$  for comparison with the MQ NMR data. As it can be seen, the values of  $E_{a,app}$  determined from the DMA data show the same trend as the MQ NMR data. Importantly, the found  $E_{a,st}$  values relate to  $RT$  at the highest used temperature of 140°C, amounting to 3.43 kJ/mol, as 6.5-15.5:1 depending on the sample, which makes a ratio of associated to open stickers  $\exp(E_{a,st}/kT) \gg 1$ , which corroborates the results obtained by SAXS and BaBa-xy16 on the negligible amount of open stickers.

All the apparent transition times determined by MQ NMR and DMA can be found in Table 8.2. The MQ-NMR-based  $\tau_e^*$  are also given at the same temperature as the DMA-based  $\tau_e^*$  for comparison. To this end,  $\tau_e^*$  should be simply multiplied by the corresponding shift factor  $a_T^{20^\circ C} = 10^{1.23} = 17$ . As can be seen, the MQ-NMR-based  $\tau_e^*$  are one to two orders of magnitude lower than the DMA-based  $\tau_e^*$ . This finding can be explained by different time windows of the two methods. The NMR time window accesses

**Table 8.2:** Apparent activation energies (in kJ/mol) and apparent sticky entanglement times (in s) determined from the MQ NMR and DMA shift factors and master curves, respectively.

Sample	MQ NMR ( $T_{\text{ref}} = 50^\circ\text{C}$ )			DMA ( $T_{\text{ref}} = 20^\circ\text{C}$ )	
	$\tau_e^{(*)}$	$\tau_e^*(20^\circ\text{C})$	$E_{\text{a,app}}^{\text{a}}$	$\tau_e^*$	$E_{\text{a,app}}$
BIIR+MI	5.9e-2	1.01	147	>81.9	113
BIIR+BI	3e-2	0.51	126	10.1	97
BIIR+HI	1.5e-2	0.26	111	2.4	83
BIIR+NI	8.5e-3	0.15	95	0.5	88
BIIR	7.7e-4				
BIIR-S 0.5 phr	(9.5e-4)		75	61	
BIIR-S 1 phr			64		
BIIR lit./th. [66, 118]	4.6e-4		61 [133]		

<sup>a</sup>  $E_{\text{a,app}} = E_{\text{a,st}}(T) + E_{\text{a,segm}}$  calculated at  $120^\circ\text{C}$

much lower time scales, namely, 0.1 to 10 ms, as compared to the DMA's time range of 5-500 ms. Thus, NMR focuses on more local motions which leads to the fact that the differences among the samples seen by NMR are revealed at higher temperatures. This point is illustrated in more detail in Fig. B.1 in Section B.3.1. The more than  $50^\circ\text{C}$  difference between the apparent onsets of the sticky dynamics as seen by NMR and DMA in turn implies that the NMR data are shifted with lower segmental shift factors within a larger temperature interval than the DMA data, which on time scale converts to shorter apparent times.

Consequently, one cannot rely on the  $\tau_e^*$  found from the NMR-based master curves, since there is no external control over the switching temperature between the segmental and sticky dynamics, but rather an intrinsic transition taking place at the temperature at which the arithmetic average of the fit interval becomes equal to  $\tau_e^*$ . Fortunately, one can determine  $\tau_e^*$  by MQ NMR also isothermally and by this means alleviate the problems related to the master curve construction. To this end, we employ the same strategy as discussed above for  $\tau_{\text{st}}^*$  determined from the apparent master curves as times at which  $C(t)$  reaches the level of entanglements  $C_e$ . To avoid errors associated with extrapolation, we extract  $\tau_e^*$  at the temperature at which  $C(t)$  crosses the  $C_e$  level within the fitting interval.

For completeness, we determine  $\tau_e^*$  values from the DMA and MQ-NMR data also isothermally. In the case of the DMA data, we determined  $\tau_e^*$  using Eq. 8.6 with the power-law exponents set fixed to the values found via the master curves analysis. In the case of the MQ-NMR data,  $\tau_e^*$  were obtained as times at which  $C(t)$  crossed the level entanglements  $C_e$ . The isothermal extraction procedure of  $\tau_e^*$  on the example of MQ NMR and

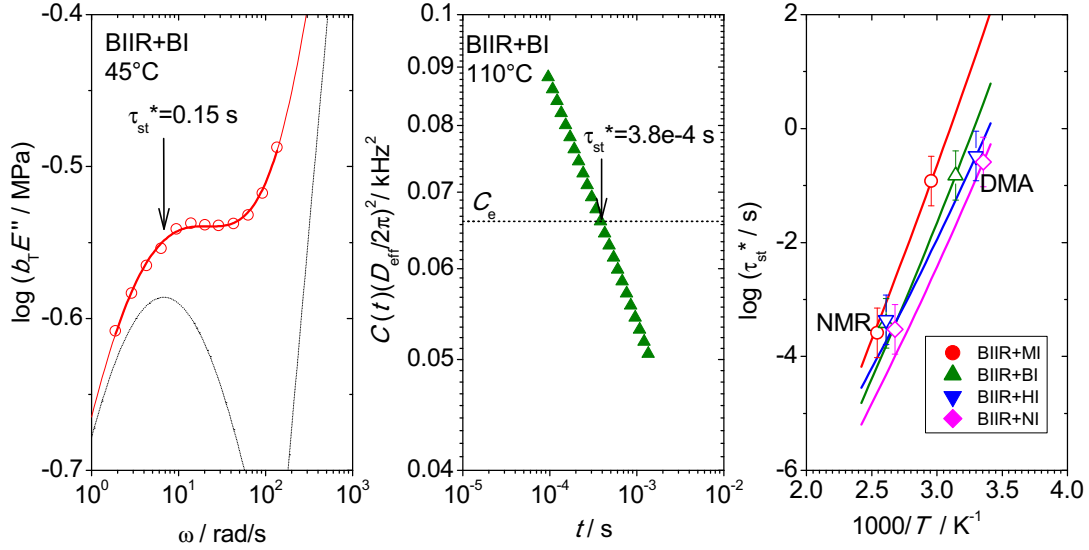


**Figure 8.12:** Extraction of sticky entanglement times  $\tau_e^*$  from isothermal data of DMA (a) and MQ NMR (b). The red line in (a) represents the fit to Eq. 8.6, with dotted black lines being a power-law- and a HN-components. (c) Temperature dependencies of the bond lifetimes of the ionic samples. The isothermally determined values of  $\tau_e^*$  from DMA (low temperatures) and MQ NMR (high temperatures) are indicated. The error bars are predominantly contributed by the batch-to-batch reproducibility. Reprinted with permission from [76]. Copyright 2019 American Chemical Society.

DMA data of BIIR+BI as well as the temperature dependencies of the extracted times for all samples is shown in Fig. 8.12. In Fig. 8.12(c), we use the temperature dependencies determined from the DMA data because they cover a larger temperature range than in the case of MQ NMR. The error bars indicated for the bond lifetimes originate predominantly from the batch-to-batch reproducibility (see Section B.5 for more details). As can be seen in Fig. 8.12(c), the MQ NMR and DMA results agree quantitatively in bond lifetime as well as activation energy, which for the first time shows that the sticky chain dynamics probed by mechanical methods in the linear regime corresponds to the ionic hopping observed by MQ NMR on a microscale thus supporting a molecular picture predicted by the sticky reptation model.

## 8.4 Sticker dynamics by broadband dielectric spectroscopy

The dielectric spectroscopy measurements, their data analysis, and interpretations were performed by Prof. Dr. Kay Saalwächter. The data were analyzed, as described in Section A.4.1, by a combination of two Havriliak-Negami (HN) functions and, at high temperatures, also the conductivity term. The analysis provides relaxation strengths  $\Delta\epsilon$ , distribution parameters  $\beta$ , and relaxation times  $\tau$  for all the relaxation processes.

All the relevant relaxation times are given in Fig. 8.13. In the lower part of the relaxation map, segmental relaxation times  $\tau_\alpha$  can be seen. For reference,  $\tau_\alpha$  values of non-modified

BIIR are also shown, which were found in a good agreement with previous results on PIB and halogenated butyl rubber [135–137]. The relaxation strength of BIIR was found to be ten times larger than of PIB due to a much stronger dipole moments on polar bromine sites. Thus, brominated isoprene units served as probes of segmental dynamics. It can be seen that  $\tau_\alpha$  values of ionic samples are somewhat lower as compared to their non-ionic counterpart. This can have a twofold explanation: (i) the probed dipole moment originates from the polar ionic groups residing in ionic aggregates, which does not reflect the behavior of the material in the bulk, (ii) the faster  $\beta$  process, well distinguished in BIIR, was not included into the analysis for the ionic samples due to the experimental noise, thus shifting the bias towards shorter times.

Looking now at the upper part of the relaxation map, one can see slower relaxation processes related to the ionic transport through the material. These are electrode polarization (EP) and ionic hopping. The latter is characterized by effective sticky bond lifetimes from DMA and MQ NMR analyses. It can be seen that the order of time scales and activation energies across the samples series is the same for both processes, which implies that the long-range ionic transport, seen in the EP, is realized through individual steps of ionic hopping of alkyimidazolium groups.

A Barton-Nakajima-Namikawa (BNN) correlation showed the coincidence of the activation energies of the EP and conductivity  $\sigma_0$  (see Fig. B9(b) for the fits), thus demonstrating that the conductivity is also driven by the same mechanism as the EP. One can notice that the  $E_{a,\text{app}}$  values from the EP (or conductivity) are by 20–30 kJ/mol larger than the corresponding  $E_{a,\text{app}}$  values of DMA/MQ NMR. As was already alluded to in Fig. 2.4, the difference likely corresponds to the additional dissociation energy (Coulomb interaction) associated with the alkyimidazolium carrying two bromine anions through the PIB matrix, thereby promoting the conductivity of counterions.

The central region of the relaxation map exhibits relaxation times related to the intra-aggregate relaxation (IAR). The relaxation times were found to follow the Vogel-Fulcher temperature dependence with Vogel temperature ( $T_V$ ) being within 20 K of the segmental  $T_V$  for pure BIIR. This finding implies that the dynamics in the ionic aggregates is coupled with segmental dynamics and, in particular, it becomes arrested when the segmental dynamics freezes at low temperatures. The only difference was BIIR+BI from the old batch exhibiting somewhat lower  $T_V$ ,  $\tau_\alpha$ , and  $E_{a,\text{app}}$ , being an outlier, due to possible solvent residues. Further, it can be seen that the high-temperature slopes are steeper than for  $\tau_\alpha$  and equal to the slopes of  $\tau_{\text{st}^*}$  within the experimental error, which indicates that motions in the ionic aggregates are subject to the same energy barrier as the ionic hopping. In literature [32, 138, 139], these relaxation times are often attributed to the second segmental relaxation ( $\alpha_2$ ) due to opening of ionic bonds and hence are equated to the bare bond lifetime ( $\tau_{\text{st}}$ ). Depending on the density of ionic groups, the bare bond lifetime can be either several orders of magnitude shorter than the effective bond lifetime from rheology  $\tau_{\text{st}}^*$  [40, 139], in the case of sparsely arranged ionic links, or both times can be similar at high densities of ionic groups [32]. The much larger values of rheological

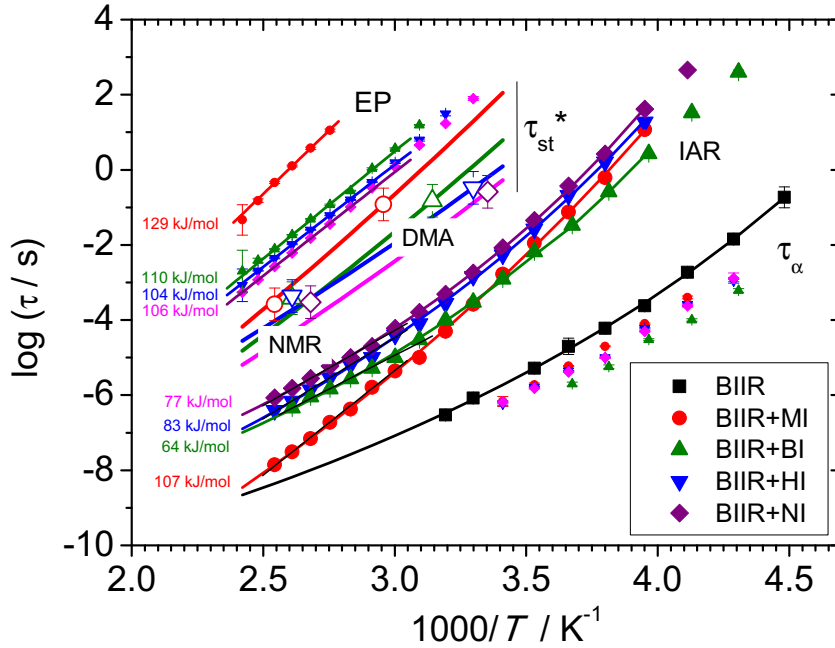


**Figure 8.13:** Relaxation map of relevant dynamic processes: segmental relaxation  $\tau_\alpha$ , intra-aggregate relaxation  $\tau_{st}^*$ , effective bond lifetime  $\tau_{st}^*$  (open symbols correspond to  $\tau_{st}^*$  isothermally determined by MQ NMR and DMA at high and low temperatures, respectively), electrode polarization (EP). The solid lines represent Arrhenius, Vogel-Fulcher fits, or a combination of both (Eq. 2.16). Reprinted with permission from [76]. Copyright 2019 American Chemical Society.

bond lifetimes for the case of sparsely arranged ionic links were explained to stem from the sensitivity of the method to an exchange of an ionic aggregate rather than to a simple ionic dissociation, which at large distances between the ionic aggregates involves numerous returns ( $J$ ) to the same ionic aggregate (and the same number of dissociations) and the diffusion to the neighboring ionic aggregate ( $\tau_{diff}$ ). The following equation represents the aforementioned statement [40]:

$$\tau_{st}^* = \tau_{st,bare}^* J + \tau_{diff} \quad (8.9)$$

Here, a simple comparison of the IAR relaxation times and  $\tau_{st}^*$  reveals that the orders of time scales across the samples series are inverse with respect to each other. According to Eq. 2.16, a larger  $E_{a,st} = E_{a,app} - E_{a,segm}$  must also lead to a larger bond lifetime, because an equilibrium concentration of dissociated stickers governing chain relaxation decreases. Thus, Eq. 2.16 cannot explain why we obtain the inverse order for  $\tau_{IAR}$  meaning that  $\tau_{IAR}$  is not directly related to the bare bond lifetime and even not proportional to it. The faster kinetics observed for the IAR can be explained by simple steric factors: larger alkyl groups need more time for positional changes.

Summarizing the above results, we present a dynamic model of the hierarchical sticky

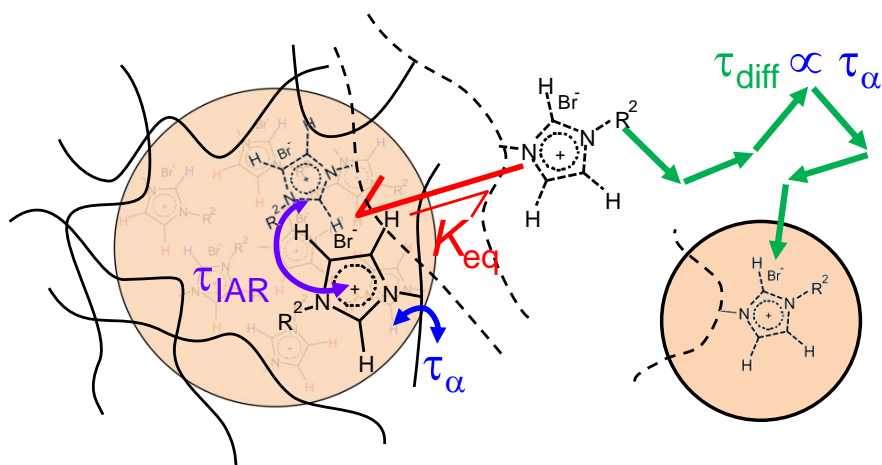


**Figure 8.14:** Dynamic model of the sticky dynamics suggesting a hierarchy of dynamic processes: segmental relaxation time  $\tau_\alpha$  serving as an attempt time for escaping from the ionic aggregate, localized ionic reorientations inside the ionic aggregate with a characteristic time  $\tau_{\text{IAR}}$  subject to an activation barrier which also governs the dissociation/association equilibrium ( $K_{\text{eq}}$ ), diffusion to the neighboring ionic aggregate on a time scale of  $\tau_{\text{diff}} \propto \tau_\alpha$ . In our case of sparsely arranged ionic groups,  $\tau_\alpha$  corresponds to the segmental time of the polymer matrix since no additional  $T_g$  was observed by DSC [17], whereas for more densely arranged ionic groups  $\tau_\alpha$  can be altered [47, 119]. Reprinted with permission from [76]. Copyright 2019 American Chemical Society.

dynamics (Fig. 8.14). The attempts to leave an ionic aggregate occur on the shortest (in this model) time scale of the segmental relaxation time  $\tau_\alpha$ . Along with it, ionic groups inside ionic aggregates undergo reorientations with an activation energy close to one needed to escape from them, as the dominant energetic contribution is breaking of numerous ionic bonds. A small fraction of dissociated stickers, defined by an equilibrium constant  $K_{\text{eq}} \propto \exp(-E_a^{\text{st}}/RT)$ , can then diffuse to the neighboring aggregate on a time scale of  $\tau_{\text{diff}} \propto \tau_\alpha$ . Evidently, a better compatibility with the polymer matrix, developing with the length of the alkyl group, reduces the total activation energy and leads to a more successful dissociation and shorter effective bond lifetimes. Also, the number of returns is expected to decrease as the attraction forces become weaker. At present, it is not possible to pinpoint  $\tau_{\text{st}}$  and  $J$ , as the former is not accessible experimentally and the latter cannot be found using an existing theoretical platform [40, 139–141] treating pairwise sticky interactions with concentration of open stickers defined by the equilibrium constant  $K_{\text{eq}}$ . In contrast, in the case of ionic aggregates, each aggregate can accommodate another sticker, and, thus, all aggregates can be considered open. Thus, a new theoretical treatment is to be developed to cover the case of stickers associating in aggregates with large aggregation numbers ( $AN \gg 1$ ).

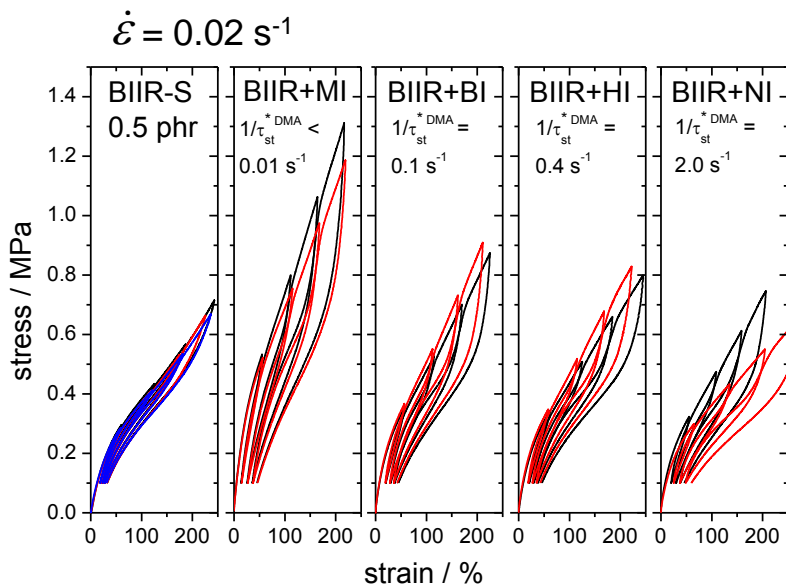


**Figure 8.15:** Cyclic uniaxial tensile experimental results at room temperature. The rates of ionic aggregate exchange  $1/\tau_{st}^{*DMA}(20^{\circ}C)$  are indicated. Different colors indicate measurements on different samples showing reproducibility. Reprinted with permission from [76]. Copyright 2019 American Chemical Society.

## 8.5 Influence of internal stresses on the effective bond lifetime

To investigate the behavior of the ionic networks in non-equilibrium conditions, mechanical experiments in the non-linear regime were carried out at room temperature. In Fig. 8.15, the response to cyclic deformations of the ionic networks was compared with the corresponding response of the permanent network. Importantly, the initial strain rate used for the cyclic experiments was lower or comparable to the rate of ionic aggregate exchange ( $1/\tau_{st}^{*DMA}(20^{\circ}C)$ ) of all the ionic networks. Therefore, ionic rearrangements are expected during the elongation. The result of these ionic rearrangements are much wider hysteresis loops manifested by the ionic samples with respect to the rather narrow hysteresis of the permanent network brought about by disentangling of polymer chains and relaxation of defects. Also, for the ionic samples the maximal stresses reached at around 200% strain reflect the ionic bond strengths and decrease with the alkyl group length.

In ref 16, in contrast to the current study, Das et al. reported that the ionic BIIR exhibited a smaller hysteresis as compared to the sulfur cross-linked BIIR. However, there is no contradiction here, since they used a ten times larger initial deformation rate as compared to our experiments. As a result of such large deformation rate ionic junctions stayed closed on the experimental time scale appearing to act as permanent cross-links [124, 142]. On top of that, the ionic sample was more cross-linked than the non-ionic sample, which led to the less pronounced hysteresis. This emphasizes that future self-

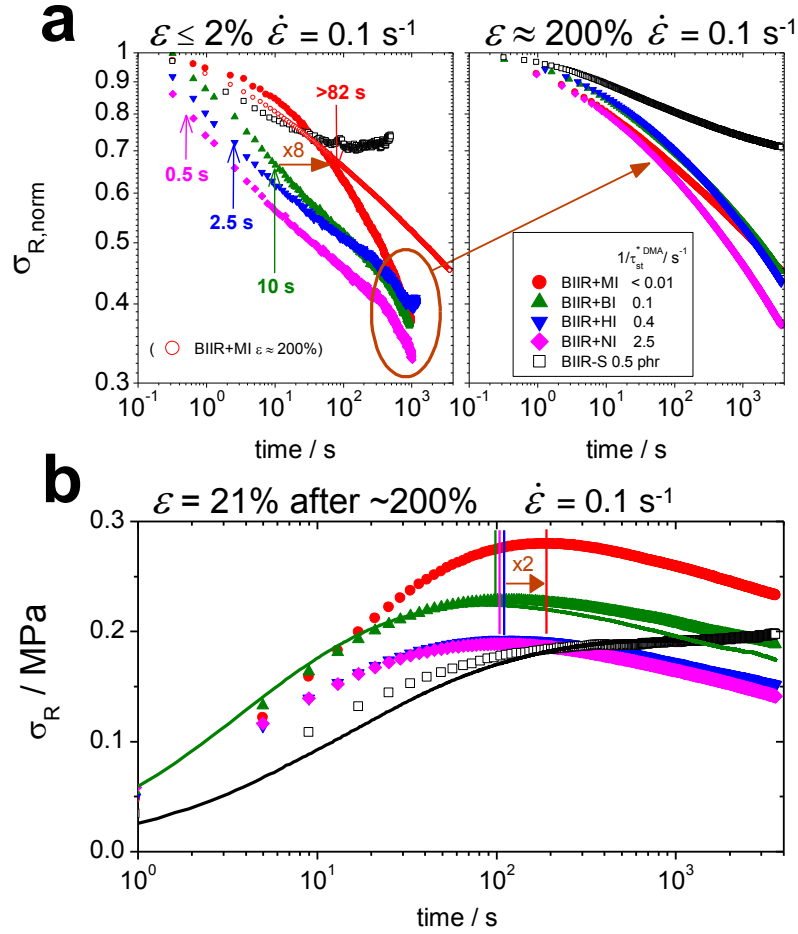


**Figure 8.16:** (a) Stress relaxation experiments at  $\leq 2\%$  (left panel) and  $200\%$  (right panel) deformation. In the left panel, the arrows indicate  $\tau_{\text{st}}^{\text{DMA}}(20^\circ\text{C})$ . In the legend,  $1/\tau_{\text{st}}^{\text{DMA}}(20^\circ\text{C})$  (the rates of ionic aggregate exchange) are specified. (b) Stress recovery and relaxation after one loading/unloading cycle up to  $\epsilon \approx 200\%$  and back to  $21\%$ . The solid green and black curves represent repeated measurements for BIIR+BI and BIIR-S 0.5 phr to check reproducibility. The initial strain rate  $\dot{\epsilon}$  was set to around  $0.1\text{s}^{-1}$ . All experiments were conducted at room temperature. Reprinted with permission from [76]. Copyright 2019 American Chemical Society.

healing rubbers based upon the present concept should feature additional permanent cross-links to prevent permanent deformation.

The kinetics of structural reorganizations was further investigated by reduced stress relaxation experiments (Fig. 8.16). The reduced stress  $\sigma_R$  can be found as  $\sigma_R = \sigma/(\lambda - \lambda^{-2})$ , where  $\sigma$  is the stress and  $\lambda$  is the stretch ratio ( $= \epsilon + 1$ ), and represents the shear modulus [15, 143]. For clarity, the data in Fig. 8.16(a) were normalized to  $\sigma_R(t = 0)$  to better distinguish the relaxation rates. The measurements were conducted at large strains of around  $200\%$  (right panel of Fig. 8.16(a)) and at small strains below  $2\%$  (left panel), corresponding to the linear regime, for comparison. It can be seen that at small strains

BIIR-S 0.5 phr shows an initial relaxation due to the aforementioned intermediate motions followed by a long-time plateau, which is ascribed to the permanent character of the covalent network. The stress relaxation decays of the ionic samples resemble the mirrored DMA data in the region of the ionic transition. The  $\tau_{st}^{*DMA}$  values are specified on the plot, and it can be seen that they roughly reflect the observed transitions. At large strains, during the loading period with the initial strain rate of  $0.1 \text{ s}^{-1}$  samples BIIR+BI/HI/NI, all possessing rates of ionic hopping larger than  $0.1 \text{ s}^{-1}$ , experienced ionic rearrangements which caused large-scale terminal relaxations to be overemphasized. On the other hand, BIIR+MI could not relax to the same extent during the loading cycle and, therefore, accumulated higher internal stresses, which rendered its initial stress relaxation faster as compared to the linear regime case.

Fig. 8.16(b) demonstrates the time dependence of the non-normalized reduced stress recorded after one loading/unloading cycle. The experiment was again carried out with the same initial strain rate as was done for the stress relaxation experiment at large deformations, thereby contraposing BIIR+MI against the rest of the samples. After unloading to  $\epsilon \approx 21\%$ , all samples were in a stress-free state, but since the applied fast-enough initial strain rate did not allow the ionic networks to completely relax during the loading/unloading cycle, residual stresses built up after the cycle. This can be observed as an initial increase of  $\sigma_R$ .

It can be seen that in the case of BIIR-S 0.5 phr the build-up of  $\sigma_R$  reaches a plateau at long times which can be again attributed to the permanent nature of the covalent cross-links unable to open and relax stress. In contrast to that, ionic networks are able to relax accumulated residual stresses by means of ionic hopping which results in the subsequent decays. When the stress relaxation equalizes the restoring elasticity contribution, a transient maximum is observed. It can be seen that the transient maximum of BIIR+MI is located at longer times and at a higher level than the maxima of the other samples, which is associated with its slowest sticky dynamics and resulting largest stored elasticity accumulated during the deformation cycle. Notably, the transient maximum of BIIR+MI is delayed with respect to the other maxima now only by a factor of two instead of the expected factor of eight as seen from the linear regime stress relaxation results. This indicates the reduction of the bond lifetime of BIIR+MI due to the forced tearing of stickers out of the ionic aggregates. This was also simulated and experimentally observed in other systems previously [82, 124, 144] and is an interesting result which is especially tempting for application of self-healing materials, since it shows that internally stressed materials can heal themselves more quickly after a damage event as compared to the pristine state.

## 8.6 Summary

A comprehensive study of structure and dynamics of ionic entangled BIIR elastomers cross-linked with different alkylimidazoliums as well as of their non-ionic counterparts was conducted employing SAXS, solid-state NMR, BDS, and mechanical methods. According

to the structural analysis performed by SAXS and NMR relaxometry, ionic groups form sparsely arranged ionic aggregates with around 20 ionic groups per aggregate that do not involve significant segmental immobilization. A special focus was laid on the elaboration of the dynamic mechanism in the ionic elastomers. To this end, MQ NMR proved to be insightful in quantifying microscale sticky chain dynamics, relying on the power-law model of the OACF [52].

A correlation of MQ NMR and DMA results showed a quantitative agreement of activation energies of ionic dissociation and effective bond lifetimes, thus proving for the first time molecular origins of the sticky reptation model [77, 80]. Furthermore, it was shown that apparent master curves are not useful for such a comparison. The activation energies and bond lifetimes were found to decrease with the length of the alkyl group of the alkyimidazoliums due to reduction of strength of ionic interactions. The time scales and activation energies from DMA and MQ NMR were then corroborated by the temperature dependencies of electrode polarization and conductivity accessed by BDS, directly linking the long-range ionic transport to the ionic hopping of alkyimidazolium stickers.

The dynamics inside ionic aggregates, as seen by BDS and MAS MQ NMR, showed an increase of motional amplitude with temperature and length of the alkyl group. The intra-aggregate relaxation, featuring the same thermal activation of relaxation times as the ionic dissociation, did not appear to correspond to the bare bond lifetime, as the extracted relaxation times were found in the inverse order with respect to the effective bond lifetimes from DMA and MQ NMR. Owing to this finding and to the fact that the current state-of-the-art theory treats predominantly pairwise associations, we cannot estimate the number of returns of an open sticker to an old aggregate before traveling to a new one. Finally, the mechanical measurements in the non-linear regime showed that the mechanical response is strongly dependent on the relationship between the deformation rate and the effective bond lifetime, and the bond lifetime decreases upon accumulation of internal stresses.



## 9 Dynamics in micellar networks of telechelic PIBs

In the following chapter, dynamic and structural properties of unentangled telechelic PIB chains, forming dynamic micellar networks by hydrogen bonding, are elucidated. Effects of a molecular architecture and nature of a supramolecular moiety on chain ends on properties of dynamic networks are detailed. To this end, a combination of SAXS, rheology, NMR, and dielectric spectroscopy was employed. In particular, it was found that star-shaped telechelic molecules form more stable networks with larger and more distantly arranged aggregates as compared to their linear counterparts. Also, stickers providing more hydrogen bonds possess longer bond lifetimes, which consequently leads to slower overall dynamics. Correlations of rheology with NMR and dielectric spectroscopy fortify the findings from Chapter 8: (i) the intra-aggregate relaxation time is not related to the bare bond lifetime of a sticker, but undergoes the same activation process as the sticker dissociation governing chain dynamics for low molecular weights between stickers; (ii) terminal stress relaxation is governed by relaxation of single chains.

### 9.1 Identification of the micellar network structure by SAXS

The SAXS data of telechelic PIBs can be seen in Fig. 9.1. The measurements and data analysis were performed by Prof. Dr. Kay Saalwächter, whereas I provided the interpretations. All signal intensities were corrected for a variable sample thickness. In all cases, one can observe a prominent peak with a shoulder at higher  $q$ -values, which was previously shown to correspond to the system of interconnected, but disordered micelles [123, 124]. In panels (a) and (b), different molecular architectures are compared for barbituric-acid-(BA-) and thymine-(Th-)functionalized samples, respectively, whereas in (c) and (d) the molecular weight and temperature effects on the SAXS data are demonstrated.

Looking, firstly, at (a) and (b), it can be seen that at a given molecular architecture scattering intensities of BA-samples are larger than of Th-samples, which can be explained by lower contrast of Th-groups and their lower cluster-bound fraction. Further, the BA- and Th-samples exhibit different trends upon the increase of the number of arms. Whereas for the BA-samples the scattering intensity ( $I(q_{\max})$ ) increases and the peak's maximum ( $q_{\max}$ ) shifts towards lower  $q$ -values, corresponding to larger distances between the micellar cores ( $r_{cc}$ ) and hence to their lower number densities, for the Th-samples the peaks' maxima also shift towards lower  $q$  values, but the scattering intensities increase in the order linear  $<4\text{arm} < 3\text{arm}$ . The scattering intensity within the series of samples with the same end-groups is related to the volume fraction of scattering centers (micellar cores). Therefore, in the case of the BA-samples, with the number density of micellar cores decreasing with the number of arms, the volume fraction of micellar cores can increase only due to the more strongly increasing size of the aggregates, i.e. the aggregation number ( $AN$ ). Using the same reasoning for the Th-samples, we conclude that  $AN$  should increase in the order linear  $<4\text{arm} < 3\text{arm}$ .

$AN$  can be estimated, as was shown in Chapter 8, using either space-filling (SF) argu-

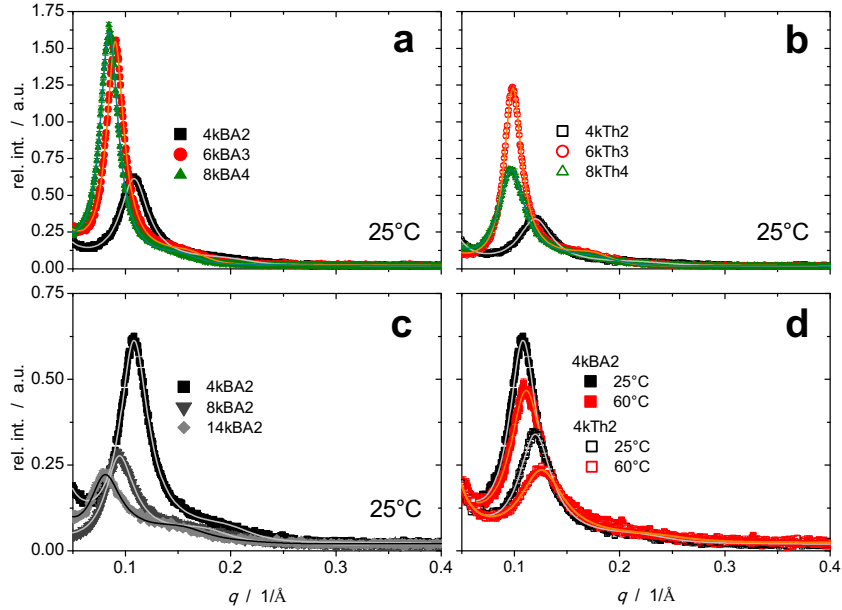


**Figure 9.1:** (a) and (b) Effect of the molecular architecture on SAXS data of PIBs end-functionalized with barbituric acid (BA) and thymine (Th), respectively. (c) Effect of the molecular weight on SAXS results for a linear BA-functionalized PIB. The data were acquired at 25°C. (d) Temperature evolution of SAXS data of 4kBA2 and 4kTh2. The curves represent fits assuming the validity of the Perkus-Yevick (PY) structure factor.

ments or fitting the SAXS data on the basis of the Perkus-Yevick (PY) model of the structure factor. The former approach necessitates a position of the peak's maximum and an assumption regarding a spacious arrangement of the aggregates (see Eq. 8.1). In Eq. 8.1, we assumed that the aggregates are arranged in the cubic lattice, whereas here it would be more reasonable to assume a body-centered cubic lattice because previous studies showed such an arrangement for monofunctionalized PIBs [123, 124]. As a result, a factor of  $\sqrt{2}$  should be added to calculations of Eq. 8.1. The Perkus-Yevick-model-based fits in turn provide, inter alia, the size of the micellar core, designated as  $R_1$ , which with knowledge of the molecular weight of end-groups ( $M_{\text{end}}$ ) can be related to  $AN$  via Eq. 8.2. All the relevant SAXS results can be seen in Table 9.1.

One can notice that both estimation strategies provide similar values for  $AN$  exhibiting the same trends that were predicted purely from the scattering intensities above. For strongly associating systems with  $E_{\text{a}}^{\text{st}} > 10RT$  (see below), rendering the number of dangling or free chains negligibly small, larger  $AN$  can be achieved by formation of numerous loops (see Fig. 9.2 for an overview of possible structures). To prove this conclusion, it is insightful to correlate  $AN$  with the difference ( $\Delta r$ ) between  $r_{\text{cc}}$  and the end-to-end distance ( $R_{\text{EE}} = bN_{\text{EE}}^{0.5} = b(M_{\text{w,EE}}/M_0)^{0.5}$ ,  $N_{\text{EE}}, M_{\text{w,EE}}$ : number of Kuhn segments and weight-averaged molecular weight between the chain ends (in stars), respectively,  $M_0$ : molecular weight of the Kuhn segment).  $\Delta r$  shows whether the next micellar core is located in the range of the size of the Gaussian chain. The comparison of  $AN$  and  $\Delta r$

**Table 9.1:** SAXS-determined structural parameters of the telechelic PIB samples

Sample	T	$q_{\max}$	$I(q_{\max})$	$r_{cc}$	$M_w^a$	$R_{EE}$	$\Delta r^b$	$M_{\text{end}}$	$R_1$	$\sigma$	AN		$\frac{N_{\text{br}}}{AN}$
	°C	1/Å		Å	g/mol	Å	Å	g/mol	Å		PY	SF	
4kTh2	25	0.12	0.34	52.5	4824	52.4	0.1	206	16	0.23	50	47	0.57
	60	0.13	0.24	50		-2.4	14		0.18	34	41	0.62	
6kTh3	25	0.098	1.23	64.1	8704	57.5	6.6	264	18.4	0.1	60	71	0.56
8kTh4	25	0.097	0.67	64.8	13764	62.6	2.2	264	17.7	0.11	53	62	0.59
4kBA2	25	0.108	0.61	58.2	5200	54.4	3.8	264	17.2	0.18	49	59	0.58
	60	0.111	0.24	56.6		2.2	16.4		0.18	42	55	0.60	
6kBA3	25	0.09	1.54	69.8	8890	58.1	11.7	322	21.4	0.13	77	90	0.53
8kBA4	25	0.084	1.61	74.2	9472	51.9	22.3	322	26.6	0.23	147	135	0.45
8kBA2	25	0.094	0.28	66.8	9480	73.5	-6.7	264	15.4	0.1	35	49	0.67
14kBA2	25	0.081	0.22	77.6	16560	97.1	-19.5	264	15.9	0.1	38	44	0.70

<sup>a</sup> Data for star samples were provided by Dr. Diana Döhler, for linear samples taken from literature [28, 29]

<sup>b</sup>  $\Delta r = r_{cc} - R_{EE}$

shows that both quantities are directly proportional if  $\Delta r > 0$ , and  $AN$  remains constant if  $\Delta r \leq 0$ , thus fortifying the above statement. In particular, it can be seen that the  $\Delta r$  values of the BA-samples are larger than these of the Th-samples, indicating larger looping (lower bridging) fractions of the former. The fractions of bridging chains, determined via Eq. 8.3 [72], are also tabulated for comparison. Note that Eq. 8.3 was derived for linear polymers and, therefore, one can expect deviations for star-architectures. Also, many loop structures formed by star-samples (e.g. (ii) in Fig. 9.2(b) and (ii), (iii), (iv) in Fig. 9.2(c)) can carry stress, such that one cannot use the bridging fractions from Table 9.1 for accounting of elastically active chains, which is especially important to keep in mind for rheological estimations of the plateau modulus.

For higher molecular weights (Fig. 9.1(c)), both scattering intensities and  $q_{\max}$  become lower because of decreasing  $AN$  and increasing distances between the micellar cores, respectively. The lower  $AN$  values for longer molecular weights can be explained by lower probability for back-looping due to steric factors and larger distances between the interacting stickers. Upon temperature elevation, shown in Fig. 9.1(d), the scattering intensities decrease somewhat, but virtually do not change their positions, which can be due to shift of equilibrium of open and closed stickers and, thus, loss of scattering contrast.

The shown differences in trends of  $AN$  for BA- and Th-samples can be explained by differences in their thermodynamics. As it will be shown below, BA, providing more

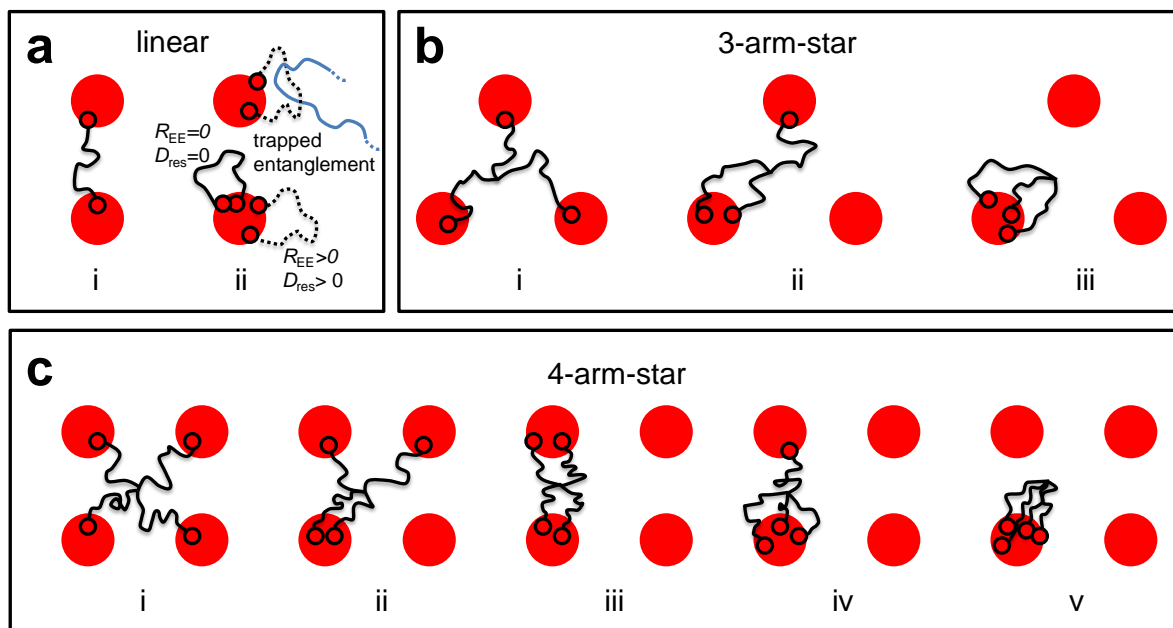


**Figure 9.2:** Possible (network) structures formed by linear (a), 3-arm- (b), and 4-arm-star (c) telechelic polymers. In (a), also, different loop structures are shown with the end-to-end distances  $R_{ee}$  equal to zero or larger than zero, leading to either complete or incomplete isotropic motion with  $D_{res}$  equal to or larger than zero, respectively. Additionally, a formation of a trapped entanglement, represented by black dotted and blue solid lines, is pictured.

possibilities for hydrogen bonding (see also Fig. 7.2(d) and (e)), is a stronger sticker than Th. As a result, the network formation in the BA-samples is mostly driven by an enthalpic factor which leads to significant intramolecular associations (looping) tending to minimize the system's energy. Consequently, the closer the stickers are located to each other in the molecule (shorter chains, more arms), the higher the probability for looping becomes. In contrast, for weaker Th-stickers, especially in the star samples, it is energetically less unfavorable to join distant clusters causing more bridging (and thus lower  $\Delta r$ ) as compared to the BA-samples. A somewhat striking (yet reproducible<sup>4</sup>) result for the Th-samples is that the 4arm-star sample exhibits a lower  $AN$  than the 3arm-star sample. Possibly, the deviation from the BA-sample's trend can be due to a more important entropic factor. To be more exact, after each association the entropic penalty for the left open stickers rises leading to a lower effective dissociation energy (energetic asymmetry [145]). Therefore, the entropic penalty for 8kTh4 can overbalance the enthalpic term letting the fourth sticker be open long enough to bridge to another molecule. This conclusion would certainly require further validations from e.g. MD simulations.

<sup>4</sup>the measurements were performed independently in the Colby and Peterlik labs by Prof. Dr. Kay Saalwächter and Univ.-Prof. Mag. Dr. Herwig Peterlik, respectively. In both cases the relative peaks' positions and intensities are as pictured in Fig. 9.1

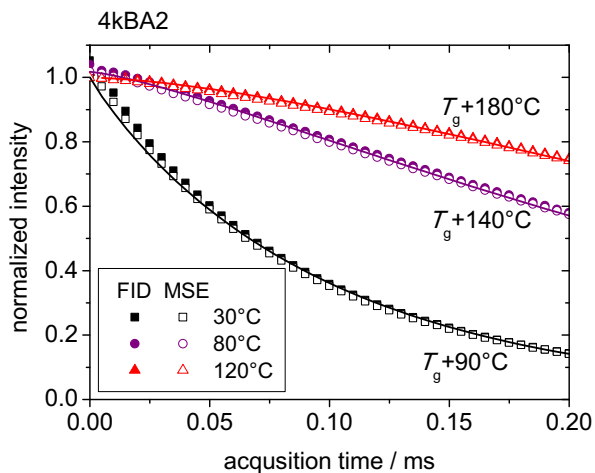


**Figure 9.3:** Single-pulse and MSE-refocused FID curves of 4kBA2 at the indicated temperatures. The solid lines correspond to a single stretched exponential fitting function proving the predominance of one dynamic phase. The Curie-correction accounting for the decrease of the total signal intensity with temperature has been applied. Note that some minor mismatches of intensity normalization (decays do not start exactly at 1) can originate from reduction of the Q-factor of the rf coil upon the temperature increase.

## 9.2 Phase composition analysis by NMR relaxometry

Similarly as for the ionic BIIR samples (see Fig. 4.2), we studied the phase composition in the telechelic PIB samples by NMR relaxometry. In Fig. 9.3, one-pulse and MSE-refocused FID decays are presented. For a reminder, the number of stretched exponential functions of the form  $f \exp(-(t/T_2)^\beta)$  ( $f, T_2, \beta$ : the fraction, spin-spin relaxation time, and the shape parameter of a given phase,  $t$ : the acquisition time) used to describe experimental data reflects the number of present phases with different dynamics. In particular, it was important to find out whether a glassy phase around micellar cores is present. As can be seen, a single stretched exponential function was sufficient to describe the data rather well in the whole studied temperature range, thus showing the predominance of only one dynamic phase corresponding to bridging and looping chains.

## 9.3 Sticky dynamics of telechelic chains by MQ NMR and rheology

The sticky chain dynamics was studied by correlation of MQ NMR and rheological results. Because MQ NMR provides microscale dynamic information, while rheology of micellar systems can be also sensitive to macroscopic rearrangement of micelles [72], we start the discussion with MQ NMR results. We refrained from the quasi-static analysis of normalized DQ build-ups ( $I_{nDQ}$ ), presented in Chapter 8, as  $I_{nDQ}$  did not reach the long-time plateau of 0.5 in many cases as a result of developed long-range dynamics. Instead, MQ NMR data were analyzed using the power-law-model-based fits (Eqs. 5.6

and 5.7) to quantify the dynamics. Notably, after having measured from low to high temperatures in the range from 0 to 120°C the measurements were repeated at the temperature corresponding to the  $C(t)$  plateau to check whether structural changes occurred. For all the studied samples, the MQ NMR data after the repeating measurement always coincided with the first measurement indicating that the network structures were always in thermodynamic equilibrium. Fig. B6 demonstrates this on the example of 4kBA2.

To alleviate the fitting uncertainties related to the lack of data points at the beginning of rather quick DQ build-ups at low temperatures (large dipolar couplings), we resorted to shorter pulse sequences, containing three (a 180° pulse flanked with two 90° pulses) or two pulses (two 90° pulses) in the excitation and reconversion blocks, as compared to twelve pulses per block in the case of the Baum-Pines-based pulse sequence used so far [47, 66]. The mentioned quick DQ build-ups, as compared with the BIIR samples from the previous chapter, stem from the presence of dynamically more constrained component, related probably to segments closer to supramolecular aggregates, which, however, never exceeded 10%.

To take advantage of the good long-time performance of the Baum/Pines pulse sequence and at the same time to have short-time data available, as provided by shorter pulse sequences, we combined the MQ data of the aforementioned pulse sequences [47] for the results obtained at 40 and 50°C. While at larger temperatures the results from the Baum-Pines pulse sequence alone could be used, below these temperatures the results from one of the short pulse sequences were sufficient for the successful fitting procedure.

The combined data can be seen in Fig. 9.4. As can be seen, the fit quality using Eqs. 5.6 and 5.7 is not very good owing to the alluded minor contribution of a dynamically

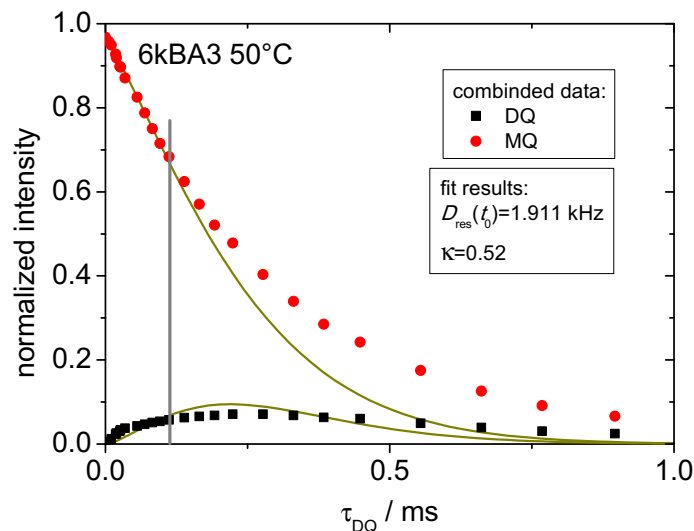


**Figure 9.4:** Combined MQ data with power-law-model-based fits (curves). The grey vertical line shows the fit's limit.

more constrained component and a rather broad dipolar couplings distribution related, in particular, to the broad distribution of bond lifetimes (see below). Nevertheless, the fit provides consistent average values of  $D_{\text{res}}(t_0)$  and  $\kappa$ , as was shown in Chapter 6. We decided not to include the second component into the fit to avoid worsening of fit stability.

Certainly, one can additionally include the log-normal distribution of dipolar couplings to the fit equations 5.6 and 5.7 to improve the fit quality. In Fig. B5, the result of the additional introduction of the log-normal distribution of dipolar couplings is demonstrated on the example of reference networks. Firstly, it can be seen that for both homogeneous and highly inhomogeneous networks the power-law-based fit with the additional distribution of dipolar couplings delivers the same distribution width parameter ( $\sigma_{\text{ln}}$ ) as the empirical fit of the  $I_{\text{nDQ}}$  data. Thus, the fit can be used to extract this important parameter from the DQ/ $\Sigma$ MQ data.

For all the telechelic PIB samples  $\sigma_{\text{ln}}$  was found to be 1-1.5 in the plateau area of  $C(t)$  (see below), resulting from the distribution of molecular weights, bond lifetimes, segmental relaxation times, and defects relaxation. The larger  $\sigma_{\text{ln}}$  values as compared to the BIIR samples, having  $\sigma_{\text{ln}} < 1$ , are in line with larger confined fractions and much larger number of loops in the case of telechelic PIBs, whose dynamics modulates analyzed MQ signals. On the other hand, tests on the model cases and also on the studied samples (PIB and BIIR) have shown that extracted  $D_{\text{res}}(t_0)$  and  $\kappa$  values are somewhat lower than the values from the fit without the log-normal distribution, which leads to  $\kappa \rightarrow 0$  in the plateau area, thereby causing largely overestimated horizontal shifts and activation energies. Therefore, we decided to refrain from using the log-normal distribution in the power-law-model-based fits for  $C(t)$  mastering.

Before the simultaneous fits of the MQ NMR data can be conducted,  $\Sigma$ MQ signals are to be corrected for the long-time tails related to the isotropically moving molecular parts. The isotropic fractions of telechelic PIBs are plotted in Fig. 9.5 as a function of temperature. For comparison, the isotropic fraction of a linear precursor with 3-4 entanglements per chains is given. The isotropic fractions of the precursor are larger than of the telechelic samples since the chain ends are free to move. The isotropic fractions of the telechelic samples are seen to be below 10% even at highest studied temperatures, which implies that the activation energy of association ( $E_{\text{a,st}}$ ) is large in all cases.

After having done the tail correction, the power-law-based fits were carried out to extract  $D_{\text{res}}(t_0)$  and  $\kappa$  values. All the extracted values are presented in Fig. 9.6. In the right panels, dynamic regimes are assigned according to the sticky Rouse model predictions of  $C(t)$  slopes [32]. The denotation follows the Doi/Edwards model [58].

In part (a), the results of PIB precursors are compared. In all cases  $D_{\text{res}}(t_0)$  decreases and  $\kappa$  increases with temperature within the whole temperature range, indicating the transition from Rouse regime (I) to free diffusion (IV). It can be seen that with an increase of the molecular weight the temperature variation of  $D_{\text{res}}(t_0)$  and  $\kappa$  becomes more protracted, which can be explained by an increase of  $\tau_{\text{R}}$ . The effect of the molecular

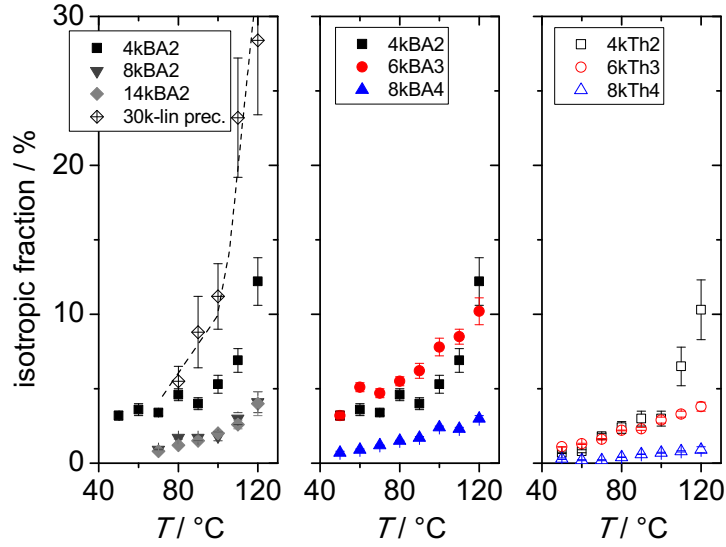


**Figure 9.5:** Isotropic fraction of PIB samples as a function of temperature. Left: linear PIBs, Center: BA-functionalized PIBs, Right: Th-functionalized PIBs. The dashed line merely guides the eye.

architecture on the polymer dynamics is masked by large experimental errors caused by the weak signal.

In (b)-(d) panels of Fig. 9.6, results of end-functionalized PIBs are presented. In contrast to the precursors, the functionalized samples feature an additional decrease of the  $C(t)$  slope between the regimes I and IV, corresponding to a weakly developed rubbery plateau (P) caused by formation of supramolecular networks. In (b), results of the linear BA-functionalized PIBs with different molecular weights are demonstrated. The measurements were carried out starting at low temperatures to show the transition to regime 0. It can be seen that the transition shifts to lower temperatures with an increase of the molecular weight owing to the reduction of  $T_g$ . In view of this, the terminal flow does not exhibit any significant changes upon the molecular weight variation.

In (c) and (d), the effect of the molecular architecture on the segmental dynamics is shown for BA- and Th-functionalized samples. Firstly, the transition to regime I occurs at around the same temperature for all the samples which is in line with the comparable  $T_g$  values. Secondly, the star-shaped samples are seen to exhibit lower slopes in the plateau area and terminal flows delayed to higher temperatures as compared to linear samples, which implies that the formed networks of the star-shaped samples are more structurally stable. Indeed, it is conceivable that in the case of linear samples a detachment of only one sticker is sufficient in order to disconnect two aggregates and impart the detached sticker a significant motional freedom, whereas in the case of star-shaped samples a less probable simultaneous detachment of two or three stickers is required. This in turn leads to elevation of the effective bond lifetime in the star-shaped samples. Also, it means that some fraction of stickers starts to open already in the plateau area, which accords with

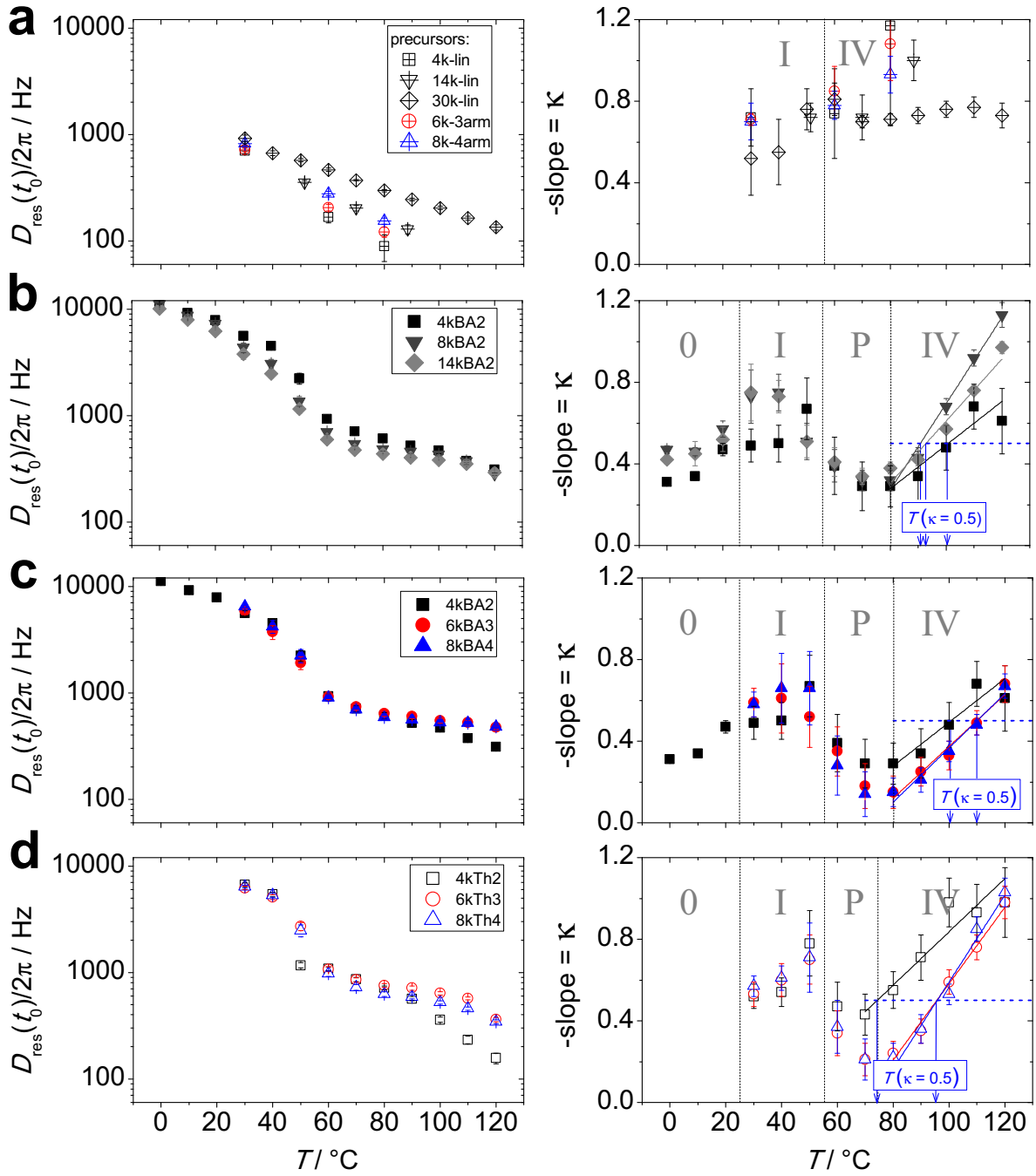


**Figure 9.6:** Temperature dependence of the extracted  $D_{\text{res}}(t_0)$  (left panels) and  $\kappa$  (right panels) values for PIB samples. (a) precursors, (b) linear BA-functionalized PIBs, (c) and (d) BA- and Th-functionalized PIBs with different molecular architectures, respectively. In the right panels, the solid lines represent linear fits, while the horizontal, dashed, blue lines with arrows indicate temperatures at which  $\kappa = 0.5$ . The black dotted vertical lines separate dynamic regimes as indicated.

the broad bond lifetime distribution. When the BA- and Th-samples are compared at a given molecular architecture, one can see that the  $C(t)$  slopes of the Th-samples in the plateau and terminal flow regions are larger, and the plateau regions are narrower, which indicates that Th is a weaker sticker than BA.

As was shown in Section 6.2, the bond lifetimes can be extracted as arithmetic averages of the fit intervals at temperatures at which  $\kappa = 0.5$ ,  $T(\kappa = 0.5)$  which must be subsequently corrected with a predefined factor dependent on the bond lifetime distribution, taken from the calibration curve in Fig. 6.4. To find exact  $T(\kappa = 0.5)$ , linear fits in the area of terminal flows were performed. The fit interval for determination of the bond lifetime was always taken at the experimental temperature being closest to the temperature determined by the linear fits. The error of such procedure is marginal, since the fit intervals at the neighboring temperatures were always similar. More significant errors arise due to the uncertainties in  $\kappa$ , which can amount to  $\pm 15^\circ\text{C}$  for  $T(\kappa = 0.5)$ . The bond lifetimes determined in such a way are plotted in Fig. 9.12 along with the bond lifetimes and intra-aggregate relaxation times found by rheology and BDS, respectively. The discussion of the found times is deferred to the Section 9.4, after introduction of rheological and BDS measurements.

The extracted  $D_{\text{res}}(t_0)$  and  $\kappa$  parameters were then used to build parts of the OACF that were shifted to construct apparent master curves. The shifting was done according to the instructions given in Chapter 6, namely, by matching  $C(\tau_{\text{DQmin}})$  points in the power-law and plateau regions and  $C(\tau_{\text{DQmid}})$  points during the multiexponential decay. The obtained apparent master curves and shift factors can be seen in Fig. 9.7.

The master curves are compared separately for different molecular architectures to emphasize the effect of the end-group on the chain dynamics. It can be seen that in all cases the master curves of the samples with same molecular weight between the end-groups coincide in regime I and at the beginning of the plateau. At longer time scales, the Th-samples exhibit an earlier onset of the terminal chain relaxation than the BA-samples. With the increase of the molecular weight, the whole master curve is seen to shift to shorter times owing to the reduction of  $T_g$  ( $-61.4^\circ\text{C}$  for 4kBA2,  $-64.5^\circ\text{C}$  for 8kBA2, and  $-64.2^\circ\text{C}$  for 14kBA2). For reference, a master curve of the linear precursor sample is also shown. It can be seen that it exhibits no plateau, as expected.

Since the presented master curves are only apparent due to uncontrolled inherent switching from the shift factor controlled by segmental to sticky dynamics (see Chapter 8 and also ref 76), the master curves construction was mostly needed to access sticky activation energies ( $E_a^{\text{st}}$ ) from the temperature dependencies of the shift factors. It can be seen that the shift factor of a precursor within the whole temperature range as well as of the telechelic PIBs at low temperatures agree rather well with the literature data of non-modified PIB, governed purely by the segmental dynamics [146]. Starting from  $30^\circ\text{C}$ , however, the shift factors exhibit some deviations from the literature data. Until around  $50^\circ\text{C}$ , the deviation can be explained by uncertainties in  $\kappa$  and  $D_{\text{res}}$  values, as the dynamics is still in Rouse regime (see Fig. 9.6). Beyond  $50^\circ\text{C}$ , in the plateau region and,

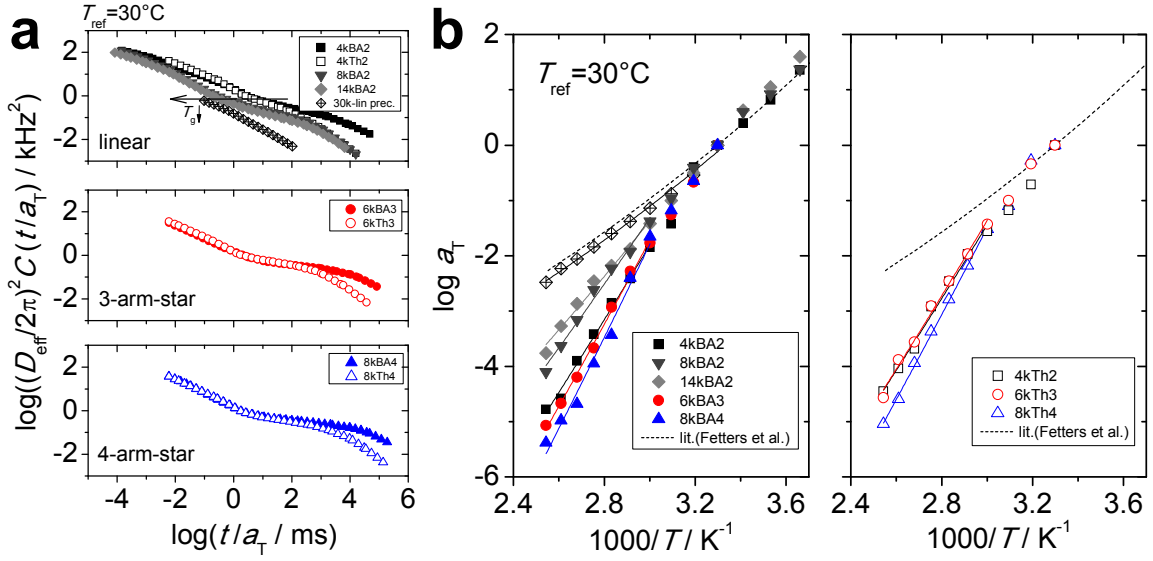


**Figure 9.7:** (a) Apparent master curves of telechelic PIB samples reduced at  $T_{\text{ref}} = 30^\circ\text{C}$ , compared separately for different architectures, as indicated. (b) Shift factors for BA- (left panel) and Th-functionalized (right panel) samples. For reference, shift factors from the literature [146] and of a precursor (linear,  $M_n \approx 30$  kDa) are given.

subsequently, in the exponential decay, the shift factors become sensitive to the sticky dynamics increasing the observed activation energy which is reflected in the enhanced slopes. Note that the switching temperature can be lower in this case ( $< 100^\circ\text{C}$ ) as compared to the ionic BIIR samples ( $> 100^\circ\text{C}$ ), possibly, because of a larger distribution stickers' bond lifetimes.

The "sticky" parts of the shift factors can be fitted with the product of the Vogel-Fulcher temperature dependence, related to the segmental dynamics of PIB with parameters taken from the literature [146] and set fixed, and the Arrhenius temperature dependence of the sticky dynamics (see Eq. 2.16). The Vogel-Fulcher temperature dependence gives an effective linearized  $E_{a,\text{segm}}$ , whereas the Arrhenius temperature dependence delivers  $E_{a,\text{st}}$  assumed to be constant. The sum of both yields an apparent activation energy ( $E_{a,\text{app}}$ ). However, since  $E_{a,\text{segm}}$  of PIB only weakly depends on temperature within the studied temperature range owing to low fragility of PIB [147],  $E_{a,\text{app}}$  can also be extracted by simple Arrhenius fits.  $E_{a,\text{app}}$  is plotted in Fig. 9.13.

The telechelic samples were then investigated by rheology. The experiments and data fitting were performed by Prof. Dr. Kay Saalwächter, whereas I interpreted the obtained results. In Fig. 9.8, one can see a frequency sweep of storage and loss moduli ( $G'$  and  $G''$ , respectively) on the example of 4kTh2 at  $25^\circ\text{C}$ . One can extract mainly three pieces of information from frequency-sweep data, namely, plateau modulus ( $G_N$ , determined at the frequency corresponding to the  $G''$  minimum [70, 133], the bond lifetime median ( $\tau_{\text{st,med}}^* \equiv 10^{\log \tau_{\text{st}}^*}$ , which will be henceforth denoted as  $\tau_{\text{st}}^*$ ) and the distribution parameter

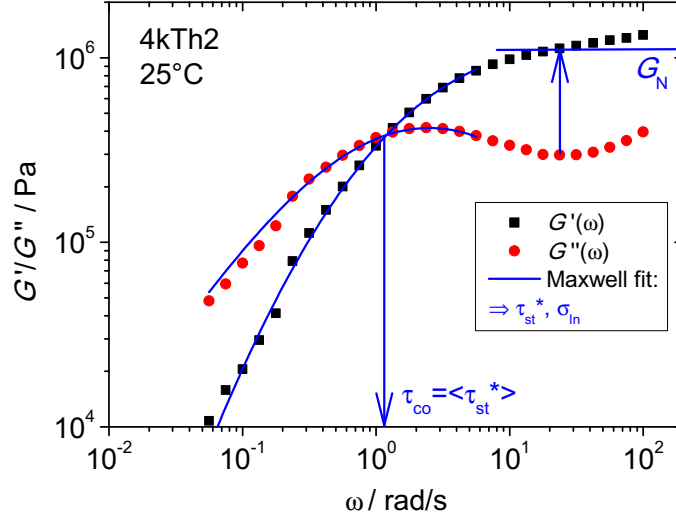


**Figure 9.8:** Frequency sweep of storage and loss moduli of 4kTh2 at 25°C. The extracted information is marked in blue, namely, the plateau modulus ( $G_N$ , the bond lifetime median ( $\tau_{st}^*$ ) and the distribution parameter ( $\sigma_{ln}$ ), determined by the Maxwell fit assuming the log-normal distribution (Eqs. 9.1 and 9.2), the crossover time ( $\tau_{co}$ ) at  $G' = G''$ , equal to the arithmetic mean value of the bond lifetimes distribution ( $\langle \tau_{st}^* \rangle$ ).

( $\sigma_{ln}$ ), and the crossover time ( $\tau_{co}$ ) at  $G' = G''$ , found to be equal to the arithmetic mean value of the bond lifetimes distribution ( $\langle \tau_{st}^* \rangle$ ), as is shown in Table B4. The fact that  $\tau_{co} = \langle \tau_{st}^* \rangle$  implies that  $\tau_{co}$  is biased to long times of the distribution and should not be used to represent the bond lifetime.  $\tau_{st}^*$  and  $\sigma_{ln}$  were determined by simultaneously fitting the terminal flow area of  $G'$  and  $G''$  with the Maxwell model additionally assuming the log-normal distribution of bond lifetimes (Maxwell fit). The equations for the simultaneous Maxwell fit read:

$$G'(\omega) = \int P(\ln(\tau_{st}^*)) \Delta G_{st} \frac{(\tau_{st}^* \omega)^2}{1 + (\tau_{st}^* \omega)^2} d \ln(\tau_{st}^*) \quad (9.1)$$

and

$$G''(\omega) = \int P(\ln(\tau_{st}^*)) \Delta G_{st} \frac{\tau_{st}^* \omega}{1 + (\tau_{st}^* \omega)^2} d \ln(\tau_{st}^*), \quad (9.2)$$

where  $P(\ln(\tau_{st}^*))$  is the log-normal distribution density function of  $\tau_{st}^*$ ,  $\Delta G_{st}$  is the relaxation strength.

In Fig. 9.9,  $G_N$  of all the telechelic PIB samples are given. For comparison,  $G_N$  values calculated using the affine and phantom models (see Eq. 8.8), taking into account contributions from both cross-links and entanglements, are also shown. Note that for polymers with molecular weights below  $M_e$  the contribution of entanglements had to be also included as otherwise the theoretically predicted values became too underestimated as compared to the experimental data. For calculations, we used  $M_e$  of unmodified PIB

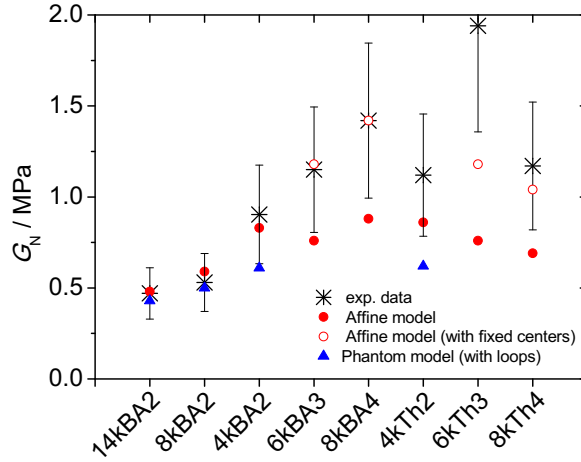


**Figure 9.9:** Plateau moduli of telechelic PIB samples at 25°C.

( $M_{e,PIB}$ ), which can, however, be different in the studied systems as entanglements in the system of interconnected micelles originate from crossings of bridging chains. Further, note that the fluctuation of stickers, covered by the phantom model, and the loops fraction could not be considered for the star-shaped polymers because the exact number of completely unbridged chains is not known.

It can be seen in Fig. 9.9 that the phantom model predictions with consideration of loops are well fulfilled for the samples with molecular weights of 8 and 14 kDa, respectively, and underestimated for the samples with the molecular weight of 4 kDa. This implies that  $M_e$  is close to the value of  $M_{e,PIB}$  for the samples with molecular weights larger than  $M_{e,PIB}$ , while  $M_e$  decreases for the samples with molecular weights below  $M_{e,PIB}$ , possibly due to constraint release effects.

Moreover, it can be seen that the Affine model cannot capture  $G_N$  of the star-shaped samples even without consideration of loops. However, in the case of the star-shaped chains their centers can be treated as cross-links, especially if all end-groups belong to different aggregates. An additional consideration of fixed chain centers leads to a better agreement with experimental data. On top of that, "phantom" factors ( $(f-2)/f$ ) of these chain centers certainly need to be considered to account for their fluctuations, which would, however, reduce the estimated plateau moduli thus worsening the agreement with the experimental data. It should be noted that the estimation is complicated by unknown fractions of polymer molecules whose ends are bridged to different associates. The somewhat too large experimentally determined plateau moduli of the star-polymers can be additionally explained by the fact that micelles can act as filler, similarly as in thermoplastic elastomers [148, 149].

As in the case of BIIR samples, the bond lifetimes for each sample were determined isothermally at the suitable temperature at which the terminal flow is well observed within

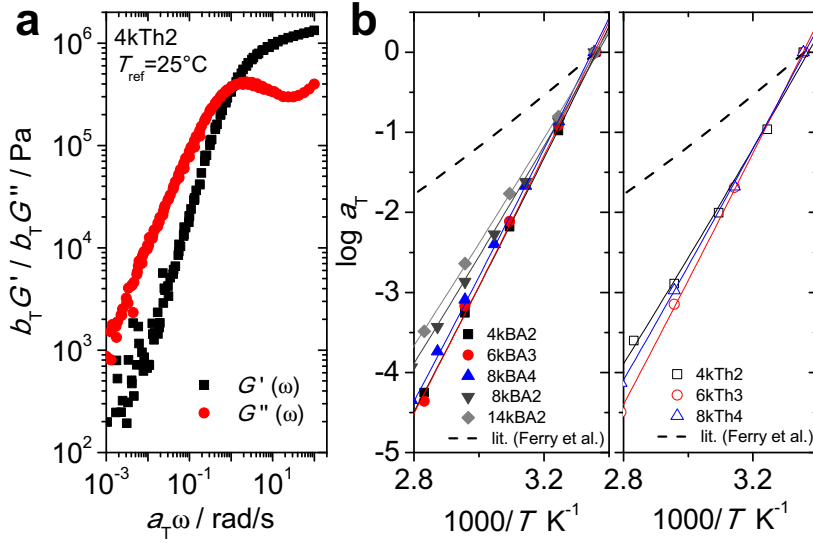


**Figure 9.10:** (a) Master curves of  $G'$  and  $G''$  for 4kTh2 reduced to  $T_{\text{ref}} = 25^\circ\text{C}$ . (b) Shift factors of BA- (left) and Th-functionalized (right) samples.

the studied frequency window, as shown in Fig. 9.8, and their temperature dependencies were taken from the horizontal shift factors. To access the shift factors, the master curve construction was carried out. The master curves of  $G'$  and  $G''$  exemplified for the case of 4kTh2 as well as the shift factors for all the samples can be seen in Fig. 9.10. Notably, although the resulting master curve of 4kTh2 looks smooth, pointing to the apparent fulfillment of the time-temperature superposition (TTS) principle, this is not the case and can be explained by the too narrow frequency window unable to cover segmental and sticky processes at the same time.

Similarly to the NMR results, the violation of TTS is reflected in enhanced slopes of the shift factors (large apparent activation energies) as compared to the shift factor of unmodified PIB. The shift factors data were analyzed again with the product of the Vogel-Fulcher and Arrhenius temperature dependencies to extract  $E_{a,\text{app}}$  (see Fig. 9.13 and Table B3). The vertical shifts were found to decay with temperature somewhat more strongly than the expected  $T_{\text{ref}}/T$  behavior, which can be related to the thermal expansion of the tool.

Furthermore, the effects of solvent or moisture residues and the reproducibility of the rheological results were studied. The effect of solvents is demonstrated in Fig. B8. It can be seen that an addition of chloroform or water has nearly no impact on rheological properties. The reproducibility was studied by comparison of results obtained in different labs. The reproducibility studies are important to show the consistency in the measurement procedure and plausibility of the observed trends. In Table B3 we compare  $G_N$ ,  $\tau_{\text{co}}$ , and  $E_{a,\text{app}}$  representing the most important structural and dynamic material characteristics. Reassuringly, all the parameters exhibit same trends across the samples' series, yet their absolute values can vary somewhat upon comparison of the results from

the different labs, which can be treated as systematic errors. In particular,  $G_N$  shows scattering of values within 30%,  $\tau_{co}$  values can differ by a factor of 2, and  $E_{a,app}$  exhibits a span of values within 10%. The indicated systematic errors can be explained by differences in experimental setups such as plates diameter, gap size, value of the axial force which become especially important because of low samples' amounts since temperature gradient and distribution of deformations and shear rates can be different in the used setups with parallel plates geometries.

## 9.4 Intra-aggregate dynamics by dielectric spectroscopy

To access local relaxation processes in the micellar cores, BDS was employed. The data were collected, analyzed, and interpreted by Kay Saalwächter, whereas I contributed to the interpretations and linked the observations with the other results. Firstly, the temperature dependence of the dielectric loss is compared at a frequency of 10 kHz. In Fig. 9.11, one can see that all samples exhibit two pronounced maxima at -10 and 70°C corresponding to the  $\alpha$  and intra-aggregate relaxations (IAR), respectively. Also, at low temperatures there can be distinguished another small maximum which can be ascribed to the local  $\beta$  relaxation. For comparison, the dielectric data of BIIR is shown. It can be seen that the maximum of the  $\alpha$  relaxation of BIIR is located at around the same temperature as the maxima of the PIB samples, which can be explained by close  $T_g$  values among the samples.

Further, it should be noted that the dielectric response is mainly contributed by the dipole moments sitting on the polar end-groups that are predominantly associated with the aggregates. Therefore, the segmental dynamics probed in such a way is affected by mobility gradients in the proximity of the chain ends and bond lifetimes distributions leading to broadening of the maxima. Analyzing the maximum of the IAR, one can notice that its position is nearly sample-independent, implying similar values of the related relaxation times. Interestingly, the high-temperature shoulder of the IAR maximum was found to be larger for older samples (see (b) part of Fig. 9.11), which means that introduction of conductive species could happen with aging. This certainly renders interpretation of conductivity and relaxation strength results intricate, and thus we refrain from their analysis.

To check whether the position of the IAR maximum can be affected by the introduced polar moieties, we compared the results of 8kBA2 in the pristine state with the results after addition of polar solvent (chloroform and water) in Fig. 9.11(c). It can be seen that the relaxation strength and conductivity increase upon addition of solvent, especially water boosts the observed conductivity, but the position of the maximum does not change which means that the introduced polar moieties merely serve diluted probes of their environment. This is in line with the rheological results above, thereby implying that the local IAR is connected to the long-range terminal process.

The dielectric data analysis was performed in analogy to the BIIR samples, see Section A.4.1 and Fig. B10 for details. In short, a combination of several Havriliak-Negami (up

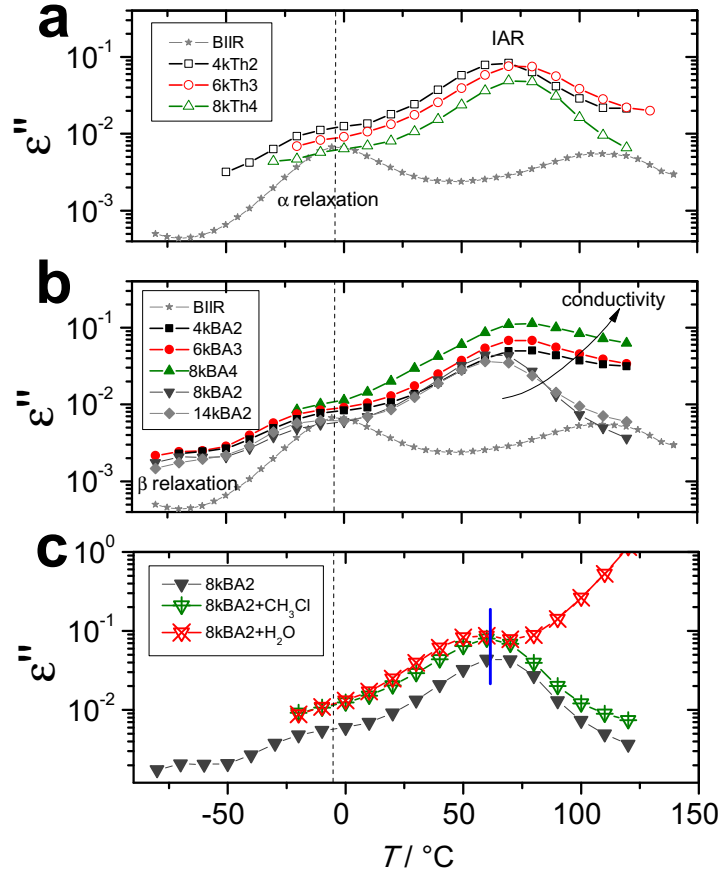


**Figure 9.11:** Temperature dependence of the imaginary part of the dielectric function  $\epsilon''$  measured at 10 kHz. (a) Th-functionalized samples. (b) BA-functionalized samples. BIIR data is given for comparison (scaled along y-axis for clarity). (c) Effect of the solvent addition on the example of 8kBA2 sample.

to three) functions and, at high temperatures, also the power-law conductivity term was used to extract all the relevant relaxation times. The Barton-Nakajima-Namikawa (BNN) correlation showed that the long-range processes possess the same activation energy (Fig. B11). However, as mentioned above, the time scales of the long-range processes are to a significant degree affected by the minor conductive moieties got into the samples with aging and therefore are not discussed further. Notably, the IAR process was not found to correlate with the conductivity trends, which implies that the extraction of  $\tau_{\text{IAR}}$  was reliable. Moreover, in all cases, except for 14kBA2, it was not possible to separate the IAR and  $\alpha$  processes because of the broad distribution of relaxation times of the former process, reflected in low  $\gamma$  values.

In Fig. 9.12 we present the comparison of time scales obtained from BDS, rheology, and NMR.

Firstly, it can be seen that  $\tau_{\alpha}$  of 14kBA2 lies lower than the expected values seen from the

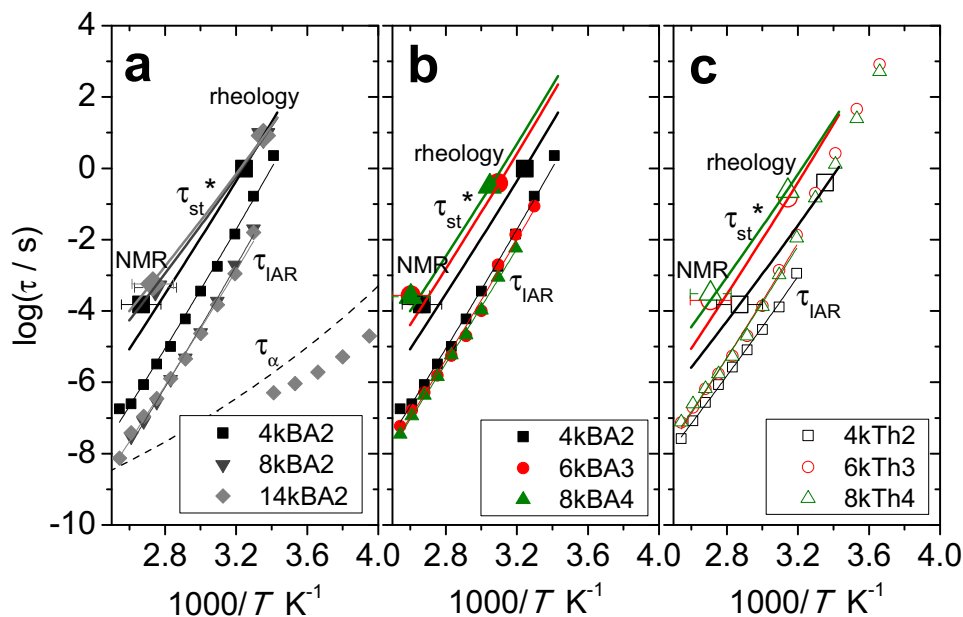


**Figure 9.12:** Relevant relaxation times extracted by dielectric spectroscopy, rheology, and NMR. (a) linear BA-functionalized samples, (b) and (c) BA- and Th-functionalized samples with different molecular architectures, respectively. The dashed line in (a) corresponds to the Vogel-Fulcher dependence of the segmental relaxation time of BIIR. The solid lines are the fits accounting for coupling of the segmental and sticky dynamics.

Vogel-Fulcher temperature dependence of BIIR. This can be explained by the mentioned difficulties in separation of the two neighboring relaxation processes and by the fact that the observed relaxation is mainly driven by fast dipole reorientations close to the micellar aggregates. On the other hand, the temperature dependence of  $\tau_\alpha$  of 14kBA2 is similar as for BIIR, which indicates that the local intra-aggregate dipole reorientations are coupled to the segmental dynamics of the surrounding "bath". Secondly, it can be seen that the relaxation times of the IAR process occupy the middle area of the relaxation maps, between the segmental and sticker exchange dynamics, similar to the situation in the ionic BIIR samples. Therefore, the end-group associates are again highly mobile internally.

The temperature dependencies of  $\tau_{\text{IAR}}$  were also analyzed with the product of the Vogel-Fulcher and Arrhenius terms to obtain values of  $E_{a,\text{app}}$ . All the values of  $E_{a,\text{app}}$  obtained by BDS, rheology, and NMR are compared in Fig. 9.13. It can be seen that despite potentially rather large systematic errors of about 30%, stemming from uncertainties in the extracted  $D_{\text{res}}(t_0)$  and  $\kappa$  values upon analysis of noisy low-intensity signals at high temperatures, NMR provides same trends as rheology across the whole samples' series.

Firstly comparing the samples with the same molecular weight between the chain ends, one can see that the BA-functionalized samples exhibit by around 10 kJ/mol larger activation energies than the samples functionalized with Th-moieties. Furthermore, there can be seen a molecular weight dependence of  $E_{a,\text{app}}$  for the BA-functionalized samples,

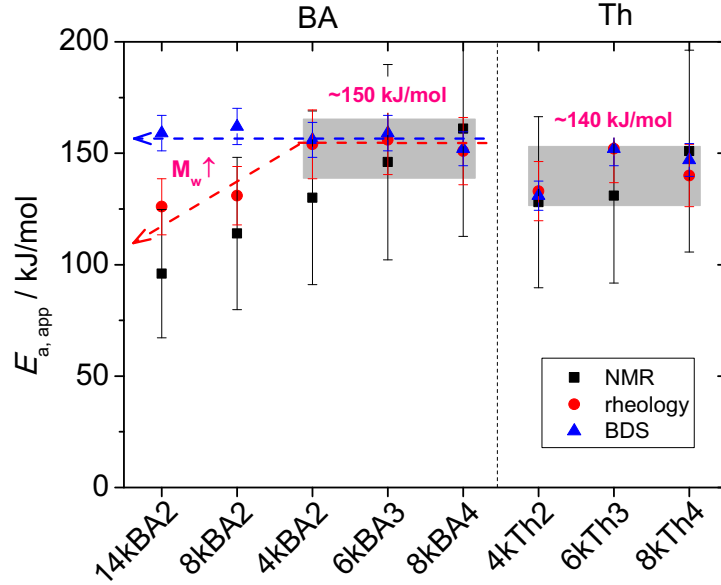


**Figure 9.13:** Apparent activation energies of the studied telechelic PIB samples accessed by dielectric spectroscopy, rheology, and NMR. The grey shaded boxes mark the values averaged over the three methods and the samples with the end-to-end chain molecular weight of 4 kDa. The dashed arrows emphasize the differences in molecular weight dependencies of apparent activation energies in BDS and rheology.

which was also reported before [124]. The reduction of  $E_{a,app}$  with the molecular weight can be caused by decrease of the volume fraction of the stickers contributing to dynamics, as was also observed in ionomers with different ionic contents [150]. Notably, BDS provides same  $E_{a,app}$  values as rheology for the samples with the molecular weight between chain ends of 4 kDa, whereas for the samples with higher molecular weights some deviations become apparent, namely,  $E_{a,app}$  accessed by BDS does not seem to depend on the molecular weight. This (i) implies that the sticky exchange dynamics is governed by the same processes occurring inside the micellar aggregates and (ii) fortifies the hypothesis that the relative contribution of the sticker dissociation to the overall transport of stickers through the material decreases with the increase of the molecular weight.

Let us now turn to the discussion of the time scales associated with dynamics of stickers ( $\tau_{IAR}$  and  $\tau_{st}^*$ ). In Fig. 9.12 it can be seen that both  $\tau_{IAR}$  and  $\tau_{st}^*$  are somewhat shorter in the case of the linear samples than for the star-shaped samples. Note that 4kBA2 is considered as an outlier with an especially prominent parasitic process seen in the BDS data, complicating the reliable determination of  $\tau_{IAR}$ . Also, the samples with different end-groups, but same architectures exhibit similar  $\tau_{IAR}$ . The mentioned observations cannot be explained in the context of Eq. 2.16 if to consider  $\tau_{IAR}$  as a bare bond lifetime, because according to Eq. 2.16  $E_{a,app}$  completely defines the dynamics. In other words, similar  $E_{a,app}$  values must lead to similar  $\tau_{IAR}$  values, and the increase of  $E_{a,app}$  must inevitably end up in the increase of  $\tau_{IAR}$ . Thus,  $\tau_{IAR}$  does not seem to be directly related

to the bare bond lifetime. Instead, the IAR process can be rather attributed to molecular reorientations inside the aggregates, as was also observed for the ionic BIIR samples. The similarities in  $\tau_{\text{IAR}}$  among the samples with different end-groups can be attributed to the similar molecular size of the used stickers, whereas the larger  $\tau_{\text{IAR}}$  values in the star-shaped samples as compared to the linear samples can be probably linked to larger aggregate sizes in the case of the star-shaped systems which increases the time for the dipole reorientations.

Finally, we discuss the effective bond lifetimes  $\tau_{\text{st}}^*$ . Notably, the values provided by rheology agree quantitatively with the values estimated by MQ NMR. This fortifies the notion that stress relaxation is governed by relaxation of single chains, thus disproving the model predictions given in refs 72 and 41, according to which stress relaxation is driven by macroscopic rearrangements of micelles involving numerous chain relaxation events.

It can be seen that  $\tau_{\text{st}}^*$  of the BA-functionalized samples are larger than these of the Th-functionalized samples, which can be primarily caused by larger  $E_{\text{a,app}}$  leading to the larger bare bond lifetime. Moreover, larger distances between the micellar aggregates observed by SAXS can result in the increase of the number of returns of the dissociated sticker back to the same aggregate, thereby increasing  $\tau_{\text{st}}^*$  [36, 40]. Also, weaker stickers can be expected to be more prone to hopping<sup>5</sup> dynamics which provides a more effective dynamic mechanism as compared to walking of stickers [145, 151].

Further, the probability of hopping reduces with the number of stickers per molecule [145] which can explain the increase of  $\tau_{\text{st}}^*$  with the number of arms. Additionally, as was alluded to in the MQ NMR results, the increase of  $\tau_{\text{st}}^*$  with the number of arms can be attributed to enhancement of motional confinement: for the linear samples, dissociation of a single sticker leads to its significant motional freedom, whereas a less probable simultaneous dissociation of two or three stickers is required in the case of the 3-arm and 4-arm-star samples, respectively, to achieve comparable motional freedom. For the linear BA-functionalized samples, there can be seen an increase of  $\tau_{\text{st}}^*$  with the molecular weight related to the increase of the diffusion time as the intra-aggregate distance increases.

## 9.5 Summary

In this chapter, we performed a systematic study of structural and dynamic properties of telechelic PIBs of various molecular architecture forming networks of interconnected micelles via establishment of hydrogen bonding. First of all, the conclusions drawn for entangled ionic elastomers in Chapter 8, regarding (i) the quantitative agreement of the effective bond lifetimes and activation energies provided by NMR and rheology as well as (ii) inability of dielectric spectroscopy to access the bare bond lifetime, could be applied for the given systems too. Consequently, following the conclusion (i), we can generalize

---

<sup>5</sup>”Hopping” corresponds to simultaneous dissociation of all stickers of the molecule and their diffusion to new aggregates, whereas ”walking” means independent diffusion of individual stickers [145]

that rheology is sensitive to whole-chain relaxation in any supramolecular polymer system, and the theoretical treatment by Semenov and Rubinstein [41, 72] predicting much more protracted macroscopic micellar rearrangements does not apply in the studied cases. Also, as suggested by conclusion (ii), dielectric spectroscopy applied to supramolecular systems with low concentration of stickers in general cannot pinpoint the bond lifetime of a single opening event, but is rather sensitive to intra-aggregate motions. These exhibit the same activation energy as the supramolecular dissociation, but do not reflect its time scale.

Further, more specific results related to peculiarities of the studied systems were obtained. Firstly, we confirmed the expectation that star-shaped molecules can form more stable networks comparing to their linear counterparts as a result of more constrained network chains leading to more confined motions of stickers. Secondly, we concluded that stickers based on barbituric acid providing more hydrogen bonds manifest larger activation energies, slowing down the overall sticky chain dynamics. Thirdly, based on SAXS-derived aggregation numbers, being in the range of 40-140, it was found that depending on the interplay of the chain molecular weight, molecular architecture, and stickers' nature, the fraction of looping and bridging chains can be varied, which in turn modulates the average distance between the micelles.

Star-shaped polymers were found to form more loops comparing to linear chains, and, consequently, feature larger average intermicellar distances. In the case of the samples end-functionalized with barbituric acid, the number of loops was found to increase with the number of arms, which was attributed to geometrical reasons in the limit of energetically driven network formation. The non-trivial deviation from this trend observed for the samples modified with weaker thymine moieties, according to which the 4-arm-star-sample featured less loops than the 3-arm-star-sample, was ascribed to a possible energetic asymmetry and resulting overbalance of the entropic term as compared to the enthalpic term [145], which led to a higher probability of bridging in the 4-arm-star-sample. However, this conclusion needs to be further validated by e.g. suitable MD simulations. Finally, despite the fact that all the studied systems consisted of short chains with the molecular weight not exceeding the critical molecular weight, trapped entanglements were needed to be involved to explain the overall plateau modulus.

## 10 Summary

In the given thesis, a new analytical approach, relying on MQ-NMR data, which can be used for quantitative dynamic studies of various complex polymer systems, was developed. To this end, the assumption of a power-law decay of the segmental orientation autocorrelation function over a limited time interval, along with the time-temperature superposition (TTS) principle, were applied. The power-law-decay assumption enabled isothermal extraction of effective bond lifetimes and anisotropy levels, whereas the TTS principle provided activation energies evaluated from obtained horizontal shift factors. The comprehensive tests were performed on different model cases, using metadata and reference samples, to adjust fitting procedure and quantify systematic errors. The use of the new approach expands a methodological toolbox for gaining mechanistic insights into structure and dynamics of complex supramolecular networks.

In total, four methods were employed for the thorough analysis, namely, SAXS, solid-state NMR, dielectric spectroscopy, and mechanic experiments, among which solid-state NMR and a number of mechanical experiments were conducted on my own, whereas results of the other methods were provided by courtesy of my supervisor, Prof. Dr. Kay Saalwächter, who obtained a range of data during his sabbatical stay at the Colby lab in spring 2018. SAXS experiments provided aggregation numbers and inter-aggregate distances. DMA/rheology and MQ NMR gave insights into network structure and sticky chain dynamics. Non-linear mechanic experiments shed light on network behavior in non-equilibrium conditions. Dielectric spectroscopy and MAS MQ NMR accessed internal dynamics inside the aggregates.

Two sets of samples were investigated: entangled ionic BIIR elastomers with tuned hydrophobicity of ionic side-groups (alkylimidazoliums) and telechelic PIBs in linear and star-architecture end-modified with hydrogen-bonding moieties of different strength (barbituric acid and thymine). All the samples were found to form sparsely arranged supramolecular aggregates with enhanced internal dynamics interconnected by nearly unperturbed Gaussian chains in a common network. As a result, no continuous layers of reduced mobility were formed around the aggregates. Also, nearly no free stickers were observed owing to large activation energies of sticker dissociation.

The BIIR samples, with around 20 stickers per aggregate, exhibited acceleration of sticky chain dynamics with increase of hydrophobicity of stickers (increase of the alkyl-group length) as a result of enhanced affinity with the polymer matrix. Activation energies were found to be in the range 88-113 kJ/mol, depending on the stickers' hydrophobicity. Further, it was found that under deformation in non-equilibrium conditions the BIIR networks respond in dependence on the relationship between the bond lifetime and the deformation rate. Interestingly, the effective bond lifetime decreases under action of accumulated internal stress, which can become practical in use for self-healing materials.

The PIB samples showed aggregation numbers depending on the interplay between molecular weight, molecular architecture, and association energy and varied between 40 and

140. The combination of the aforementioned parameters tunes the number of looping and bridging chains, which in turn modulates the intra-aggregate distance. Moreover, we validated that samples with more arms are more dynamically confined, due to more constrained networks and lower probability of hopping, which results in slower sticky dynamics. Also, it was found that stickers providing more hydrogen bonds expectedly possess larger apparent activation energies. Barbituric-acid stickers showed apparent activation energies of around 150 kJ/mol, whereas thymine-stickers were somewhat weaker with apparent activation energies of about 140 kJ/mol.

The correlation of MQ-NMR and rheological results in both samples' sets revealed for the first time that rheology is sensitive to sticky whole-chain relaxation, thereby dismissing the theoretical predictions of Semenov and Rubinstein on macroscopic micellar rearrangements [41, 72], but validating the sticky Rouse and sticky reptation theories [32, 77, 80, 81]. Additional insights obtained from dielectric spectroscopy results suggested that the central equation of the theory of sticky dynamics, linking the observed effective bond lifetime with a product of segmental relaxation time and thermodynamics of stickers also holds true, as both  $\alpha$  and sticky relaxations (inside and outside the aggregates) diverge approaching the glass transition temperature. Further, it was emphasized that one should not rely on master curve construction for comparison of dynamic time scales between the methods featuring different experimental time windows, since the breadth of a master-curve of a system exhibiting two activation processes with different temperature dependencies is a function of absolute temperature. Therefore, the choice of "switching temperature", at which the horizontal shift is switched from overlapping segmental relaxation features to overlapping sticky relaxation features, completely defines the outcome.

The previous notion that dielectric spectroscopy is able to provide a bond lifetime of a single opening event [32, 36, 39, 40] was found to be erroneous in systems with low concentration of stickers. This was possible owing to the studied sets of samples differing with sticker moieties. According to the predictions of sticky theories, the difference in thermodynamics among the samples should be reflected in the single and effective bond lifetimes in the same way. However, in the case of ionic BIIR sample series, the intra-aggregate relaxation exhibited an inverse trend as compared to the effective bond lifetimes extracted by MQ-NMR and rheology. In the case of telechelic PIB samples, effective bond lifetimes of the barbituric-acid-modified samples were one order of magnitude larger comparing to the thymine-modified samples, contradicted by similar intra-aggregate relaxation times among the samples. Thus, the intra-aggregate relaxation can be rather attributed to intra-aggregate reorientations of stickers dependent on the sticker size.

Moreover, it was found that the intra-aggregate relaxation exhibits a rather similar activation energy as sticker dissociation, suggesting that reorientation of a sticker is a prerequisite for breaking of supramolecular bonds. Since a bare bond lifetime remains intangible and the current state-of-the-art theoretical treatment largely pertains to the case of pairwise associations, it was not possible to estimate more subtle mechanistic de-

---

tails such as number of returns of a dissociated sticker to an old aggregate before hopping to a neighboring one. Thus, further work on this issue represents a suitable direction for future mechanistic studies.



# Appendices

## A Experimental Details

SAXS, dielectric spectroscopy, and a part of the rheology results were collected and provided by courtesy of my supervisor Prof. Dr. Kay Saalwächter during his sabbatical stay at Penn State University, State College, PA, USA, in 2018.

### A.1 SAXS measurements

The temperature-variable SAXS measurements were carried out on Xenocs Xeuss 2.0 setup with a Pilatus detector in virtual detection mode with a weighted azimuthal averaging in the temperature range from 25 up to 140°C. Before the measurements, the samples were annealed at 140°C for 24 hours.

### A.2 Solid-state NMR experiments

**BIIR samples.** The low-resolution, time-domain NMR experiments were conducted on Bruker Minispec mq20 benchtop spectrometers operating at Larmor frequency of 20 MHz ( $B_0 = 0.47$  T) with 90° and 180° pulses of 1.6 or 2.8 and 3.3 or 5.2  $\mu$ s and a dead time of 14 or 12  $\mu$ s, respectively. For the measurements, the samples in the form of  $\varnothing$ 8 mm discs were placed into 10 mm o.d. NMR tubes which were filled with argon and flame-sealed to prevent degradation. The high-resolution NMR experiments were carried out on a Bruker Avance III spectrometer ( $B_0 = 9.4$  T) with the triple resonance 4 mm magic-angle-spinning (MAS) probe. The samples were put inside sealable Kel-F inserts which were then brought into a ZrO<sub>2</sub> rotor closed by a Vespel cap. In this case, the 90° pulse was set to 3  $\mu$ s, and a 180° pulse to twice this value. The MAS frequency was 10 kHz. To isolate the imidazolium signals from the overlapping aliphatic signals of much larger intensity, the latter were considered as a baseline in a narrow spectral range around the imidazolium signals and subsequently subtracted. The acquired NMR spectra were referenced by setting a methyl signal to the known value of the chemical shift determined by solution-state NMR. For all the NMR experiments, the experimental temperature was varied by a Bruker BVT 3000 temperature control unit with an accuracy of around 1 K utilizing dry, pressurized air.

**PIB samples.** Due to rather small sample amounts, time-domain static solid-state NMR experiments were carried out on a Bruker Avance III spectrometer with an Oxford magnet at <sup>1</sup>H Larmor frequency of 200 MHz ( $B_0 = 4.7$  T) using a static probe. 90° pulses were set to 2  $\mu$ s, 180° pulses were twice as long. Samples, placed in the flame-sealed NMR tubes filled with Argon, were always placed in the middle of the rf coil, where the  $B_1$  magnetic field irradiated by the transmitter is the most homogeneous. A temperature unit controller regulated the temperature of a sample with accuracy of 0.5 K using heated

## A EXPERIMENTAL DETAILS

---

pressurized air.

**Table A1:** The 32-step phase cycle needed to select the pathway of the DQ pulse sequence shown in Fig. 4.4

Step	$\Delta\Phi$	$-\Delta p \times \Delta\Phi$		$\Phi_r$	$-\Delta p \times \Phi_r$		$\Phi_{\text{rec}}$
		$2\Delta\Phi(\text{DQ})$	$0^\circ(\text{ref})$		$\Phi_r$	DQ	ref
magnetization along z:							
1	0°	0°	0°	0°	0°	0°	0°
2	90°	180°	0°	0°	0°	180°	0°
3	180°	0°	0°	0°	0°	0°	0°
4	270°	180°	0°	0°	0°	180°	0°
5	0°	0°	0°	90°	90°	90°	90°
6	90°	180°	0°	90°	90°	270°	90°
7	180°	0°	0°	90°	90°	90°	90°
8	270°	180°	0°	90°	90°	270°	90°
9	0°	0°	0°	180°	180°	180°	180°
10	90°	180°	0°	180°	180°	0°	180°
11	180°	0°	0°	180°	180°	180°	180°
12	270°	180°	0°	180°	180°	0°	180°
13	0°	0°	0°	270°	270°	270°	270°
14	90°	180°	0°	270°	270°	90°	270°
15	180°	0°	0°	270°	270°	270°	270°
16	270°	180°	0°	270°	270°	90°	270°
magnetization along -z:							
17	0°	0°	0°	0°	0°	180°	180°
18	90°	180°	0°	0°	0°	0°	0°
19	180°	0°	0°	0°	0°	180°	180°
20	270°	180°	0°	0°	0°	0°	0°
21	0°	0°	0°	90°	90°	270°	270°
22	90°	180°	0°	90°	90°	90°	90°
23	180°	0°	0°	90°	90°	270°	270°
24	270°	180°	0°	90°	90°	90°	90°
25	0°	0°	0°	180°	180°	0°	0°
26	90°	180°	0°	180°	180°	180°	180°
27	180°	0°	0°	180°	180°	0°	0°
28	270°	180°	0°	180°	180°	180°	180°
29	0°	0°	0°	270°	270°	90°	90°
30	90°	180°	0°	270°	270°	270°	270°
31	180°	0°	0°	270°	270°	90°	90°
32	270°	180°	0°	270°	270°	270°	270°

A.2 Solid-state NMR experiments

**Table A2:** A new time-efficient phase cycling organization of the DQ pulse sequence

Step	$-\Delta p \times \Delta \Phi$		$\Phi_r$	$-\Delta p \times \Phi_r$	$\Phi_{rec}$	
	$2\Delta\Phi(\text{DQ})$	$0^\circ(\text{ref})$		$\Phi_r$	DQ	ref*
$\Delta\Phi = 0^\circ$						
1	$0^\circ$	$0^\circ$	$0^\circ$	$0^\circ$	$0^\circ$	$0^\circ$
2	$0^\circ$	$0^\circ$	$90^\circ$	$90^\circ$	$90^\circ$	$90^\circ$
3	$0^\circ$	$0^\circ$	$180^\circ$	$180^\circ$	$180^\circ$	$180^\circ$
4	$0^\circ$	$0^\circ$	$270^\circ$	$270^\circ$	$270^\circ$	$270^\circ$
5	$0^\circ$	$0^\circ$	$0^\circ$	$0^\circ$	$180^\circ$	$180^\circ$
6	$0^\circ$	$0^\circ$	$90^\circ$	$90^\circ$	$270^\circ$	$270^\circ$
7	$0^\circ$	$0^\circ$	$180^\circ$	$180^\circ$	$0^\circ$	$0^\circ$
8	$0^\circ$	$0^\circ$	$270^\circ$	$270^\circ$	$90^\circ$	$90^\circ$
$\Delta\Phi = 90^\circ$						
1	$180^\circ$	$0^\circ$	$0^\circ$	$0^\circ$	$180^\circ$	$0^\circ$
2	$180^\circ$	$0^\circ$	$90^\circ$	$90^\circ$	$270^\circ$	$90^\circ$
3	$180^\circ$	$0^\circ$	$180^\circ$	$180^\circ$	$0^\circ$	$180^\circ$
4	$180^\circ$	$0^\circ$	$270^\circ$	$270^\circ$	$90^\circ$	$270^\circ$
5	$180^\circ$	$0^\circ$	$0^\circ$	$0^\circ$	$0^\circ$	$180^\circ$
6	$180^\circ$	$0^\circ$	$90^\circ$	$90^\circ$	$90^\circ$	$270^\circ$
7	$180^\circ$	$0^\circ$	$180^\circ$	$180^\circ$	$180^\circ$	$0^\circ$
8	$180^\circ$	$0^\circ$	$270^\circ$	$270^\circ$	$270^\circ$	$90^\circ$
$\Delta\Phi = 180^\circ$						
1	$0^\circ$	$0^\circ$	$0^\circ$	$0^\circ$	$0^\circ$	$0^\circ$
2	$0^\circ$	$0^\circ$	$90^\circ$	$90^\circ$	$90^\circ$	$90^\circ$
3	$0^\circ$	$0^\circ$	$180^\circ$	$180^\circ$	$180^\circ$	$180^\circ$
4	$0^\circ$	$0^\circ$	$270^\circ$	$270^\circ$	$270^\circ$	$270^\circ$
5	$0^\circ$	$0^\circ$	$0^\circ$	$0^\circ$	$180^\circ$	$180^\circ$
6	$0^\circ$	$0^\circ$	$90^\circ$	$90^\circ$	$270^\circ$	$270^\circ$
7	$0^\circ$	$0^\circ$	$180^\circ$	$180^\circ$	$0^\circ$	$0^\circ$
8	$0^\circ$	$0^\circ$	$270^\circ$	$270^\circ$	$90^\circ$	$90^\circ$
$\Delta\Phi = 270^\circ$						
1	$180^\circ$	$0^\circ$	$0^\circ$	$0^\circ$	$180^\circ$	$0^\circ$
2	$180^\circ$	$0^\circ$	$90^\circ$	$90^\circ$	$270^\circ$	$90^\circ$
3	$180^\circ$	$0^\circ$	$180^\circ$	$180^\circ$	$0^\circ$	$180^\circ$
4	$180^\circ$	$0^\circ$	$270^\circ$	$270^\circ$	$90^\circ$	$270^\circ$
5	$180^\circ$	$0^\circ$	$0^\circ$	$0^\circ$	$0^\circ$	$180^\circ$
6	$180^\circ$	$0^\circ$	$90^\circ$	$90^\circ$	$90^\circ$	$270^\circ$
7	$180^\circ$	$0^\circ$	$180^\circ$	$180^\circ$	$180^\circ$	$0^\circ$
8	$180^\circ$	$0^\circ$	$270^\circ$	$270^\circ$	$270^\circ$	$90^\circ$

\* acquisition always done with the receiver set to the reference phase

### A.3 Mechanical experiments

**BIIR samples.** Dynamic mechanical analysis (DMA) was performed on the DMA Q800 instrument. The frequency sweeps were done from 0.3 until 30 Hz within the temperature range between -50 and 140°C with a 5°C step. At each temperature the samples were equilibrated for 3 minutes. All dynamic measurements were carried out in the linear viscoelastic region, which was determined from stress-strain curves. The master curve construction was conducted with the  $\tan \delta$  data sets to obtain the horizontal shift factors. The storage and loss moduli ( $E'$  and  $E''$ , respectively) at different temperatures were then corrected by multiplication with the entropic factor  $T_{\text{ref}}/T$  ( $T_{\text{ref}}$  is the reference temperature), after which vertical shift factors  $b_T$  were additionally applied to obtain a data overlap at different temperatures.

Tensile experiments in the linear and non-linear viscoelastic regimes were done on the Instron 5565 tensile tester with a 100 N load cell at room temperature. The specimens were prepared in the form of rectangles with 4 or 5 mm width,  $\sim 1$  mm thickness and  $\sim 20$  mm length. The changes in length were monitored using the video extensometer. The cyclic uniaxial stress-strain experiments were performed with loading/unloading cycles in four steps: until 50, 100, 150, and 200% strains, at the initial strain rate ( $\dot{\epsilon}$ ) of 0.02 s<sup>-1</sup>. The stress relaxation experiments were conducted at  $\dot{\epsilon} = 0.1$  s<sup>-1</sup>.

Auxiliary rheology measurements were performed on an Ares LS rheometer equipped with a convection oven using  $N_2$  gas. The measurements were conducted in the linear regime (shear strain was set to 1%) on punched sample discs with a diameter of 8 mm adapted according to the diameter of the used parallel plates with a gap of about 0.8 mm, defined by the thickness of the sample sheet. To achieve a good contact with the plates, samples were pre-conditioned in the tool at 140°C for 5-10 min under an initial normal force of 500 g applied for a short time and then reduced to 20 g for most of the time. Master curve construction was carried out with  $\tan \delta$  to obtain visually smooth curves after which vertical shifting was applied to loss and storage moduli for a good overlap. The temperature variation was accomplished starting from 140°C and then cooling down to 25°C.

**PIB samples.** Rheology measurements were performed on an Ares LS rheometer with a convection oven using  $N_2$  gas. Before the measurements, samples were dried for several days at 80°C under vacuum. The measurements were done in the linear regime (shear strain was set to 3%, while the shear thinning was only observed above 10%) with parallel plates with a diameter of 3 mm and a gap of about 1 mm. To establish complete filling of the gap, spherical pieces of samples were pre-pressed in the tool for a short time at 100°C, which was above the softening temperatures for all samples. Master curve construction was carried out with  $\tan \delta$  to obtain visually smooth curves after which vertical shifting was applied to loss and storage moduli for a good overlap. Temperature variation was performed starting from 120°C and then cooling down to 25°C.

## A.4 Broadband dielectric spectroscopy (DS)

The dielectric function of the samples was measured between 0.1 and  $10^6$  Hz at temperatures ranging from  $-50$  to  $+140^\circ\text{C}$  using a Novocontrol Alpha broadband dielectric analyzer equipped with a Quatro cryosystem employing evaporated liquid  $\text{N}_2$  as a cooling and heating agent, with a temperature stability of around 0.2 K. In the case of BIIR samples, disc-shaped specimens of about 16 mm diameter, punched from ca. 1 mm thick rubber sheets and dried in a vacuum oven at  $70^\circ\text{C}$  for several days, were press-molded for ca. 30 min. at  $140^\circ\text{C}$  between disc-shaped polished brass electrodes (upper electrode diameter of 15 mm), placing 3 Teflon spacers of 3 mm diameter in three smaller punched holes to ensure a final capacitor spacing of 0.75 mm. BIIR+BI was available only in the form of 2 mm sheets, which required rescaling of the timescale of the electrode polarization process by  $0.75/2$  to compare with the other results [134]. In the case of telechelic PIB samples, 20-50 mg of the sample material was brought between two brass electrodes (the diameter of the upper electrode was 10-15 mm) inside a Teflon washer, 0.25 mm thick and 6-9 mm wide, serving as a spacer. To enable a good contact between the sample and electrodes, a weight was additionally placed on top after which the whole assembly was annealed in a vacuum oven at  $100^\circ\text{C}$  for ca. 1 h. Details on the data analysis are presented below.

### A.4.1 Analysis of dielectric spectra

The dielectric spectra manifest themselves as an overlap of several relaxation processes involving segmental ( $\alpha$ ) and intra-aggregate relaxations (IAR), rather weak relaxation related to impurities or inhomogeneities of supramolecular aggregates (IAR'), electrode polarization (EP), and a conductivity contribution. The first four processes can be described by the Havriliak-Negami function of the form  $\epsilon^*(\omega) = \Delta\epsilon/(1 + (i\omega\tau)^\beta)^\gamma$ , while the conductivity contribution is  $\epsilon''(\omega) = (\sigma_0/\epsilon_0)\omega^{-1}$  ( $\epsilon_0$ : the vacuum permittivity). Depending on the experimental temperature, different relaxation processes were detectable within the studied frequency range, see Fig. 8.13(a). At low temperatures, the segmental and intra-aggregate relaxations could be observed, whereas upon temperature elevation the segmental relaxation shifted out of the probed frequency range, and EP, IAR' as well as conductivity contributions emerged instead. As a result, at each temperature up to three HN functions needed to be used and at high temperatures the conductivity-related power-law term was additionally required to describe the dielectric data. To stabilize the fits, the storage  $\epsilon'$  and loss  $\epsilon''$  components of the complex permittivity [134] were fitted simultaneously. In most of the cases, the asymmetry parameter  $\gamma$  was close to unity and therefore held fixed. Note that in the case of the BIIR samples IAR' was not well discernible due to its small relaxation strength. Instead, it was addressed by setting the power law of the conductivity component as a free parameter, which enabled a better capture of the  $\epsilon''$  minimum. To access the EP process, hidden by the dominant conductivity contribution, according to the Kramers-Kronig relations the derivative quantity  $\epsilon''_{\text{deriv}}(\omega) = -(\pi/2)(\partial\epsilon'(\omega)/\partial\ln\omega)$ , exempted from the conductivity term, can be analyzed instead [152]. The fits were firstly performed on  $\epsilon''_{\text{deriv}}$  providing the HN

parameters that were set subsequently fixed for the full fits on  $\epsilon''$  including additionally the conductivity term. Note that the analytical form of the HN function for  $\epsilon''_{\text{deriv}}$  differs from that for  $\epsilon''$ . However, the difference becomes negligible for  $\beta < 1$ , so that the same analytical representations can be used [152].

## B Supplementary results

### B.1 Supplementary SAXS results

**Table B1:** The SAXS-determined structural parameters of the investigated ionic BIIR samples

Sample	T °C	$q_{\max}$ 1/Å	$I(q_{\max})$	$f$	$f_{\text{eff}}^{\text{a}}$	$R_1$ Å	$\sigma$	$R_2$ Å	$\rho$ g/cm <sup>3</sup>	$M_{\text{AI}}$ g/mol	$AN$
BIIR+MI	25	0.110	0.105	0.163	0.019	12.2	0.10	24.9	1.03	161.9	29
	60	0.112	0.098	0.156	0.019	12.0	0.15	24.1	1.00		27
	100	0.118	0.089	0.156	0.021	11.6	0.10	22.7	0.96		23
	140	0.120	0.089	0.162	0.017	10.9	0	22.9	0.93		19
BIIR+BI	25	0.095	0.071	0.121	0.017	13.8	0.19	26.4	0.95	203.9	31
	60	0.101	0.064	0.115	0.018	13.1	0.22	24.3	0.92		26
	100	0.107	0.061	0.143	0.017	11.6	0	23.7	0.89		17
	140	0.112	0.058	0.115	0.014	11.7	0.07	23.6	0.86		17
BIIR+HI	25	0.111	0.066	0.145	0.030	13.6	0.10	22.8	0.95	231.9	25
BIIR+NI	25	0.110	0.064	0.114	0.016	11.7	0.10	22.6	0.95 <sup>b</sup>	273.9	13

<sup>a</sup>  $f_{\text{eff}} = f \left( \frac{R_1}{R_2} \right)^3$ ,

<sup>b</sup> interpolated from densities of octyl- and decylimidazoles taken in ref 128.

As can be seen in Table B1, the volume fractions of hard spheres and of the ionic cores ( $f_{\text{eff}}$ ) do not change with the length of the alkyl group or temperature. Taking into account that the average distance between ionic aggregates is similar in all the samples, this finding implies that (i) aggregation numbers should be also similar, and (ii) the number of free, unbound ionic groups does not change with temperature. Indeed, the aggregation numbers are rather similar among the samples. However, at the same time, the aggregation numbers are seen to decrease with temperature and also BIIR+NI exhibits a two times smaller aggregation number as compared to the other samples at 25°C. This deviation from the expected trend of unchanging aggregation numbers predominantly originates from changes in  $R_1$ , the only Perkus-Yevick parameter entering Eq. 8.2, and can be explained by the dynamic nature of the ionic aggregates. Upon decrease of the ionic bond strength which occurs either with temperature or with the length of the alkyl group, the ionic groups can increasingly gain spatial freedom, but still stay in the vicinity of the ionic cores, which, subsequently, leads to the apparent decrease of  $R_1$  (and  $AN$ ) seen by SAXS. On the other hand, BIIR+MI and BIIR+BI show similar  $AN$  values within a 115°C range, although their bond lifetimes are undoubtedly different. This means that ionic groups of BIIR+BI, more mobile than the ones of BIIR+MI, stay close

to the ionic aggregates. Further, the distribution of sizes of ionic aggregates was found to be low and invariant to experimental temperature in all the samples.

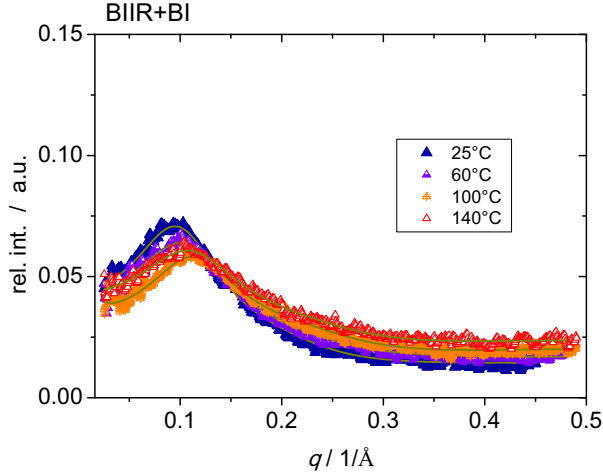


**Figure B1:** Temperature-dependent SAXS data of BIIR+BI. The solid lines are the fits according to the Perkus-Yevick model [122–124]. Reprinted with permission from [76]. Copyright 2019 American Chemical Society.

## B.2 Supplementary NMR results

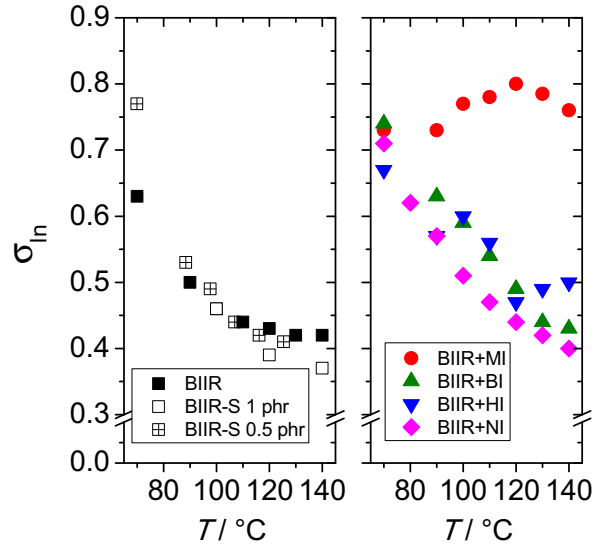


**Figure B2:** Results of  $I_{nDQ}$  build-up analysis under static conditions estimating the heterogeneity of the studied networks in the form of  $\sigma_{ln}$ . The left panel summarizes the non-ionic samples and the right panel ionic BIIR networks. Reprinted with permission from [76]. Copyright 2019 American Chemical Society.

In Figure B2,  $\sigma_{ln}$ , reflecting the structural and dynamic heterogeneity, is plotted as a function of temperature for all the samples. In the left panel, one can see that the non-

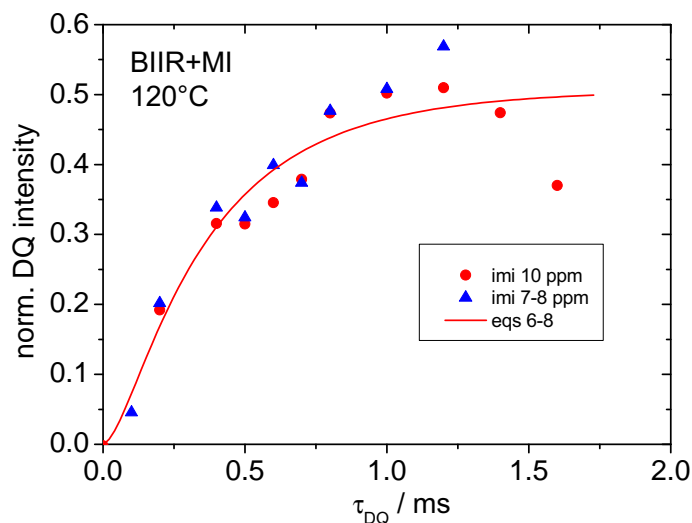


**Figure B3:** The  $I_{nDQ}$  build-ups of imidazole signals at 7-8 and  $\sim 10$  ppm on the example of BIIR+MI at  $120^\circ\text{C}$ . The red line indicates the fits assuming the log-normal distribution of  $D_{res}$ . Reprinted with permission from [76]. Copyright 2019 American Chemical Society.

ionic samples have almost the same large  $\sigma_{ln}$  which decrease with temperature. This can be explained by the presence of intermediate dynamics (chain motions within the tube, relaxation of defects originating from inseparable signals of dangling chains and loops), which causes stretching of the  $I_{nDQ}$  signals and in turn apparent distribution of  $D_{med}/2\pi$ . In the right panel, one can observe a similar trend for the temperature dependency of  $\sigma_{ln}$  in the BIIR+BI/BI/NI samples, yet the overall level of the dynamic heterogeneity is higher than in the non-ionic samples, which can be ascribed to an additional dynamic heterogeneity brought by the sticky dynamics of ionic links and also to their random arrangement in polymer backbones (composition heterogeneity). In contrast to this trend of the temperature dependence of  $\sigma_{ln}$ , BIIR+MI exhibits a slight increase of the dynamic heterogeneity with temperature. Such persistently high level of the dynamic heterogeneity within the whole studied temperature range could be explained by a broader distribution of its bond lifetimes.

The MQ NMR data of the alkylimidazolium cross-links acquired by BaBa-xy16 were analyzed using the simultaneous fits to the power-law-model, as exemplified in Figure B4 for BIIR+MI at  $120^\circ\text{C}$ . Note that the BaBa-xy16 experiments were performed under MAS conditions which caused incomplete refocussing of the obtained DQ and MQ signals at odd multiples of the rotor period. This was not a problem for the  $I_{nDQ}$  signals due to the normalization of the intensity drops, but must be accounted for in this case by masking the corresponding data points (points in red). The extracted  $D_{res}(t_0)$  and  $\kappa$  values of alkylimidazolium signals of all the samples are specified in Table B2, the corresponding results of the network chains are also added for comparison.

The comparison of  $D_{res}(t_0)$  among the samples leads to the same conclusions that were ob-

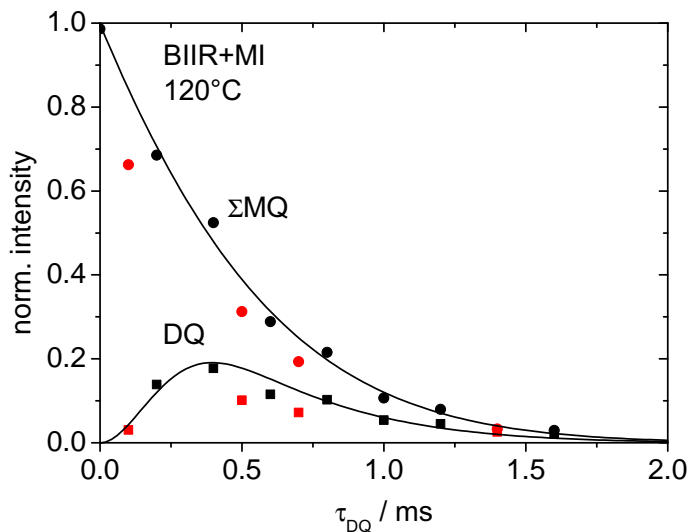


**Figure B4:** The DQ and MQ signals acquired with the BaBa-xy16 pulse sequence for BIIR+MI at 120°C. The solid lines are the power-law-model-based fits [52]. Some of the data points (in red) had to be masked to remove the effects of incomplete intensity refocussing at fractions of the rotor period. Reprinted with permission from [76]. Copyright 2019 American Chemical Society.

**Table B2:** Results of the power-law-model-based analysis of  $^1\text{H}$  MQ NMR data for ionic links and network chains

Sample	ionic links (alkylimidazoliums)				network chains			
	$D_{\text{res}}(t_0)/2\pi$ / Hz		$\kappa$		$D_{\text{res}}(t_0)/2\pi$ / Hz		$\kappa$	
	120°C	140°C	120°C	140°C	120°C	140°C	120°C	140°C
BIIR+MI	1069	521	0.07	0.10	280	228	0.16	0.20
BIIR+BI	312		0.07		267	223	0.20	0.22
BIIR+HI	215	142	0.04	0.16	271	223	0.27	0.30
BIIR+NI	192		0.07		242	206	0.25	0.26

tained from the analysis of the  $D_{\text{med}}$  values and, therefore, are not discussed here further. Again, a more interesting discussion offers the analysis of the  $\kappa$  values. One can see that the  $\kappa$  values of the alkylimidazoliums are lower than those of the network chains, which again evidences that the alkylimidazolium groups act as ionic cross-links. Considering that  $D_{\text{res}}(t_0)$  decreases quite strongly with temperature and  $\kappa$  stays low, indicating the fast limit dynamics and rendering it not possible to average  $D_{\text{res}}(t_0)$  by simple dynamics acceleration predicted by the TTS principle, we can conclude that averaging of  $D_{\text{res}}(t_0)$

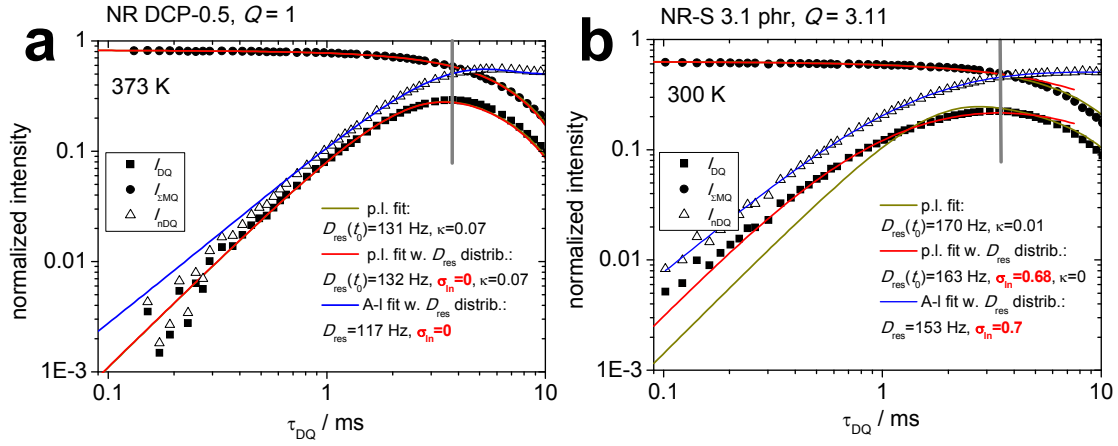


**Figure B5:** Comparison of performances of power-law-model-based fits with and without log-normal distribution of dipolar couplings on the example of MQ NMR data of homogeneous (a) and highly heterogeneous networks (b). Unswollen ( $Q = 1$ ) natural rubber (NR) cross-linked with dicumylperoxide (DCP) served as a homogeneous network, whereas swollen ( $Q = 3.11$ ) sulfur cross-linked NR represented a heterogeneous network. The fit results are given in the legends. For reference, quasi-static fits (Eq. 4.13) of  $I_{nDQ}$  data and their results are also presented.

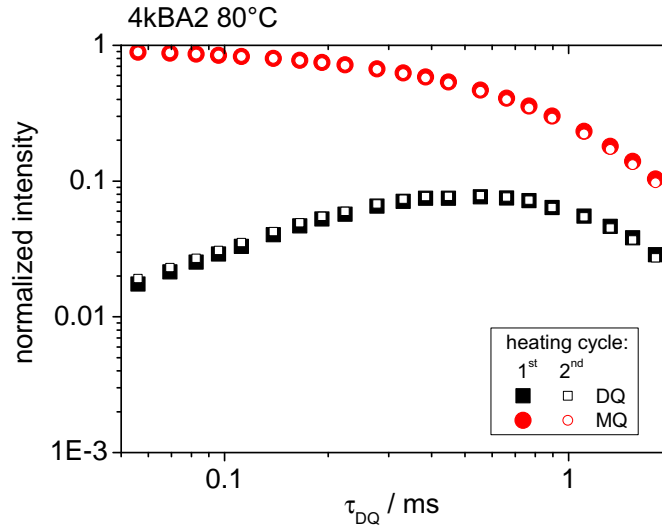


**Figure B6:** Overlapping MQ NMR data acquired during two heating cycles of 4kBA2 at 80°C.

is in this case predominantly driven by increase of the motional amplitude inside the ionic aggregates. This is corroborated by the increase of dielectric relaxation strengths of intra-aggregate relaxation with temperature as seen in Fig. B9(a).

### B.3 Supplementary mechanical results (DMA, rheology)

#### B.3.1 Influence of the used frequency window on the bond lifetime extracted from a master curve.

In Fig. B7, metadata for the loss modulus  $E''(\omega)$  generated for the sum of two relaxation processes (segmental and sticky) assuming the validity of the Maxwell model are presented. The analytical form of the data reads:

$$E''(\omega) = \Delta E_{\text{segm}} \frac{\tau_{\text{segm}}(T)\omega}{1 + (\tau_{\text{segm}}(T)\omega)^2} + \Delta E_{\text{st}} \frac{\tau_{\text{st}}^*(T)\omega}{1 + (\tau_{\text{st}}^*(T)\omega)^2}, \quad (\text{B.1})$$

where  $\Delta E_{\text{segm}}$  and  $\Delta E_{\text{st}}$  are the relaxation strengths for segmental and sticky processes,  $\tau_{\text{segm}}(T)$  and  $\tau_{\text{st}}^*(T)$  are the segmental and sticky relaxation times, respectively.

The temperature dependencies of the two relaxation times were assumed to be Arrhenius-like, with the values at 293 K being equal to  $10^{-5}$  and 100 s and activation energies ( $E_{\text{a,segm}}$  and  $E_{\text{a,app}}$ ) to 50 and 100 kJ/mol for segmental and sticky process, respectively. In particular, the sticky process comprises contributions from the segmental and sticky dynamics, as predicted by Eq. 2.16, and, therefore, its activation energy is an apparent quantity  $E_{\text{a,app}} = E_{\text{a,segm}} + E_{\text{a,st}}$ , with  $E_{\text{a,st}}$  being an activation energy of the ionic dissociation.

In Fig. B7(a), the  $E''(\omega)$  maxima are seen to shift towards larger frequencies with temperature as a result of temperature dependencies of the corresponding relaxation times. It can be seen that the maximum of the sticky process shifts more strongly than the maximum of the segmental process, because its temperature dependence additionally includes the sticky dynamics contribution. As a result, the shape of  $E''(\omega)$  curves changes with temperature (see Fig. B7(b), where the frequency scale is normalized with  $\tau_{\text{segm}}$  for clarity), and, namely, the breadth becomes narrower. This leads to an apparent violation of the time-temperature superposition (TTS) principle and to the fact that the master curve's shape is a function of an absolute temperature. Assuming that the data are available on the full frequency scale such that both relaxation processes are observed, one has a choice to shift the data with respect to either the segmental or sticky process [153], the corresponding shift factors are presented in Fig. B7(f) as dashed lines. In reality, however, the probed frequency scale is experimentally restricted to 5-6 orders of magnitude in the best case, which can make one of the two processes invisible depending on the experimental temperature and the time scales separation. As a result, one ends up firstly shifting with respect to the higher frequency process and then switches to the lower frequency process when it becomes detectable at higher temperatures.

Provided the experimental frequency window is narrow (1-2 orders of magnitude), the TTS can even appear to be fulfilled, indicating a rheologically simple behavior, which is actually not the case [32, 150, 154]. In the cases when the sticky process is still not detectable at the chosen  $T_{\text{ref}}$ , a sticky bond lifetime determined via the master curve analysis will be underestimated by a factor of  $a_{\text{T st}}^{T_{\text{switch}}} / a_{\text{T segm}}^{T_{\text{switch}}}$ , where  $a_{\text{T segm}}^{T_{\text{switch}}}$  and  $a_{\text{T st}}^{T_{\text{switch}}}$  are the shift factors for the relaxation times  $\tau_{\text{segm}}$  and  $\tau_{\text{st}}^*$ , respectively, taken at  $T_{\text{switch}}$ ,

### B.3 Supplementary mechanical results (DMA, rheology)

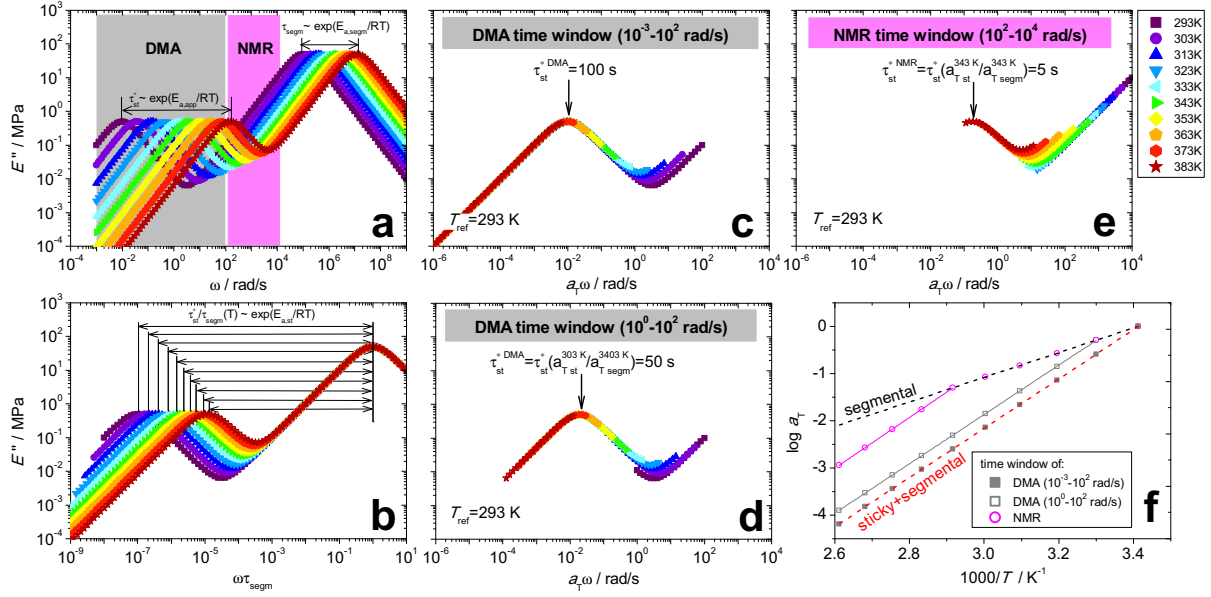


**Figure B7:** Metadata for the loss modulus  $E''(\omega)$  generated for the sum of two relaxation processes (segmental and sticky) assuming the validity of the Maxwell model. (a)  $E''(\omega)$  data at different temperatures. The temperature dependencies of the segmental and sticky relaxation times are marked with arrows. The shaded boxes indicate time windows used in the DMA and NMR analyses. (b)  $E''(\omega)$  data at different temperatures with a frequency scale normalized by a segmental relaxation time, thereby emphasizing the temperature dependence of separation of the two relaxation processes. (c), (d), and (e)  $E''(\omega)$  data from (a) displayed within DMA or NMR time windows, respectively, shifted with respect to the sticky process once it becomes observed. The resulting apparent sticky bond lifetimes reduced due to this shifting procedure are specified. (f) The obtained shift factors for the used DMA and NMR time windows. The dashed lines correspond to the segmental (black) and the sum of segmental and sticky (red) shift factors. The solid lines indicate Arrhenius fits yielding  $E_{a,\text{app}} = 100$  kJ/mol.

being the switching temperature beyond which the shifting is done with respect to the sticky process.

Fig. B7(c), (d), and (e) exemplify a master curve construction using different experimental frequency windows. In (c) and (d), the total frequency range typically attainable on DMA/rheology machines and the DMA frequency range used in this work are considered (0.001-100 and 1-100 rad/s, respectively), whereas in (e) the frequency window of NMR (100-10000 rad/s) is taken for comparison. Admittedly, one never uses such high frequencies for rheological measurements, but here it was done merely as the proof of concept. One can see that (i) only by accessing low frequencies in (c) it is possible to shift with respect to the sticky process starting directly from  $T_{\text{ref}}$ , in (d) and (e), in turn, the sticky process is still not well developed at  $T_{\text{ref}}$  to be considered for shifting, which directly shows that the choice of the frequency range affects the shape of the resulting master curve; (ii) the NMR frequency window detects the sticky process at much higher temperatures than the DMA frequency window, which leads to a more pronounced underestimation of

the sticky bond lifetime (factor of 20 vs 2 for DMA) and a more delayed observation of the sticky shift factor.

Thus, the above analysis shows that for an exact determination of sticky bond lifetimes by DMA/rheology one should construct master curves of sticky polymeric systems with caution, paying especial attention to the choice of such  $T_{\text{ref}}$  at which the sticky process is well developed. If, however, two methods sensitive to different time windows are used and the same  $T_{\text{ref}}$  is chosen, the method with the higher frequency window would inevitably give a lower sticky bond lifetime. Further, to disclose the segmental contribution of the activation energy hidden in the sticky process, one needs to either use a frequency window wide enough to cover both segmental and sticky processes to perform two mastering procedures [153] or an already known segmental shift factor in the studied temperature range.

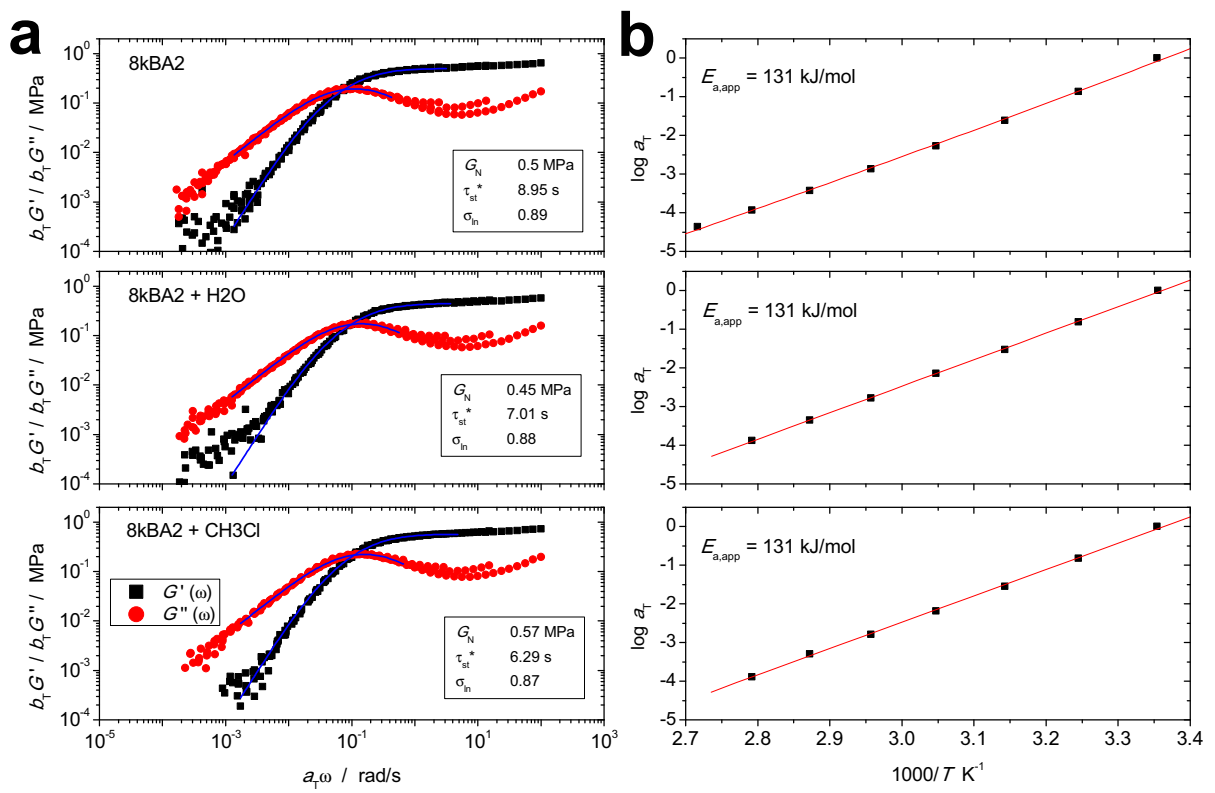


**Figure B8:** (a) Master curves of  $G'$  and  $G''$  for 8kBA2 in the pristine state and after addition of water or chloroform. (b) Corresponding shift factors.

## B SUPPLEMENTARY RESULTS

**Table B3:** Comparison of rheological results obtained in different labs

Sample	$G_N(25^\circ\text{C}) / \text{MPa}$			$\tau_{\text{co}}(25^\circ\text{C}) / \text{s}$			$E_{\text{a,app}} / \text{kJ/mol}$		
	TTA <sup>a</sup>	Binder <sup>b</sup>	Colby <sup>c</sup>	TTA	Binder	Colby	TTA	Binder	Colby
4kTh2		1.10	1.12		1	1		142	133
6kTh3		1.47	1.94		14	22		140	152
8kTh4		0.91	1.17		14	20		133	140
4kBA2	1.02	0.44	0.90	28	16	31	171	161	154
6kBA3		0.90	1.15		173	167		144	156
8kBA4		1.07	1.42		262	262		140	151
8kBA2	0.69		0.53	34		13.2	149		131
14kBA2	0.32		0.47	28		12	139		126

<sup>a</sup> Thurn-Albrecht lab, experiments conducted by Dr. Tingzi Yan

<sup>b</sup> Binder lab, experiments conducted by Dr. Diana Döhler

<sup>c</sup> Colby lab, experiments conducted by Prof. Dr. Kay Saalwächter

**Table B4:** Comparison of the crossover time ( $\tau_{\text{co}}$  in s) with the arithmetic mean value of the lognormal distribution of bond lifetimes ( $\langle \tau_{\text{st}}^* \rangle$  in s)

Sample	$\tau_{\text{st}}^*$	$\sigma_{\ln}$	$\langle \tau_{\text{st}}^* \rangle^{\text{a}}$	$\tau_{\text{co}}$
4kTh2	0.43	1.2	0.9	0.83
6kTh3	6.13	1.63	23.1	22
8kTh4	9.83	1.19	20	20
4kBA2	8.8	1.63	33.2	31.3
6kBA3	49.6	1.52	157.5	167
8kBA4	70.1	1.63	264.6	262
8kBA2	8.95	0.89	13.3	13.2
14kBA2	7.67	0.95	12	12

$$^{\text{a}} \langle \tau_{\text{st}}^* \rangle = \exp(\ln \tau_{\text{st}}^* + \sigma^2/2)$$

## B.4 Supplementary dielectric spectroscopy results

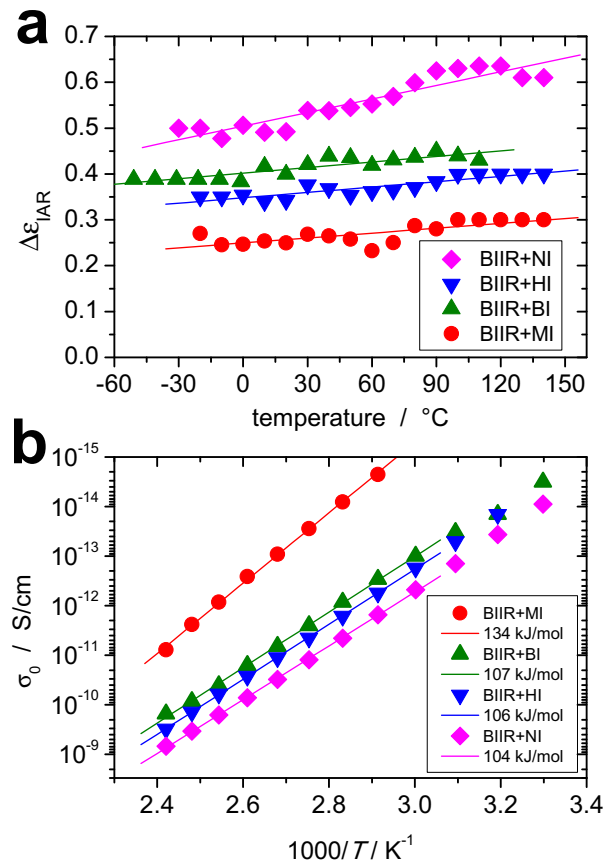


**Figure B9:** (a) Relaxation strengths of the intra-aggregate relaxation in the ionic BIIR samples as a function of temperature. (b) Arrhenius plot of the conductivity. Note the inverted y-axis for a better comparison with  $\tau_{\text{EP}}$  in Fig. 8.13(b).

## B SUPPLEMENTARY RESULTS

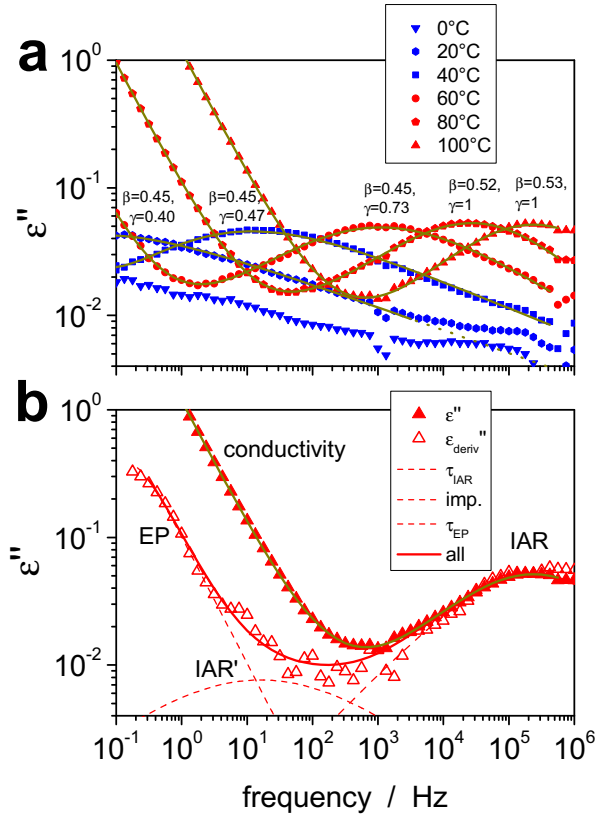


**Figure B10:** (a) Frequency sweeps of the imaginary part of the dielectric function of 6kTh3 at indicated temperatures.(b) Analysis of the dielectric loss data at 100°C exhibiting several relaxation process such as intra-aggregate relaxation (IAR), impurities- or -inhomogeneities-related relaxation (IAR'), electrode polarization (EP), and conductivity.

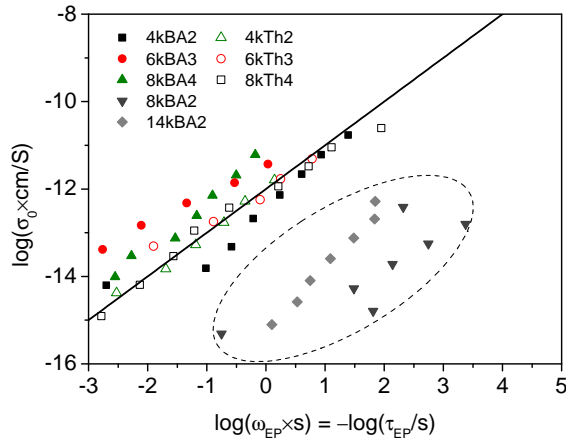


**Figure B11:** Barton-Nakajima-Namikawa (BNN) plot correlating the conductivity  $\sigma_0$  and the relaxation time of the electrode polarization  $\tau_{EP}$ . The solid line indicates a slope of 1. The dashed area encompasses the results for 8kBA2 and 14kBA2 for which  $\tau_{EP}$  was too long and could not be reliably detected, and  $\tau_{IAR'}$  was used for the correlation instead.

## B.5 Influence of free, unbound alkyimidazoles on dynamic properties. Data reproducibility

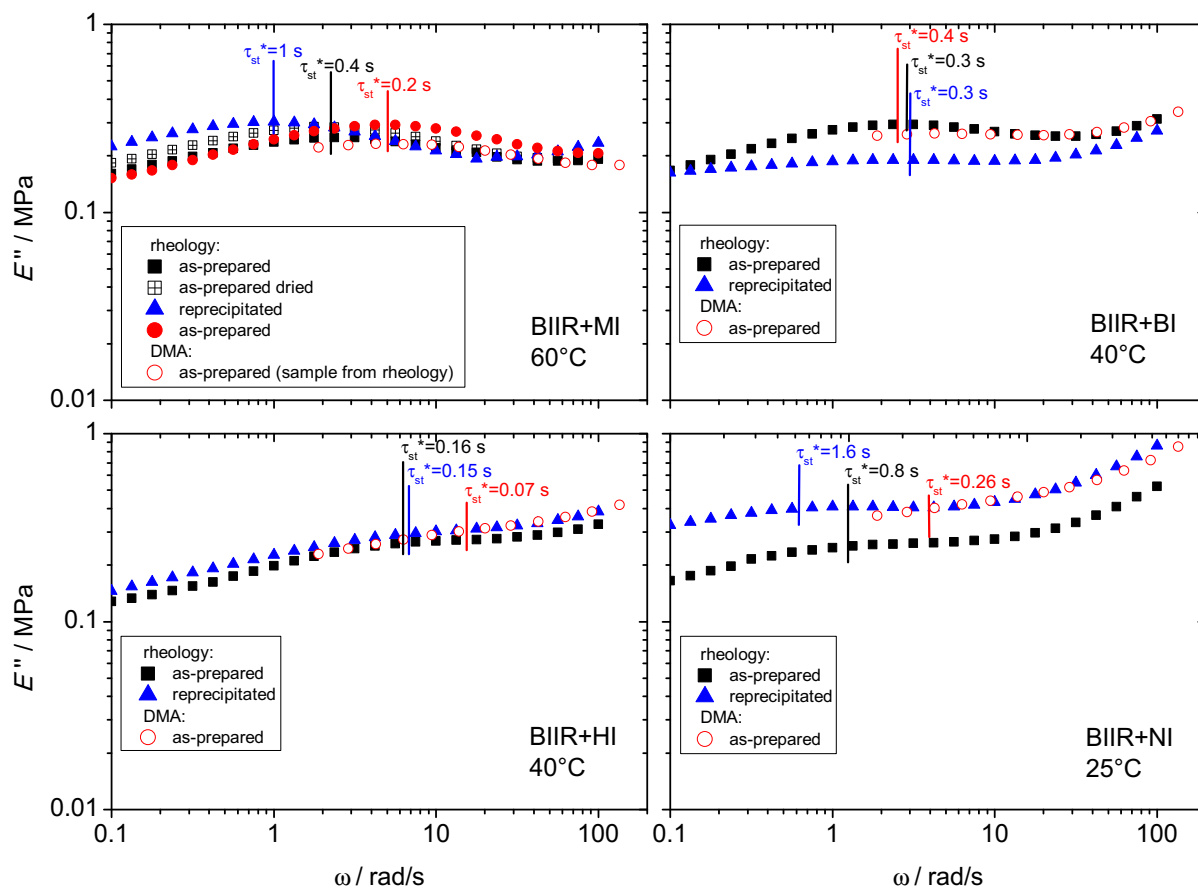


**Figure B12:** Frequency sweeps of the loss modulus in the range of the ionic peak for ionic networks conducted (i) on different devices (rheology and DMA) and (ii) for different samples to examine the device and sample-to-sample reproducibility as well as the influence of free, unbound alkyimidazoles and moisture on dynamic properties. Rheological shear moduli were multiplied by a factor of three to compare with the DMA's results on the absolute y-scale. The experimental temperatures and extracted bond lifetimes are indicated. The latter were determined by means of Eq. 8.6 (not shown for clarity).

Since some measurements were performed with free, unbound alkyimidazoles left in the samples due to their excess with respect to the reactive groups, whereas the others were conducted after the removal of free alkyimidazoles by reprecipitation, it is important to show the effect of free alkyimidazoles on the dynamic properties ( $\tau_{st}^*$ ). Fig. B12 demonstrates this effect on the mechanical data and at the same time shows the reproducibility of the data as to the measurements on different devices and samples' batches. As can be seen for BIIR+MI, the data obtained from rheological and DMA measurements (solid and open red circles, respectively), which were performed on the same sample batch, exhibit the same bond lifetimes. This enables the direct comparison of the rheological

## B SUPPLEMENTARY RESULTS

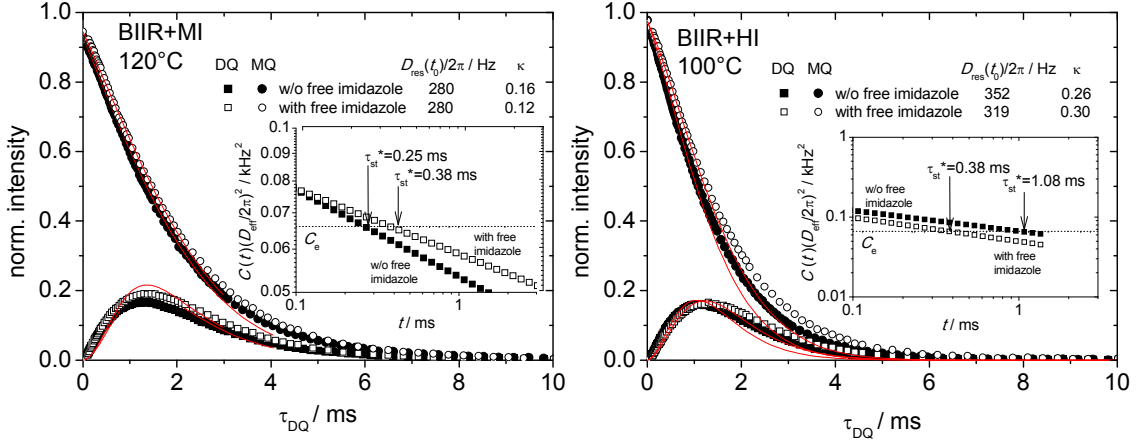


**Figure B13:** MQ NMR data of BIIR+MI (left) and BIIR+HI (right) at indicated temperatures. The red lines represent power-law-model fits (Eqs. 5.6 and 5.7). The insets show  $C(t)$  decays constructed out of the fit results with extracted bond lifetimes indicated.

and DMA data for the other samples too. Some deviations in the magnitudes of  $E''$  from rheology and DMA can be explained by errors in measurements of dimensions of prepared specimens and by differences in the attachment of the specimens in the tools (contact with the tool).

The next comparison pertains to the effect of moisture again on the example of BIIR+MI. Both dried and as-prepared samples exhibit the same bond lifetimes, which indicates that water molecules do not change the relevant dynamics in the ionic aggregates. Finally, a comparison of samples with and without free alkyimidazoles across the series of ionic networks allows us to conclude that the effect of free alkyimidazoles on the bond lifetime is marginal: only for BIIR+MI and BIIR+NI the difference in the bond lifetimes of the corresponding samples reaches a factor of two at most, which can be rather ascribed to a batch-to-batch reproducibility issue.

To fortify the statement that free alkyimidazoles have no impact on dynamic properties of the ionic networks, MQ NMR measurements were carried out on samples of BIIR+MI and BIIR+HI with and without free alkyimidazoles at the temperatures at which their  $C(t)$  cross the level of entanglements  $C_e$  within the applied fit intervals, so that their bond lifetimes can be directly determined (see Fig. B13). In Fig. B13 it can be seen that the removal of free alkyimidazoles causes opposite effects on the bond lifetime, and, namely, the bond lifetime decreases in the case of BIIR+MI by around 30% and increases in the case of BIIR+HI by a factor of three. The opposite effects and also the fact that the effects differ from the ones found in the mechanical data above imply that free alkyimidazoles do not affect dynamic properties of the ionic networks, and the differences between the samples arise from the batch-to-batch reproducibility issues.

## References

- [1] R. B. Seymour and H. F. Mark, editor. *Application of polymers*. Plenum Press, New York, 1988.
- [2] F. Mohammad, editor. *Specialty polymers: Materials and Applications*. International Publishing House Pvt. Ltd., New Delhi, 2007.
- [3] Accident and serious incident reports: Airworthiness. [https://www.skybrary.aero/index.php/Accident\\_and\\_Serious\\_Incident\\_Reports:\\_AW](https://www.skybrary.aero/index.php/Accident_and_Serious_Incident_Reports:_AW). Accessed: 13.05.2019.
- [4] B. Murphy, J. O’Callaghan, M. Fox, L. Ilcewicz, and J. H. Starnes Jr. Structural Analysis for the American Airlines Flight 587 Accident Investigation – Global Analysis. Technical Memo AIAA 2005-2254, NASA, 2005.
- [5] R. M. Jones. *Mechanics Of Composite Materials*. Taylor and Francis, Inc., New York, 1999.
- [6] J. Hale. Boeing 787 from the Ground Up. [https://www.boeing.com/commercial/aeromagazine/articles/qtr\\_4\\_06/AERO\\_Q406.pdf](https://www.boeing.com/commercial/aeromagazine/articles/qtr_4_06/AERO_Q406.pdf), 2006. Accessed: 14.05.2019.
- [7] J. R. Jambeck, R. Geyer, C. Wilcox, T. R. Siegler, M. Perryman, A. Andrady, R. Narayan, and K. L. Law. Plastic waste inputs from land into the ocean. *Science*, 347:768–771, 2015.
- [8] D. K. Schneiderman and M. A. Hillmyer. 50th Anniversary Perspective: There Is a Great Future in Sustainable Polymers. *Macromolecules*, 50:3733–3749, 2017.
- [9] R. A. Register and R. K. Prud’homme. Melt rheology. In M. R. Tant, K. A. Mauritz, and G. L. Wilkes, editors, *Ionomers: Synthesis, Structure, Properties and Applications*, pages 208–256. Blackie Academic & Professional, New York, USA, 1997.
- [10] L. Zhang, N.R. Brostowitz, K. A. Cavicchi, and R. A. Weiss. Perspective: Ionomer Research and Applications. *Macromol. React. Eng.*, 8:81–99, 2014.
- [11] M. Behl and A. Lendlein. Shape-memory polymers. *Mater. Today*, 10:20–29, 2007.
- [12] W. M. Huang, Z. Ding, C. C. Wang, J. Wei, Y. Zhao, and H. Purnawali. Shape-memory polymers. *Mater. Today*, 13:54–61, 2010.
- [13] J. Kumpfer and S. J. Rowan. Thermo-, Photo-, and Chemo-Responsive Shape-Memory Properties from Photo-Cross-Linked Metallo-Supramolecular Polymers. *J. Am. Chem. Soc.*, 133:12866–12874, 2011.

## REFERENCES

---

- [14] P. Zare, A. Stojanovic, F. Herbst, J. Akbarzadeh, H. Peterlik, and W. H. Binder. Hierarchally Nanostructured Polyisobutylene-based Ionic Liquids. *Macromolecules*, 45:2074–2084, 2012.
- [15] R. Long, K. Mayumi, C. Creton, T. Narita, and C.-U. Hui. Time Dependent Behavior of a Dual Cross-Link Self-Healing Gel: Theory and Experiments. *Macromolecules*, 47:7243–7250, 2014.
- [16] A. Das, A. Sallat, F. Böhme, M. Suckow, D. Basu, S. Wießner, K. W. Stöckelhuber, B. Voit, and G. Heinrich. Ionic Modification Turns Commercial Rubber into a Self-Healing Material. *ACS Appl. Mater. Interfaces*, 7:20623, 2015.
- [17] M. Suckow, A. Mordvinkin, M. Roy, N. K. Singha, G. Heinrich, B. Voit, K. Saalwächter, and F. Böhme. Tuning the Properties and Self-Healing Behavior of Ionically Modified Poly(isobutylene-*co*-isoprene) Rubber. *Macromolecules*, 51:468, 2018.
- [18] J. G. Poulakis and C. D. Papaspyrides. A model process for the recycling of a Surlyn<sup>®</sup> Ionomer. *Adv. Polym. Tech.*, 19:203, 2000.
- [19] T. Xavier, J. Samuel, and T. Kurian. Synthesis and Characterization of Novel Melt-Processable Ionomers based on Radiation Induced Styrene Grafted Natural Rubber. *Macromol. Mater. Eng.*, 286:507, 2001.
- [20] S. Bagrodia, G. L. Wilkes, and J. P. Kennedy. New Polyisobutylene-Based Model Elastomeric Ionomers: Rheological Behavior. *Polym. Eng. Sci.*, 26:662, 1986.
- [21] H. H. Tønnesen and J. Karlsen. Alginate in drug delivery systems. *Drug Dev. Ind. Pharm.*, 28:621–630, 2002.
- [22] Y. Bar-Cohen. Current and future developments in artificial muscles using electroactive polymers. *Expert Rev. Med. Devices*, 2:731–740, 2005.
- [23] Z. Ye, P. Hou, and Z. Chen. 2D maneuverable robotic fish propelled by multiple ionic polymer-metal composite artificial fins. *Int. J. Intell. Robot. Appl.*, 1:195–208, 2017.
- [24] Advances in Dielectric Elastomers for Actuators and Artificial Muscles. P. Brochu and Q. Pei. *Macromol. Rapid Commun.*, 31:10–36, 2010.
- [25] W. H. Binder, editor. *Self-Healing Polymers: From Principles to Applications*. Wiley-VCH, Weinheim, 2013.
- [26] M. D. Hager and S. v. d. Zwaag and U. S. Schubert, editor. *Self-healing Materials*. Springer, Switzerland, 2016.
- [27] D. B. Amabilino, D. K. Smith, and J. W. Steed. Supramolecular materials. *Chem. Soc. Rev.*, 46:2404–2420, 2017.

## REFERENCES

---

- [28] F. Herbst, K. Schröter, I. Gunkel, S. Gröger, T. Thurn-Albrecht, J. Balbach, and W. H. Binder. Aggregation and Chain Dynamics in Supramolecular Polymers by Dynamic Rheology: Cluster Formation and Self-Aggregation. *Macromolecules*, 43:10006–10016, 2010.
- [29] F. Herbst, S. Seiffert, and W. H. Binder. Dynamic Supramolecular poly(isobutylene)s for self-healing materials. *Polym. Chem.*, 3:3084–3092, 2012.
- [30] D. Döhler, H. Peterlik, and W. H. Binder. A dual crosslinked self-healing system: Supramolecular and covalent network formation of four-arm star polymers. *Polymer*, 69:264–273, 2015.
- [31] A. R. Brás, C. H. Hövelmann, W. Antonius, J. Teixeira, A. Radulescu, J. Allgaier, W. Pyckhout-Hintzen, A. Wischnewski, and D. Richter. Molecular Approach to Supramolecular Polymer Assembly by Small Angle Neutron Scattering. *Macromolecules*, 46:9446, 2013.
- [32] Q. Chen, G. J. Tudryn, and R. H. Colby. Ionomer dynamics and the sticky Rouse model. *J. Rheol.*, 57:1441, 2013.
- [33] A. Shabbir, I. Javakhishvili, S. Cervený, S. Hvilsted, A. Skov, O. Hassager, and N. J. Alvarez. Linear Viscoelastic and Dielectric Relaxation Response of Unentangled UPy-Based Supramolecular Networks. *Macromolecules*, 49:3899, 2016.
- [34] H. Goldansaz, C.-A. Fustin, M. Wübberhorst, and E. v. Ruymbeke. How Supramolecular Assemblies Control Dynamics of Associative Polymers: Toward a General Picture. *Macromolecules*, 49:3899, 2016.
- [35] B. Gold, C. H. Hövelmann, C. Weiss, A. Radulescu, J. Allgaier, W. Pyckhout-Hintzen, A. Wischnewski, and D. Richter. Sacrificial bonds enhance toughness of dual polybutadiene networks. *Polymer*, 87:123, 2016.
- [36] B. J. Gold, C. H. Hövelmann, N. Lühmann, N. K. Székely, W. Pyckhout-Hintzen, A. Wischnewski, and D. Richter. Importance of Compact Random Walks for the Rheology of Transient Networks. *ACP Macro Lett.*, 6:73, 2017.
- [37] W. J. MacKnight and T. R. Earnest. The Structure and Properties of Ionomers. *J. Polym. Sci: Macromol. Rev.*, 16:41, 1981.
- [38] F. Frenzel, M. Y. Folikumah, M. Schulz, A. M. Anton, W. H. Binder, and F. Kremer. Molecular Dynamics and Charge Transport in Polymeric Polyisobutylene-Based Ionic Liquids. *Macromolecules*, 49:2868, 2016.
- [39] M. Müller, U. Seidel, and R. Stadler. Influence of hydrogen bonding on the viscoelastic properties of thermoreversible networks: analysis of the local complex dynamics. *Polymer*, 36:3143, 1995.

## REFERENCES

---

- [40] E. B. Stukalin, L.-H. Cai, N. A. Kumar, L. Leibler, and M. Rubinstein. Self-Healing of Unentangled Polymer Networks with Reversible Bonds. *Macromolecules*, 46:7525, 2013.
- [41] N. Semenov and M. Rubinstein. Dynamics of Entangled Associating Polymers with Large Aggregates. *Macromolecules*, 35:4821–4837, 2002.
- [42] Y. Jia, A. Kleinhammes, and Y. Wu. NMR Study of Structure and Dynamics of Ionic Multiplets in Ethylene-Methacrylic Acid Ionomers. *Macromolecules*, 38:2781, 2005.
- [43] S. Nojiri, H. Yamada, S. Kimata, K. Ikeda, T. Senda, and A. W. Bosman. Supramolecular polypropylene with self-complementary hydrogen bonding system. *Polymer*, 87:308, 2016.
- [44] S. Chen, T. Yan, M. Fischer, A. Mordvinkin, K. Saalwächter, T. Thurn-Albrecht, and W. H. Binder. Opposing Phase-Segregation and Hydrogen-Bonding Forces in Supramolecular Polymers. *Angew. Chem. Int. Ed.*, 56:13016–13020, 2017.
- [45] A. Rapp, I. Schnell, D. Sebastiani, S. P. Brown, V. Percec, and H. W. Spiess. Supramolecular Assembly of Dendritic Polymers Elucidated by  $^1\text{H}$  and  $^{13}\text{C}$  Solid-State NMR Spectroscopy. *J. Am. Chem. Soc.*, 125:13284, 2003.
- [46] R. Zhang, T. Yan, B.-D. Lechner, K. Schröter, Y. Liang, B. Li, F. Furtado, P. Sun, and K. Saalwächter. Heterogeneity, Segmental and Hydrogen Bond Dynamics, and Aging of Supramolecular Self-Healing Rubber. *Macromolecules*, 46:1841–1850, 2013.
- [47] M. A. Malmierca, A. González-Jiménez, I. Mora-Barrantes, P. Posadas, A. Rodríguez, L. Ibarra, A. Nogales, K. Saalwächter, and J. L. Valentín. Characterization of Network Structure and Chain Dynamics of Elastomeric Ionomers by Means of  $^1\text{H}$  Low-Field NMR. *Macromolecules*, 47:5655–5667, 2014.
- [48] A. Dardin, R. Stadler, C. Boeffel, and H. W. Spiess. Molecular dynamics of new thermoplastic elastomers based on hydrogen bonding complexes: a deuteron nuclear magnetic resonance investigation. *Makromol. Chem.*, 194:3467, 1993.
- [49] D. J. Roach, S. Dou, R. H. Colby, and K. Mueller. Nuclear magnetic resonance investigation of dynamics in poly(ethylene oxide)-based lithium polyether-ester-sulfonate ionomers. *J. Chem. Phys.*, 136:014510, 2012.
- [50] M. R. Chierotti and R. Gobetto. Solid-state NMR studies of weak interactions in supramolecular systems. *Chem. Commun.*, pages 1621–1634, 2008.
- [51] M. Monkenbusch, M. Krutyeva, W. Pyckhout-Hintzen, W. Antonius, C. H. Hövelmann, J. Allgaier, A. Brás, B. Farago, A. Wischniewski, and D. Richter. Molecular View on Supramolecular Chain and Association Dynamics. *Phys. Rev. Lett.*, 117:147802, 2016.

## REFERENCES

---

- [52] (a) A. Mordvinkin and K. Saalwächter. Microscopic observation of the segmental orientation autocorrelation function for entangled and constraints polymer chains. *J. Chem. Phys.*, 146:094909, 2017; (b) A. Mordvinkin and K. Saalwächter. Erratum: "Microscopic observation of the segmental orientation autocorrelation function for entangled and constraints polymer chains" [*J. Chem. Phys.* 146, 094902 (2017)]. *J. Chem. Phys.*, 148:089901, 2018.
- [53] S. P. Brown, I. Schnell, J. D. Brand, K. Müllen, and H. W. Spiess. The competing effects of  $\pi$ - $\pi$  packing and hydrogen bonding in a hexabenzocoronene carboxylic acid derivative: A  $^1\text{H}$  solid-state MAS NMR investigation. *Phys. Chem. Chem. Phys.*, 2:1735, 2000.
- [54] P. J. Flory. *Statistical Mechanics of Chain Molecules*. Hanser Publishers, USA, 1989.
- [55] G. Strobl. *The Physics of Polymers: Concepts for Understanding Their Structures and Behavior*. Springer-Verlag, Berlin, 2007.
- [56] M. Rubinstein and R. H. Colby. *Polymer Physics*. Oxford University Press, New York, 2003.
- [57] M. Doi. *Soft Matter Physics*. Oxford University Press, Oxford, UK, 2013.
- [58] M. Doi and S. F. Edwards. *The Theory of Polymer Dynamics*. Oxford University Press, New York, 1986.
- [59] L. R. G. Treloar. *The Physics of Rubber Elasticity*. Clarendon Press, Oxford, UK, 2005.
- [60] S. F. Edwards and T. A. Vilgis. The effect of entanglement in rubber elasticity. *Polymer*, 27:483–492, 1986.
- [61] G. Heinrich, E. Straube, and G. Helmis. Rubber elasticity of polymer networks: Theories. *Adv. Polym. Sci.*, 85:33–87, 1988.
- [62] J. D. Davidson and N. Goulbourne. A nonaffine network model for elastomers undergoing finite deformations. *J. Mech. Phys. Solids*, 61:1784–1797, 2013.
- [63] J. Zhu and J. Luo. Effects of entanglements and finite extensibility of polymer chains on the mechanical behavior of hydrogels. *Acta Mech*, 229:1703–1719, 2018.
- [64] P.E. Rouse. A theory of the linear viscoelastic properties of dilute solutions of coiling polymers. *J. Chem. Phys.*, 21:1272–1280, 1953.
- [65] T. Dollase, R. Graf, A. Heuer, and H. W. Spiess. Local Order and Chain Dynamics in Molten Polymer Blocks Revealed by Proton Double-Quantum NMR. *Macromolecules*, 34:298–309, 2001.

## REFERENCES

---

- [66] M.-L. Trutschel, A. Mordvinkin, F. Furtado, L. Willner, and K. Saalwächter. Time-Domain NMR Observation of Entangled Polymer Dynamics: Focus on All Tube-Model Regimes, Chain Center, and Matrix Effects. *Macromolecules*, 51:4108, 2018.
- [67] Y. Ding and A. P. Sokolov. Breakdown of Time-Temperature Superposition Principle and Universality of Chain Dynamics in Polymers. *Macromolecules*, 39:3322–3326, 2006.
- [68] D. G. Fesko and N. W. Tschoegl. Time-temperature superposition in thermorheologically complex materials. *J. Polym. Sci. C*, 35:51–69, 1971.
- [69] A. Herrmann, V. N. Novikov, and E. A. Rössler. Dipolar and Bond Vector Correlation Function of Linear Polymers Revealed by Field Cycling  $^1\text{H}$  NMR: Crossover from Rouse to Entanglement Regime. *Macromolecules*, 42:2063–2068, 2009.
- [70] C. Liu, J. He, E. v. Ruymbeke, R. Keunings, and C. Bailly. Evaluation of different methods for the determination of the plateau modulus and the entanglement molecular weight. *Polymer*, 47:4461–4479, 2006.
- [71] J. W. Steed and D. R. Turner and K. J. Wallace. *Core Concepts in Supramolecular Chemistry and Nanochemistry*. John Wiley and Sons, Ltd, Chippingham, 2007.
- [72] A. N. Semenov, J.-F. Joanny, and A.R. Khokhlov. Associating Polymers: Equilibrium and Linear Viscoelasticity. *Macromolecules*, 28:1066–1075, 1995.
- [73] P. G. de Gennes. Reptation of a Polymer Chain in the Presence of Fixed Obstacles. *J. Chem. Phys.*, 55:572–579, 1971.
- [74] R. C. Ball, P. T. Callaghan, and E. T. Samulski. A simplified approach to the interpretation of nuclear spin correlations in entangled polymeric liquids. *J. Chem. Phys.*, 106:7352–7361, 1997.
- [75] J. Roovers. Estimation of the contribution of tube renewal in the terminal relaxation of linear polybutadiene. *Polymer*, 30:2174–2179, 1989.
- [76] A. Mordvinkin, M. Suckow, F. Böhme, R. H. Colby, C. Creton, and K. Saalwächter. Hierarchical Sticker and Sticky Chain Dynamics in Self-Healing Butyl Rubber Ionomers. *Macromolecules*, 52:4169–4184, 2019.
- [77] L. Leibler, M. Rubinstein, and R. Colby. Dynamics of reversible networks. *Macromolecules*, 24:4701–4707, 1991.
- [78] M. Ahmadi, L. G. D. Hawke, H. Goldansaz, and E. v. Ruymbeke. Dynamics of Entangled Linear Supramolecular Chains with Sticky Side Groups: Influence of Hindered Fluctuations. *Macromolecules*, 48:7300–7310, 2015.

## REFERENCES

---

- [79] M. J. Mateyisi, J.-U. Sommer, K. K. Müller-Nedebock, and G. Heinrich. Influence of weak reversible cross-linkers on entangled polymer melt dynamics. *J. Chem. Phys.*, 148:244901, 2018.
- [80] Q. Chen, Z. Zhang, and R. H. Colby. Viscoelasticity of entangled random polystyrene ionomers. *J. Rheol.*, 60:1031, 2016.
- [81] R. H. Colby, X. Zheng, J. Sokolov M. H. Rafailovich, D. G. Peiffer, S. A. Schwarz, Y. Strzhemechny, and D. Nguyen. Dynamics of Lightly Sulfonated Polystyrene Ionomers. *Phys. Rev. Lett.*, 81:3876, 1998.
- [82] R.S. Hoy and G. H. Fredrickson. Thermoreversible associating polymer networks. I. Interplay of thermodynamics, chemical kinetics, and polymer physics. *J. Chem. Phys.*, 131:224902, 2009.
- [83] F. A. Bovey and P. A. Mirau. *NMR of Polymers*. Acad. Press, San Diego, Calif., 1996.
- [84] M. H. Levitt. *Spin dynamics: basics of nuclear magnetic resonance*. John Wiley and Sons, Chichester, England, 2008.
- [85] K. Schmidt-Rohr and H. W. Spiess, editors. *Multidimensional Solid-State NMR and Polymers*. Academic Press, London, 1994.
- [86] M. J. Duer. *Solid-state NMR Spectroscopy: principles and applications*. Blackwell Science, Oxford, 2002.
- [87] S. Matsui. Multiple-quantum NMR on structure, orientation, morphology and dynamics of polymers, biomolecules and ordered tissues. *Chem. Phys. Lett.*, 179:187–190, 1991.
- [88] R. Fechete, D. E. Demco, and B. Blümich. Chain orientation and slow dynamics in elastomers by mixed magic-Hahn echo decays. *J. Chem. Phys.*, 118:2411–2421, 2003.
- [89] K. Schäler, M. Roos, P. Micke, Y. Golitsyn, A. Seidlitz, T. Thurn-Albrecht, H. Schneider, G. Hempel, and K. Saalwächter. Basic principles of static proton low-resolution spin diffusion NMR in nanophase-separated materials with mobility contrast. *Solid State Nucl. Magn. Reson.*, 72:50–63, 2015.
- [90] A. Maus, C. Hertlein, and K. Saalwächter. A Robust Proton NMR Method to Investigate Hard/Soft Ratios, Crystallinity, and Component Mobility in Polymers. *Macromol. Chem. Phys.*, 207:1150–1158, 2006.
- [91] M. Mauri, Y. Thomann, H. Schneider, and K. Saalwächter. Spin-diffusion NMR at low field for the study of multiphase solids. *Solid State Nucl. Magn. Reson.*, 34:125–141, 2008.

## REFERENCES

---

- [92] R. Bärenwald, Y. Champouret, K. Saalwächter, and K. Schäler. Determination of Chain Flip Rates in Poly(ethylene) Crystallites by Solid-State Low-Field  $^1\text{H}$  NMR for Two Different Sample Morphologies. *J. Phys. Chem. B*, 116:13089–13097, 2012.
- [93] K. Schäler, A. Achilles, R. Bärenwald, C. Hackel, and K. Saalwächter. Dynamics in Crystallites of Poly( $\epsilon$ -caprolactone) As Investigated by Solid-State NMR. *Macromolecules*, 46:7818–7825, 2013.
- [94] K. Schäler, E. Ostas, K. Schröter, T. Thurn-Albrecht, W. H. Binder, and K. Saalwächter. Influence of Chain Topology on Polymer Dynamics and Crystallization. Investigation of Linear and Cyclic Poly( $\epsilon$ -caprolactone)s by  $^1\text{H}$  Solid-State NMR Methods. *Macromolecules*, 44:2743–2754, 2011.
- [95] K. Saalwächter. Microstructure and molecular dynamics of elastomers as studied by advanced low-resolution nuclear magnetic resonance methods. *Rubber Chem. Technol.*, 85:350–386, 2012.
- [96] A. Eisenberg, B. Hird, and R. B. Moore. A New Multiplet-Cluster Model for the Morphology of Random Ionomers. *Macromolecules*, 23:4098, 1990.
- [97] J.-S. Kim and A. Eisenberg. Ion aggregation and its effect on ionomer properties. In S. Schlick, editor, *Ionomers: Characterization, Theory, and Applications*, pages 7–31. CRC Press, Boca Raton, USA, 1996.
- [98] K. Saalwächter. Proton multiple-quantum NMR for the study of chain dynamics and structural constraints in polymeric soft materials. *Prog. NMR Spectrosc.*, 51:1–35, 2007.
- [99] K. Saalwächter. Multiple-Quantum NMR Studies of Anisotropic Polymer Chain Dynamics. In Webb G., editor, *Modern Magnetic Resonance*. Springer, Cham, 20167.
- [100] K. Saalwächter. Robust NMR Approaches for the Determination of Homonuclear Dipole-Dipole Coupling Constants in Studies of Solid Materials and Biomolecules. *ChemPhysChem*, 14:3000, 2013.
- [101] K. Saalwächter, F. Lange, K. Matyjaszewski, C. F. Huang, and R. Graf. BaBa-xy16: Robust and broadband homonuclear DQ recoupling for applications in rigid and soft solids up to the highest MAS frequencies. *J. Magn. Reson.*, 212:204, 2011.
- [102] R. R. Ernst, G. Bodenhausen, and A. Wokaun. *Principles of Nuclear Magnetic Resonance in One and Two Dimensions*. Clarendon Press, Oxford, 1987.
- [103] J. Keeler. *Understanding NMR spectroscopy*. Wiley, Chichester, England, 2010.
- [104] M. Levitt and R. Freeman. NMR Population Inversion Using a Composite Pulse. *J. Magn. Reson.*, 33:473–476, 1979.

## REFERENCES

---

- [105] J. Baum and A. Pines. NMR Studies of Clustering in Solids. *J. Am. Chem. Soc.*, 108:7447–7454, 1986.
- [106] P.W. Anderson and P. R. Weiss. Exchange Narrowing in Paramagnetic Resonance. *Rev. Mod. Phys.*, 25:269–276, 1953.
- [107] F. Vaca Chávez and K. Saalwächter. NMR Observation of Entangled Polymer Dynamics: Tube Model Predictions and Constrained Release. *Physical Review Letters*, 104:198305, 2010.
- [108] F. Vaca Chávez and K. Saalwächter. Time-Domain NMR Observation of Entangled Polymer Dynamics: Universal Behavior of Flexible Homopolymers and Applicability of the Tube Model. *Macromolecules*, 44:1549–1559, 2011.
- [109] K. Saalwächter, M. Klüppel, H. Luo, and H. Schneider. Chain Order in Filled SBR Elastomers: a Proton Multiple-Quantum NMR Study. *Appl. Magn. Reson.*, 27:401–417, 2004.
- [110] K. Saalwächter, B. Herrero, and M. A. López-Manchado. Chain Order and Cross-Link Density of Elastomers As Investigated by Proton Multiple-Quantum NMR. *Macromolecules*, 38:9650–9660, 2005.
- [111] W. Chassé, J. L. Valentin, G. D. Genesky, C. Cohen, and K. Saalwächter. Precise dipolar coupling constant distribution analysis in proton multiple-quantum NMR of elastomers. *J. Chem. Phys.*, 134:044907, 2011.
- [112] L. Jakisch, M. Garaleh, M. Schäfer, A. Mordvinkin, K. Saalwächter, and F. Böhme. Synthesis and Structural NMR Characterization of Novel PPG/PCL Conetworks Based upon Heterocomplementary Coupling Reactions. *Macromol. Chem. Phys.*, 219:1700327, 2017.
- [113] F. Furtado, J. Damron, M.-L. Trutschel, C. Franz, K. Schröter, R. C. Ball, K. Saalwächter, and D. Panja. NMR Observations of Entangled Polymer Dynamics: Focus on Tagged Chain Rotational Dynamics and Confirmation from a Simulation Model. *Macromolecules*, 47:256–268, 2014.
- [114] F. Vaca Chávez and K. Saalwächter. Time-Domain NMR Observation of Entangled Polymer Dynamics: Analytical Theory of Signal Functions. *Macromolecules*, 44:1560–1569, 2011.
- [115] R. Graf, A. Heuer, and H. W. Spiess. Chain-Order Effects in Polymer Melts Probed by  $^1\text{H}$  Double-Quantum NMR Spectroscopy. *Phys. Rev. Lett.*, 80:5738, 1998.
- [116] K. Saalwächter and A. Heuer. Chain Dynamics in Elastomers As Investigated by Proton Multiple-Quantum NMR. *Macromolecules*, 39:3291–3303, 2006.

## REFERENCES

---

- [117] W. Chassé, M. Lang, J.-U. Sommer, and K. Saalwächter. Cross-Link Density Estimation of PDMS Networks with Precise Consideration of Networks Defects. *Macromolecules*, 45:899–912, 2012.
- [118] J. E. Mark. *Physical properties of Polymers Handbook*. Springer, New York, 2007.
- [119] A. Eisenberg. Clustering of Ions in Organic Polymers. A Theoretical Approach. *Macromolecules*, 3:147, 1970.
- [120] S. Candau, A. Peters, and J. Herz. Experimental evidence for trapped chain entanglements: their influence on macroscopic behavior of networks. *Polymer*, 22:1504–1510, 1981.
- [121] T. Maruyama, M. Nakajima, S. Ichikawa, Y. Sano, H. Nabetani, S. Furusaki, and M. Seki. Small-Angle X-Ray Scattering Analysis of Stearic Acid Modified Lipase. *Biosci. Biotechnol. Biochem.*, 65:1003, 2001.
- [122] D. J. Kinning and E. L. Thomas. Hard-Sphere Interactions between Spherical Domains in Diblock Copolymers. *Macromolecules*, 17:1712, 1984.
- [123] T. Yan, K. Schröter, F. Herbst, W. H. Binder, and T. Thurn-Albrecht. Nanostructure and Rheology of Hydrogen-Bonding Telechelic Polymers in the Melt: From Micellar Liquids and Solids to Supramolecular Gels. *Macromolecules*, 47:2122–2130, 2014.
- [124] T. Yan, K. Schröter, F. Herbst, W. H. Binder, and T. Thurn-Albrecht. What Controls the Structure and the Linear and Nonlinear Rheological Properties of Dense, Dynamic Supramolecular Polymer Networks? *Macromolecules*, 50:2973, 2017.
- [125] F. H. Allen, O. Kennard, D. G. Watson, L. Brammer, A. G. Orpen, and R. Taylor. Tables of Bond Lengths determined by X-Ray and Neutron Diffraction. Part 1. Bond Lengths in Organic Compounds. *J. Chem. Soc. Perkin Trans. 2*, 0:S1, 1987.
- [126] E. J. Roche, R. S. Stein, T. P. Russel, and W. J. MacKnight. Small-Angle X-Ray Scattering Study of Ionomer Deformation. *J. Polym Sci. Polym. Phys. Ed.*, 185:1497, 1980.
- [127] D. L. Handlin, W. J. MacKnight, and E. L. Thomas. Critical Evaluation of Electron Microscopy of Ionomers. *Macromolecules*, 14:795, 1981.
- [128] M. S. Shannon and J. E. Bara. Properties of Alkylimidazoles as Solvents for CO<sub>2</sub> Capture and Comparisons to Imidazolium-Based Ionic Liquids. *Ind. Eng. Chem. Res.*, 50:8665, 2011.
- [129] C. Ye and J. M. Shreeve. Rapid and Accurate Estimation of Densities of Room-Temperature Ionic Liquids and Salts. *J. Phys. Chem. A*, 111:1456, 2007.

## REFERENCES

---

- [130] A. J. Arduengo III, R. L. Harlow, and M. Kline. A Stable Crystalline Carbene. *J. Am. Chem. Soc.*, 113:361, 1991.
- [131] J. Y. Z. Chiou, J. N. Chen, J. S. Lei, and I. J. B. Lin. Ionic liquid crystals of imidazolium salts with a pendant hydroxyl group. *J. Mater. Chem.*, 16:2972, 2006.
- [132] M. Lang and J.-U. Sommer. Analysis of Entangled Length and Segmental Order Parameter in Polymer Networks. *Phys. Rev. Lett.*, 104:177801, 2010.
- [133] J. D. Ferry. *Viscoelastic Properties of Polymers*. John Wiley and Sons, Toronto, 1980.
- [134] F. Kremer and A. Schönhals, editors. *Broadband Dielectric Spectroscopy*. Springer, Berlin, 2003.
- [135] K. Kunal, M. Paluch, C. M. Roland, J. E. Puskas, Y. Chen, and A. P. Sokolov. Polyisobutylene: A Most Unusual Polymer. *J. Polym. Sci. B. Polym. Phys.*, 46:1390–1399, 2008.
- [136] D. Richter, A. Arbe, J. Colmenero, M. Monkenbusch, B. Farago, and R. Faust. Molecular Motions in Polyisobutylene: A Neutron Spin Echo and Dielectric Investigation. *Macromolecules*, 31:1133–1143, 1998.
- [137] J. Wu, G. Huang, Q. Pan, J. Zheng, Y. Zhu, and B. Wang. An investigation on the molecular mobility through the glass transition of chlorinated butyl rubber. *Polymer*, 48:7653–7659, 2007.
- [138] U. H. Choi, Y. Ye, D. D.d.l.Cruz, W. Liu, K. I. Winey, Y. A. Elabd, J. Runt, and R. H. Colby. Dielectric and Viscoelastic Responses of Imidazolium-Based Ionomers with Different Counterions and Side Chain Lengths. *Macromolecules*, 47:777, 2014.
- [139] B. J. Gold, C. H. Hövelmann, N. Lühmann, N. K. Székely, W. Pyckhout-Hintzen, A. Wischnewski, and D. Richter. Importance of Compact Random Walks for the Rheology of Transient Networks. *ACS Macro Lett.*, 6:73–77, 2017.
- [140] M. Rubinstein and N. Semenov. Thermoreversible Gelation in Solutions of Associating Polymers. 2. Linear Dynamics. *Macromolecules*, 31:1386–1397, 1998.
- [141] M. Rubinstein and N. Semenov. Dynamics of Entangled Solutions of Associating Polymers. *Macromolecules*, 34:1058–1068, 2001.
- [142] J. Guo, R. Long, K. Mayumi, and C.-Y. Hui. Mechanics of a Dual Cross-Link Gel with Dynamic Bonds: Steady State Kinetics and Large Deformation Effects. *Macromolecules*, 49:3497–3507, 2016.
- [143] K. Mayumi, A. Marcellan, G. Ducouret, C. Creton, and T. Narita. Stress-Strain Relationship of Highly Stretchable Dual Cross-Link Gels: Separability of Strain and Time Effect. *ACS Macro Lett.*, 2:1065–1068, 2013.

## REFERENCES

---

- [144] P. J. Skrzyszewska, J. Sprakel, F. A. de Wolf, R. Fokkink, M. A. Cohen Stuart, and J. van der Gucht. Fracture and Self-Healing in a Well-Defined Self-Assembled Polymer Network. *Macromolecules*, 43:3542–3548, 2010.
- [145] P. B. Rapp, A. K. Omar, B. R. Silverman, Z.-G. Wang, and D. A. Tirell. Mechanisms of Diffusion in Associative Polymer Networks: Evidence for Chain Hopping. *J. Am. Chem. Soc.*, 140:14185–14194, 2018.
- [146] L. J. Fetters, W. W. Graessley, and A. D. Kiss. Viscoelastic Properties of Polyisobutylene Melts. *Macromolecules*, 24:3136–3141, 1991.
- [147] K. Kunal, M. Paluch, C. M. Roland, J. E. Puskas, Y. Chen, and A. P. Sokolov. Polyisobutylene: A Most Unusual Polymer. *J. Polym. Sci. Part B Polym. Phys.*, 46:1390–1399, 2008.
- [148] New multiphase thermoplastic elastomers by combination of covalent and association-chain structures. C. Hilger and R. Stadler. *Makromol. Chem.*, 191:1347–1361, 1990.
- [149] G. Holden and H. R. Kricheldorf and R. P. Quirk, editor. *Thermoplastic elastomers*. Hanser, Munich, 2004.
- [150] R. A. Weiss, J. J. Fitzgerald, and D. Kim. Viscoelastic Behavior of Lightly Sulfonated Polystyrene Ionomers. *Macromolecules*, 24:1071–1076, 1991.
- [151] J. Ramirez, T. J. Dursch, and B. D. Olsen. A Molecular Explanation for Anomalous Diffusion in Supramolecular Polymer Networks. *Macromolecules*, 51:2517–2525, 2018.
- [152] M. Wübbenhorst and J. van Turnhout. Analysis of complex dielectric spectra. I. One-dimensional derivative techniques and three-dimensional modelling. *J. Non-cryst. Solids*, 305:40–49, 2002.
- [153] Z. Zhang, C. Huang, R. A. Weiss, and Q. Chen. Association energy in strongly associative polymers. *J. Rheol.*, 61:1199, 2017.
- [154] A. Susa, A. Mordvinkin, K. Saalwächter, S. v. d. Zwaag, and S. J. Garcia. Identifying the Role of Primary and Secondary Interactions on the Mechanical Properties and Healing of Densely Branched Polyimides. *Macromolecules*, 51:8333–8345, 2018.

## Acknowledgments

First of all, I would like to express my deep gratitude to my supervisor Prof. Dr. Kay Saalwächter who gave me the opportunity to work on this interesting project. His continuous support and motivation as well as immense knowledge in the fields of NMR and polymer science have predetermined successful unraveling of many scientific mysteries which we encountered in the framework of my project. Furthermore, I benefited a lot from the results he obtained during his research stay at Penn State University. I should not also forget to thank him for the opportunity to visit various international conferences and, specifically, for enabling my further development by doing a research stay at ESPCI, Paris.

Also, I would like to acknowledge all my collaborators for their advice and fruitful discussions. Special thanks go to: Diana Döhler and Prof. Dr. Wolfgang H. Binder as well as Marcus Suckow and Dr. Frank Böhme for providing me with telechelic PIB and ionic BIIR samples, respectively. I always appreciated how fast you answered all my e-mails and addressed my doubts and questions. I wish myself only such collaborators in the future. In addition, I would like to thank my mentor in the iRTG program Prof. Dr. Thomas Thurn-Albrecht for his support and helpful advice at our meetings.

Certainly, I would like to thank all my colleagues in the NMR group for your support, unforgettable time, and a lot of fun we had inside and outside of work. Particularly, I would like to thank Frank Lange and Marie-Luise Trutschel, my first office mates, who considerably helped me at the beginning of my work not only with technical aspects of NMR experiments, but also with learning German language. Furthermore, I would like to thank my current office mates Maria Camilles and Farhad Shahsavan for a pleasant working atmosphere and a lot of fun we had during making games for after-defense entertainment.

Finally, my very special and sincere thanks go to my family. I am deeply indebted to my parents for constant believing in me and for their mental and financial support, without which it would not have been possible to obtain education in Germany. Last but not least, I would like to thank my wife Zhanna Evgrafova, a person who gives me the power to keep going every day. Thank you very much for your love, care, support, and your amazing pieces of life advice that kept me sane during my entire PhD.



# Curriculum Vitae

## Personal data

Name: Anton Mordvinkin  
Date of birth: 13.07.1989  
Place of birth: Volzhsky, Russia  
Nationality: Russian

## Education

11/2014 – present     Doctoral Studies  
                                 MLU Halle-Wittenberg  
10/2012 – 10/2014     Master of Science  
                                 MLU Halle-Wittenberg  
09/2006 – 06/2011     Diploma  
                                 D. Mendeleev University of Chemical Technology of Russia  
                                 Moscow  
09/1996 – 06/2006     School no. 32 "UNESCO Associated School Eureka-Development"  
                                 Volzhsky

## Work Experience

11/2014 – 12/2019     Research assistant  
                                 MLU Halle-Wittenberg  
09/2011 – 09/2012     Chemical engineer  
                                 Medical company AVANSEPT MEDICAL  
                                 Moscow  
11/2009 – 06/2011     Chemical analyst  
                                 Scientific production company Technoprom  
                                 Moscow

Halle (Saale), August 2019

Anton Mordvinkin



## List of publications

1. [A. Mordvinkin](#), M. Suckow, F. Böhme, R. H. Colby, C. Creton, and K. Saalwächter. Hierarchical Sticker and Sticky Chain Dynamics in Self-Healing Butyl Rubber Ionomers. *Macromolecules*, 52:4169–4184, 2019.
2. A. Susa, [A. Mordvinkin](#), K. Saalwächter, S. v. d. Zwaag, and S. J. Garcia. Identifying the Role of Primary and Secondary Interactions on the Mechanical Properties and Healing of Densely Branched Polyimides. *Macromolecules*, 51:8333–8345, 2018.
3. M.-L. Trutschel, [A. Mordvinkin](#), F. Furtado, L. Willner, and K. Saalwächter. Time-Domain NMR Observation of Entangled Polymer Dynamics: Focus on All Tube-Model Regimes, Chain Center, and Matrix Effects. *Macromolecules*, 51:4108, 2018.
4. L. Jakisch, M. Garaleh, M. Schäfer, [A. Mordvinkin](#), K. Saalwächter, and F. Böhme. Synthesis and Structural NMR Characterization of Novel PPG/PCL Conetworks Based upon Heterocomplementary Coupling Reactions. *Macromol. Chem. Phys.*, 219:1700327, 2018.
5. M. Suckow, [A. Mordvinkin](#), M. Roy, N. K. Singha, G. Heinrich, B. Voit, K. Saalwächter, and F. Böhme. Tuning the Properties and Self-Healing Behavior of Ionically Modified Poly(isobutylene-*co*-isoprene) Rubber. *Macromolecules*, 51:468, 2018.
6. S. Chen, T. Yan, M. Fischer, [A. Mordvinkin](#), K. Saalwächter, T. Thurn-Albrecht, and W. H. Binder. Opposing Phase-Segregation and Hydrogen-Bonding Forces in Supramolecular Polymers. *Angew. Chem. Int. Ed.*, 56:13016–13020, 2017.
7. (a) [A. Mordvinkin](#) and K. Saalwächter. Microscopic observation of the segmental orientation autocorrelation function for entangled and constraints polymer chains. *J. Chem. Phys.*, 146:094909, 2017; (b) [A. Mordvinkin](#) and K. Saalwächter. Erratum: "Microscopic observation of the segmental orientation autocorrelation function for entangled and constraints polymer chains" [*J. Chem. Phys.* 146, 094902 (2017)]. *J. Chem. Phys.*, 148:089901, 2018.



## **Eidesstattliche Erklärung**

Hiermit versichere ich, dass ich die vorliegende Arbeit selbstständig und ohne fremde Hilfe verfasst, andere als die von mir angegebenen Quellen und Hilfsmittel nicht benutzt und die den benutzten Werken wörtlich oder inhaltlich entnommenen Stellen als solche kenntlich gemacht habe.

Ich erkläre, dass ich keine anderweitigen Promotionsversuche unternommen habe, und die vorliegende Dissertation weder in der jetzigen noch in einer anderen Fassung einer anderen wissenschaftlichen Einrichtung vorgelegt wurde.

Halle (Saale), den. 20.08.2019

Anton Mordvinkin